Quantification and impact of microcarrier collisions during mesenchymal stem cell culture in bioreactors

Charlotte Maillot

École doctorale 608 : Sciences et Ingénierie des Molécules, des Produits, des Procédés et de l'Énergie

THÈSE

Présentée et soutenue publiquement pour l'obtention du grade de

Docteur en Génie des Procédés, des Produits et des Molécules

Université de Lorraine

Et

Docteur en Sciences de l'Ingénieur

Université de Liège

Par

Charlotte Maillot

le 16 Décembre 2022

Quantification and impact of microcarrier collisions during mesenchymal stem cell culture in bioreactors

Thesis supervisor : **Pr. Eric Olmos**
Thesis co-supervisors : **Pr. Dominique Toye & Dr. Natalia De Isla**

Jury

Pr. Joaquim Cabral,	University of Lisbon, Portugal	Reviewer
Pr. Jérôme Morchain,	University of Toulouse, France	Reviewer
Dr. Amanda Brun,	University of Paris, France	President
Dr. Angélique Delafosse,	University of Liège, Belgium	Invited
Pr. Eric Olmos,	University of Lorraine, France	Thesis supervisor
Pr. Dominique Toye,	University of Liège, Belgium	Thesis co-supervisor
Dr. Natalia De Isla,	University of Lorraine, France	Thesis co-advisor

Université de Lorraine
Laboratoire Réactions et Génie des Procédés (LRGP)
UMR CNRS 7274, Nancy, FRANCE

Acknowledgments

Les travaux présentés ici ont été menés au sein de l'équipe BioProMo du laboratoire des réactions et génie des procédés (LRGP) de l'Université de Lorraine à Nancy, en cotutelle avec le laboratoire products environment and processing (PEPS) de l'université de Liège et en co-encadrement avec l'unité mixte de recherche 7365 ingénierie moléculaire et physiopathologie articulaire (IMoPA) de Nancy. Je tiens à remercier le Dr. Laurent Falk, directeur du LRGP de m'avoir accueuilli au sein de son laboratoire pendant ces travaux ainsi que l'équipe PEPS à Liège.

Je remercie également le Pr. Joaquim Cabral ainsi que le Pr. Jérôme Morchain de rapporter ma thèse. De plus, j'aimerais remercier Dr. Amanda Brun et Dr. Angélique Delafosse d'avoir accepté d'évaluer le travail effectué en tant qu'examinatrice et membre du Jury respectivement.

De plus, je souhaite remercier chaleureusement mes encadrant(e)s de thèse pour leur accompagnement, soutien et précieux conseils lors de ces travaux. Un grand merci à Natalia d'avoir apporté ton expértise dans ce travail, aiguillé les études et facilité les échanges avec l'IMoPA. Merci Dominique pour ta disponibilité, tes questions et remarques toujours pertinentes, et ta bonne humeur pendant l'encadrement sur 3 ans. Malgré les conditions particulières liées à l'épidémie de Covid, nous avons toujours réussi à touver des solutions pour maintenir la part des travaux réalisés à Liège. Les allers-retours pendant 48 h en Wallonie ont rhythmée une partie de ma deuxième année et ont toujours été fait avec grand plaisir! Ces séjours fractionnés m'ont enrichi tant d'un point de vu personnel (je sais maintenant que l'expérience de la boulette liégoise n'est pas à renouveller) que professionnel (j'ai pu voir des équipements que je n'aurais jamais imaginé pouvoir comprendre ni utiliser). Pour terminer, évidemment j'aimerais remercier Eric pour tout ton soutien au cours de ces trois années. En trois ans de thèse tu as réussi à toujours être là pour chacune de mes questions, pour m'aider dans tous mes problèmes (l'approvisionnement plus ou moins aléatoire des matières premières, le vol de mon PC en fin de deuxième année, un confinement imposé alors que les travaux venaient de commencer *etc.*). Que ce soit autour d'un café, d'une bière, lors d'un aller-retour à Liège, je ne pourrais pas oublier toutes ces discussions. Un vrai grand merci à toi !

En parallèle j'aimerais évidemment remercier tous ceux qui ont participé à ma santé mentale pendant 3 ans (et accessoirement aussi, à une part sa dégradation). Je ne pourrais commencer par d'autres que mes mentors, mes modèles, mes idloles : la team Trop Mimi. Jonathan, ta capacité à aider les autres et remonter le moral est vraiment extraordinaire. Même si j'ai peut être essayé de te tuer quelques fois dans les Vosges, tu n'a jamais cessé de partager des photos pour remonter le moral quand les cultures ne voulaient pas pousser. Ton apport de smarties a non seulement aidé à ma créativité

(je me sens actuellement en mesure de devenir achitecte), mais aussi à renforcer ma maniaquerie. Heureusemnt qu'il y avait Dr. Caro pour contrer ça dans notre bureau. Merci Caro de m'avoir formé, aidé, et soutenu pendant ces années de thèse. Ca fait du bien de pouvoir parler avec quelqu'un qui a, elle aussi, passé ses weekends au labo devant un microscope... Et merci aussi à Anne, Adrien, Noum, Emile, Céline et Julien qui ont fait parti des rencontres qui m'ont fait du bien pendant ces années! Enfin merci aux vrais Best Of du LRGP : Bastien, Marine et Astrid (TeamCultureCell) de m'avoir supporté pendant la fin de rédaction mais aussi aux autres Best Of du LRGP Emma, Xavier, Alaric, Liliane, Delphine, Eusebe, Laureline, Ibrahima et tous les autres membres permanents ou non du LRGP ainsi que tous les membres de l'équipe à Liège avec qui j'ai pu partager un café ou le déjeuner. Enfin, j'aimerais remercier Angélique, Naceur, Mégane et Amandine sans qui une partie de ce travail n'aurait pas été possible.

Un grand merci à la meilleure coloc de Nancy (Audrey, Amélia et Nico sans oublier pistache et gros chat), mais aussi au meilleur voisin de Nancy (Charlie le meilleur!), et aux meilleurs presques voisins de Nancy, Ludivine et David. Je pense que sans les nuits de Catan, de Living Forest, de Dice Forge (je ne vais malhereusement pas pouvoir nommer tous mes jeux préférés), je n'aurais jamais tenu 3 ans à Nancy. Merci aux joueurs des clubs de badminton du Grand Est (dont il est peu probable que quelqu'un lise un jour ces lignes mais qui ont aussi fait pour moi partie des rencontres inoubliables).

J'aimerais aussi remercier Annael, Maelys, Jeanne, Pauline, Olivia, Thierry, Victor, Pouya, Marc, Mike et probablement 1 milliard d'autres ; parcequ'il est evident pour moi que ces dernières années m'ont apporté beaucoup plus que ce qui est écrit dans ce manuscrit. Que ce soit des discussions sur le traitement de données acoustiques avec Thierry dans les pré-Alpes, une mise à plat de mon code Matlab avec Annael à Lyon, ou des discussions sur le les femmes dans monde de la recherche avec Pauline et Olivia dans le Jura, vous êtes tou(te)s dans ce manuscrit sous une forme plus ou moins cachée!

Enfin j'aimerais remercier André Simon qui m'a encouragé pendant toutes ces années. Je n'ai connu personne de plus fière que lui du travail mené et de mon choix de faire une thèse. Ma thèse, soutenue 50 ans après la sienne dans la même ville de Nancy, lui est dédicacé.

Contents

List of Figures

List of Tables

Nomenclature

Variables

C	Impeller off bottom clearance	m
C_M	Coefficient of cell membrane electrical properties	$\mathrm{F\,m^{-2}}$
D	Impeller diameter	m
D_{32}	Mean sauter diameter	m
d_p	Particle diameter	m
E_c	Energy of a particle-particle collision	J
F_c	Critical polarization frequency	Hz
g	Gravity component	$\mathrm{m\,s^{-2}}$
h	Average inter-particle distance	m
H_l	Liquid height	m
k	Kinetic decay constant (Chap 2)	$\mathrm{h^{-1}}$
$k_{collision}$	Collision constant (Chap 2)	$\mathrm{h^{-1}}$
m	Mass	g
N	Agitation rate	$\mathrm{s^{-1}}$
P	Power	W
P	Pressure	Pa
Q	Flow rate	$\mathrm{m^3\,s^{-1}}$
$q_{A/B}$	Specific rate of consumption or production of A from B	$\mathrm{g\,g^{-1}\,h^{-1}}$
$r_{aggreg.}$	Average radius of microcarrier-cell aggregates	m
T	Tank diameter	m
T	Temperature	K or °C
t	Time	h
u	Velocity	$\mathrm{m\,s^{-2}}$
V	Volume	$\mathrm{m^3}$
X	Viable cell density	–
X_p	Particle Mass Fraction	$\mathrm{g\,l^{-1}}$
$Y_{A/B}$	Transformation yield of A from B	$\mathrm{g\,g^{-1}}$

Greek letters

α	Volume fraction (microcarriers)	$\mathrm{m^3\,m^{-3}}$
α_{dielec}	Permittivity slope	$\mathrm{pF\,cm^{-1}\,MHz^{-1}}$
β	Volume fraction (particles)	$\mathrm{m^3\,m^{-3}}$
ϵ_{dielec}	Permittivity	$\mathrm{pF\,cm^{-1}}$
λ_k	Kolmogorov length	m
μ	Specific growth rate	$\mathrm{d^{-1}}$
μ_l	Liquid viscosity	Pa s
μ_{app}	Specific apparent growth rate	$\mathrm{d^{-1}}$
μ_{max}	Specific maximum growth rate	$\mathrm{d^{-1}}$
ν_l	Liquid kinematic viscosity	$\mathrm{m^2\,s^{-1}}$

Ψ	Theoretical growth rate without particle interactions (Chap 2)	–
ρ	Density	$\mathrm{kg\,m^{-3}}$
τ_k	Kolmogorov time scale	$\mathrm{Pa\,s}$
τ_p	Particle relaxation time	$\mathrm{Pa\,s}$
ε	Turbulent energy dissipation	$\mathrm{m^2\,s^{-3}}$

Dimensionless number

Fr	Froude number	–
N_p	Power number	–
N_Q	Pumping number	–
N_Q	Pumpung / Flow number	–
N_js	Just-suspended agitation rate	–
Re	Reynolds number	–
St	Stokes number	–

Subscripts

f	Final
i	Initial
js	Just-suspended
kin	Kinetic
l	Liquid
max	Maximum
obs	Observed
p	Particle
ref	Reference
s	Solid
v	Volume
w	Weight

Abbreviations

API	Active Pharmaceutical Ingredient
ASC	Adult Stem Cell
AT	Adipose Tissue
ATF	Alternate Tangential Flow
ATMP	Advanced Therapy Medicinal Product
ATP	Adenosin Tri-Phosphate
BM	Bone Marrow
CFD	Computational Fluid Dynamics
CFR	Code of Federal Regulations
cGMP	Current Good Manufacturing Practices
cGMP	Current Good Manufacturing Practise
CHO	Chinese Hamster Ovary
CPP	Critical Process Parameter
CQA	Critical Quality Attribute
DNA	DeoxyriboNucleic Acid
DOE	Design of Experiments
EC	Embryonic Carcinoma
EEd	Elephant-Ear down impeller
EF	Erlenmeyer Flasks
EMA	European Medicines Agency

ESC	Embryonic Stem Cell
EU	European Union
FDA	Food and Drug Administration
FFT	Fast Fourier Transform
FMEA	Failure Modes and Effects Analysis
FTIR	Fourier Transform Infrared Technology
GDP	Gross Domestic Product
HLA	Human Leukocyte Antigen
HPL	Human Platelet Lysate
HTPGd	HTPG down impeller
ICH	International Conference on Harmonisation
IL	InterLeukin
IMP	Investigational Medicinal Product
IND	Investigational New Drug
iPSC	Induced Pluripotent Stem Cell
ISCT	International Society for Cellular Therapy
mAB	Monoclonal Antibody
MHC	Major Histocompatibility Complex
MSC	Mesenchymal Stem Cell
NK	Natural Killer
OPV	Ongoing Process Verification
OTR	Oxygen Transfer rate
OUR	Oxygen Uptake Rate
PAT	Process Analytical Technologies
PD	Population Doublings
QBD	Quality By Design
QTTP	Quality Target Product Profile
ROS	Reactive Oxygen Species
RPN	Risk Priority Number
RT4B	4-bladed Rushton turbine
RT6B	6-bladed Rushton turbine
SF	Spinner Flasks
STR	Stirred Tank Reactor
TCD	Total Cell Density
TFF	Tangential Flow Filtration
UC	Umbilical Cord
VCD	Viable Cell Density
WHO	World Health Organization
WJ	Wharton's Jelly

Introduction

Advanced therapy medicinal products or (ATMPs) are innovative medicines used for humans that are based on genes, tissues or cells. They are typically classified into three main types of medicines, (1) gene therapy medicines which work by inserting recombinant genes into a patient to address genetic disorders, cancer or long term diseases, (2) somatic cell therapy medicines which contain cells or tissues that have been manipulated to change their biological characteristics or expanded ex-vivo to cure, diagnose or prevent diseases, and (3) tissue engineered medicines which contain cells or tissues that have been modified so they can be used to repair, regenerate or replace human tissues (Figure 1). The use of Mesenchymal Stem Cells (MSC's) in clinical trials matches the definition provided by the European Medicines Agency (EMA) for applications as both somatic cell therapy medicines and tissue engineered medicines depending on the clinical application targeted and mode of action proposed.

Specifically, the use of MSCs in the pharmaceutical industry has been flourishing since the discovery of the remarkable microenvironment that these cells provide when tissue damage occurs [1]. Contrary to general beliefs, MSCs seem to exert their function by orchestrating progenitor cells to execute tissue specific repair responses and not through their *in vivo* differentiation in damaged tissues [2]. Their therapeutic effects have been attributed to immunomodulatory and trophic bioactive factors secreted along with cell contact mediated responses [3–5]. Fundamental understanding of the therapeutic properties of MSCs has encouraged their use as innovative cell therapy candidates to treat a variety of diseases including bone/cartilage, heart, neuro degenerative, autoimmune and lung diseases which are mediated by *ex vivo* tissue engineering strategies, MSC transfusion, or the injection of secreted bioactive products. As a result, and according to the final clinical use, the production strategy of MSCs has various constraints concerning cell quality or their produced molecules.

Nonetheless, the amount of MSC's which can be extracted from a single donor are, in general, not sufficient to meet clinical needs. As a result, an ex-vivo expansion phase is required, traditionally performed using monolayer or multilayer flasks of different sizes. Although this method of expansion is well documented in literature, it is labour intensive due to the required manual passaging of cells between different

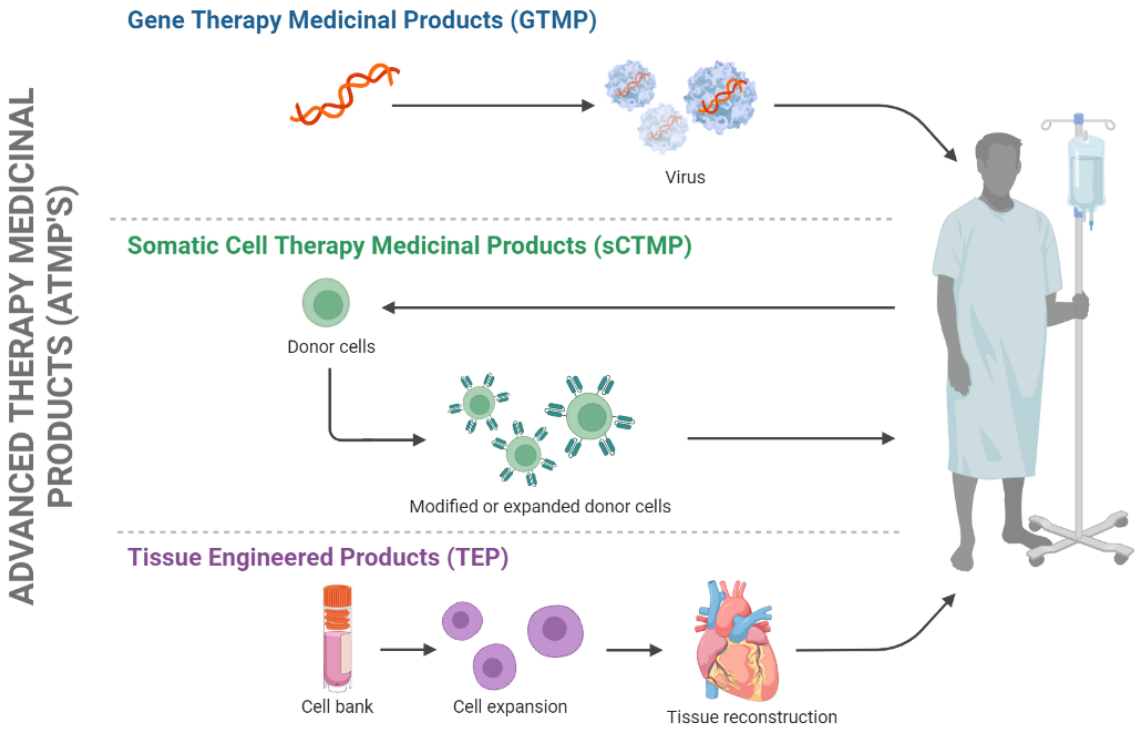

Figure 1: Different Advanced Therapy Medicinal Products (ATMPs) and their classification according to the European Medicines Agency (EMA).

containers. Furthermore, the risk of contamination increases with the number of container systems and passages, increasing GMP production complexity. For larger scale manufacturing, a shift to 3D cultures in easily scalable bioreactors may be a solution to simplify the expansion phase and increase process productivity while reducing the risk of contaminations and GMP production costs. In order to do so, the adherent MSC's can be cultured on small micro-particles in suspension (microcarriers) on which they can expand. However, data concerning MSC cell culture in bioreactors and using microcarriers still remain scarce and the fine-tuning of process parameters (such as agitation methods, medium composition, feeding strategy etc.) to increase yield and quality is still in early stages of development. To our knowledge, out of the 1468 clinical trials involving MSC's (search performed on clinicaltrials.gov in October 2022 suing key words "mesenchymal stem cell"), no clinical studies using a bioreactor-based MSC expansion strategy have been or are ongoing.

In this mindset, understanding the hydro-mechanical constraints that take place in an agitated bioreactor during MSC cell cultures on microcarriers is a prerequisite to optimize bioreactor geometry and agitation conditions. For this, various studies have been focused on understanding the fluid dynamics of agitated bioreactors leading to a consensus for an optimal agitation rate at or close to the just suspended state N_{js} (i.e. when all particles are in suspension and stay restless close to the bottom of the tank for only a few seconds) [6, 7]. However, little is known on the impact of the particles

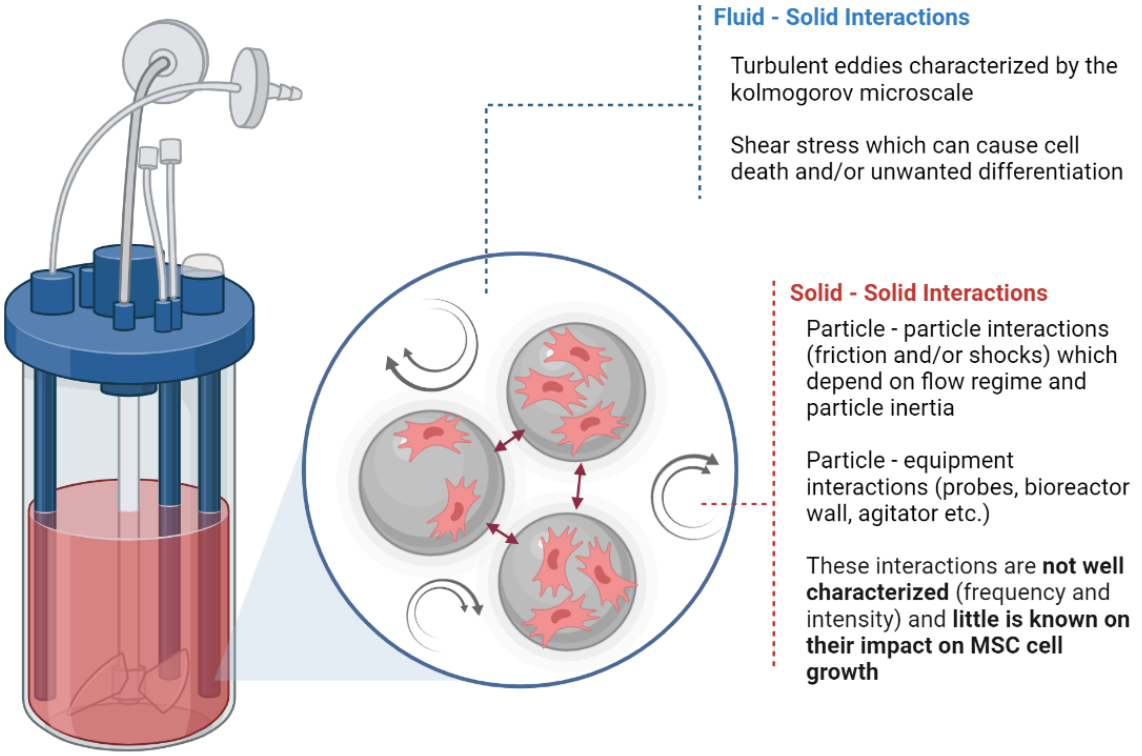

Figure 2: Hydrodynamic parameters involved during MSC cell culture on microcarriers in Bioreactors.

themselves (microcarrier friction or collisions) on cell culture performance (growth rate, lag phase, cell death, aggregation...) and cell quality (differentiation, genetic stability, senescence...). In addition, these hydromechanical constraints may have different impacts in both steady state (N_{js}) and transient agitation regimes microcarrier settling and/or microcarrier re-suspension) (Figure 2).

In order to fully understand the impact of microcarrier collisions on MSC's, it is important to know the quantity and intensity of the shocks that cells perceive continuously during cell culture. These constraints ill ultimately depend on the bioreactor geometry (impeller geometry, tank geometry, quantity of plunging elements etc.) as well as the microcarrier characteristics (size, porosity, rigidity etc.) and on the agitation characteristics during the dynamic phases in the process. In this mindset, several experimental approaches to understand these mechanical constraints were proposed in view of aiding the successful use of these types of processes. The results obtained will be presented in four chapters.

- **Chapter 1** presents a literature review of experimental approaches that may be used as a basis for the quantification of microcarrier-microcarrier collisions. For this, the ways in which MSCs exert their therapeutic potential will be presented as well as existing technologies for the expansion of MSCs in small and large scales. In addition, methods for the quantification of microcarrier-microcarrier

collisions will be presented.

- **Chapter 2** details results obtained in small scales (Erlenmeyer and spinner flasks) which aimed at evaluating the impact that particle collisions could have on MSCs grown on microcarriers. For this, MSC cultures on microcarriers were performed at different concentrations and by adding plastic particles during expansion. Accordingly, cell cultures were performed with varying levels of particle collisions.

- **Chapter 3** details two experimental approaches to determine particle-particle collisions in a 700 mL bioreactor. For this, the evolution of local particle concentrations were evaluated for different particle concentrations as well as how these local particle concentrations evolved during suspension. The analysis were based on light attenuation measures of Cytodex-1 particles. In addition, acoustic signals were measured in the same bioreactor to which large particles were added. Changing agitator size and shape was used to define if particle-sensor collisions could be modelled in these conditions.

- **Chapter 4** finally describes the impact of particle-particle interactions on MSC growth in a 700 mL bioreactor. For this, mechanical stresses were generated either by adding plastic particles (in conditions that could be compared to conditions presented in Chapter 2) or by performing intermittent agitation cycles.

Bibliography

[1] T. R. Olsen, K. S. Ng, L. T. Lock, T. Ahsan, and J. A. Rowley. Peak msc — are we there yet? *Frontiers in medicine*, 5:178, 2018.

[2] H. Yagi, A. Soto-Gutierrez, B. Parekkadan, Y. Kitagawa, R. G. Tompkins, N. Kobayashi, and M. L. Yarmush. Mesenchymal stem cells: Mechanisms of immunomodulation and homing. *Cell Transplantation*, 19(6):667–679, 2010.

[3] K. English. Mechanisms of mesenchymal stromal cell immunomodulation. *Immunology & Cell Biology*, 91(1):19–26, 2013.

[4] M. Honczarenko, Y. Le, M. Swierkowski, I. Ghiran, A. M. Glodek, and L. E. Silberstein. Human bone marrow stromal cells express a distinct set of biologically functional chemokine receptors. *Stem Cells*, 24(4):1030–1041, 2006.

[5] A. M. Betancourt. New cell-based therapy paradigm: induction of bone marrow-derived multipotent mesenchymal stromal cells into pro-inflammatory msc1 and anti-inflammatory msc2 phenotypes. *Mesenchymal Stem Cells-Basics and Clinical Application II*, pages 163–197, 2012.

[6] A. C. Schnitzler, A. Verma, D. E. Kehoe, D. Jing, J. R. Murrell, K. A. Der, M. Aysola, P. J. Rapiejko, S. Punreddy, and M. S. Rook. Bioprocessing of human mesenchymal stem/stromal cells for therapeutic use: current technologies and challenges. *Biochemical Engineering Journal*, 108:3–13, 2016.

[7] C. Loubière, C. Sion, N. De Isla, L. Reppel, E. Guedon, I. Chevalot, and E. Olmos. Impact of the type of microcarrier and agitation modes on the expansion performances of mesenchymal stem cells derived from umbilical cord. *Biotechnology Progress*, 35(6):e2887, 2019.

Chapter 1

State of the Art

Contents

1.1 Human mesenchymal stem cells and their characteristics

1.1.1 Breakthroughs and characterization of human stem cells

Our current understanding of the human body undeniably takes its roots from pioneering work performed in the 17^{th} century by Antoine Van Leeuwenhoek and his development of single lensed microscopes, which launched a series of groundbreaking scientific discoveries towards understanding the way in which living organisms are organized and function. In particular, by prototyping over 25 different microscopes, the Dutch scientist successfully observed and described various unicellular organisms including freshwater protozoa or large bacteria species isolated from the human mouth [1]. Specifically, his correspondence with the English scientist Robert Hook led to the first notion of *the cell* as an autonomous structure. These discoveries were further expanded in Mattias Schleiden and Theodor Schwanns cell theory that all living organisms either consist of a single cell or are composed of cells which grow and divide [2], and through Rudolf Ludwig Karl Virchow's vision postulating that all cells derive from pre-existing cells : *Ominis cellula e cellula* [3]. These theories, and the decades of scientific research which resulted from them, have led us to the current notion that cells can be considered as the building blocks of life, capable of assembling into complex structures at different scales through orchestrated division and differentiation. In this context, the precursors of our tissues and organs, now defined as stem cells, have a considerable role to play in maintaining and repairing the various structures that compose us. In addition, gaining information on how our cells continuously regenerate throughout our lives via these precursor cells can also be used to understand and model various pathologies, their evolution, and ways to mitigate their risks.

Discovering stem cells

The term "Stem Cell" was initially used to describe cells in early embryonic stages of development. In 1868, German scientist Ernst Haeckel first characterized a fertilized egg as a *stammzelle*, an evolutionary concept to describe precursor cells which can give rise to all of the different cell types of a multi-cellular organisms [4] (Figure 1.1). Two German zoologists Theodor Boveri and Valentin Haecker further characterized stem cells by proposing that they have (1) a self-renewal capacity and (2) the capacity to form different cell types (the authors described first elements of pluripotency) [5]. Interestingly, John Gurdon observed in the early 1960s that cells are not locked in their differentiation state but rather that differentiation has certain reversible aspects. He demonstrated this principle by showing that it was possible to obtain an adult fertile frog after injecting a differentiated frog cell nucleus into an egg cell from which the nucleus had been removed (technique later used to clone Dolly the sheep) [6]. As a

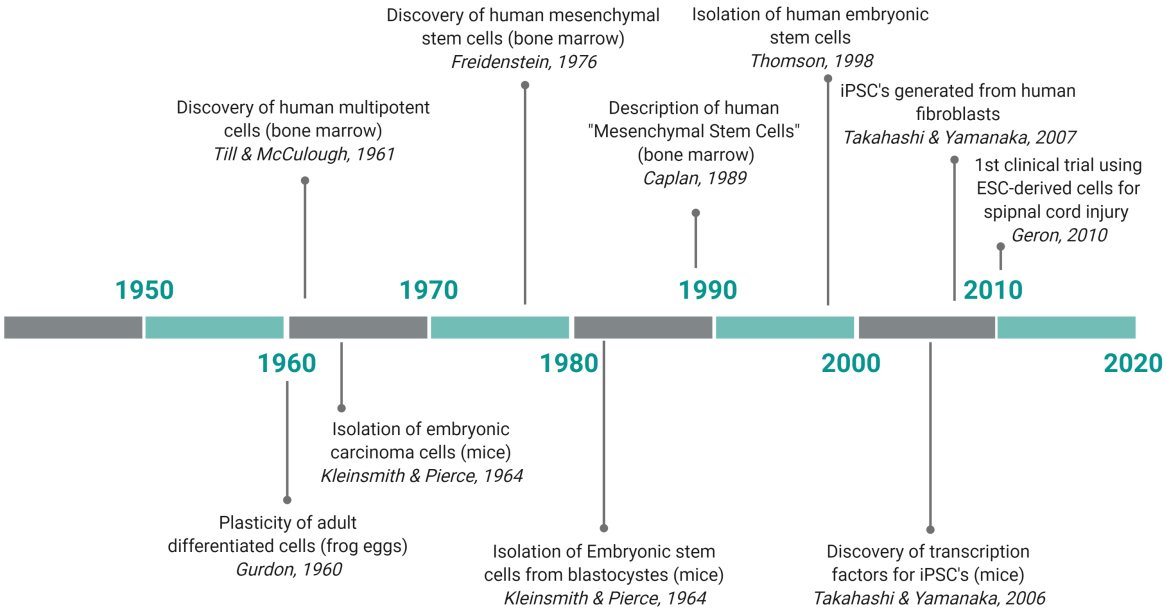

Figure 1.1: Major events and scientific advances concerning stem cell research.

result, differentiated cells retain the information required to give rise to all cell types in the body. In parallel, the isolation of cells resembling early embryonic cells from mice terato-carcinomas was performed in 1964 by Kleinsmith and Pierce and called embryonic carcinoma (EC) cells. These cells were found to meet the definition of pluripotent stem cells proposed at the time (*i.e.* self-renewal and differentiation capacities). EC cells, however, were not ideal pluripotency models due to their aneuploid karyotype.

In addition, the notion of stem cells as precursors for differentiated tissue cells in adult organs was demonstrated in 1961 by Canadian scientists James Till and Ernest McCulloch. The authors showed the existence of bone marrow cells which could proliferate and generate various differentiation levels of hematopoietic tissue in the spleens of animals exposed to super-lethal irradiation doses [7]. Several years later, in 1976, these cells were successfully isolated from bone marrow by Freidenstein and colleagues and later shown to have the capacity to differentiate *in vitro* into cells from mesenchymal lineages. They were subsequently named mesenchymal stem cells (MSCs) by Caplan and colleagues in 1989 (summarized in [8]).

More recently, in 1981, Martin Evans and Matt Kauffman successfully identified, isolated and cultured embryonic stem (ES) cells from mouse blastocytes (Nobel prize, 2007 [9]). This study proved to be a turning point in the study of stem cells, since ES cells could now be used in experiments outside the blastocyte. In 1998, the isolation of the first human ES cells was performed by American scientist James Thomson. These studies were not without ethical concerns and protests which ultimetely led the U.S. President George W. Bush to introduce a ban on federal funding for research on newly created human embryonic stem cell lines in 2001 (eventually revoked by President Barack Obama in 2009 [10]).

As described above, the notion of stemness and pluripotency was not only observed at different stages of development (embryonic vs adult cells) but also in different contexts (carcinoma vs healthy cells, for example). The definition of stem cells has evolved throughout the years and, in parallel, cells which match these unique properties have been discovered in various, and sometimes unsuspected, adult tissues.

MSC definition by the ISCT

The most widely accepted characteristics to define mesenchymal stem cells was proposed by the international society for cellular therapy (ISCT) [11]. This definition is based on three attributes which can easily be verified with sufficient equipment (Figure 1.2). To begin with, MSCs are adherent cells and therefore must have maintained adherence capacity in standard culture conditions. While it is possible to expand MSCs without adherence [12], these protocols typically require very specific culture conditions, and these cells, if maintained under more standard conditions, would be expected to demonstrate adherence in order to be considered as MSCs. In addition, MSCs are expected to have maintained multi-potency and thus have the capacity to differentiate, in defined *in-vitro* conditions, into specific mesenchymal cell lineages (osteoblasts, adipocytes and chondroblasts). Lastly, surface antigen expression, which can rapidly be used to identify cell populations through flow cytometry for example, has been used extensively to define and characterize stem cells. Accordingly, MSCs are expected to express defined surface markers including CD105, CD73 and CD90. In addition, the ISCT recommends to test a set of other surface markers associated with other cell types which are likely to be present in MSC cultures, typically hematopoietic cells. Testing for these additional cell markers ensures a sufficiently pure population of MSCs is obtained.

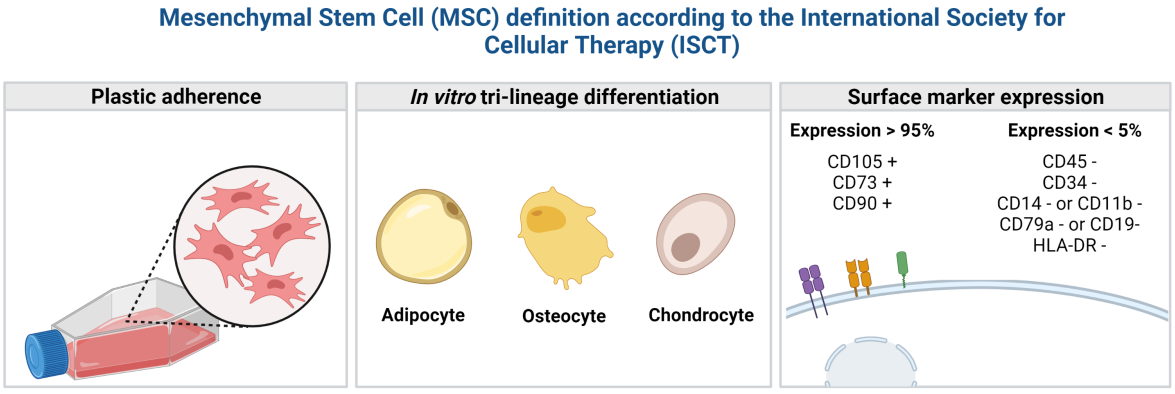

Figure 1.2: Criteria defining MSCs according to the international society for cellular therapy (ISCT).

Stem cell classification

As it has been described above, the spectra of cells which match the characteristics typically associated with stem cells is quite vast. To date, these cells are typically categorized depending on the level of differentiation (*i.e.* potency) that cells can undergo (Figure 1.3).

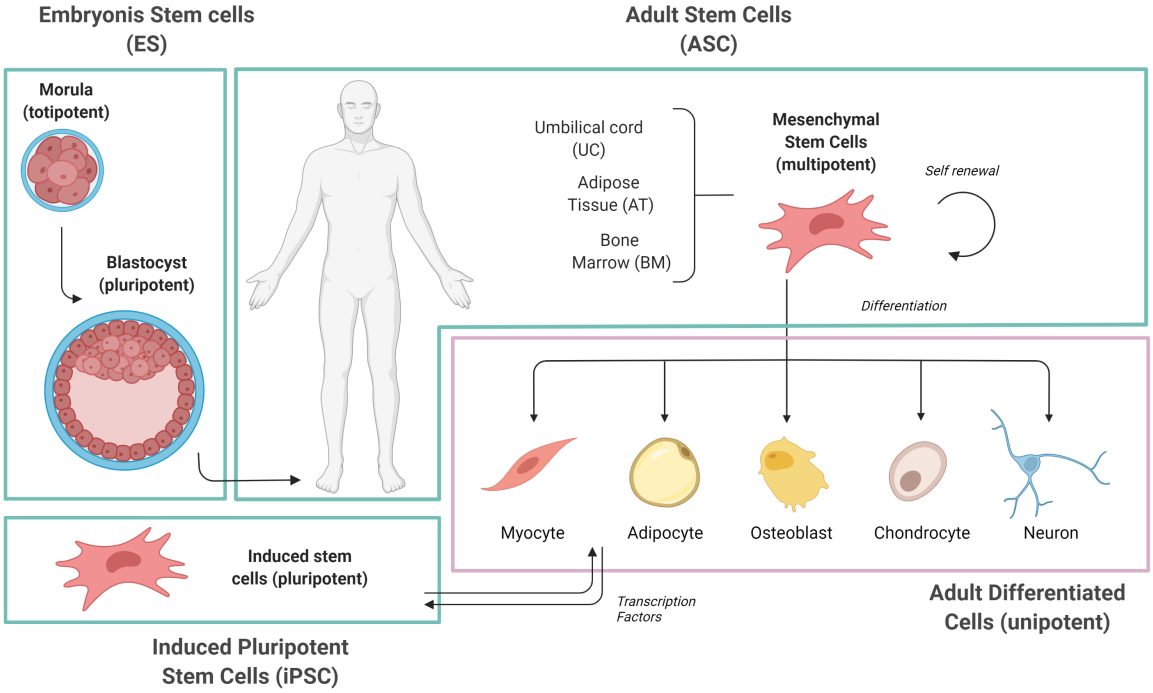

Figure 1.3: Schematic representation of stem cell classifications and their pluripotency.

Much like understanding how to grow trees from seeds, the core of stem cell research began with understanding embryology and the way human beings evolve from a single cell after fertilization. To begin with, *totipotent* stem cells have the capacity to develop into an entire living organism and can thus give rise to all of the cell types of this given organism. These early embryonic cells then give rise to *pluripotent* stem cells which compose the inner cell mass of the blastula. Although the pluripotent stem cells of the blastula can divide into most or all cell types of an organism, these cells alone are not able to develop into an entire organism. Further along embryogenesis, cells give rise to various tissues and evolve towards *multipotent* stem cells which are oriented towards certain specialized cells in specific cell lineages. Certain adult cell lines such as mesenchymal stem cells have maintained a multipotent phenotype, enabling functions of organ maintenance and repair through differentiation or, in certain cases trans-differentiation.

It can be noted that the presence of adult multipotent stem cells have been found in various tissues (summarized in [14]). The most common sources of MSCs used in clinical settings are adipose tissue (AT), bone marrow (BM) and umbilical cords (UC). Although cells from these different tissues meet the requirements to be considered

Table 1.1: Advantages and disadvantages of mesenchymal stem cells (MSCs) from bone marrow (BM), adipose tissue (AT), and umbilical cord (UC) (adapted from [13]).

Source	Advantages	Disadvantages
Adipose Tissue (AT)	• Easily accessible. • Isolation up to 500 times greater than BM. • Faster proliferation and greater immunosuppressive effects (*vs.* BM-MSC). • Angiogenic and anti-apoptotic cytokine secretion. • More prone to differentiate towards adipocyte lineages.	• Less osteogenic and chondrogenic potential (*vs.* BM-MSC). • Yield and differentiation highly dependent on donor characteristics (*i.e.* age).
Bone Marrow (BM)	• Highly studied and documented. Considered as the gold standard. • Most common source in clinical trials. Established clinical history. • High chondrogenic and osteogenic potential.	• Invasive and painful collection procedure with risk of infection. • Limited supply. • Yield and differentiation highly dependent on donor characteristics (*i.e.* age).
Umbilical Cord (UC)	• Safe and non-invasive collection procedure. Abundant supply. • Low impact of passage on aging. • Hypo-immunogenicity. Low risk of GvHD. • Higher proliferation potential and engraftment capacity (*vs.* BM-MSC and AT-MSC).	• Low osteogenic potential (*vs.* BM-MSC). Low adipogenic potential.

as stem cells, certain important physiological and morphological changes have been noted and should be kept in mind (summarized in Table 1.1). For this reason, the nomenclature associated with these multipotent cells has been the center of debates. These led the ISCT to publish a position paper which can be used as a guideline for the use of a scientifically accurate and standardized terminology [15]. Accordingly, the authors propose that plastic-adherent cells typically described as *mesenchymal stem cells* be termed *multipotent mesenchymal stromal cells* and that the term mesenchymal stem cell be reserved for cells which have demonstrated stem characteristics. The relevance of this nomenclature takes its roots from the observation that cells isolated by plastic adherence (for example from bone marrow), have broad biological properties and are not a uniform population of cells. In addition, authors recognize that the current data describing these cells is insufficient to affirm that these cells are stem cells. Since, in both cases, the term MSC can be used, authors recommend the acronym to be properly defined according to the demonstrated cell characteristics.

Lastly, certain reversible aspects of differentiation were noted throughout the discovery of stem cells and their characterization. The apotheosis of this theory was demonstrated in 2006 by Shinya Yamanaka and his colleagues when 24 specific transcription factors allowed the reprogramming of adult mature differentiated cells into what they called induced pluripotent stem cells (iPSCs). These reprogrammed cells were found to have the capacity to proliferate unlimitedly and differentiate into almost every cell type of the human body and thus attained pluripotency. The discovery of these cells had a significant impact on disease modelling which was recognized by the shared Nobel prize in physiology and medicine in 2012 with Gurdon. It has recently been confirmed that cells differentiated from patient-specific iPSCs were able to appropriately model disease mechanisms that are found in humans which make these cells a suitable model for drug screening, pharmacology or toxicity studies (reviewed in [16]).

MSCs extracted from umbilical cords

When first discovered, adult mesenchymal stem cells generated significant excitement around their translational applications, however, questions remain about their clinical utility and, in particular, on how the source of MSCs chosen can impact the clinical applications downstream. As described above, MSCs have been found in a variety of tissues including bone marrow, umbilical cords and adipose tissue (3 most common sources described in literature). It is likely that, in a clinical optic, the source of MSCs chosen should be tailored to the therapeutic application targeted and according to donor tissue accessibility. Since traditionally, umbilical cord tissues have been regarded as a waste product after birth, the ethical controversy around isolating MSCs from umbilical cord tissue was significantly reduced compared with obtaining MSCs from bone marrow. In this regard, the discovery that MSCs were both abundant and easily

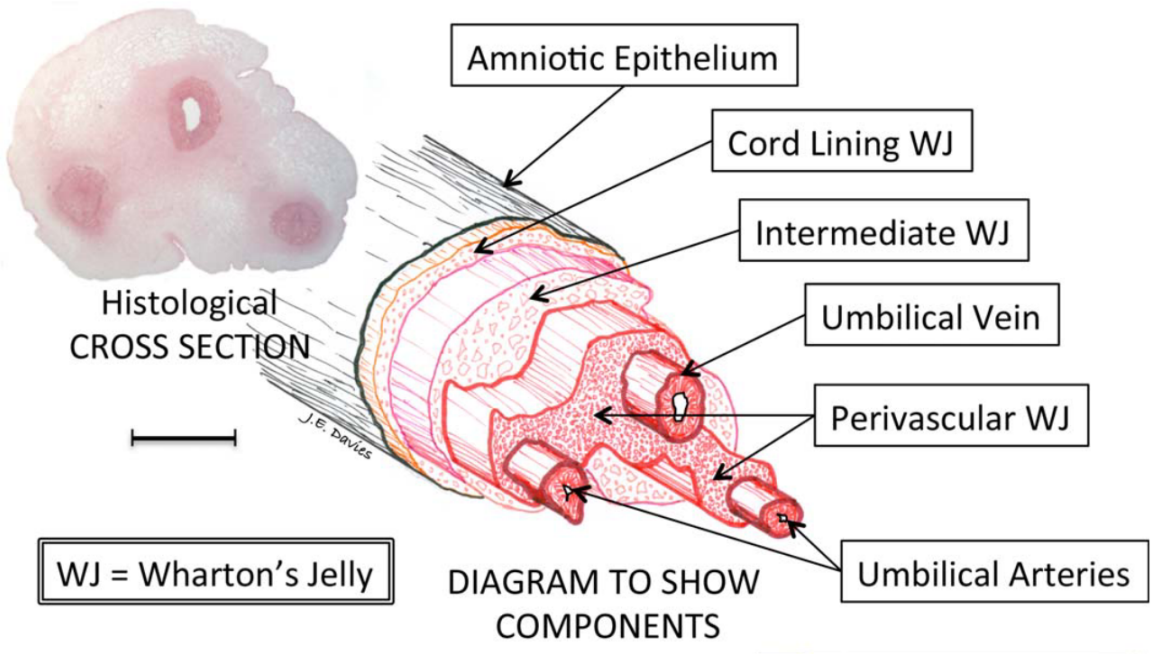

Figure 1.4: Human umbilical cord anatomical structure with a three-dimensional exploded diagram. The diagram was made by directly tracing the outlines of the various features in the histological section, then shifting them along the tilted longitudinal axis. Scale Bar = 55 mm. [20].

extracted from discarded umbilical cords (UC), indicated that this tissue could be a sustainable source of MSCs for clinical applications.

Anatomically, the human umbilical cord is composed of an outer layer of amniotic epithelium enclosing a vein and two arteries embedded within a connective tissue known as the *Wharton's jelly* (Figure 1.4). This tissue was first described by Thomas Wharton in 1656, and is primarily made of collagen and proteoglycans but also contains fibroblast-like cells and MSCs. Notably, cells extracted from umbilical cords were found to have low expressions of major histocompatibility complex (MHC) class I, and the absence of MHC class II molecules [17], as well as a lack of co-stimulatory ligands such as CD40, CD80 and CD86 [18]. As a result, UC-MSCs seem to exhibit a reduced immunogenicity which may be a significant asset for therapeutic applications. Enzymatic extraction protocols (using protease cocktails including collagenases, hyaluronidases and trypsin) or non-enzymatic extraction protocols (using spontaneous migration on plastic surfaces) have been described to successfully extract MSCs from the umbilical cord connective tissue [19].

1.1.2 Therapeutic applications of mesenchymal stem cells

Overview of clinical applications of MSCs

Advanced therapy medicinal products (ATMPs), including stem cell therapies, could be the key to treat the deadliest current diseases as well as a plethora of diseases with current limited available treatments. In 2016, the world health organization (WHO) analyzed the most common death causes worldwide [21]. Out of the top 5 causes of deaths, only one currently has no clinical trial ongoing using mesenchymal stem cells (MSCs) (Table 1.2). Although access to cell therapies in less developed countries is not foreseeable in the near future and not all patients suffering from these diseases could be eligible for cell-based therapies, advancing these therapies up to the standardized production of approved drugs (phase IV) clearly makes long-term economic sense and will have a positive impact on global health.

Table 1.2: Top 5 global causes of death according to WHO in 2016 [21] and current maximum MSC clinical trial phase advancement (U.S. national library of medicine database).

	# Deaths	**Max. completed phase**	**Example Ref.**
Cardiovascular Disease	9.43 Million	Phase 3	NCT02672267
Stroke	5.78 Million	Phase 2	NCT01297413
Chronic obstructive pulmonary disease	3.04 Million	Phase 3	NCT04018729
Lower respiratory infections	2.96 Million	None	*N.A.*
Alzheimers Disease / Dementia	1.99 Million	Phase 2	NCT03117738

The relevance is also noted in the amount of registered clinical trials using MSCs. A clear increase in these clinical trials has been observed since the beginning of this century (Figure 1.5). While less than 19 new clinical trials involved MSCs between 1995 and 2005, 490 new clinical trials were added between 2016 and 2020. In June 2020, 1,138 clinical trials were registered worldwide using MSCs to investigate their therapeutic potential and this trend continues to increase [22]. It is worth noting that 65 clinical trials using MSCs were registered in 2020 for the treatment of COVID-19 due to their multi-functional mode of actions (further detailed below) [23]. The rapidity with which these clinical trials were registered and conducted proves the relevance of all of the fundamental and experimental studies which have been ongoing in the past decade. Although limited information is available concerning the detailed advancement of certain clinical trials (possibly due to intellectual property rights), the clinical trials website remains a powerful source of information to understand which human pathologies are targeted using MSCs. Examples of completed phase 3 clinical trials and their completion date can be found in Table 1.3 (also reviewed in [23]). The few examples

Table 1.3: Examples of completed phase 3 clinical trials using MSCs and their completion date.

	Description
NCT05122234 Indonesia - Nov 2021	MSC secretomes were administered in 20 patients with severe COVID-19 symptoms in view of reducing specific inflammatory markers.
NCT04224207 Turkey - Jan 2020	In animal models, WJ-MSCs were found to effectively stop the progression of retinal degeneration and rescue dormant photo-receptors. In this clinical trial, between 2 and 6 million allogenic WJ-MSCs (expanded by Onkim Stem Cell Technologies, Turkey) were implanted in the sub-tenon space behind the eyes of of 32 enrolled participants in view of observing an impact on visual acuity and retinal thickness [24].
NCT03766217 Brazil - Dec 2019	Autologous dental pulp MSCs were associated with bio-materials (hydroxyapatite/collagen) to repair the alveolar cleft in 62 children.
NCT01541579 Worldwide - Nov 2016	120 million allogenic AT-MSCs were injected in 278 patients with Crohn's disease to detect disease remission and improved quality of life. After one year, the follow up study, showed that Cx601 was safe and effective compared to a placebo [25].
NCT01873547 China - Dec 2015	Studies in animal models show that MSC transplantation can improve the neurological function of spinal cord injury without any severe side effects. This trial has transplanted UC-MSCs in 100 patients with spinal cord injuries in view of repairing the damaged nerve function.
NCT01759823 India - Oct 2015	Autologous BM-MSCs injected in the pancreas of patients with type II diabetes to support beta cell/resident stem cell activation and survival.
NCT01873625 Iran - Dec 2011	60 patients with knee osteoarthritis were injected with BM-MSCs in view of resurfacing articular cartilage to reduce pain and retrieve motility.
NCT01392105 South Korea - May 2010	1 million autologous BM-MSCs per patient kg were injected in patients with damaged myocardium in view of repairing the damaged muscular tissue.

described bring to light the geographic diversity and modes of actions of clinical trials which are successfully progressing along the clinical pipeline. Accordingly, one can note that a worldwide effort is ongoing for research and development of MSC-based therapeutics to make them rapidly available for patients.

Autologous and allogenic cell therapies in the case of MSCs

The majority of clinical trials concern autologous therapies for which the patient's own cells are sampled and injected at the spot of injury: 66 % of the 47 BM-MSC clinical trials analyzed by Ikebe et al. [26] and 58 % of the 12 human studies using ASCs reviewed by Bateman and colleagues [27]. For these therapies in particular (where the initial quantity of cells is limited and depends on donor characteristics), repeatable expansion of the patient's own cells is necessary, all without compromising quality and patient safety. On the other hand, human trials of MSCs have shown no adverse reactions

to allogenic (HLA-identical or mismatched [28]) versus autologous MSC transplants [29, 30]. These results encourage the possibility of a cell bank inventory for MSC therapies in the future, similar to the already existing banks for biotechnology cell-produced products. In the case of allogenic therapies, scaling up expansion processes could bring these therapies to a larger number of patients and reduce the cost of therapies.

Conditioned medium and MSC extracellular vesicles

Extracellular vesicles (EVs) are small membrane-surrounded particles secreted by almost all cell types. Specifically, EVs are a heterogeneous group of structures including exosomes (originating from the endosomal system) and micro-vesicles which are shed from the plasma membrane. They are involved in cell-to-cell communication pathways and play important roles in physiological responses and pathological conditions. Recently, the role of MSC-derived EVs in regenerative medicine has been intensively investigated, particularly since the discovery that the effect of MSCs are most probably exerted in a paracrine manner (demonstrated for example in rat ischemic heart model [31]). As a result, the media in which MSCs are produced (*i.e.* conditioned media) can be therapeutically active in itself. For example, exosomes derived from allogeneic BM-MSCs were used to treat 24 SARS-CoV-2 positive patients meeting criteria for severe COVID-19 as well as moderate-to-severe acute respiratory distress syndrome. In total, 17 patients recovered, 3 patients remained critically ill though stable, and 4 patients expired for reasons unrelated to the treatment. Overall, after one treatment, patients' clinical status and oxygenation improved, associated with a significant increase in absolute neutrophil count and increasing CD3+, CD4+, and CD8+ lymphocyte counts. In conclusion, owing to its safety profile, capacity to restore oxygenation, down-regulate cytokine storm, and reconstitute immunity, BM-MSC EVs seem to be promising therapeutic candidates for severe COVID-19 [32]. Similarly, MSC-derived EVs could be interesting candidates to treat many various diseased in a paracrine manner.

Regulatory specifications

In 2011, 123 available clinical trials concerning MSC's registered by the US National Library of Medicine were analyzed by Trounson et al. The authors showed that these clinical trials address a wide range of indications such as bone/cartilage, heart, neurodegenerative, immune / autoimmune and lung diseases [33]. The same authors analyzed the 374 registered clinical trials in 2015 and showed the indications remain similar but, interestingly, the distribution by phase has also not moved (in both cases, only 7 % of clinical trials passed onto phase 3). Authors suggest the products are not moving out of the clinical pipeline [34]. In 2020, 803 studies were registered and only 54 (7 %) were ongoing phase 3 or later. Although great progress has been made since 2011 to understand MSC therapies, several lead trials have either undergone early termination

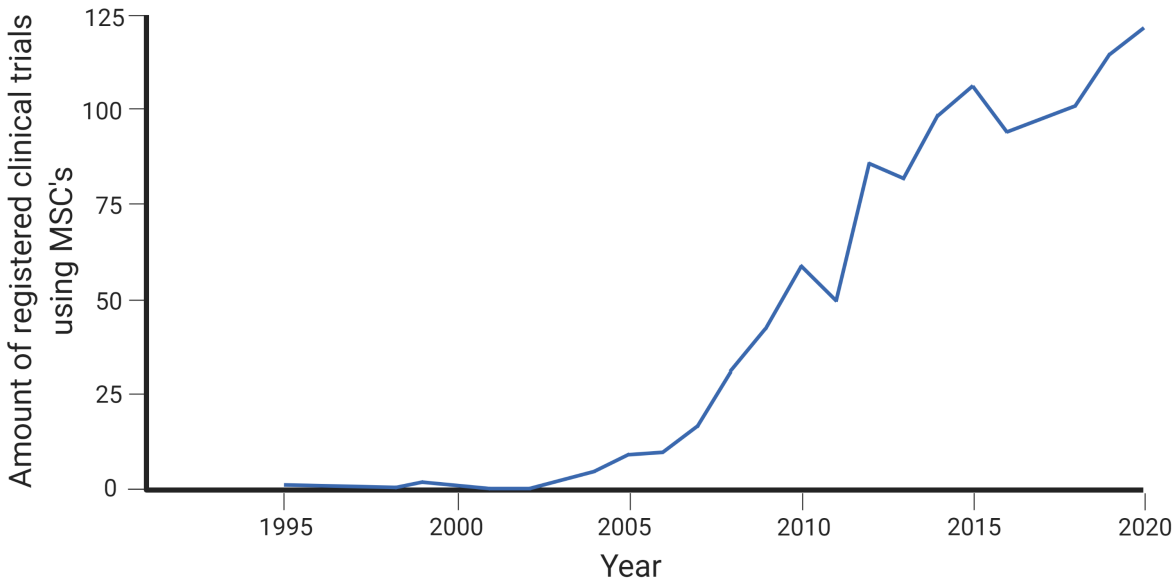

Figure 1.5: Amount of registered clinical trials using MSCs until 2020 (adapted from [22]).

or failed to meet the requirements for phase progression (reviewed in [35]). It seems that important bottlenecks still remain to produce high quality MSC's and pass onto commercial development of these therapies.

In addition, ATMPs are faced with challenging regulatory specifications at each phase. In Europe, requirements of regulation 1394/2007 must be met, and in the United States the code of federal regulations (CFR) title 21-part 1271 relative to human cells, tissues and cellular and tissue-based products should be followed [36] as well as 21 CFR part 210, 211 (current good manufacturing practice (cGMP)) and 21 CFR 610 (general biological product standards). As these therapies are, in general, new drug products, an investigational new drug (IND) application will often be required and should follow 21 CFR part 312 relative to INDs (including data from animal pharmacology, toxicology studies, clinical protocols and supporting information) in the United states, or investigational medicinal product (IMP) application in Europe. Other specific requirements may be requested when submitting new therapeutic products to other countries. Notably, clinical data indicate that most clinical trials using stem cells have been registered or completed in the United States, in european countries such as France, Germany, Italy, Spain, or the United Kingdom or in certain Asian countries such as China and South Korea (Figure 1.6). Regardless of the country, the regulatory setting demands a solid quality-based research foundation to show that the MSC's produced will not cause unwanted effects in patients. However, high variability exists between protocols used in current clinical trials using MSC's [26]. This important variability, which is also widely present in research papers, proves the difficulty to define a universal optimal process.

Lastly, in cellular therapies, the fact that the final product is composed of living cells poses novel problematics compared to tradition biological pharmaceutical prod-

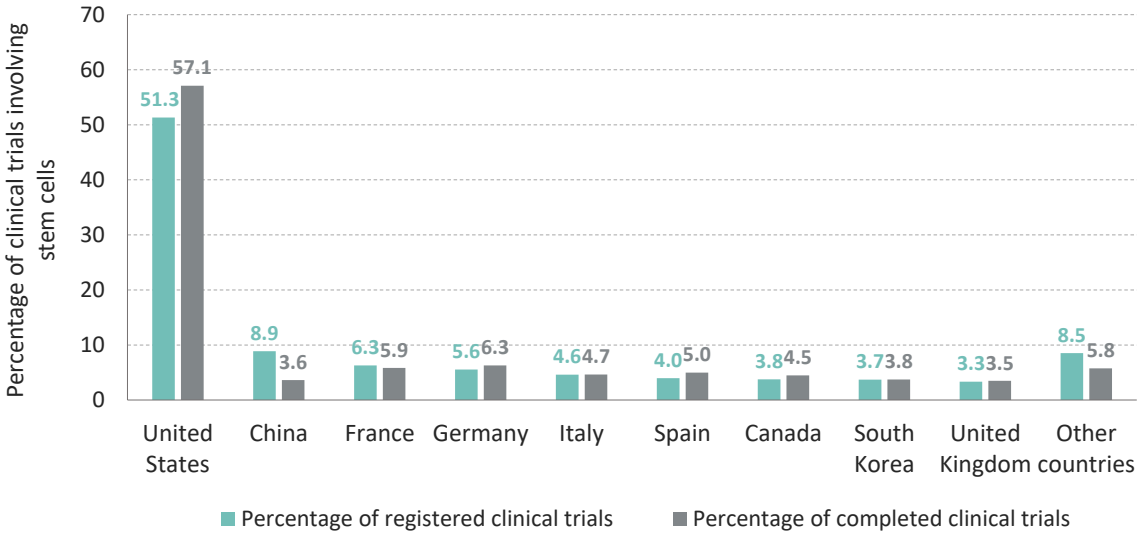

Figure 1.6: Percentage of completed and registered MSC clinical trials worldwide (adapted from [37]).

ucts. For example, cell delivery systems have shown limited success. Fewer than 5 % of injected cells persist at the site of injection within a few days of transplantation [38]. The yield is even lower for MSC-based therapies where less than 1 % of MSCs persist over 7 days following injection [39, 40]. Low survival rate can possibly be caused by exposure to inflammatory micro-environments, washout, immune destruction or apoptosis. This may, or may not, lead to unwanted effects in patient's being administered these therapies.

MSC modes of action as cell therapy products

In addition to these known characteristics, it is however important to keep in mind the modes of actions which MSCs exert and may be used in various clinical settings. The definition provided by the ISCT specifies the minimal requirements for cells to be characterized as MSCs but does not indicate to what extent these cells have the capacity to exert the therapeutic action expected. More specifically, unique properties of MSCs such as (1) migration to the site of injury, (2) cell activation (3) promotion of pathogen clearance if required and (4) modulation of inflammation, may need to be verified before clinical administration [41]. The following paragraph will briefly summarize certain demonstrated modes of actions of MSCs. The description is voluntarily non-focused, considering that extremely detailed reviews of these mechanisms have been extensively published and that it is not the objective here [41, 42].

Briefly, an emerging concept in the MSC field is that MSCs do not have spontaneous immunomodulatory properties but require an activation to exert these effects at the site of injury *in-vivo*. For this, MSCs have been shown to sense inflammation and migrate towards sites of injury, possibly by chemotaxism and reacting to concentration gradients of a wide range of inflammatory molecules. For example, MSCs seem

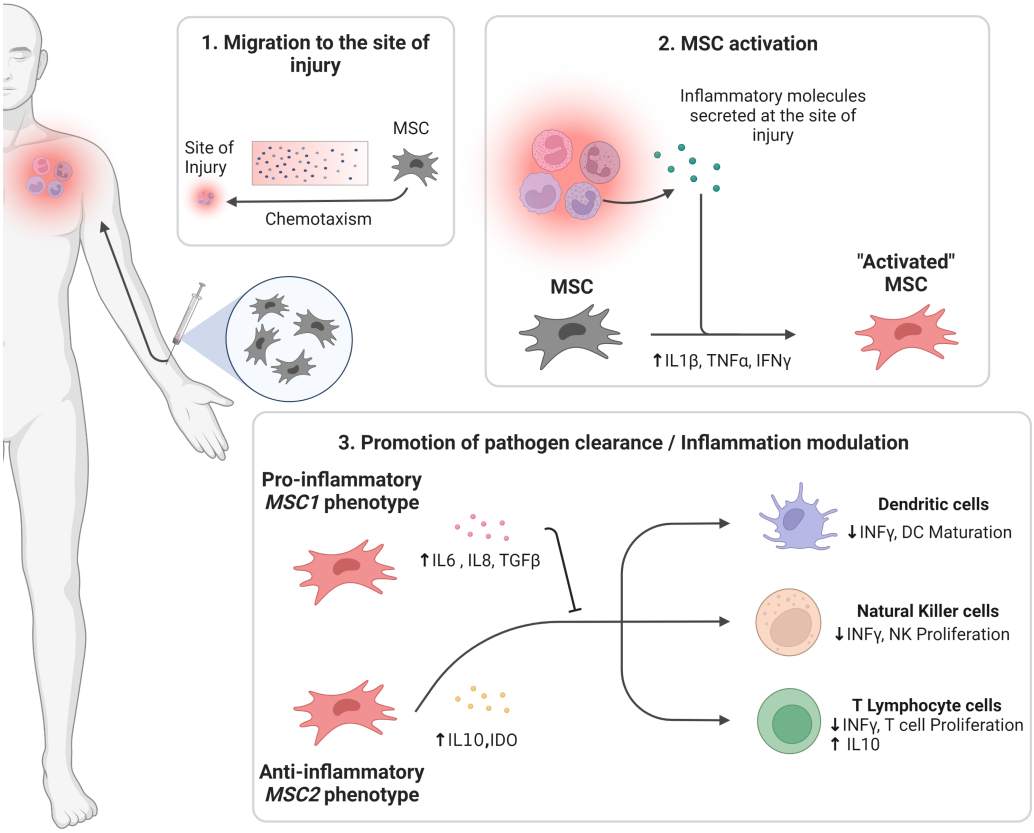

Figure 1.7: Simplified MSC modes of actions in immunomodulation (based on [45]).

to express the chemokine receptors CCR1, CCR4, CCR7, CXCR5 and CCR10 which may be involved in this process [43]. Various other proteins, growth factors, cytokines, chemokines and receptors have also been shown to be involved in this process (reviewed in [41]). Once the cells have reached the damaged tissue, the secreted cytokines at the site of inflammation such as interferon γ (IFN-γ), tumor necrosis factor α (TNF-α) or interleukin 1β (IL1β) have been demonstrated to successfully activate MSCs in modulating the perceived immune responses [44]. This activation typically results in the regulation of certain MSC immunomodulatory molecules such as transforming growth factor β (TGF-β) specific interleukins. It seems that various priming pathways may occur based on the microenvironment that the MSCs are exposed to. For example, MSCs may be activated via TLR3 signalling which may lead to anti-inflammatory MSCs (producing indoleamine-2,3-dioxygenase (IDO), prostaglandin E2 (PGE2), Interleukin 4 (IL4) and Interleukin 1RA (IL1RA)). However, in other cases, this priming may activate the TLR4 signalling pathway which may lead to pro-inflammatory MSCs (producing IL6, IL8 and TGF-β) [41] which may also lead to promoting lymphocyte T helper 2 response by inhibiting tumor necrosis factor-alpha (TNF-α) and interferon-gamma (IFN-γ) production and increasing interleukin 10 (IL-10). These findings indicate that MSCs are receptive to environmental cues and may have the capacity to promote pathogen clearance or immune suppression (Figure 1.7).

1.1.3 Bio-mechanical constraints and cell signalling

It is worth noting that mesenchymal stem cells are, by nature, sensitive to hydro-mechanical forces in their *in-vivo* environment. The tensile / shear forces and pressure forces perceived by MSCs may be efficient bio-mechanical cues to target their replication, migration, activation and/or differentiation. The following paragraphs will detail, rapidly, the mechanisms which are currently known concerning MSCs in view of keeping these mechanisms in mind for the development of clinically viably expansion processes.

Perception of tensile forces and shear

To begin with, the mechanisms of actions which seem to explain the impact of shear stress on MSCs include the presence of integrins (cell surface adhesion receptors) on MSC membranes which specifically bind to extracellular matrix compounds and supports cell adhesion on growth supports [46]. Since these integrins are also connected to elements of the cellular cytoskeleton, cells can both exert and perceive forces from their extracellular environment (Figure 1.8). These signals have been shown to induce cellular responses such as differentiation [47] and/or cell migration. For example, shear stresses between 9 and 22 dyn cm^{-2} may stimulate MSC differentiation towards osteoblastic phenotypes [48]. Various mechano-transduction signalling pathways may be activated via these integrin-mediated pathways, including force-induced exposure of various peptide sequences, the opening of mechano-induced ion channels and receptor-ligand interactions. Certain enzymatic sites, under these mechanical stresses, may be activated or deactivated (thoroughly reviewed in [49]). In addition, the fluidity of cell membranes may also be impacted by tensile forces, which may also be perceived by elements of the cell cytoskeleton and lead to similar signalling pathways. These complex cascades of events may partially explain how shear stress values around 10 dyn cm^{-2} have been associated with the increased production of angiogenic factors such as VEGF [50], for example. However, it should be kept in mind that the modes and effects of these pathways are, to date, not completely elucidated for animal cells, and thus knowledge on the impact of mechanical forces on MSCs is to date still quite obscure.

Notably however, there seems to be a dynamic and reversibility in these cell signalling pathways. To begin with, the integrin binding and signalling pathways have been shown to be reversible, through assembly and disassembly of certain protein complexes. These results indicate the cells capacity to dynamically respond to its macro-environment. For example, cells cultivated on stiff and then soft scaffolds were found to revert to a morphology observed when cells are cultivated on only soft scaffolds (the reverse was also found to be true) [51]. In addition, the perception of cyclic mechanical constraints during MSC expansion could determine cell fate and differentiation [51]. Cells cultivated under repeated intermittent mechanical stresses after having been co-

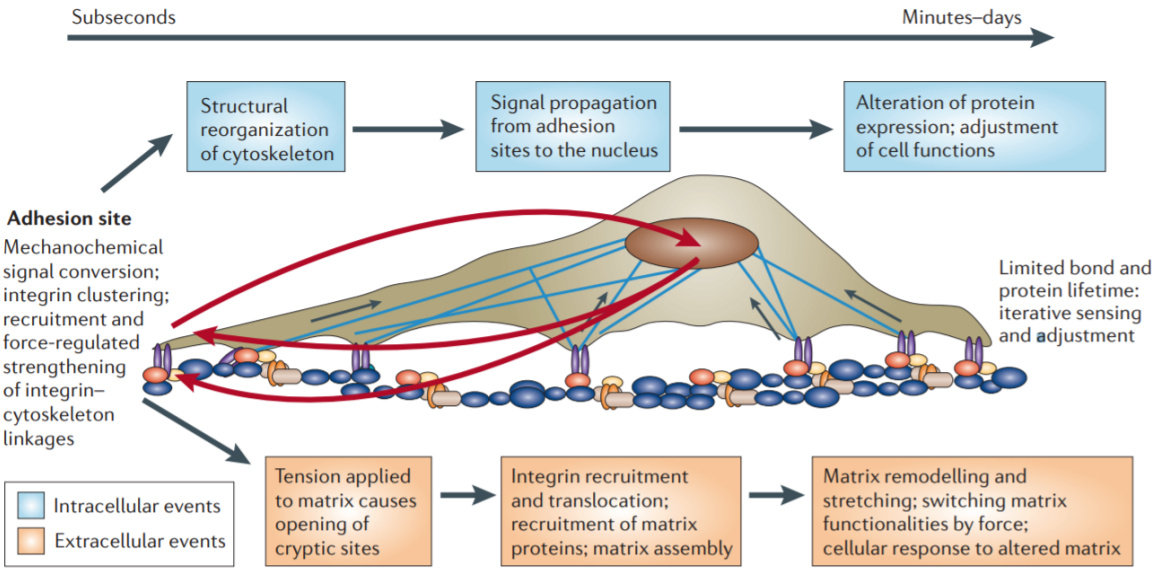

Figure 1.8: Schematic representation of mechano-transduction pathways (adapted from [49]).

cultured with ligament cells were found to express a greater ligament phenotype than cells which had only been co-cultured with ligament cells. Mechanical stimulation alone was not sufficient, however, to induce this cell differentiation, indicating that both mechanical and biochemical receptors should be involved [52]. Lastly, cells which were cultivated under repeated mechanical constraints (through the change in scaffold rigidity every 2 days) were found to have a significantly reduced growth rate depending on the frequency to which the mechanical constraints were applied indicating that dynamic mechanical constraints may hinder MSC cell growth [51].

Perception of pressure forces and collisions

Much like cells perceive tensile forces, they, without doubt, also perceive pressure forces present in their macro environment. As early as 1960, it was proposed that tissue deformation or stretching induces the formation of fibrous connective tissue while compression induces cartilage formation [53]. Later, researchers have made use of finite element analysis, to predict the influence of hydrostatic pressure and distortional strain on tissue differentiation [54, 55]. These models suggest that high levels of compressive hydrostatic stress may encourage chondrogenesis while low hydrostatic stress may induce osteogenesis (Figure 1.9). In other studies, compression [56, 57] and hydrostatic pressure [58] increased both chondrogenic and osteogenic differentiation of MSCs.

In dynamic compression regimes, chondrogenesis (and alterations in cartilage-specific gene expression including SOX-9, collagen II, collagen X and aggrecan) has also been demonstrated as well as an impact on intracellular calcium signalling. Specifically, higher dynamic frequencies and higher compression amplitudes induced the greatest chondrogenic gene expression, while lower amplitude/lower frequency conditions induced a greater ratio of osteogenic markers (osterix, collagen I) to chondrogenic markers

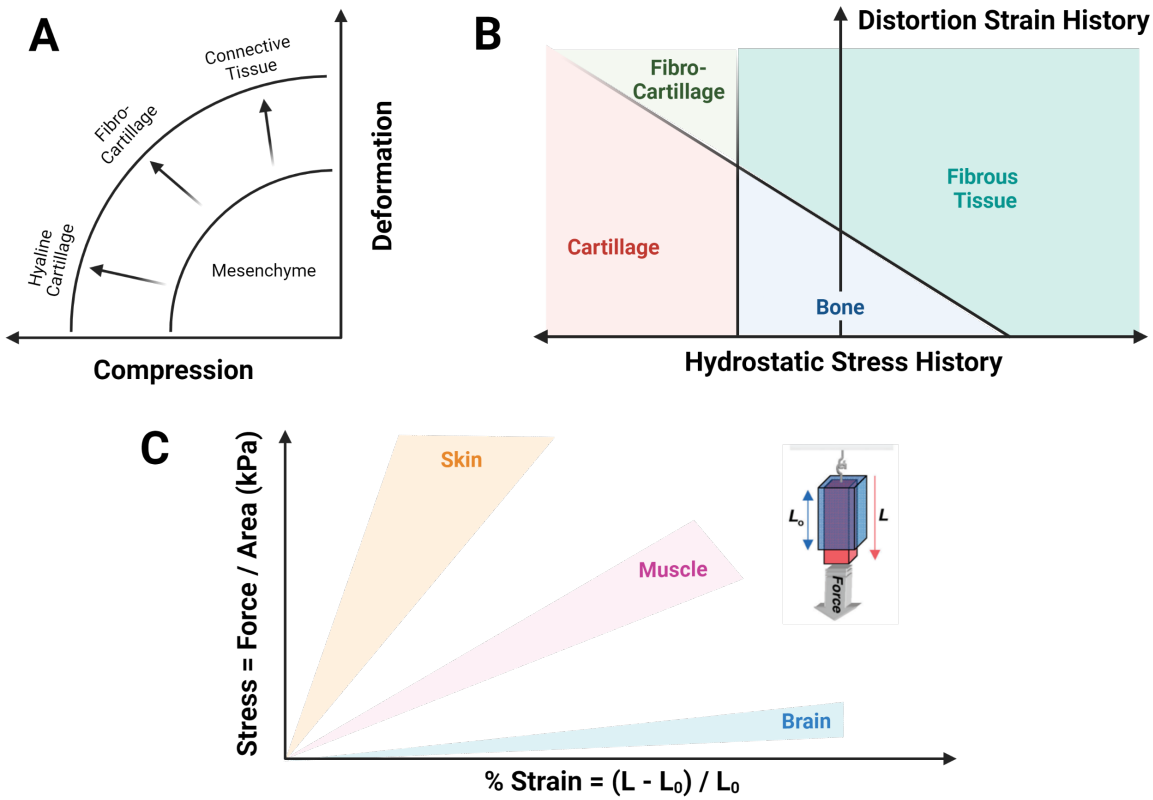

Figure 1.9: Theoretical models developed by (A) Pauwels [53] (B) Carter and Beaupre [55] and (C) Discher (adapted from [47]) that describe the relationship between the mechanical environment and mesenchymal tissue differentiation.

(thoroughly reviewed in [59]).

As a result, the commitment of MSCs to different lineages in response to mechanical stress most likely results from different types, magnitudes, and/or frequencies of forces. In addition, other cell types may be induced depending on mechanical and chemical cues in cell macro environments. For example, applying various stresses and strains to MSCs has been proposed to lead to the differentiation into other cell types such as skin, muscle and brain [47] (Figure 1.9, C). However, much more remains to be discovered about the effect of different levels of mechanical stimulation (reviewed in [60]). One must keep in mind that, from a biological viewpoint, it seems unlikely that universal critical values of either strain and/or shear may exist to predict the differentiation MSCs as these mechanisms are typically multi-parametric and may vary according to the intrinsic cellular parameters emanating from donor characteristics and extrinsic parameters such as chemical factors and gradients.

1.1.4 Manufacturing requirements for a scalable production of MSCs

A brief introduction on the healthcare sector

The healthcare industry which includes curative, preventive, rehabilitative and palliative care solutions, has, over the years, been supported by the development of new drugs and technologies. While ancient healthcare providers can be traced back to Mesopotamia (essentially based on knowledge of local flora and a rational observation of the human body), practices have evolved by scientifically studying plants and spreading knowledge through new printing machinery and paper production. In addition, the technological advances in medicine, chemistry and biology in the 19^{th} and 20^{th} centuries gave physicians better tools to understand, monitor and treat diseases. For example, the discovery and isolation of anesthetics, antiseptics, antibiotics and vaccines were effectively used to limit and treat diseases which were increasingly spreading due to globalization and the transport revolution.

Accordingly, in 1899, the synthesis and commercialization of Aspirin (acetylsalicylic acid) provided an alternative to the typically used sodium salicylate in the treatment of rheumatic diseases. This molecule was found to have similar therapeutic effects without the typical undesirable secondary effects. Later, an effective Polio vaccine was created in 1952 and tested throughout the U.S. several years later. At the same period, the first organ transplant was performed by successfully grafting a kidney from a donor into his twin brother. These examples show that, throughout the ages, the medical sector has evolved and diversified. In addition, the sector diversification was also accompanied by an increase in the health market capital. While estimates of health expenditures indicated about 1 % of a country's total gross domestic product (GDP) in 1900, the organisation for economic co-operation and development (OECD) statistics brought that proportion up to around 5 % in 1970 (5.2 % in France, 4.4 % in Japan, and 6.2 % in the U.S.) and found it to be continuously increasing until the present day. In 2015, health expenditures accounted for 11 % of GDP in France, 11.2 % in Japan, and 16.9 % in the U.S. This increase in global health market and expenses shows the prominent role that the healthcare industry has in industrialized countries, particularly due to increased quality of life and longevity. Lastly, the development of accessible therapeutic options is consistent with the UNESCOs sustainable development goals for 2030, in particular Goal number 3 *Good health and well-being*.

Manufacturing MSCs : trends and costs

Clinical applications of MSCs have seen a tremendous escalation in the last decade. Accordingly, manufacturing processes and equipments will need to face these demands and provide easily scalable and robust solutions. Given the large target patient populations with typical dose sizes of 10 to 100 million cells per patient, and engineered tissues being constructed with over 100 million to over 10 billion cells, an unprece-

dented demand has been created for hMSCs [61, 62]. In addition, it is possible that progress in biotechnology and the capacity to manufacture high quality stem cell products at a reasonable cost, may also provide opportunities to expand existing markets or launch entirely new ones with these cell products at its core. For example Olsen et al. have projected that applications such as hMSC-derived products, cell-based products or engineered tissues / organs will require (for each general application) the production of over 10^{14} MSCs in 2040. In addition, the authors suggest that approximately 12.5 $\times 10^{21}$ MSCs will be required to meet the needs of emerging industries which may include bio-engineered materials or various sources of lab-grown meat [62].

Interestingly, authors also compare the MSC market growth to the previous market growth of monoclonal antibodies, for which the first FDA approval for human use was granted in 1986. However, since then, several mAbs have been rejected by the FDA and caused significant panic in the mAb industry. Much like in 2016 where out of the 8 top-selling blockbuster drugs, 5 were mAbs, it is possible that a similar trajectory will be occurring for MSCs in the next decade (Figure 1.11), composed of few extremely successful blockbuster therapies and many unsuccessful failures. Authors predict 74 MSC-based and 12 iPSC-based therapeutic products in 2040 if the following requirements can be achieved :

- Clinical trials will be ongoing using bio-fabricated tissues and / or organs.
- Large scale bioreactors ($>$ 1000 L) will be used for the production of cells following GMP guidelines.
- Large manufacturing sites will be dedicated solely to the production of MSC products.
- The cost per million MSCs will be below $ 0.50.
- Clean meat produced with MSCs will be available for less that $ 100 per pound.
- Tissue engineering or combination products will dominate the market.

Over the last 10 years, hMSC costs have gone from about $ 1,000 per million MSCs to about $ 100 per million cells. The costs are expected to continue to decrease down to around $ 10 per million MSCs over the next 10 years [62]. The most probable way to achieve the reduction of costs will inevitably to change manufacturing technology as it has been thoroughly described in [63] and presented in Figure 1.10. Briefly, this study allows us to identify the fact that changing the MSC production strategy will ultimately impact the investment required for research and development (*i.e.* automated bioreactors will require more research than planar standard T-Flask cell cultures) but also, in parallel, will allow the production of significantly higher quantities of cells per batch thus increasing product heterogeneity (due to larger batches) and should lead to the reduction of global production costs and effort. A through review of T-Flask based-cell culture for MSC production can be found in Section 1.2, while, the review

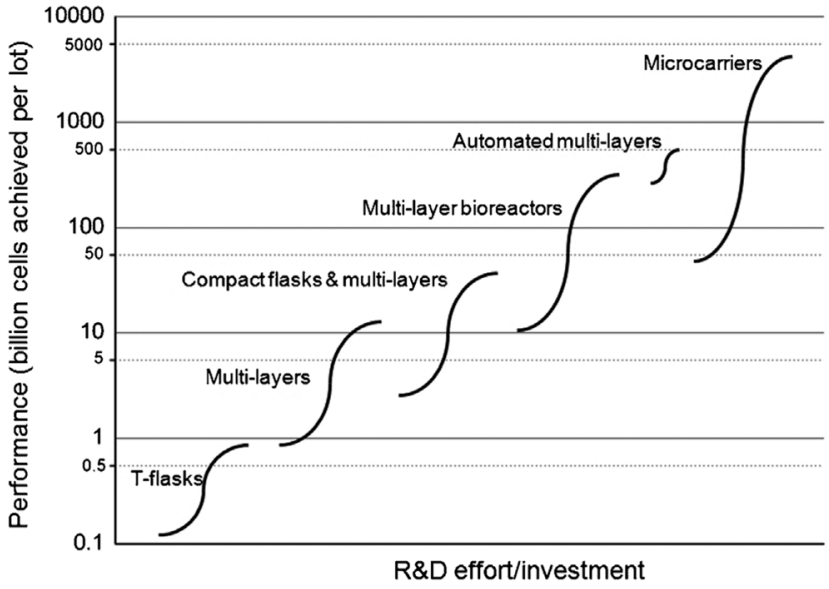

Figure 1.10: Conceptual illustration of a technology S-curve showing the evolution of MSC expansion technologies. The limits of each S-curve correspond to the amount of cells achieved by the smallest and largest size of each technology type when using the maximum number of units. The x-axis represents qualitatively the Research and Development effort required for a company currently using T-flasks to change to other cell expansion technologies (adapted from [63]).

of processes on the opposite side of the spectrum, such as microcarrier-based systems, will be further detailed in Section 1.3.

Manufacturing challenges

To date, the largest manufacturing challenge to meet the future MSC requirements remains technological challenges for the safe and cheap production of high quality cells. Although certain bioreactor-based technologies (which have proved their efficacy in scaling up mAb production) exist for MSCs, the living nature of the final end product brings additional complexity into this known process. Many manufacturing innovations and scientific understanding are still required to successfully produce these cells. In addition, the relatively well known downstream processes typically used to purify small molecules or mAbs are not adapted to much larger elements or their living nature (typical chromatography steps which require the elution of the product through shifting osmolarity, pH or by size exclusion are ineffective for live cell products). In addition, since MSCs are, by nature, adherent cells, the process will ultimately require a detachment step for which no current technology fully meets the requirements of unit operation yield, viability after detachment and efficiency (all within the future cGMP environment). As the downstream processing solutions are generated to meet these requirements, costs of MSC manufacturing will drop.

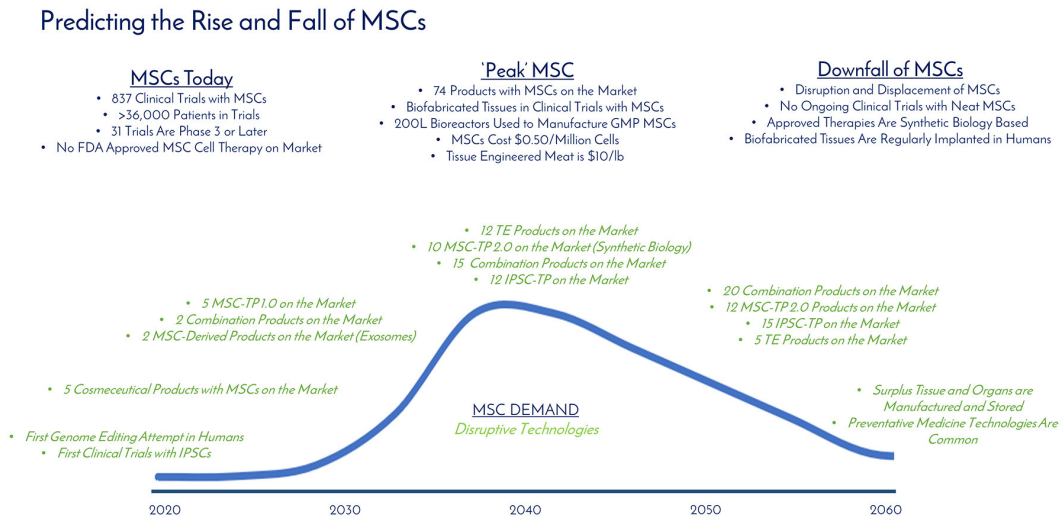

Figure 1.11: Predicting the rise and fall of MSCs. The current, "peak," and downfall stages of MSC demand are detailed with milestones over time (blue). Disruptive technologies (green) that are developing in parallel that have the potential to displace MSC demand are detailed over time. "Peak" MSC is predicted to occur in 2040 (adapted from [62]).

1.1.5 Section summary

Our tissues are constantly regenerating and adapting to external or internal stresses. In order to do so, our organisms are capable of renewing damaged tissues by having specific precursor cells self-organize and differentiate into the damaged cell types. These precursor cells, which are now called mesenchymal stem cells (MSCs), are cells present in a wide range of adult tissues (bone marrow, adipose tissue, umbilical cords, dental pulp, specific zones in organs *etc.*). Due to these tissue variations, the definition of minimal criteria to characterize MSCs has evolved throughout the years and come to the conclusion proposed by the international society for cellular therapy (ISCT) in 2006. The proposition has been extensively used as minimal and sufficient criteria to characterize MSCs in view of their utilization in clinical applications. Due to the diversity of modes of actions discovered, a broad-spectrum of clinical applications have been discovered and are currently ongoing further development. However, in order to match the clinical demand to come, the production of high quality cell products will be required. As a result, the ways and techniques used to expand MSCs in static and dynamic conditions will be the object of the next sections.

1.2 Mesenchymal stem cell expansion in standard tissue flasks

A literature review of publications expanding human mesenchymal stem cells (hMSCs) in various two-dimensional culture conditions was performed and was published as a scientific review article in Biotechnology Advances [64]. This article was written in view of comparing the expansion processes typically found in literature and bringing to light to what extent certain parameters may, or may not, have a demonstrated impact on defined critical quality attributes. For this, a quality by design approach was used to determine the most impacting parameters on MSC quality quantified by a criticality indicator during the two main manufacturing stages (cell extraction and cell amplification). Understanding the impact of process parameters in standard tissue flask (T-Flask) cell cultures is an essential prerequisite to understand the impact of these parameters (and others) in the case of more complex processes, for example, in microcarrier-based cell culture systems in bioreactors which will be the object of the following section.

Quality by design to define critical process parameters for mesenchymal stem cell expansion - Biotechnology Advances, 2021 - C. Maillot, C. Sion, N. De Isla, D. Toye, E. Olmos

1.2.1 Introduction

Advanced therapy medicinal products (ATMPs) are a class of bio-pharmaceuticals comprised of innovative therapeutics such as gene therapies, tissue engineered products or cell therapies. Notably, the development of genetically engineered T-cells (CAR-T) and stem cell products have triggered a recent wave of applications. For example, over twice as many clinical trials using mesenchymal stem cells (MSC) were registered by the US national library of medicine between 2011 and 2015. These cutting-edge products were shown to address a wide range of indications such as bone / cartilage, heart, neuro-degenerative, immune / autoimmune diseases [34]. More recently, MSC-based products have been shown to be efficient in cases of acute respiratory distress syndrome (ARDS) for example for the treatment of COVID-19 patients [65, 66]. However, the distribution of these products by phase was shown not to evolve, indicating the products were not moving out of the clinical pipeline (only 7 % of clinical trials passed onto phase 3) [33, 34]. A rapid search of the NIH database (https://clinicaltrials.gov/) for MSC-based clinical trials in 2020 seems to indicate a similar distribution, possibly due to incomplete quality standards during early development phases. For example, 73 % of interviewed companies producing ATMPs have faced manufacturing and quality assurance issues which may be related to inconsistencies between the laboratory and

scale-up phase or issues with quality standard definitions [67]. Although great progress has been made since 2011 to understand and develop MSC therapies, several lead trials have either undergone early termination or failed to meet the requirements for phase progression [35]. Thus, it seems that important bottlenecks still remain to produce high quality MSCs and pass onto commercial development of these therapies. In this regard, using new tools and methodologies, such as the quality by design (QBD) approach, may be an essential foundation to help products achieve commercialization.

1.2.2 Defining a quality-based approach for cGMP manufacturing

The quality by design approach.

QBD is a scientific and risk-based approach to product development which is currently flourishing in the pharmaceutical industry [68]. Using this methodology brings the definition of quality standards early in the process development stages. In this mind-set, the QBD method begins by defining the desired product characteristics from a patient and clinical perspective : the quality target product profile (QTPP) (Figure 1.12). These requirements are then used to define critical quality attributes (CQAs) which will be necessary and sufficient to guarantee product efficacy and safety. Each CQA should be routinely tested (with rapid, sensitive and reliable procedures [69]) and stability should be maintained within a defined range [70]. Once the quality attributes are defined, it is important to understand how the production process will impact these quality attributes. In this regard, the critical process parameters (CPPs) will be determined as well as their defined ranges. Working within these ranges (*i.e.* the design space) should ensure consistent product quality regardless of the set of parameters used. During routine manufacturing, ongoing process verification (OPV) should then be put in place according to a defined control strategy of these CPPs in order to easily detect shifts or abnormalities which may impact the quality of the final drug product.

Identifying critical process parameters.

In order to define and compare the criticality of process parameters, an approach inspired by the risk priority number (RPN) was proposed. The method has typically been used for failure mode and effect analysis (FMEA) [71–76] in order to prioritize potential failures based on their severity (S), occurrence (O) and ease of detection (D). For this, scores between 1 and 10 are defined according to a predefined scale suggested by the IEC 60812 for each factor (S, O and D) and are multiplied to obtain the RPN number. Issues with the highest RPN value are therefore the most critical and should be addressed first.

Using this basis, an *"impact score"* was determined to evaluate the expected impact of each process parameter on each CQA. A similar strategy has been proposed by the

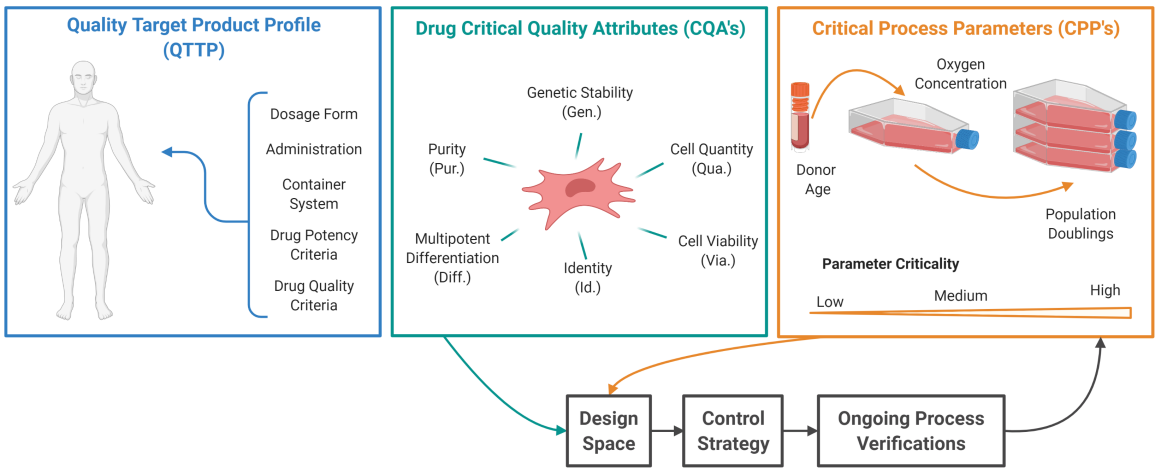

Figure 1.12: Overview of the quality by design process for mesenchymal stem cell manufacturing. Drug product characteristics are described in the quality target product profile according to patient requirements in order to identify critical quality attributes which will be sufficient to guarantee product safety and efficacy. The identification of critical process parameters and their impact on the defined CQAs leads to the definition of the design space within which manufacturing processes can be performed without altering product quality. The definition of a control strategy and ongoing process verifications are then required to monitor the process and detect potential deviations during the process.

CMC Biotech working group using a five-level scale to evaluate the impact of CQAs in a monoclonal antibody production process case study [77]. Although the attribution of a given impact score was based on available literature and scientific knowledge, it remains, by nature, a subjective quantification. In this study, the scale proposed was reduced to three risk levels for an easier and less subjective assessment (Table 1.4). Admittedly, three-level hierarchies are common in literature for criticality evaluations [78]. When no literature was available, an impact score of 1.1 was set to account for uncertainty, considering a low parameter impact if little literature exists. Based on RPN calculations in FMEAs, a RPN number for each QTPP attribute was calculated by the product of its factors. However, since not all QTPP attributes were defined by the same number of parameters, a correction factor was applied on all RPN calculations for a better comparability between results. Lastly, an overall RPN calculation was defined, calculated through the average of the RPN calculations of all QTPP attributes in order to define the most critical parameters for the overall quality of cells and to present an overview of the production process as a whole.

1.2.3 Using Quality By Design for MSC manufacturing

Defining the quality target product profile (QTPP).

In order to understand their therapeutic potential, two categories of cell-based medicinal products using MSCs will be described, on the basis of existing reviews [79, 80] and similar QBD examples [81] (Table 1.5). To begin with, MSCs exhibit tropism for

Table 1.4: Impact score used for risk priority number calculations.

Impact	Criteria	Score
Low	No discernable effect on CQA, homogeneous results published in literature	1
Low	No results published in literature	1.1
Medium	Unknown effect on CQA due to heterogeneous results published in literature	2
High	Known effect on CQA, homogeneous results published in literature	3

sites of tissue damage [82] and generate local regenerative environments (secretion of anti-inflammatory factors [83], stimulation of local cell-mediated repair processes [84]). In addition, MSCs have interesting immunomodulatory properties by activating and/or modulating the maturation of various immune cells including T-Lymphocytes [29], B lymphocytes [85], natural killer (NK) cells [86] and dendritic cells [40]. However, evidence suggests that these properties may intrinsically depend on the micro environment in which the cells are grafted [87]. For example, excess cytokine production (growth factors, chemokines *etc.*) or an uncontrolled immunosuppressive effect can stimulate tumor growth [88] or favour an inflammatory response [89]. As a result, sufficient purity and quality of these products will be required for their successful development. In addition, their properties should be preserved as well as their capacity to adapt *in-vivo* to avoid adverse effects. On the other hand, MSCs are able to differentiate into different tissues of mesodermal lineages such as bone, cartilage, tendon, muscle or fat cells [84]. It has also been suggested that MSCs can differentiate into ectodermal lineage cells such as neurons or epithelium cells, but also endodermal lineage cells such as hepatocytes [87]. As a result, cells can be used for *ex-vivo* tissue engineering using adapted scaffolds such as extracellular matrix scaffolds [90], or on polymeric scaffolds [91]. In this case, the specific and controllable differentiation potential needs to be maintained. The differentiation may also be of interest *in-vivo*, although MSC differentiation in the acute phase of injury is unlikely and regeneration is most-likely mediated by their trophic function or cell-cell contact rather than differentiation.

Defining critical quality attributes (CQAs).

Building upon previous quality-based approaches for MSC manufacturing [92], the attributes which affect the QTPP defined in Table 1.5 are proposed as well as suggested acceptance criteria for these parameters, mandatory per FDAs code of federal regulations (21-CFR) (Table 1.6). The acceptance criteria proposed are based on literature data but should, without any doubt, be adapted to individual applications.

Dosage Strength. A generalized optimal dose without adverse side-effects is not expected since likely depends on disease, route of administration, frequency and other

Table 1.5: Generic quality target product profile for mesenchymal stem cell therapy.

ICH Q8 recommendation	**Undifferentiated cell transplantation**	***In-vitro* differentiation**
Intended use in clinical setting (route of administration, dosage form, delivery systems *etc.*)	Allogenic or autologous MSC transplant at the site of injury	Transplantation of differentiated autologous tissues
Dosage strength(s)	1-2 $\times$ 10^6 cells/patient kg	*N.A. (as necessary for tissue constructs)*
Container closure system	Frozen product for injection	Reconstructed *in vitro* tissue
Therapeutic potency and attributes affecting pharmacokinetic characteristics	Immunomodulatory properties through secreted biomolecules and/or cell-cell contact after MSC homing mechanisms	Specific and controlled differentiation; functional *in vivo* accepted tissue graft
Drug product quality criteria (e.g., sterility, purity, stability and drug release)	Fully sterile ; absence of external contaminations ; Frozen stability ; high viability after thawing	Sterility ; *In vivo* stability ; low tissue immunogenicity

parameters [79]. It is therefore likely that the number of cells required at the end of the expansion process will vary and, ideally, the process should keep flexibility in this regard. The dosage strength will depend, from a process perspective, on cell quantity and cell viability throughout the process.

- Cell Quantity (Qua.) Final cell quantity can be directly obtained by viable cell counting of the detached cells after expansion. During the expansion process, this parameter is intrinsically linked to the different step yields (from initial cell extraction to final detachment phase) as well as the final concentration. Although it would be interesting to perform the cell culture process in concentrated conditions to reduce equipment volume, it should be kept in mind that an increased concentration may cause the aggregation of cells or an increased viscosity which may impact the lot-to-lot homogeneity of the final product or cause needle clogging during patient administration [38].

- Cell Viability (Via.) Viability can easily be determined after cell detachment using exclusion staining such as trypan blue or flow cytometry techniques. In order to achieve robust and cost-effective large-scale manufacturing, it is important to maintain a high level of viability, typically greater than 90 % all throughout the process. In certain exceptional cases, a lower limit of 70 % can be acceptable for the finished product [69].

Therapeutic Potency. Potency is the specific ability of a product to effect a given result when administered according to defined posology. This characteristic is influ-

enced by 3 target attributes: identity, differentiation capacity and *in-vivo* effect for which testing should comply with 21CFR section 600.3 recommendations.

- Identity (Id.) The cells produced during and after expansion must have maintained the characteristics of MSCs, at the risk of expanding the wrong cell type. In 2006, the international society for cellular therapy (ISCT) proposed a list of cell markers which can identify MSCs [11] and which continues to be used. It should be noted that there are debates concerning the robustness of ISCT cell markers for MSC characterization [92] and that additional RNAs or proteins could be used to complete the criteria proposed [93, 94]. In this mindset, the review of the 20 most-used production markers in 66 MSC-based product submissions to the FDA calls for caution regarding the need for further characterization, especially for non-bone marrow derived MSCs [95]. It is likely that the definition proposed is neither exhaustive nor universal.

- In-vitro differentiation capacity (Dif.) MSC differentiation capacity was separated from identity markers for clarity in the analysis. Although some quantitative descriptions have been proposed for MSC differentiation [96], they globally remain rare. Most articles qualitatively evaluate the capacity of a sample to undergo differentiation and the proportion of cells which have the tri-lineage differentiation capacity is, in most cases unknown. However, since routine testing of clonal populations would require long analysis and delay product release, this CQA has been evaluated in a qualitative manner (ie, sub-populations of the final cell culture sample must be able to differentiate into the three lineages and variations between conditions may be visually defined).

- Expected in-vivo effect (Viv.) The last quality attribute impacting potency is the capacity of the cells to exert their appropriate *in-vivo* effect. Functionality assays are typically measured through *in-vitro* co-cultures with T-cells, for example, but tests should ultimately depend on the target therapy [69]. Although this attribute is rarely measured, information was included when possible.

Product quality. In order to keep a homogeneous nomenclature between sections, the term drug quality will be used according to its use in ICH Q8 guidelines (*i.e.* characteristics required to avoid adverse effects after administration such as sterility, purity and stability of the product).

- Genetic stability (Gen.) Many studies have shown an increased senescent state after an *ex-vivo* culture of MSCs, for which replication is limited by the Hayflick limit and telomere length [97]. Generally, senescent cells display a characteristic large, flattened morphology and are characterized by an irreversible G1 growth arrest involving the repression of genes that drive cell cycle progression and the

up-regulation of cell inhibitors like p53/p21 (primarily due to telomere dysfunction and DNA damage) and p16/RB (oncogenes, chromatin disruption and various stresses [98]). Senescent cells secrete factors that are pro-inflammatory [99], stimulate tissue aging and tumorigenesis [87, 100]. Although data suggests a higher genetic stability of MSCs compared to other cell sources such as embryonic stem cells (ESC) or induced pluripotent stem cells (iPSC) [101], more routine and thorough genetic phenotyping would be required to further understand these possibly critical effects. It is still unclear, however, how such data would be interpreted, and what level of genetic abnormality would be required to disqualify a cell line for clinical use [102]. For simplification, these problematics have been regrouped into a qualitative attribute called genetic stability.

- Cell Purity (Pur.) The last quality attribute concerns the absence of contamination during the process. Ideally, sterility testing should be performed after each critical manipulation step during cell culture in order to detect fungal, bacterial or mycoplasma contamination of the cells. The presence of contaminations compromises the safety of therapeutic products. Furthermore, the final cell product should be free of other cell contaminants which could have adverse effects *in-vivo*. For example, the presence of 25-50 % of non-MSC cells within the cell population causes a dose-dependant diminution of differentiation potential *in-vivo* and *in-vitro* [91]. Although this amount of contamination may seem high, and purity is expected to be higher than 75 % at the end of cell culture, it should be kept in mind that, after clinical applications, the injected MSCs will be diluted with host connective tissue, at a factor which is difficult to predict.

Defining critical process parameters (CPPs)

Maintaining high quality standards within a production facility requires a rigorous understanding of the interaction between process parameters and the impact of their potential deviation on product quality (*i.e.* defined CQAs). In the case of MSC culture, the most common manufacturing technique is composed of two main stages, each with a set of co-dependent parameters.

Cell Extraction. To begin with, MSCs are extracted from a suitable donor and an appropriate tissue source. Although the majority of clinical trials have used cells isolated from bone marrow aspirations (BM), extraction protocols remain invasive and painful. Alternative tissue sources include discarded umbilical cords (UC) [108] or lipoaspirate-derived adipose tissue (AT) [109] which offer an easily accessible, low cost and pain-free source of MSCs. Independently of tissue source, the extracted cell population has typically been composed of only a small proportion of MSCs (less than 0.05 % in the case of BM [110]). As a result, cells need to be carefully selected to obtain

Table 1.6: The definition of critical quality attributes for mesenchymal stem cell therapy based on the defined quality target product profile.

QTTP	**CQA**	**In-process parameter**	**Acceptance criteria**	**Ref.**
Dosage Strength	Final Cell Quantity (Qua.)	Individual step yield	(>85 %)	
		Expansion rate	As high as possible	
		Concentration	As high as possible without aggregation or increasing viscosity	[38]
	Viability (Via.)	Cell viability	>90 %	[69, 80, 103, 104]
Potency	MSC Identity (Id.)	Adherence to plastic	Yes	[11]
		Specific positive antigen expression $\geqslant$ 95 %	CD105+, CD73+, CD90+	
		Specific negative antigen expression $\leqslant$ 2 %	CD45-, CD34-, CD14- or CD11b-, CD79 α - or CD19-, HLA-DR-	
	Multipotent Differentiation (Dif.)	Osteoblast, Adipocyte and Chondroblast	Yes (*in-vitro*)	[11]
	In Vivo Effect (Viv.)	To be defined for each application	*Not Applicable.*	[105]
		Ex: Inhibition of T-Cell growth in co-cultures		[69]
Product Quality	Genetic stability (Gen.)	Karyotype	23 Pairs of Chromosomes	
		Human Telomerase Reverse Transcriptase activity (hTERT) / Telomere length	High expression of hTERT	[106]
		in-vivo tumour formation (in mice)	Absent	[69]
		Morphology	small, spindle-form	[98]
	Purity (Pur.)	Sterility testing for each lot	$\leqslant$ 10 CFU/mL for test organisms	[69, 103]
		Mycoplasma assay for each lot	No detectable Mycoplasma (by PCR)	
		Endotoxin assay for each lot	$\leqslant$ 5.0 EU/mL (Limulus amebocyte lysate LAL)	[69]
		Cell purity	$\geqslant$ 70 %	[104, 107]

a homogeneous initial population of MSCs [79, 87, 110–113]. The question of which tissue source or extraction method might be optimal for any given clinical situation is, however, not yet clearly understood due to important quality variations reported in literature [79, 87, 96, 114–116]. Lastly, the extraction phase typically ends with a cryopreservation step for logistic purposes (expansion of the cells is rarely performed at the site of extraction) [26]. Studies generally tend to show that cryopreservation has little impact on CQAs and that traditional cryopreservation techniques can be considered robust for pre-clinical trials [103].

Overall, the most noteworthy characteristic, at this stage, is the considerable donor-to-donor and intra-population heterogeneity [117–119] which is particularly critical for allogenic therapies since each donor brings a "one to many" associated risk in case of un-detected infection or functional abnormality [120]. In this regard, donor age seems to be the most important factor [121], for example through a decreased quantity of cells extracted was generally lower in older patients [115] possibly due to a reduced plastic attachment [122] or to a lower initial titer of MSCs [91] (see Table 1.7). Evidence also suggested that expression levels of MSC markers may vary upon age [123] as well as an altered differentiation potential ('adipogenic switch' described in most studies [98, 124]). In addition, age seemed to reduce cell growth [125], increase doubling times [115, 126], reduce replicative lifespan [125, 127] and increase genetic instability [123, 125]. Since donor age is the only parameter which scored a RPN value greater than 9 (see Figure 1.13), it can be considered as the only CPP at this stage. However, the combination of parameters as a whole, for example patient illness such as diabetes [128] or obesity [129], make it difficult to predict, at a large scale, how many cells can initially be extracted for each donor and whether the quality and purity of these cells will meet the requirements for clinical applications.

Cell Amplification. After the initial extraction phase, cells undergo an amplification phase using mono-layer flasks (tissue flasks) of different sizes [26] in order to expand the initial cells to a reproducible target concentration for administration. This method of expansion is well documented in literature [130] but labour intensive due to the required manual passaging of cells between different containers. Furthermore, the risk of contamination increases with the number of container systems and the required number of passages. This risk can be reduced by limiting the number of containers (through cell stack systems for example [131]), using fully automated processes [132] or developing fully closed production systems [133, 134], although these options are not yet fully explored in clinical facilities. Furthermore, in most clinical trials, cells were expanded using defined basal cell culture media, composed of all the elements required for cell growth such as an energy source (glucose often supplemented with L-glutamine), essential amino-acids and specific ions (calcium, magnesium, potassium, sodium *etc.*) [26]. In addition, these chemically defined media were, in most studies,

completed with 5 to 20 $\%_{v/v}$ bovine serum or xeno-free alternatives such as human platelet lysate (HPL) [69], which provides complementary factors such as hormones, substrate-attachment molecules or binding proteins [135, 136]. Notably, the choice of supplementation type and concentration has been shown to impact bone formation capacity [137] and immunomodulatory effects [138–140]. In parallel, seeding density has been at the center of various studies [26] but results remain controversial, leading to low overall RPN scores. The only parameters which scored RPN ratings over 9 (and may therefore be considered as critical) seem to be the amount of population doublings that cells undergo and the oxygen concentration used during cell culture (see Figure 1.13).

Cell culture duration can typically be calculated using either the number of passages (usually performed using enzymatic detachment such as trypsination) or the number of population doublings (PD) that the cells undergo. The population doublings, rather than the amount of passages, should be considered when comparing studies due to high variability between research teams in seeding densities and confluence before harvest. This renders the comparison between cells at a same passage difficult [141]. In this regard, the number of population doublings will determine the maximum amount of cells that can be obtained through cell culture since proliferation typically remains within the Hayflick limit of around 20-60 population doublings [142–148]. The most described reason for senescence during cell culture is a reduced telomere length throughout culture (50 - 100 bp/PD) [98, 125, 146] associated with very low levels of telomerase activity indicating cells are not "repairing" the shortened telomeres [148]. It can be noted that the shift towards senescence may be gradual over time (possibly though the progressive regulation of genes [142, 144, 149] and early signs of senescence (for example through change in morphology or an increased doubling time) have been observed as early as a few days after culture [150, 151]. In addition, increase of population doublings has also been associated with a loss of multipotency [141, 148] as early as 18-20 population doublings [150] as well as reduced immunosuppressive capacities [140] or an increased tumorgenicity [148].

MSCs are naturally present in tissues for which dO_2 concentrations can vary between 1 and 7 % of O_2 saturation depending on the host tissue and tissue vasuclarization [152, 153]. The most common belief is that *ex-vivo* expansion should be performed in conditions close to the physiological environment from which the cells were extracted, since the amount of oxygen available for cells will have an impact on cell metabolism. For example, an increased growth has been observed in hypoxic conditions (1 $\%_{v/v}$ O_2 in the head-space) [154] as well as an increased lifespan (3 $\%_{v/v}$ O_2 in the head-space) [153, 155] compared to normoxic conditions. Some authors propose that cells have a higher susceptibility to cell death at elevated O_2 concentrations for which viability is reduced [153]. In addition, the differentiation potential seems to be impacted [153, 154, 156] as well as the cell secretome [153] and genetic aberrations [155, 157].

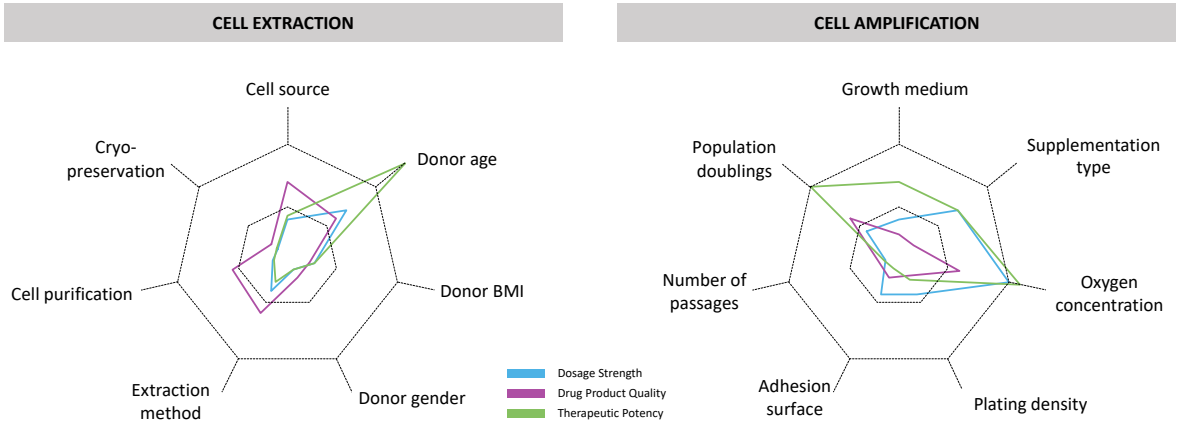

Figure 1.13: Impact of cell extraction and amplification parameters on the quality target product profile attributes. All parameters in the inner zone have a risk priority number rating below 4 (possible impact on two critical quality attributes). All parameters outside the exterior zone have risk priority number ratings above 9 (proven impact on two critical quality attributes).

These studies tend to show the quality of cells produced in normoxic conditions may not meet the requirements for clinical use and this parameter should be continuously monitored. Furthermore, it should be kept in mind that, in the case of culture in T-flasks, the oxygen concentration available for the cells is difficult to predict as depends on medium height, density of cells, oxygen consumption, and the incubator characteristics and the concentration is also influenced by the multiple re-perfusion of room air oxygen concentrations during medium changes, passaging or other manipulations [158].

Furthermore, it can be noted that there are vast controversies in the published data when evaluating the impact of these parameters independently. The review of existing data seems to suggest that there are important interactions between parameters (for example oxygen concentration and nutrient requirements, or cell age and the impact of population doublings) which are still difficult to predict or analyze, but may have a critical impact on the quality of the MSC products.

Overview of the cell culture process. Overall process parameter criticality during MSC cell culture was evaluated to identify the most critical parameters throughout the process (see Figure 1.14). The data suggests that the most critical parameters (as a whole, and assuming an identical weight for all of the CQAs) are cell source, donor age, supplementation type, oxygen concentration and the amount of population doublings that the cells undergo during this phase. These parameters all exceed the global average RPN limit of 4. In order to meet requirements for quality specifications, these parameters should typically be controlled during the expansion phase, have science-based specifications, and their impact should clearly be defined. It is noteworthy, however, that it is difficult to predict how various independent parameters interact during MSC production processes, in particular with regard to deviation accumulations. As a result,

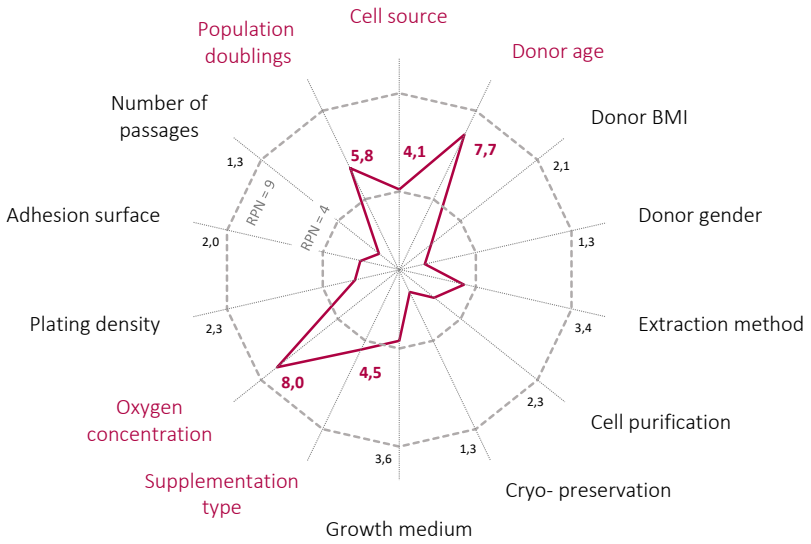

Figure 1.14: Impact of process parameters throughout MSC manufacturing. All parameters in the inner zone have a global risk priority number rating below 4 (low criticality). All parameters outside the exterior zone have risk priority number ratings above 9 (high criticality).

using additional tools such as design of experiments (DOE) to detect and understand these interactions may be required to further define the design space of quality based MSC manufacturing.

1.2.4 Future challenges

Although great progress has been made to understand and develop cell expansion in two dimensional flasks, these manufacturing processes are not economically viable to supply the predicted requirements for clinical research of cell therapies and tissue engineering products [159]. For larger scale manufacturing, new automated technologies [132] with greater yields per lot and which reduce equipment occupation space within production facilities, will be required [160]. In this regard, trends are shifting towards 3D cultures using scalable bioreactors [161, 162] which are already extensively used in the pharmaceutical industry and are generally well known (online monitoring, maintenance procedures, cleaning validation *etc.*). In order to do so, the adherent MSCs are no longer cultured in planar conditions but using new scaffolds such as microcarriers, hollow fibre or packed bed systems. In addition, the possibility of a fully closed system significantly reduces contamination risks, equipment volume, and will ultimately reduce costs of GMP production [134]. It should be noted that data concerning MSC cell culture in bioreactors still remains scarce and fine-tuning of process parameters to increase quality and yield is still in early stages of research. Only one clinical trial using bioreactor-based expansion of MSCs seems to have been published (NCT00919958 [163], key words "Mesenchymal Stem Cell" and "Bioreactor" in https://clinicaltrials.gov/). Understanding the physical and biological mechanisms as well as their kinetic evolution

during the different cell culture stages will help unlock current bottlenecks towards quality driven protocols. Using similar QBD methodologies, online monitoring data, and modelization techniques (reviewed in [164]) during early-phase process development could be the key to a successful scale-up process and approved commercialization by health authorities.

Table 1.7: Process parameters during cell extraction and cell expansion and their impact on critical quality attributes. For each parameter, an impact score between 1 and 3 was attributed based on literature and according to Table 1.4.

		Strength		Potency			Quality	
Parameter	**Range**	**Qua.**	**Via.**	**Id.**	**Dif.**	**Viv.**	**Gen.**	**Pur.**
Cell Source	BM, UC, AD	3 [114, 165]	1 [96]	1 [96, 109, 127, 165, 166]	3 [96, 114, 115, 165, 167, 168]	1.1	2 [114, 165]	2 [169, 170]
Age	< 10 to > 70	3 [98, 121–123, 126, 171, 172]	2 [123, 126]	2 [121–123, 172]	3 [115, 121–123, 125, 142]	2 [173–176]	3 [123, 125, 177]	1.1
BMI	< 25, 25-30, > 30	2 [109, 115]	1.1	1 [115]	2 [115]	1.1	1.1	1.1
Gender	Man, Woman	1 [115, 171]	1.1	1 [115]	1 [115]	1.1	1.1	1.1
Extraction	Various protocols	3 [112, 135, 171, 178, 179]	1 [178]	1.1	1 [135, 178]	2 [178]	1.1	3 [180]
Purification	Antigen, MACS, FACS	1.1	1.1	1 [113]	1 [113, 181]	1.1	1 [169]	3 [110, 169, 181] , [113]
Cryopreservation	Yes, No	1 [123, 182]	1 [103, 182, 183]	1 [182]	1 [182]	1.1	1 [183]	1.1
Growth medium	Various	3 [179, 184]	1 [185]	1 [184]	2 [184, 185]	3 [179, 184]	1.1	1.1
Supplementation type	FBS, HPL	3 [136, 137, 139, 140, 170, 186, 187]	2 [187]	1 [136, 139, 186–188]	2 [135, 136, 139, 170, 172, 186, 188]	3 [136–140, 188]	1 [139, 186, 187]	1 [139]
Plating density	10^{-1} - 10^{5} MSCs /cm^2	3 [26, 189, 190]	1.1	1 [179]	2 [179, 190]	1 [179]	1.1	1 [189]
Adhesion surface	Varied	3 [179]	1.1	1 [179]	1 [179]	1 [179]	1.1	1.1
Oxygen	2-21 % O_2	3 [153–155]	3 [153]	1.1	3 [153, 154, 156, 158, 191]	3 [153, 154]	3 [153–155, 157]	1.1
Passages	1 - 15	1 [170]	1.1	1 [144]	1 [170, 192]	1.1	1 [144, 170, 192]	1.1
Population doublings	up to 50 PD	3	1.1	1 [140, 146, 148], [193]	3 [146, 189, 190], [150], [193]	3 [140, 148, 150]	3 [125, 146, 151], [142], [193]	1.1

1.3 Mesenchymal stem cell expansion on microcarriers using bioreactors

As presented in the previous chapter, expanding MSCs using 2D flasks, although well documented in literature, remains a complex task. In addition, this method of culture is typically space consuming, even considering the fact that multilayer flasks have been developed to increase the surface available per volume unit. The use of flasks also typically requires the manual passaging of cells inside several different containers which increases the risks of batch contaminations. Increasing the amount of containers also typically increases heterogeneity within a lot since small variations in oxygen or pH between containers can impact the way cells expand. Lastly, the measurement and control of parameters (*i.e.* oxygen concentration, pH and/or local nutrient concentrations) is typically hard to perform rendering these processes difficult to automate.

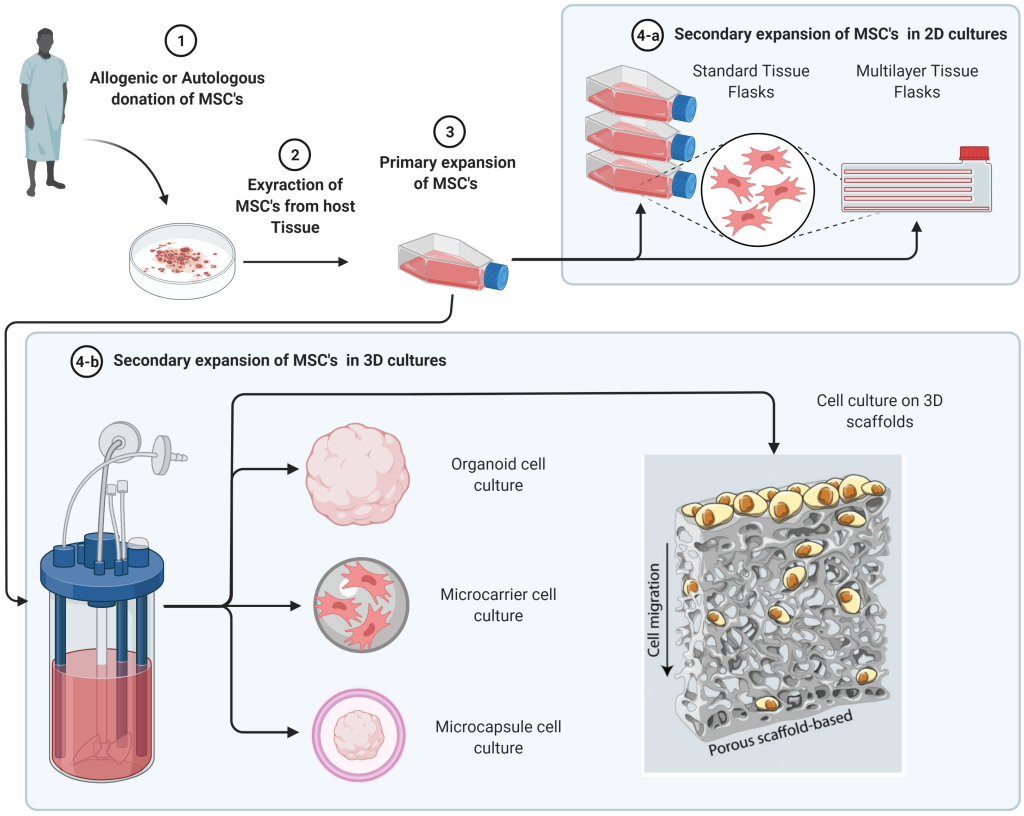

Figure 1.15: Overview of MSC cell expansion processes in both 2D and 3D cultures. Scaffold representation adapted from [194].

For larger scale manufacturing, a shift to 3D cultures using easily scalable bioreactors may be essential to produce high-quality and reproducible stem cell products [161, 162]. In order to do so, the adherent MSC's are cultured using matrices directly incorporated in the cell culture system, embryoid bodies (small aggregates of cells in suspension), micro-capsules containing the cells, or microcarriers (small particles in suspension on which adherent stem cells expand) (Figure 1.15). Using 3D culture

brings flexibility to the process, enables high density cell expansion in conditions which can easily be monitored, reduces the risk of contamination, and should ultimately reduces the cost of GMP manufacturing [195]. In addition, these culture systems can be adapted to various agitation conditions and at different scales making scale down and scale up easier to perform (Erlenmeyer flasks, spinner flasks, wave bioreactors, rotating wall systems *etc.*). However, **data concerning MSC cell culture in bioreactors still remains scarce and the fine-tuning of process parameters** (such as impeller design, feeding strategy, aeration methods *etc.*) **and operating conditions** (such as agitation rate, medium composition *etc.*) **to increase yield and quality is still in early stages of development.**

1.3.1 Process engineering for an enhanced MSC expansion

The need to develop automatable and easily scalable processes for MSC expansion arises not only from the fact that donors can only provide a limited amount of cells and so cannot meet alone the clinical needs to come ; but also from the strict regulatory guidelines imposed by local health authorities and the expected pressure from social security members to bring down therapeutic costs. Altogether, trends from past pharmaceutical sectors, for example monoclonal antibodies (mAb), are valuable road-maps. These sectors have, over the years, been a great source of innovation in mammalian cell expansion process engineering by developing cell culture systems and analytical tools (feeding systems, cell retention systems, single-use systems, online analytical systems, automation *etc.*).

Notably, the recent shift of mAb production processes from typical batch to fed-batch to continuous production led to a substantial reduction in product costs. To begin with, the continuous process switch reduces the overall capital costs required from \$165 million to \$53 million. Consequently, the global cost of active pharmaceutical ingredient (API) production was reduced from from \$99/g API to \$61/g API thus digging a net value difference between fed-batch and continuous processes of \$720 million over 15 years [196]. In addition, substantial process optimization and engineering have led to greater productivity in these processes (antibody production can now achieve titers of approximately 5 g L^{-1} at the end of the production phase, when only about 50 mg L^{-1} would typically be obtained in 1986 [197]). Increasing product titer during the process will also undeniably have an impact on the cost of goods since lower equipment volumes will be required to produce the same quantity of active pharmaceutical ingredient (API). For example, increasing product titer from 0.1 to 1 g L^{-1} was estimated to reduce the cost of goods from \$ 1500 to \$ 260/g [198]. Lastly, the scale of the equipments available continues to expand. In the 1990s, a bioreactor volume of 10 000 L was considered very large scale but now many companies have installed several 25 000 L bioreactors for total bioreactor capacities achieving over 150 000 L worldwide [198, 199].

These trends and innovations will certainly pave the way for cell therapy manufacturing development and optimization to define processes with highly productive processes (reviewed in [200]). Using easily scalable bioreactors remains, to this day, the most viable option. However, product specific problematics and constraints will need to be addressed specifically for these new therapeutic products for which the cells are no longer cultured as factories to produce a single protein or product, but rather for the production of complex products such as extracellular vesicles, or even as the product themselves in the case of cell therapies. In this context, unresolved factors continue to be relevant such as the choice of equipment, feeding strategies (including microcarrier feed) and online / offline monitoring of product quality.

MSC metabolic pathways and factors impacting growth

In order to sustain viability and growth, stem cells require sufficient nutriments (energy source, salts, amino acids *etc.*) throughout their culture. For this, different defined or undefined cell culture medium have been used (*ex.* α-MEM, DMEM), and are typically supplemented with animal serum such as fetal bovine serum (FBS), or human blood-derived alternatives such as human platelet lysate (HPL) at a concentration of 1 % to 10 $\%_{v/v}$ (reviewed in [201]). These added elements supplement the basal medium in proteins, growth factors, vitamins, hormones, fatty acids and lipids. All of these elements combined should provide a sufficiently rich environment for cells to properly expand and maintain viability while also limiting the accumulation of possibly toxic elements and / or byproducts.

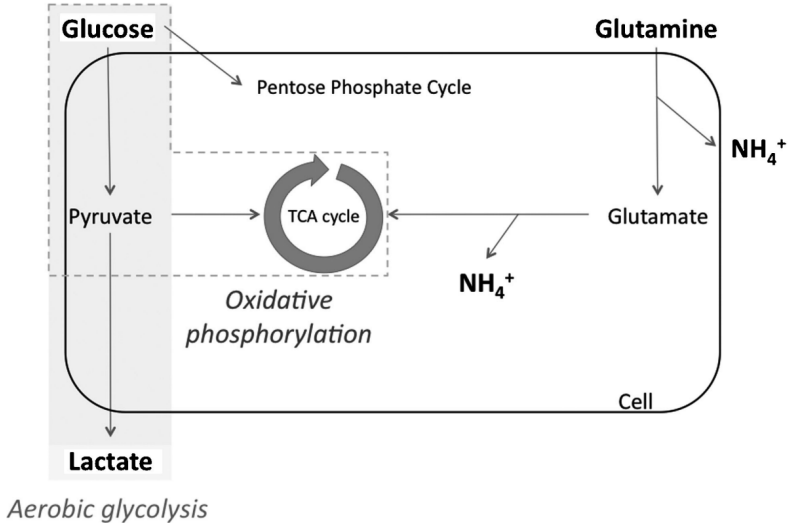

Figure 1.16: Simplified version of the main metabolic pathways of animal cells. Proliferating cells, such as stem cells, rely primarily on aerobic glycolysis (shaded in gray) to generate energy as an alternative to the oxidative phosphorylation (dashed line). (Adapted from [202]).

- **Glucose.** To begin with, glucose is the most important source of energy for cell growth and maintenance and its availability can have powerful impacts. For example, exposure of hMSC to high glucose concentrations (20 mM) has been reported to enhance hMSC proliferation [203]. On the other hand, reducing glucose concentration (from 25 to 2.5 mM) was also found to enhance hMSC proliferation and reduce senescence by inducing aerobic metabolism [204]. Other authors advise to limit glucose concentrations during culture between 0.13 and 1 mM to prevent a limitation by glucose starvation [202]. From a process perspective, these empirical set-points can be used to determine feeding strategies according to known metabolism. For example, the specific consumption rates (q_{gluc}) of approximately 8 - 9 pmol cell^{-1} day^{-1} [205, 206], 10 pmol cell^{-1} day^{-1} [207] or between 14 to 17 pmol cell^{-1} day^{-1} [202] have been reported for BM-MSCs cultivated under normoxia conditions (for which oxygen concentration is close to that of the native MSC tissue environment). These results were obtained during cultivation of MSCs on T-Flasks, Synthemax II microcarriers, and on 12 well plates respectively and can be used to prevent glucose starvation in these systems. However, variations of a factor of 2 in the specific glucose consumption rate have been observed between AD-MSCs and BM-MSCs during the first 5 days of culture [208]. Caution must be kept in mind when comparing metabolic results due to the high impact of culture conditions, cell passage and donor age (reviewed in detail in Section 1.2.3).

- **Glucose uptake.** The glucose molecule, once assimilated by the cell, can be utilized either by oxidative phosphorylation (if sufficient oxygen is present around the cell) or by anaerobic glycolysis to produce units of the energy organic compound adenosine tri-phosphate (ATP) (Figure 1.16). The metabolic route activated typically depends on the quantity of oxygen which is available for cell metabolism and can be measured during cell cultures by, for example measuring the production yield of lactate from glucose. While oxidative phosphorylation will typically produce low lactate concentrations but high available ATP concentrations (36 moles of ATP molecules will be generated for 1 mol of glucose molecule consumed), glycolysis will generate much higher lactate concentrations and lower ATP levels (2 moles of ATP per glucose mole consumed). For BM-MSCs, glucose metabolic transformation yield to lactate ($Y_{lac/gluc}$) of approximately 2 [206] or even higher than 2 [202] was observed indicating that metabolism is not primarily based on mitochondrial oxidative phosphorylation and that other carbon sources are metabolized by the cells in these conditions. Although glycolysis is a less efficient metabolic pathway in terms of ATP production, this is counterbalanced by the excess availability of glucose provided by the culture medium in most studies. In such conditions, cells have been shown to favour glycolysis which

could generate ATP at a faster rate than oxidative phosphorylation [209, 210]. In addition, MSCs are typically contained in tissues for which the amount of oxygen is limiting, which favours glycolysis and contributes to limit the amount of endogenous reactive oxygen species (ROS) which have been associated with oxidative damage to DNA, proteins and lipids [210]. Lastly, recent studies have demonstrated that enhanced glycolysis was associated with elevated therapeutic effects of MSCs by promoting survival, proliferation capacities and increasing the secretion of pro-growth factors / factors for tissue regeneration (thoroughly reviewed in [211]).

- **Glutamine.** Apart from a constituent of proteins (via protein biosynthesis), glutamine is also an important energy source for mammalian cell culture. Glutamine is metabolically assimilated to α-ketoglutarate (α-KG) which is then converted to pyruvate. Specifically, glutamine is also known to have an important role to start cell proliferation, namely as supplier of carbon in the form of mitochondrial oxaloacetate and nitrogen for other amino acid synthesis [212]. Accordingly, studies have shown that the consumption of glutamine (q_{glut}) may decrease throughout MSC cell culture with levels varying from approximately 50 pmol cell^{-1} day^{-1} during the first 3 days of culture to less than 10 pmol cell^{-1} day^{-1} after the 5^{th} day of culture [202]. However, other studies have suggested that glutamine not be an important energy source for human MSCs with average disappearance rates of 4.5 pmol cell^{-1} day^{-1} corrected to specific glutamine consumption rates of 0.007 pmol cell^{-1} day^{-1} [206] when a 10 % spontaneous decomposition per day is assumed [213]. Other studies have shown that the metabolic by-product α-KG was required for BM-MSC proliferation, specification and differentiation [214] and that glutamine metabolism had a crucial role in the regulation of MSC immune functions [215]. In order to further understand how glutamine is assimilated by MSCs during their cell culture, the average conversion yield of glutamine to NH_3 ($Y_{NH_3/Glut}$) can be calculated. This rate has been found to be approximately 1.6 [206]. However, since it is well known that glutamine naturally degrades during the cell culture, at rates of approximately 10 % per day, and that NH_3 is a product of this spontaneous degradation, it is difficult to determine to what extent the values measured correspond with either spontaneous degradation or cell metabolism. In addition, NH_3 is also formed in other amino acid metabolic pathways such as glutamate and serine [206].

- **Metabolic by-products.** Metabolic studies of human ES cells have shown that high levels of metabolic waste products, particularly lactate (25 mM) and ammonium (0.8 mM), and low pH (6.6) obtained at the late stages of cell propagation could cause cell growth arrest and reduce the population of cells expressing pluripotency markers [216]. Other studies determined, high levels of lactate

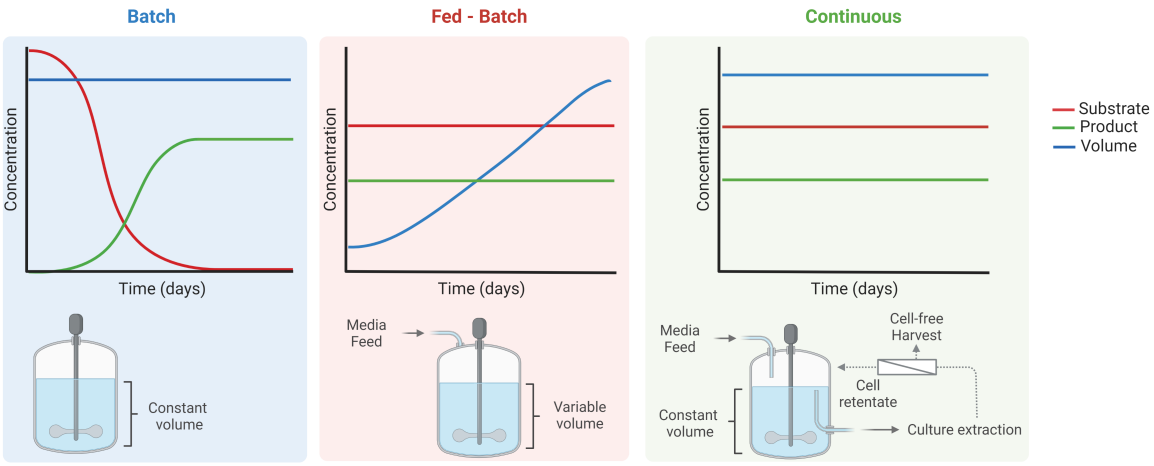

Figure 1.17: Schematic representation of batch, fed-batch and continuous processes.

(35.4 mM) and ammonia (over 2.4 mM) as having inhibitory effects on hMSC cell proliferation [206]. As a result, accurately controlling glucose and glutamine concentration and NH_3 concentration in the cell culture medium seems to be important, particularly at the end of cell cultures where by-products tend to accumulate (even if glutamine metabolism significantly reduces after the first few days of culture [202]).

Feeding strategies in bioreactors

As described above, the elements impacting MSC cell metabolism can have detrimental effects on many key expansion factors including cell proliferation, senescence, and attributes associated with cell quality. It can be noted that, in almost all published studies cultivating MSCs on microcarriers, the feeding strategy, which is often empirical, is sufficient to ensure both sufficient substrate concentrations and to prevent cultures from being performed under toxic concentrations of metabolic by-products [208]. For this, four major modes of culture have been described in bioreactors, specifically applied to microcarrier-based systems (Figure 1.17). Notably, in the case of adherent cells, the available cell culture surface, brought to the cell culture through the addition of various concentrations of microcarriers, will be considered as a substrate, much like feeding the cell culture with nutrients or oxygen.

- **Batch cultures.** These cultures are performed in a fixed culture volume composed of an initial concentration of nutrients which will be consumed over time and for which by-products of cell metabolism will be secreted in the cell culture medium. This mode of culture is a completely closed mode of culture from a metabolic point of view and therefore is the mode of culture with the least contamination risks. However, cell yields are typically modest due to nutrient limitation at the end of the cell culture or eventually an inhibition of growth by cell metabolic waste products. Since pluripotent stem cells (ES and iPS cells) depend on the

regular supply of growth factors to maintain stemness [217], strict batch processing is essentially incompatible for their prolonged expansion. The description of ES aggregate cultures inoculated at very low seeding concentrations ($2 - 8 \times 10^4$ cells per mL) in 125 mL suspension stirred bioreactors have been described [218] but were also associated with low final cell concentrations which would be incompatible with requirements from the industrial sector. Lastly, the culture of WJ-MSC on microcarriers in batch mode was found to only last a few days due to nutrient depletion [219, 220] which reinforces the idea that this mode of culture is unsuitable for MSC expansion.

- **Draw-fill feeding strategies.** The most common feeding strategies to date concern the manual replacement of a specific volume of the cell culture supernatant at given times, most often through empirical knowledge on how cells grow, and taking into account practical aspects. For this, microcarriers are left to settle by manually stopping the agitation and a given quantity of the cell culture supernatant is extracted and replaced by fresh medium containing nutrients and specific growth factors required for MSC expansion. The replacement of a given quantity of the cell culture supernatant is also used in order to limit the accumulation of byproducts such as ammonium or lactate and therefore limits the possible growth inhibition due to high concentrations of these elements. For example, human MSC culture on Plastic microcarriers in a vertical wheel system was found to be effective by replacing 25 % of the cell culture volume every 12 hours after the second day of culture [221]. Other work performed using microcarrier-based expansion of BM-MSCs in spinner flasks showed that changing the feeding regime from a replacement of 25 % of the working volume every 2 days to replacing 25 % of the medium every day prevented glucose starvation, limited the accumulation of ammonium (which initially reached possibly inhibiting concentrations of 3.5 mM) and increased process productivity [222]. In general, studies tend to use a 25 % to 50 % media exchange rate every 2 or 3 days [223–231].

- **Fed-batch cultures.** This mode of culture is used in order to limit the accumulation of by products and substrate limitations. For this, cell cultures are continuously fed by the addition of fresh medium at a constant or variable dilution rate. As a result, since medium is added during the cell culture, the overall cell culture volume will increase. These processes are typically limited by the size of the bioreactors used, but should limit the amount of medium used compared to traditional draw-fill feeding strategies by approximately 70 % [228] as well as limit the risk of contamination [223]. Lastly, using fed-batch processes allows for a continuous cell culture where manual settling of microcarriers is not required to feed the cell culture. In the case of MSCs, fed-batch processes (by adding 2 % of the working volume of Rooster Replenish-MSC-XF solution) were shown to

increase process productivity compared to batch processes when MSCs were expanded on Corning Low Concentration Synthemax II microcarriers in a single use vertical wheel bioreactor [232]. These effects were only found when feeding was performed in the optimal time however. Waiting too long (*i.e.* over 4 days) before feeding the cells caused cell modifications and a decreased cell growth which could not be reversed by adding fresh medium (yields were reduced by over 35 % in these cases). In addition, current trends are aiming to add, during the cell culture, fresh growth surfaces at specific time-points in order to prolong the cell expansion process. For this, the ability of cells to migrate from a colonized microcarrier to a fresh microcarrier, or *bead-to-bead*, is expected. However, certain studies show little impact of adding additional microcarriers on day 3 of the cell culture in a fed-batch process [232]. In another study, authors investigated the addition of fresh coated glass microcarriers when changing cell culture scale from 200 mL to 1 L. In this study, the simultaneous addition of cell culture fresh media to dilute waste by-products and addition of fresh growth surface proved to be successful since no change in the apparent growth rate (0.53 and 0.55 h^{-1} respectively) was observed at the feeding time, indicating the fresh microcarriers were successfully colonized and used to maintain growth [233].

- **Perfusion cultures.** The last large process category for cell culture concerns continuous or perfusion cell cultures, during which cells are continuously fed by the addition of fresh medium, but a fixed volume is imposed by simultaneously removing the same amount of cell culture medium. Perfusion systems have the advantage of constantly removing toxic or inhibitory metabolic by-products that can be detrimental to cell growth while maintaining constant nutrient concentrations. In addition, the significant reduction in equipment volume associated with high density perfusion cell cultures makes these processes suitable candidates for using next generation single use bioreactors. For this, certain techniques such as membrane filtration, tangential flow filtration (TFF), alternating tangential flow filtration (ATF), vortex flow fiber systems or spin filters, have been used to separate live cells from the cell culture supernatant and cell debris, in view of injecting the viable cells back into the bioreactor and preventing the loss of the cells during the cell culture [234]. These types of processes have led to a two- to five-fold increase in CHO cell density compared to fed-batch processes thus leading to higher volumetric productivity which can also be sustained for longer periods of time [235]. In the case of MSCs, a perfusion rate of 0.25 day^{-1} was applied for the expansion of BM-MSCs in a 400 mL bioreactor [223]. For this, cells and microcarriers were kept inside the bioreactor through a modified alternating tangential flow (ATF) system (Repligen Corporation, Massachusetts, USA). In parallel, other authors tested a tangential flow filtration (TFF) system

in a computer-controlled Biostat Qplus STR (Sartorius Stedim Biotech, Gottingen,Germany) for the expansion of BM-MSCs on Synthemax II microcarriers. At day 6 of culture, empty microcarriers were added (32 g L^{-1}), increasing the microcarrier concentration from 16 g L^{-1} up to 48 g L^{-1} [236]. However, ensuring that the colonization of these fresh microcarriers is efficient and homogeneous is not an easy task. In this regard, authors suggested an intermittent stirring rate profile (On:15 rpm for 5 min; Off: 0 rpm for 55 min) from day 6 to day 9 [236]. Lastly, microcarrier concentration can be seen not only as a possibly limiting substrate, but also possibly as a limiting by-product since fully colonized microcarriers will no longer provide available cell culture surface, but rather contribute to additional hydro-mechanical constraints within the bioreactor. Accordingly, expansion factors of approximately 60 were obtained by developing an innovative perfusion process to ensure the colonization of fresh microcarriers while extracting colonized microcarriers via a decantation tube [237].

A brief notion of bioreactor design

As presented above, various parameters during the cell culture can have significant impact on how cell expansion is performed. The following paragraph will briefly summarize the diversity of bioreactor equipment and geometries that have been and will continue to be used for the expansion of adherent mammalian cells grown as cell aggregates or on microcarriers.

To begin with, mammalian cells can be easily cultured under dynamic conditions in simple devices known as roller bottles. For this, cells are attached (or not) to the interior surface of cylindrical bottles which are then placed in a rotating apparatus to ensure homogenization of each individual bottle. For example, hepatic cells were found to grow as organoids in these cell culture conditions [238]. However, roller systems are limited in terms of culture control caused by the individual containers, are expensive, and require thorough handling (much like traditional T-Flasks). More advanced bioreactor systems that can accommodate dynamic culture conditions and automation may be the solution to reduce the amount of containers. For example, NASAs Biotechnology Group developed an alternative bioreactor design, the rotating wall vessel, which simulates micro-gravity conditions for mammalian cell cultivation (reviewed in [239]). The two available configurations, high aspect ratio vessel (HARV) and the slow turning lateral vessel (STLV) have successfully been used to culture stem cells as well as a variety of cell types in micro-gravity [240]. Similar approaches using a vertical wheel system has demonstrated the ability to expand BM-MSCs on Corning Low concentration Synthemax II microcarriers [232]. Using a different approach, the wave bioreactor placed on a rocking motion platform, (composed of a disposable bag, partially filled with media and inoculated with cells, with the remainder inflated with air) has also

been used for Cultispher S-microcarrier-based MSC cultivation [241]. Finally, fluidized bed bioreactors consist in a column inside which particles are floating due to fluid flow and / or aeration methods. Although these reactors could provide alternatives to the conventional stirred tank reactors (as they have been successfully used to expand mice fibroblasts on coral scaffolds of 9 mm^3 as well as to support the differentiation of human BM-MSCs to bone [242]), limited documentation exists concerning their use for the culture of MSCs for therapeutic applications.

As previously described, the equipment geometries which can be used for the culture of human MSCs on microcarriers is extremely vast, even if most studies published tend to focus on orbitally agitated systems (*i.e.* spinner flasks) or mechanically stirred bioreactors [243]. Regardless, innovative process engineering could lead to the discovery of processes which could potentially increase MSC yield and potency and to significantly reduce production costs (validation, cleaning, facility size, training, *etc.*).

Online parameter measurement and quality-based approaches

The successful implementation of MSC cultures in bioreactors will require the equipments to adequately measure and regulate physico-chemical variables (pH, dissolved oxygen, temperature *etc.*) and biochemical inputs (nutrients, metabolites, growth factors *etc.*). Process controls have the ability to increase process robustness and capability when taking into account kinetic data including growth rates, death rates, metabolic uptake and production of waste products [244]. These data, accumulated during process development could also be coupled with mathematical modelling of cell functions specific to stem cell culture in order to increase process understanding and predictions. For example, cell-level kinetic parameters were modelled according to secreted molecule-mediated extracellular networks for blood stem cells, providing valuable information with regard to cell culture output heterogeneity [245]. In this regard, process analytical technology (PAT) is an umbrella term that covers a range of tools and is often cited as being an important component of other innovative initiatives, such as quality by design (QBD), real-time release, and continuous manufacturing. According to the FDA, "the goal of PAT is to enhance understanding and control the manufacturing process, [...] quality cannot be tested into products; it should be built-in or should be by design".

(1) Online monitoring of viable cell density (VCD). In the case of MSC cell cultures on microcarriers, the online measurement of the viable cell density in bioreactors is crucial since offline measurements of cell density can be fastidious, may be prone to errors, and enhances contamination risks. Examples of offline cell density measurement include using automated or manual counting of Trypan blue staining of detached cells [246], fluorescent staining of cells attached to microcarriers [247], counting of cell

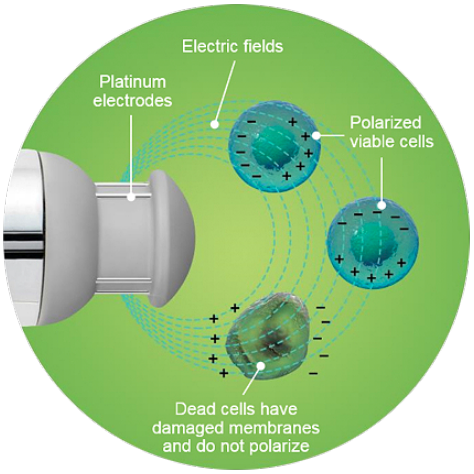

Figure 1.18: Schematic representation of the dielectric sensor provided by Hamilton (reproduced from the technical documentation from Hamilton available online).

nuclei after cell lysis [248], or cell metabolic quantification such as the MTT assay [249]. Online measures include optical density measurements, acoustics, Raman spectroscopy, and fluorescence spectroscopy. However, until recently, most methods for the monitoring of cell concentrations were not applicable to immobilized cell cultures using microcarriers. The most common current technologies include optical techniques based on light absorbance and/or scattering, real-time imaging, particle size analysis and measurements of culture fluid density [250].

For example, dielectric spectroscopy is a technique based on the measurement and analysis of cellular electrical properties in a conducting medium (Figure 1.18). Applied to cell culture, the capacitance and conductivity of cells is measured over a range of frequencies by being placed in an alternating electric field between two electrodes. Under this alternating electrical field, cells act as capacitors and are polarized and depolarized accordingly (ε_{dielec}). Since dead cells cannot be polarized, dielectric spectroscopy only measures live cell concentrations. Typically, these probes are able to produce a wide range of electric frequencies and can measure the change in the electric current-voltage relation in the presence of this alternating electrical field (permittivity) at each frequency generated. The graphical representation of these data is called the polarization curve (Figure 1.19) and is then used to derive information on the cells. For example, the characteristic frequency F_c which corresponds to the abscissa of the inflection point of the polarisation curve, may provide an indication of the average cell diameter. In addition, the slope of this curve near the inflexion point, α_{dielec}, can be used for information on the distribution of cell diameters. Dielectric measures of adherent Vero cells on Cytodex 1 microcarriers showed that online viable cell density can be measured this way [251]. This method has also been validated for MSCs grown on Corning Synthemax II-coated dissolvable microcarriers for which the online measure at 300 kHz was found to accurately match offline measures of cell density [237].

It is notable that cells have different dielectric profiles depending on their growth

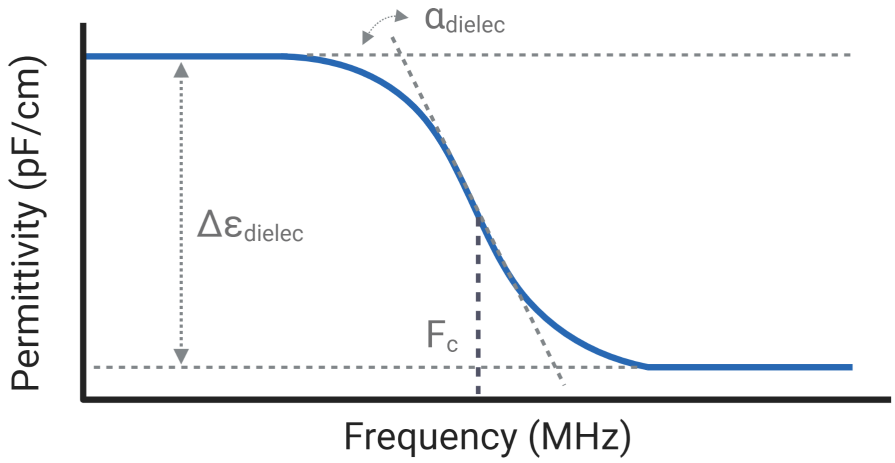

Figure 1.19: Cell polarization based on the applied frequency. Cells fully polarize at low frequency and hardly polarize at high frequencies. Scanning the polarization at various frequencies can be used to determine the maximum polarization ($\Delta\varepsilon_{dielec}$), the critical frequency (F_c) and the slope of the permittivity curve (α_{dielec}).

conditions. For example, cells grown in aggregates have a weaker permittivity signal in comparison to spherical cells in suspension, and a shift in the critical frequency was also noted [252, 253]. In addition, adherent growing cells seem to have dielectric signals which differ from single suspended spherical cells and also compared to cells grown on microcarriers.

(2) Online monitoring of dissolved oxygen (dO_2). As described in Section 1.2.3, oxygen tension is a crucial element of the MSC microenvironment *in-vivo* and impacts many cell quality attributes *in-vitro*. As a result, precise and reproducible measures of dO_2 is also critical and equipments should ensure the oxygen transfer rate (OTR) in the bioreactor remains greater than the oxygen uptake rate (OUR) required by MSCs. For this, various online probes to measure dissolved gasses exist including electro-chemical sensors such as the Clark-type dissolved oxygen sensor developed in 1953. These sensors typically measure a current flow proportional to a quantity of gas which permeates through a gas-permeable polyethylene membrane. However, the gas diffusion through the membrane is typically associated with quite long probe response times and a limited lifespan due to the natural degradation of the membrane over time. As a result, optical techniques based on fluorescent quenching in the presence of oxygen have been developed. These methods are based on the Stern-Volmer equation and provide non destructive local measurements of dissolved oxygen without using a membrane technology (and thus increasing response time and probe life span) (reviewed in [254]).

(3) Online monitoring of metabolic substrates or products. To date, few technologies allow for the online monitoring of certain crucial parameters including metabolic substrates or by-products. In this mindset, Raman monitoring of mammalian cell bio-

processes has grown increasingly popular since glutamine, glutamate, glucose, lactate, ammonium, viable cell density (VCD), and total cell density (TCD) monitoring was validated in a bioreactor with an antibody-producing CHO cell line. Interestingly, the Raman technology provides an extremely large amount of information from a single probe and can be used to predict osmolality, antibody titer, antibody glycosylation, and amino acid concentrations in the millimolar concentration range (reviewed in [255]). For example, calibrations over ranges of 3–14 g L^{-1} glucose (17–78 mM), 0.5–2.5 g L^{-1} lactate (6–28 mM), and 2–5 mM glutamate were reported. The technology is based on high frequency vibrations of individual molecules which can then generate spectral results and be analysed, typically through machine learning or AI algorithms. Other analytical options include using small multi-parametric sensors which can, for example, be placed in small capsules within the bioreactor (such as the process analytical technology Capsule (PATsule) developed by the Tyndall National Institute, Cork, and the National Institute for Bio-processing Research and Training (NIBRT) which is currently expected to measure pH, pO_2 and temperature online). Similar devices including online enzymatic biosensors or chemo-sensors can also be placed outside a sampling loop or on sampling ports (examples reviewed in [256]). To date the online monitoring of metabolic substrates or products during MSC production processes on microcarriers has not yet been routinely demonstrated.

(4) Online monitoring of cell quality. The successful online monitoring of certain quality attributes online may be one of the next challenges that the cell therapy sector will face. The premise of emerging technologies such as fourier transform infrared spectroscopy (FTIR) and Raman spectroscopy may pave the way for the next era of biopharmaceutical production. Briefly, Raman spectroscopy measures relative frequencies at which a sample scatters radiation, unlike IR spectroscopy which measures absolute frequencies at which a sample absorbs radiation. Interestingly, Raman spectroscopy was successfully validated to track the process of differentiation of murine and human ESCs (for which nucleic acid content in the spectral region 770 – 880 cm^{-1} was found to be significantly different depending on the levels of differentiation). Similar results were obtained with IR sensors to monitor mESC differentiation in nucleic acid regions (1700 – 1600 cm^{-1}) or lipidic regions (2852 – 2959 cm^{-1}). In the case of MSCs, the differentiation into osteocytes was associated with Raman spectral changes in the hydroxyapatite region (950 – 960 cm^{-1}), suggesting the presence of calcium phosphate species which are mineralization markers as well as FTIR spectroscopic signatures which indicate the presence of calcium phosphate salts (1100 cm^{-1}). This paragraph was summarized from the recent review of Raman / FITR applications in stem cell differentiation which provides a much greater level of detail on how these technologies are currently being used and various other examples of differentiation including adipogenic and chondrogenic as well as the use of these technologies with iPSCs [257].

1.3.2 Using microcarriers as growth supports for MSC expansion

As introduced in the beginning of this subsection, there are various scalable methods of MSC expansion which can be used in combination (or not) with Stirred Tank Reactors. The use of microcarriers remains, to this day, the most viable and easily implementable process option in STRs. Importantly, the choice of microcarrier-based processes for expansion at different scales allows for a relatively precise modulation of the available cell surface throughout the cell culture as this available surface is directly proportional to the amount of microcarriers which are added in the system. Furthermore, additional surfaces can easily be added during culture by, for example, monitoring microcarrier colonization and adding fresh microcarriers at specific times. For example, innovative perfusion processes have demonstrated that it is possible to maintain cell expansion in bioreactors by adding fresh microcarriers and that cells successfully colonize these fresh microcarriers [237]. Implementing batch, fed-batch and perfusion cell cultures in bioreactors was shown to increase the expansion factors of these processes from 5 to 43 to 60 respectively culminating in 800 million cells obtained in a 1.5 L bioreactor in 10 days. By searching the PubMed database using key words "(Wharton's Jelly) AND (microcarrier)" as well as "(Umbilical Cord) AND (microcarrier)", processes performed on MSCs from the same source and at different scales can be compared (Table 1.8). It can be noticed that a variety of cell culture systems as well as a variety of microcarriers have been tested with MSCs isolated from the Wharton's Jelly, and that this trend seems to be continuing to progress. However, to our knowledge, out of the 10 353 clinical trials involving MSC's in 2021, **no clinical studies using a bioreactor-based MSC expansion strategy on microcarriers have been or are ongoing**, possibly indicating the need to continue fundamental research towards understanding how both solid and liquid phases interact and impact MSC cell culture in agitated conditions.

Microcarrier characteristics and impact on MSCs

Microcarriers are typically spherical beads (diameter ranging from 100 to 300 µm) with a density close to that of the medium in which they are expected to be used. As a result, they can easily be maintained in suspension with limited stirring. With these expected characteristics, various types of microcarriers have been synthesized and commercialized for cell expansion (glass, diethylaminoethyl (DEAE)-dextran, acrylamide, polystyrene, collagen, alginate *etc.*) (extensively reviewed in [269]). Typical variations between these microcarriers include particle porosity (macro-porous microcarriers will allow cells to expand within its matrix while non porous microcarriers will only allow cells to grow on the surface of the microcarriers), surface coating (certain microcarriers have specific functional groups grafted on the exterior of the polymer chains to enhance cell adhesion while others have specific coatings on the surface which mimic the extracellular matrix to promote adhesion and growth), stiffness and size (Figure 1.20).

Table 1.8: Comparison of relevant expansion processes of umbilical cord MSCs on microcarriers in the PubMed database. EF : Erlenmeyer Flasks, SF : Spinner Flasks, B : Bioreactors, R : Cell Nest Roller, STR : Stirred Tank Reactor, VW : Vertical Wheel.

Culture System	**Working Volume**	**Microcarrier Type**	**Inoculum**	**Expansion Factor**	**Growth phase**	**Ref.**
EF	25 mL	Cytodex 1 (2.4 g L^{-1}) & Star Plus (25 g L^{-1})	0.8 × 10^5 cells mL^{-1}	0.1 - 0.6	5 days	[258]
SF	50 mL	Homemade MC (14 g L^{-1}) & Cytodex 3 (4 g L^{-1})	0.45 × 10^5 cells mL^{-1}	7 - 11	7 days	[228]
B	300 mL	Homemade MC (31 g L^{-1})	1.2 × 10^5 cells mL^{-1}	N/A	5 days	[228]
EF	25 mL	Cytodex 1 (2 g L^{-1})	0.8 × 10^5 cells mL^{-1}	2 - 3	9 days	[259]
B	500 mL	Cytodex 3 (2 g L^{-1})	0.24 × 10^5 cells mL^{-1}	N/A	N/A	[260]
SF	200 mL	Star Plus (0.1 g L^{-1})	8000 cells cm^{-2}	2.5	N/A	[261]
SF	N/A	N/A	0.5 × 10^5 cells mL^{-1}	18	7 days	[262]
SF	100 mL	Various MC (25 g L^{-1})	8000 cells cm^{-2}	13 - 16	6 days	[263]
SF	80 mL	Plastic (12 g L^{-1})	1 × 10^5 cells mL^{-1}	13	6 days	[264]
R	60 mL	Various alginate/PEG (1 g L^{-1})	0.25 × 10^5 cells mL^{-1}	12	7 days	[265]
SF	100 mL	Cultispher S (1 g L^{-1})	1 × 10^5 cells mL^{-1}	5.3	5 days	[220]
STR	800 mL	Cultispher S (1 g L^{-1})	0.25 × 10^5 cells mL^{-1}	7.5	4 days	[220]
VW	60 mL	Plastic (33 g L^{-1})	0.8 × 10^5 cells mL^{-1}	21	7 days	[221]
B	30 mL	Polystyrene CellBind (300 - 360 cm^2)	3000 - 4500 cells cm^{-2}	N/A	21 days	[266]
B	500 mL	Polystyrene CellBind (6000 cm^2)	3000 - 4500 cells cm^{-2}	N/A	11 days	[266]
SF	100 mL	Plastic (5 g L^{-1})	0.1 × 10^5 cells mL^{-1}	21	8 days	[267]
B	800 mL	Plastic (5 g L^{-1})	6100 cells cm^{-2}	9	7 days	[267]
VW	60 mL	Plastic (33 g L^{-1})	0.8 × 10^5 cells mL^{-1}	N/A	9-10 days	[268]
SF	120 mL	Cytodex 1 (2500 cm^2)	1200 cells cm^{-2}	N/A	N/A	[219]
B	1500 mL	Cytodex 1 (2500 cm^2)	1200 cells cm^{-2}	N/A	7 - 10 days	[219]

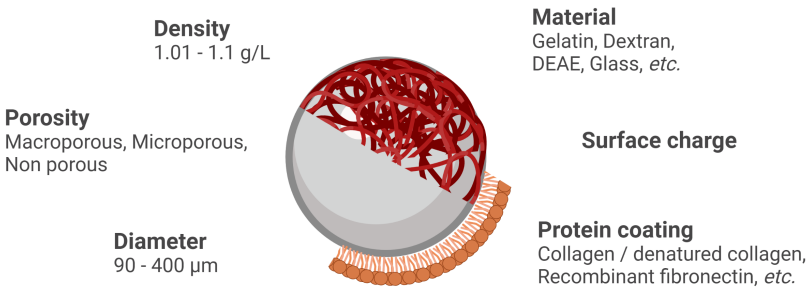

Figure 1.20: Schematic representation of microcarrier characteristics.

Since structure and mechanical characteristics are key aspects of the native MSC tissue environment (ultimately conditioning cell fate via various mechano-transduction pathways), the choice of microcarrier type will also be key in successfully expanding MSCs on microcarriers. Specifically, cell attachment capacity, distribution on microcarriers, expansion and ease of detachment have been shown to depend on microcarrier type [247].

Consequently, engineering geometrical and topographical attributes (size, rigidity, shape, composition *etc.*) of *ex-vivo* cell growth surfaces may be crucial for process development stages as it is known that these characteristics specifically activate downstream signalling pathways affecting morphology, proliferation, and differentiation (see paragraph 1.1.3 for further details). It must be kept in mind that, to date, little characterization has been performed to determine the physical characteristics of microcarriers including for example, particle stiffness or the way these particles will be distorted when reacting to the mechanical constraints imposed by the agitation culture (shear and/ or collisions). These constraints are certainly perceived by the cells which grow on them, but it is not yet clear to what extent they may have an impact.

MSC adhesion mechanisms on microcarriers

When using microcarriers as growth supports, the first step of the process is to facilitate cell adhesion on the carriers. To begin with, weak electrostatic bonds form between the cells and the microcarrier surface. This phase may be enhanced if the microcarrier surface is charged and possibly depends on the charged elements present in the medium which may obstruct or enter in competition with the charged sites on the microcarriers. It should be noted that certain microcarriers may have a chemical composition which promotes the adsorption of unwanted proteins at its surface, which may then inhibit cell adhesion. For example, DEAE-coated microcarriers were found to adsorb albumin, resulting in a reduced cell attachment and growth [270]. As a result, certain seeding strategies with these types of microcarriers may require the reduction of HPL or serum during the initial attachment phase to increase the quantity of cells attached.

In the second stage, cells start to flatten and this results in an increased cell-surface contact zone as well as an increase in the number of connections. During these steps,

a cytoskeleton remodelling (including for example vinculin and cadherin aggregation) starts to take place approximately 100 seconds after the cell identified an induction signal [271]. Other studies identified that other focal adhesion complexes can take several minutes to be established [272]. Globally, the general consensus tends to state that the first 5 to 20 minutes of adhesion can be considered as the "initial adhesion" phase [273]. However, the mechanisms and duration of the morphological changes have been shown to depend on the characteristics of the adherent cells and the support on which they are attaching. For example, flattening and spreading was observed during approximately 2 hours for CHO cells or Mckoy fibroblasts on a polystyrene surface [274]. In another study, the use of micro-electrodes to monitor cell spreading (verified with immuno-fluorescent images) showed that NIH3T3 embryonic mice fibroblast cell attachment on fibronectin-coated wells was accompanied by immediate spreading which was maximal after approximately 1 hour [275]. Lastly, the change in magnetic resonance during African green monkey cell spreading on a gold electrode was found to stabilize after approximately 0.8 hours [276]. Overall, this attachment process should last between 5 and 120 minutes and end in cells having achieved a flat fibroblast-like appearance, fully spread over the surface of contact [277].

The hydrodynamic environment to which the cells are subject to during this lapse of time also impacts how cells will attach to the surface of the microcarriers. Although static cell seeding has been successfully validated onto microcarriers [278, 279], most studies tend to show that agitation has a promotional effect on cell attachment and growth due to the better cell distribution on the microcarriers. However, it seems important to note that agitation rate should be optimized in a way to avoid cell damage and cell-microcarrier aggregate formation in these early process stages. In this regard, using intermittent agitation cycles have been reported as effective strategies for seeding [208, 223, 267, 280–282] although may also contribute to the formation of microcarrier aggregates and thus may not be as optimal as commonly established. A summary of the variety of agitation cycles used for seeding can be found in [283] and [284]. Agitating too early may cause certain cells to not be sufficiently bound to the microcarriers and therefore not have access to the growth surface. For example, Dos Santos and colleagues observed 22 % and 23 % initial attachment yields of BM-MSCs and AD-MSCs respectively by using intermittent agitation cycles of 15 min followed by a 2 h static phase. In this study, these cycles were repeated during 24 h [231]. On the other hand, waiting too long before agitating can cause attachment heterogeneity where certain microcarriers or certain zones on specific microcarriers may contain higher local cell concentrations. For example, after a 2 h static adhesion phase, it was found that agitation for 2 hours increased the attachment efficiency of hES cells on Cytodex-1 microcarriers as well as the attachment efficiency on microcarriers with various coatings when compared to continuing static adhesion [285]. Lastly, it can be noted cell attachment to microcarriers is a probabilistic phenomenon which follows a

Poisson distribution [280] and is affected by the cell-to-bead ratio. While lower cell-to-bead ratios typically result in unoccupied microcarriers [286], higher cell-to-bead ratios may promote cell-microcarrier aggregates (observed in [287]) and also increase the amount of unattached cells at the end of the seeding phase.

As described above, cell adhesion characteristics significantly vary in literature and remains a topic not completely elucidated. Intermittent agitation cycles are vastly used for seeding of MSCs onto microcarriers and yet, surprisingly, little is known on how these agitation cycles affect cell adhesion, how these cycles may be perceived by the cells and to what extent the may affect the cells grown on them.

MSC and microcarrier aggregation

Once MSCs have been seeded on microcarrier surfaces, they continuously expand until the entire surface available is covered by cells (*i.e.* confluence). At this stage it can be noted that a microcarrier covered by cells and the large amount of extracellular matrix that these cells synthesize is expected to be substantially heavier. After confluence, cells continue to proliferate which usually results in cell-microcarrier aggregates (clumping) [288]. These aggregates are, in most cases, undesirable since they increase culture heterogeneity (resulting in non-reproducible cell counts) and impede mass transfer to or from the cells [287]. To prevent aggregate formation two strategies can be used: (1) modulating agitation during the culture [289] (which may have detrimental impacts on MSC growth, see Section 1.4) or (2) addition of fresh microcarriers to enable the transfer of cells from full microcarriers to empty ones (also known as bead-to-bead transfer, described in the next paragraph).

MSC bead-to-bead transfer

During the hMSC expansion process on microcarriers, the available surface for cell growth rapidly becomes a major bottleneck. However, it has recently been demonstrated that hMSCs are able to transfer from a confluent microcarrier to an empty microcarrier in a process referred to as *bead-to-bead transfer* [237, 290]. The capacity of cells to efficiently colonize a *fresh* microcarrier enables process developers to add new surfaces at strategic time-points during the culture, thereby avoiding the need to harvest prematurely and potentially increasing the scalability of such processes in perfusion or fed-batch modes. However, increasing microcarrier concentration by adding particles during the process may require slightly higher agitator speeds to ensure that full suspension is maintained [291] and also generate additional collisions that occur between beads, both of which may adversely impact hMSC culture viability.

MSC detachment mechanisms

Although the vast majority of publications concerning MSC expansion on microcarriers focuses on the upstream process, the downstream process must also be taken into consideration and optimised. Harvesting MSCs attached to microcarriers continues to be a challenge both for daily sampling and for the final detachment of the cells. To date, three main separation strategies have been used: (1) enzymatic dissociation combined with high stirring speed inside or outside the bioreactor [229, 231] or using non-continuous mixing [292] (2) enzymatic separation without any form agitation/mixing [293, 294], and (3) microcarrier degradation / dissolution [237]. It can be noted that significant variations in the detachment yield have been observed when changing the microcarrier type and therefore that the choice of microcarrier which has the greatest expansion capacities may not be the best option for larger scale manufacturing, taking into account downstream processing. For example, although Cytodex-1 microcarriers were found to have promising attachment and expansion performances, other microcarriers such as Star-Plus and Plastic-Plus showed a better compromise in agitated conditions taking into account detachment [247]. In this mindset, innovative growth supports are currently being developed and tested to increase altogether process efficiency [295]. For more information on cell attachment and/or detachment, readers are advised to read the recent and thorough review proposed by Derakhti et al. [277]. Lastly, it is notable that regardless of the detachment strategy chosen, the isolated cells will then need to be further separated to retain microcarriers and possible microcarrier fragments or fines to get safe microcarrier-free cell products [296].

1.3.3 Microcarrier-microcarrier interactions during MSC expansion

Ideally, cell culture should tend to be performed with a maximal microcarrier concentration to increase the available surface for cell culture and maximize growth (while maintaining small batch volumes). However, increasing microcarrier concentration has typically been associated with a reduced cell growth and a reduced maximum cell number per microcarrier [279, 297–299]. The detrimental effects have sometimes been attributed to collisions between particles without any quantification or scientific proof. The next paragraphs will introduce the known notions on how microcarrier concentration affects human adherent cell culture in view of understanding what physical elements may intervene in these processes.

Impact of microcarrier concentration during human cell expansion

Pioneering cultures of human fibroblasts at microcarrier concentrations between 0.05 and 15 g L^{-1} indicated that cell growth seems to be impacted by microcarrier concentration. Notably, cells grown in higher microcarrier concentrations were found to have

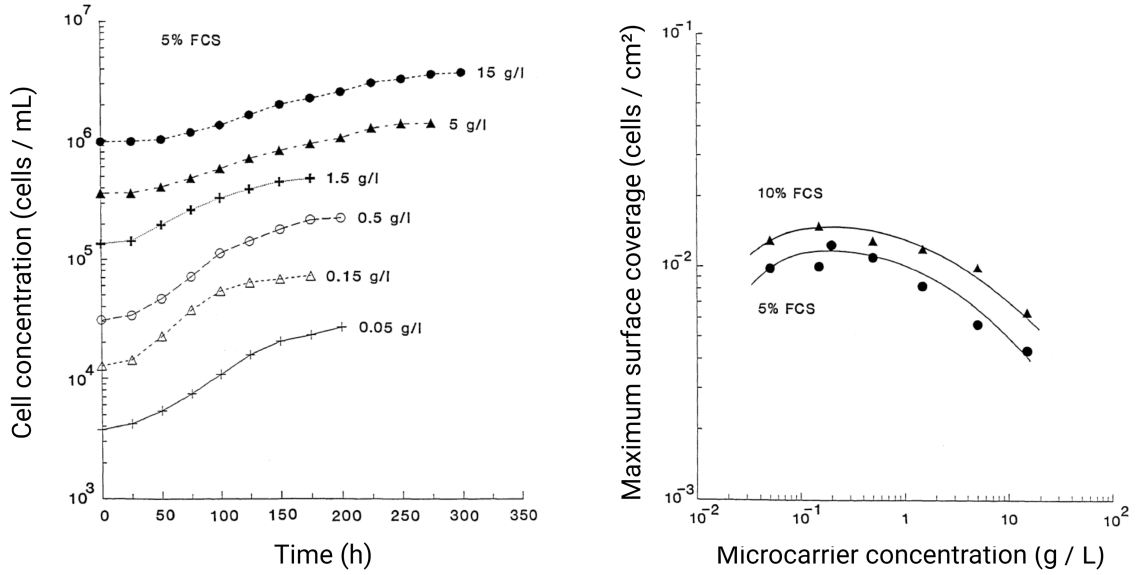

Figure 1.21: Impact of microcarrier concentration on cell growth (adapted from [297]). Left, fibroblast cell growth at various Cytodex 1 concentrations. Right, final cell surface concentration obtained at various Cytodex 1 concentrations.

longer lag phases and a decreased growth rate (Figure 1.21, left). This is confirmed by experiments duplicated with higher serum concentrations (Figure 1.21, right). The authors propose that increasing microcarrier concentrations has two antagonistic effects on growth. Firstly, increasing microcarrier concentration increases the cell concentration during the cell culture for a same seeding cell concentration. Since animal cells often secrete growth factors in their extra-cellular medium, it is possible that increasing the cell concentration also promotes growth through these growth factors. However, after a certain threshold of approximately 1 g L^{-1}, the growth rate measured in these conditions was found to be significantly decreased, possibly due to microcarrier-microcarrier collisions which inhibit cell growth or due to the secretion of cell-derived inhibitors or toxic by-products. In addition, cultures performed at high microcarrier concentrations were found to have lower relative surface coverage at the end of the cell culture (a two-fold increase in microcarrier concentration resulted in a 10 % reduction of surface coverage indicating cells are reaching lower levels of confluency). These results indicate that certain mechanisms at high microcarrier concentrations are preventing cells from achieving full confluence on the microcarriers. In addition, morphological changes were also noted in cultures performed at high concentrations (*i.e.* cells had a morphology which was more "spread out").

Notably, the results obtained on growth can be modelled using Equation 1.1 [297]. Accordingly, the growth rate in a microcarrier-based system μ_{app} can be defined with a constant growth rate γ, a fixed death rate q_1 which depends on the hydrodynamic stresses in the agitated system (*i.e.* shear caused by agitation and viscosity) and a fixed death rate q_2 caused by microcarrier-microcarrier interactions and therefore

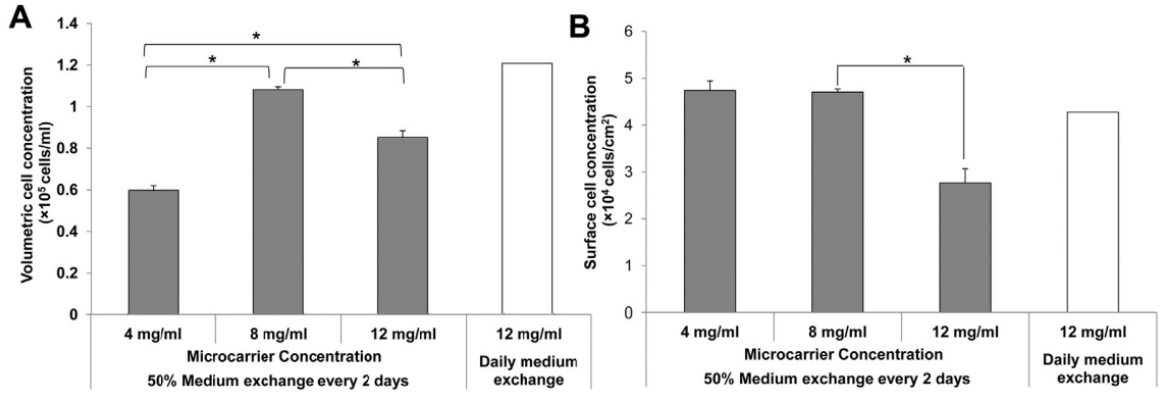

Figure 1.22: Effect of microcarrier concentration on MSC expansion in spinner flasks at different microcarrier concentrations (A) Volumetric cell concentration and (B) surface cell concentration were determined. Error bars indicate standard deviation (n = 3). *P < 0.05 (adapted from [299]).

microcarrier concentration C_m.

$$\mu_{app} = \gamma - q_1 - q_2 \times C_m \tag{1.1}$$

Other studies performed on human MSCs grown on Cytodex 3 microcarriers seemed to indicate that increasing microcarrier concentration from 3000 to 7500 microcarriers per mL had a deleterious effect on cell growth in different experimental conditions which included changing the agitator type, seeding concentration *etc.* [279]. However, **the limited number of concentrations tested provides much less information than those proposed for human fibroblastic cell cultures.**

A last study was performed to determine the impact of particle concentration on MSC growth and showed that at low microcarrier concentrations, increasing microcarrier concentration had little impact on cell colonization (*i.e.* the surface cell concentration at the end of cell cultures at 4 mg/mL and at 8 mg/mL were similar) but also resulted in higher final volumetric cell concentrations due to the added cell surface per unit of volume (Figure 1.22) [299]. As a result, in these cases, a small increase in microcarrier concentration seemed to improve process efficiency. However, increasing this microcarrier concentration from 8 to 12 mg/mL was associated with a decreased volumetric concentration associated with a decreased final surface cell concentration. As a result, in high microcarrier concentrations, MSCs seem to not have the capacity to achieve optimal confluence of the microcarriers and, thus, the yields of these processes are reduced.

Impact of adding particles during human cell expansion on microcarriers

In order to determine to what extent particle-particle interactions have a detrimental effect on mammalian cell growth, certain authors proposed to perform microcarrier cell cultures to which various concentrations of particles were added. Since cell growth

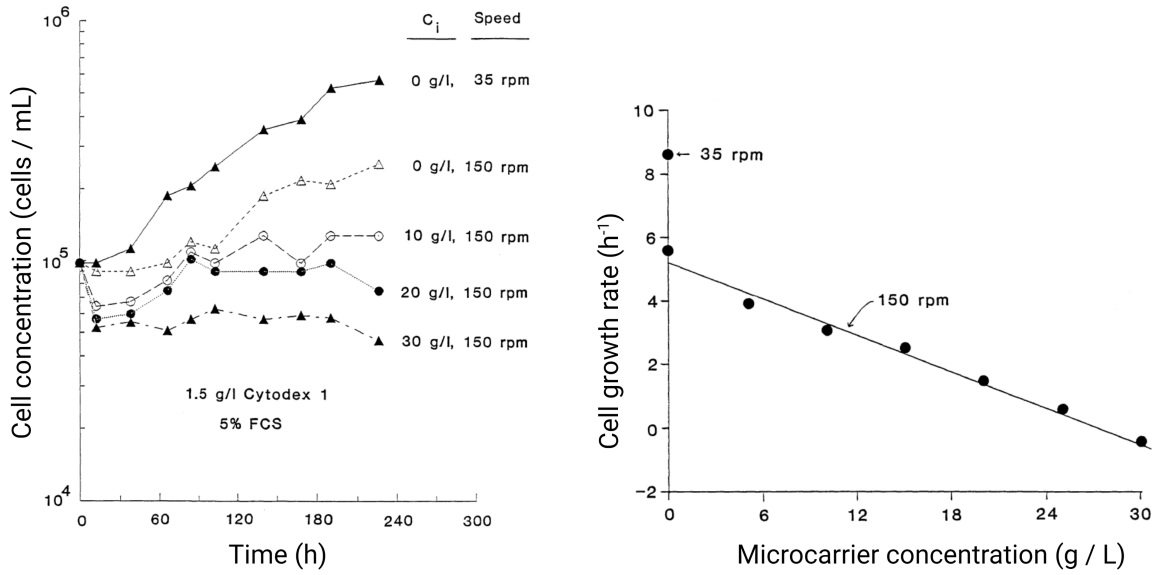

Figure 1.23: Impact of particle concentration on cell growth (adapted from [297]). Left, effect of inert microcarriers on net growth at high agitation. Right, Net growth rate evolution according to inert particle concentration added during FS-4 cell culture on Cytodex 1 microcarriers.

was shown to be negligible on these added particles, these particles add specific hydro-mechanical constraints without providing any additional cell culture surface.

To begin with, experiments performed with human FS-4 fibroblasts at low agitation rates (35 rpm) seemed to show that the viable cell concentration was not significantly impacted by increasing particle concentration up to 28 g L^{-1}. Authors suggested that cells were not affected by hydro-mechanical constraints (shear and/or microcarrier collisions) in mild agitation conditions [297]. However, when increasing the agitation rates from 35, to 60 and then to 150 rpm, a significant impact on cell growth was observed indicating that cells, in these conditions, were affected by the increased hydrodynamic stresses. Notably, higher quantities of cell debris were noticed at high agitation rates and authors suggested that they may be caused by an increased amount of cell lysis due to shear (validated by measuring the amount of DNA present in the cell culture medium throughout the cell culture) [300]. The authors therefore repeated the experiments performed with increasing particle concentrations (between 0 and 30 g L^{-1}) but this time at a higher agitation rate of 150 rpm (Figure 1.23). Results clearly indicate that, at high agitation frequencies, the impact of adding particles during microcarrier-based cell expansion had a significant impact on cell growth. The inhibition was found to be linearly correlated to the concentration of added particles. Authors noted that the impact of these particles was especially noteworthy during the cell attachment phase (only 54 % of cells were found to be successfully attached to the microcarriers after 12 hours with the addition of 30 g L^{-1} of particles).

In order to further explain these results, Croughan and colleagues have proposed to further detail Equation 1.1. In the case of added particles at a concentration C_i, the

growth rate should also be reduced by microcarrier-particle collisions. the resulting damage should have a frequency of, on average, half of that which would occur if both particles had cells (Equation 1.2). This correlation seems to only be valid for sufficiently high agitation rates. Notably, in these experiments, the average spacing between microcarriers was calculated by the authors as ranging between 50 to 380 µm while the average Kolmogorov length scales ranged from 50 to 60 µm.

$$\mu_{app} = \gamma - q_1 - q_2 \times C_m - \frac{q_2}{2} \times C_i \tag{1.2}$$

As a result, **it seems that microcarrier concentration is an important parameter to take into consideration and that a compromise between process efficiency, microcarrier confluence and specific growth rate may be required**.

1.3.4 Section summary

In order to meet the upcoming clinical requirements, manufacturing large quantities of human mesenchymal stem cells will be required. For this, cells can be expanded in standard T-Flasks (or multilayer T-Flasks) but these processes remain complex and variable as it has been extensively reviewed in Chapter 1.2. As a result, new expansion processes have been and are still ongoing development, including cultivating MSCs on microcarriers which can be used as suspended growth supports in agitated Stirred Tank Reactors. However, it is now clear that engineering choices such as the way cells are fed during the process, bioreactor and agitator geometry, the type and quantity of microcarriers used *etc.* may have significant impacts on the cells produced. Fundamental scientific questions around these parameters seem to remain unanswered and are the object of dynamic and innovative research and development projects.

As a result, the following paragraph will be focused on a very specific aspect of microcarrier-based process engineering : **how has microcarrier or particle concentration been measured in STRs?** These elements will be presented in view of understanding the geometrical distribution of particles at both the just-suspended state (N_{js}) and during transient phases where microcarriers sediment and are re-suspended (for example when agitation is stopped and started again). The comprehension of these topics are expected to be crucial to further understand how microcarrier concentration and agitation regime may modulate MSC growth and death. **To date, little is known, in the case of MSC's, about the role and impact of microcarrier-microcarrier collisional forces on cell growth, death and quality** (phenotype, differentiation capacity, senescence, immunomodulatory properties *etc.*). **The aim of the next chapter is therefore to present elements which can be used to describe, quantify and model microcarrier-microcarrier interactions** (collisions, frictions, aggregation *etc.*) **in both steady states and transient phases**.

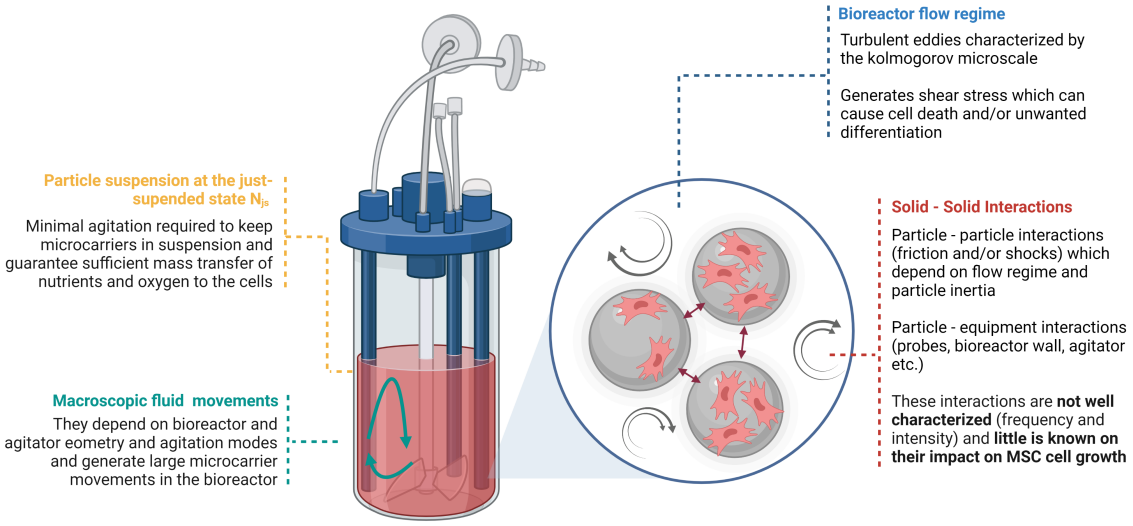

Figure 1.24: Schematic representation of mechanical constraints in bioreactors during MSC culture.

1.4 Characterization of hydro-mechanical stresses in bioreactors

Liquid-solid mixing operations are prevalent in various industries ranging from petrochemical industries to pharmaceuticals. Regardless of the industry, mixing plays a pivotal role to ensure the homogeneity of a given system, in particular when density differences between the liquid and solid phases leads to a settling of the solids. It can be noted that various forces including drag forces (due to fluid motion), frictional forces (due to particle-particle interactions, particle-wall collisions, particle-fluid collisions) and gravitational forces (due to buoyancy and particle weight) impact solid particles in a stirred tank [301]. The different theoretical, experimental and numerical approaches to characterize solid suspensions in agitated reactors will be further described below (schematically presented in Figure 1.24).

1.4.1 Suspension of microcarriers at the just-suspended state

In the case of microcarrier-based expansion processes, a critical parameter is the agitation needed in order to (i) ensure the full-suspension of microcarriers and (ii) guarantee sufficient mass transfer of nutrients and oxygen to the cells. In this context, a minimal agitation rate (typically called the just suspended state or N_{js}) needs to be set to successfully suspend the microcarriers, while inducing the lowest hydrodynamic shear stress. Briefly, to keep the particles in a just-suspended state, it is necessary that the vertical component of the force by which liquid acts on (typically generated by the impeller speed) remains greater than the gravitational force which typically pulls the particles downwards. If the agitation is too low, the microcarriers will not properly

be maintained in suspension and settle at the bottom of the culture vessels, impairing cell growth and promoting aggregation [281, 287]. However, if agitation is too high, the associated hydrodynamic shear stress generated by the impeller may compromise cell viability and functionality [48, 302, 303]. As a result, ensuring the minimal agitation is set in the bioreactor seems to be an important element for microcarrier-based expansion processes.

Experimental approaches to measure Njs

The earliest and most common method for characterizing the just-suspended state consists in a visual technique during which a mirror is placed under the bottom of a transparent tank. In this setup, N_{js} is defined as the impeller speed for which no particle remains longer than 1 or 2 seconds at the bottom of the tank [304]. Other experimental approaches include measuring the height of the microcarrier slurry compared to the total height, measuring the power input consumption, using tracer particles, pressure measurements *etc.* (reviewed in [305]). Empirical correlations using these techniques mostly describe the effect of fluid and particle physical properties (solid and liquid density, fluid viscosity, particle size *etc.*), impeller type, and scale on N_{js} and lead to models with more or less robustness to predict N_{js}.

Theoretical and numerical approaches to calculate Njs

Through visual observations, Zwietering successfully developed an empirical equation to calculate N_{js} with visual observations (Equation 1.3). The correlation involves a S coefficient (which depends on the geometrical characteristics of the impeller and its size), the impeller diameter D, the kinematic viscosity ν_L and density ρ_L of the liquid, particle density ρ_p, diameter d_p, and mass fraction X_p, and the gravity component g. Different computational approaches have also been used to determine the agitation required for the just-suspended state by solving fundamental physical equations, among which the Navier Stokes equations. For example, N_{js} was predicted through CFD by observing how the volume of packed particles evolves over time or by determining the local particle residence time in mesh cells at the bottom agitated bioreactor systems [306].

$$N_{js} = S \times \nu_L^{0.1} \times \left(\frac{g(\rho_p - \rho_L)}{\rho_L} \right) \times X_p^{0.13} \times d_p^{0.2} \times D^{-0.85} \tag{1.3}$$

Various other models have been proposed to estimate N_{js} by fitting various experimental geometries and approaches (thoroughly reviewed in [301]). Specifically, in the case of microcarrier systems in bioreactors, the recent adaptation of the Zwietering equation into Equation 1.4 proved to provide a much more precise estimation of N_{js} [306]. In order to further precise the Zwietering correlations in a specific bioreactor

system with Cytodex 1 microcarriers, this work tested 95 configurations and included 40 complementary measurements by varying agitator type, scale, as well as a variety of geometrical aspects (for example by varying the agitator diameter or height). In addition, three different modelling approaches were used and, in most cases, estimated with greater precision the N_{js}. Specifically the model described in Equation 1.4 was found to be especially robust to predict the Reynolds number at the just-suspended state Re_{js} in these conditions. Factors K and A were found to depend on agitator geometry and were defined for HTPG, Elephant Ear and Rushton turbine impellers in this study.

$$Re_{js} = K \times \alpha_s^A \times \left(\frac{C}{T}\right)^{1/3} \times \left(\frac{D}{T}\right)^{0.6} \times \left(\frac{d_p}{D}\right)^{-0.4} \times \left(\frac{\mu_L}{(\rho_p - \rho_L) \cdot g^{0.5} \cdot T^{1.5}}\right)^{-28/45} \quad (1.4)$$

1.4.2 Bioreactor flow regime and shear stress

Agitation intensity is one of the most critical parameters to be considered and, in most cases is set to the minimal agitation rate sufficient to keep particles in suspension, for the reasons expanded above. However, this minimal agitation will depend on the physical properties of the equipment, fluid, particles and cells. It should be noted that the level of agitation may have significant downstream impacts caused by impacts on cell expansion. To begin with, high levels of agitation have been associated with detrimental effects on growth kinetics, cell viability, differentiation ability, and clonogenic ability, although it is still difficult to prove that the cell 'damage' reported is in fact caused by agitation (reviewed in [296]). It should be kept in mind that early work on mammalian cells cautioned about the risk of cell degradation due to 'shear sensitivity', but that these concepts are currently evolving and may have notable nuances which are not yet fully explained [291]. Lastly, the reasons behind the choice of agitation rate in published work on microcarriers are not often given explicitly.

Macroscopic movements of the fluid

To begin with, several studies have compared different agitation regimes for a given system, not only to determine the optimal setup for MSC adhesion and expansion, but also to evaluate the overall fluid flow. For example, agitator geometry will generate macroscopic flow patterns in the bioreactor [307]. Axial, down pumping modes push particles downwards (suspension is achieved when these particles slide up on the side of the walls) and large macroscopic particle loops are generated by this type of agitation. In contrast, other agitation modes (radial or mixed) push microcarriers inwards and can generate other types of macroscopic loops, mainly around the impeller region (Figure 1.25).

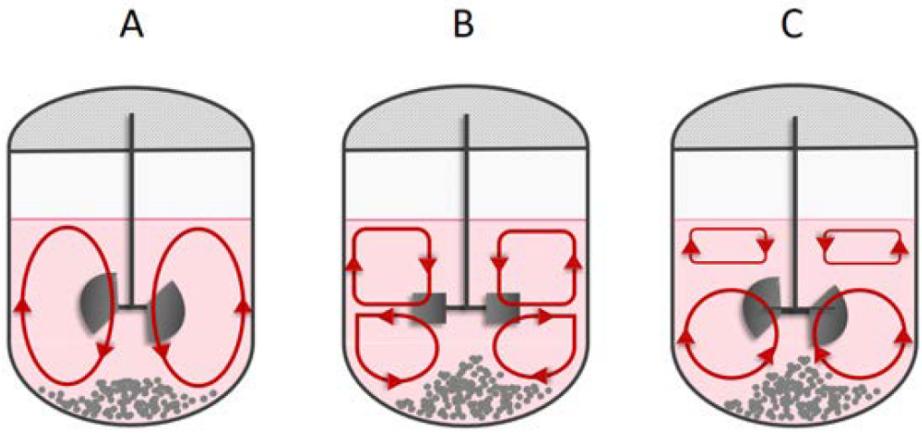

Figure 1.25: Flow patterns observed when agitation is below the just suspended state. (A) Down pumping mode, (B) Radial flow, (C) Mixed flow impellers in up pumping mode.

Kolmogorov's theory of turbulence

The most common approach to further understand the fluid flow remains Kolmogorov's theory of turbulence, which is verified when a turbulent regime is encountered within the bioreactor. This theory states that the statistical characteristics of fluid motion have a universal size and structure which depend solely on the turbulent energy dissipation rate ε (measured in $m^2\ s^{-3}$) and the kinematic viscosity of the medium ν (measured in $m^2\ s^{-1}$) (Equation 1.5).

$$\lambda_k = \left(\frac{\nu^3}{\varepsilon}\right)^{1/4} \tag{1.5}$$

For this, Reynolds numbers need to be sufficiently high (*i.e.* Re > 10^3 - 10^4, calculated according to Equation 1.6, the fluid density ρ, impeller speed N, tank diameter D and fluid viscosity μ).

$$Re = \frac{\rho \times N \times D^2}{\mu} \tag{1.6}$$

According to this theory, large turbulent eddies transport their kinetic energy into smaller turbulent eddies until they reach a characteristic size λ_k, also called the Kolmogorov scale where the energy is then dissipated (Figure 1.26). By supposing that the power injected into the bioreactor is equal to the dissipated power, the average dissipated power $\langle\varepsilon\rangle$ can be calculated according to Equation 1.7. This energy will typically depend on the impeller design (represented by the power number N_p), the impeller speed N, the impeller diameter D and the liquid volume V. Notably, agitation speed alone is not an efficient metric to compare bioreactors due to important variations in geometry, size *etc.*. A better option for comparing between different bioreactors is to use an estimation of the mean specific energy dissipation rate into the medium ε.

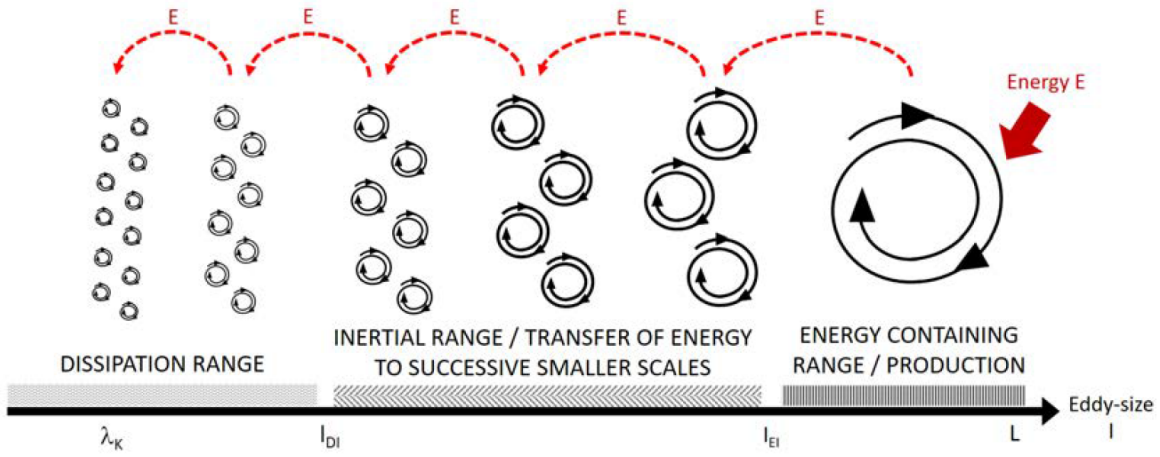

Figure 1.26: Turbulent eddy energy transfer according to the Kolmogorov cascade theory (adapted from [307]).

$$\langle \varepsilon \rangle = \frac{N_p \times N^3 \times D^5}{V} \tag{1.7}$$

Cell damage due to elements of turbulence

Various studies have shown that cell damage may occur depending on the difference between the Kolmogorov microscale of turbulence and microcarrier size d_p. For human FS-4 fibroblasts, a critical Kolmogorov length was determined as being $2/3^{rds}$ of the average microcarrier diameter [297] (Figure 1.27) but this limit may depend on the cell type and microcarrier used for cell culture. These results were obtained by culturing human fibroblasts on a constant microcarrier concentration and by using fluids of various viscosities. Other values of $\lambda_k = 0.4\ d_p$ and $1/3\ d_p$ were found as having no significant impact for BM-MSCs while lower cell growth were reported for $\lambda_k < 1/4\ d_p$ [308, 309]. Regardless of the setpoint, most studies show that decreasing this length scale either by reducing viscosity or by increasing the dissipated energy, has a significant impact on growth (see Chapter 1.1.3 for biological aspects of MSC damage in response with hydro-mechanical constraints).

1.4.3 Local particle concentration and heterogeneity notions in STRs

Determination of local particle concentration in STRs

From a statistical perspective, microcarrier-microcarrier interactions should be proportional to the local amount of particles and thus the local particle concentration. Briefly the techniques which can be used to determine local particle concentrations can be either intrusive or not and will have specific accuracy, complexity and resolution (reviewed in [301]). These techniques, in general, measure particle heterogeneity within the vessel and thus, when performed at various agitation speeds, can also, for example, detect the minimal agitation required for suspension. Accordingly, the measuring

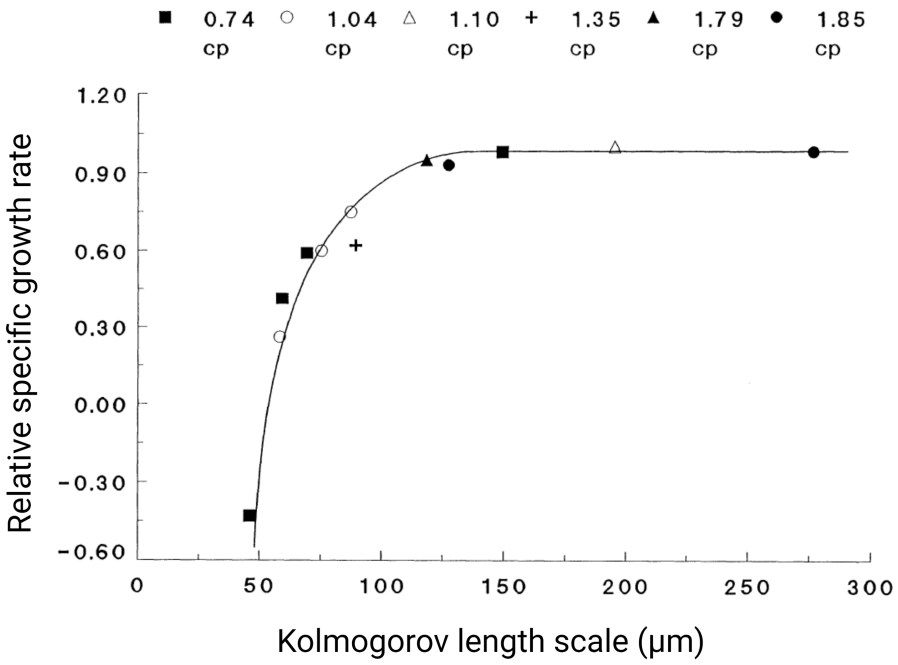

Figure 1.27: Relative growth rate vs. Kolmogorov eddy length scale for FS-4 cultures with 0.2 g L^{-1} of Cytodex 1 microcarriers (adapted from [300]).

technique will depend on the experimental scope, precision and accuracy required, ease of operation, equipment availability, cost, and safety / environmental concerns.

- **Local sampling.** The easiest technique to determine local solid concentrations in a stirred vessel is to analyze a sample at various precise locations throughout the tank [310, 311]. However, as sampling is, by nature, an intrusive method of analysis, it is very difficult to obtain an accurate sample without impacting liquid and solid movements. As a result, these methods have been widely discussed [312].

- **Local pressure measures.** Local particle concentrations can also be measured through the pressure that a greater particle concentration generates. For example, pressure gauge measures were preformed at the base of the reactor tank to determine a wide range of particle concentrations without significantly impacting macroscopic fluid and particle flows [313, 314]. However, the local impact of the dynamic head in these systems has also been discussed and may lead to imprecise measures [315]. In addition, if non-intrusive measures are required, the use of local pressure gauges are, by nature, limited to the tank surface and therefore provide little information on how these particle concentrations evolve within the reactor or in certain critical zones such as around the impeller.

- **Optical techniques.** Studies have used optical techniques in order to measure particle concentration distribution, principally due to their non-invasive nature and local precision. For example studies have used a laser to light up a the bottom of the vessel and recording optical measurements reflected on a mirror [316], or

by using techniques measuring the light attenuation of microcarriers in the entire vessel [317]. Intrusively, endoscopes can also be used to locally generate light and measure how it is attenuated [318]. Turbidity sensors can also be used to measure light scattering due to particles within fluids [319]. More recent studies include using particle image velocimetry (PIV), laser sheet and image analysis (LISA), planar laser-induced fluorescence (PLIF), laser doppler velocimetry (LDV) *etc.* (reviewed in [301]).

- **Ultrasonic techniques.** Sound waves are transmitted in a continuous liquid phase. However, when the sound wave is in contact with a solid phase, it is reflected. As a result, by measuring sound speed and amplitude in a continuous liquid phase and with different particle concentrations, it is possible to determine local particle concentrations. These techniques, like optical techniques, can have the receiver inside or outside the stirred reactor, making the method intrusive or not. They have successfully been used to determine critical agitation speed for suspension and measures of particle heterogeneity [320]. Notably, a technique called the ultrasound velocity profiler (UVP) has been used to determine particle velocity profiles which has the advantage of being usable in opaque systems and with high solid concentrations but poor temporal resolution [321].

- **Computational Fluid Dynamics.** Computational fluid dynamics (CFD) numerically simulates fluid flows by solving Navier-Stokes equations. In the case of solid-liquid systems such as microcarriers suspended in the cell culture medium, CFD can be used to simulate local particle concentrations. For example, CFD simulations of ProNectin-F and Hillex II microcarriers in spinner flasks was performed and identified nearly stagnant flow regimes under the impeller (Figure 1.28), which could possibly lead to microcarrier sedimentation and agglomeration [227]. Similar stagnant regions were observed and simulated in larger bioreactors equipped with elephant ear impellers for the growth of adipose-tissue derived stem cells [248]. Lastly, CFD simulations of Cytodex-1 microcarriers in 1 L Stirred Tank Reactor equipped with a HTPG impeller, was successfully performed to determine N_{js} and concentration heterogeneity (specifically in the bioreactor bottom where experimental data was found to be scarce) [306, 317].

Dispersion models to determine heterogeneity

In order to further characterize solid suspension in the liquid phase, most studies tend to look at the relative standard deviation (RSD) in dispersion models (Equation 1.8). In these models n_s represents the number of sampling positions, α_i and $\langle \alpha_i \rangle$ represent local solid fractions and average solid fractions in the system respectively. These approaches give much more information than simply determining N_{js} and also may give information

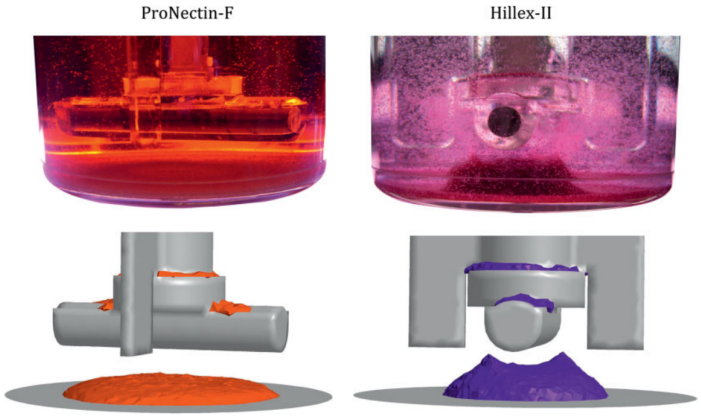

Figure 1.28: Comparison of observed (top) and CFD predicted (bottom) microcarrier distributions for ProNectin-F (left) and Hillex II (right) microcarriers in spinner flasks (adapted from [227]).

on the spatial distribution of the particles for a given average particle concentration. Notably, a fully homogeneous suspension would be obtained when this RSD value approaches 0.

$$RSD = \sqrt{\frac{1}{n_s}\sum_{i=1}^{n_s}\frac{\alpha_i}{\langle\alpha_i\rangle} - 1} \tag{1.8}$$

1.4.4 Measuring and modelling particle collisions in STRs

Measuring particle collisions

The recent development and application of techniques and models to characterize the flow and concentration of particles during MSC cell culture (computational fluid dynamics and light attenuation techniques for example) have brought crucial information concerning shear stress and power dissipation during MSC cell culture. However, these experiments have not yet considered the interaction between the solid particles. In order to fully understand the impact of microcarrier collisions on MSCs, it is important to quantify the frequency and intensity of the collisions that cells perceive continuously during cell culture and which will ultimately depend on the bioreactor geometry (impeller geometry, tank geometry, quantity of plunging elements *etc.*), operating conditions (agitation rate, culture volume, microcarrier concentration *etc.*), as well as the microcarrier characteristics (size, porosity, rigidity *etc.*). As a result, experimental techniques or models to quantify the number and intensity of microcarrier collisions have yet to be proposed in agitated bioreactors.

- **Electro-chemical sensors** An interesting technique was proposed by Del Pozo et al. in 1993 to determine local collision frequency of free-floating particles within a fluidized-bed column [322]. In this system, spherical glass beads (ρ = 2500 kg m^{-3}) with an average diameter of 5 mm were placed in a three-phase solid

- liquid - gas system. Small quantities of silver spheres with the same density as the glass beads were also added as tracer particles. The electro-chemical reduction of dissolved oxygen at the surface of a 5 mm tethered silver sphere was used to determine the amount of interactions between the tethered particle and the free-floating tracer spheres. When a silver sphere was brought into contact with a fixed probe, the diffusion current increased due to the increased surface (essentially the surface was doubled) where the chemical reduction took place which was then analyzed by an external software. Authors then calculated the average collision frequency (CF) of the n_t particles according to the amount of collisions detected N_c between the n_c tracer particles and the electrode over the time t (Equation 1.9).

$$CF = \frac{N_c}{t} \times \frac{n_t}{n_c} \tag{1.9}$$

In this preliminary work, the authors were unable to obtain information on the force with which the particles were interacting since the generated signal essentially saturated the sensor and no information about collision intensity or duration was collected.

- **High speed cameras** Another approach to determine particle-particle collisions consists in using high-speed cameras with sufficient resolution to track individual particles. For this experimental measurements particle collisions were observed inside a liquid fluidized bed by particle tracking in an index-matched array. Collision detection was based on the use of a peak acceleration threshold of the instantaneous speed of colored tracers (and validated by comparing with theoretical models) [323].

- **Piezoelectric sensors** Online acoustic emission sensors (hydrophones) are, in most cases, composed of a piezoelectric transducer that generates an electric potential when subjected to a pressure change, such as a collision with a particle or a sound wave. The technology has been used for the characterization of various bi-phasic or tri-phasic systems which are, in majority applied to chemical or petrochemical industries. For example, in gas-liquid two phase systems, piezoelectric sensors have been applied to detect and characterize bubble size and frequency [324, 325]. In addition, piezoelectric sensors have been used in free fall experiments to detect particle impact of glass of Al_2O_3 beads (879 kg m^{-3}) [324] or to detect flow regime transitions, particle activity and particle collision intensity of low-density polyethylene (921 kg m^{-3}, 600 μm) [326] and sand particles (2640 kg m^{-3}, 160 - 600 μm) [327].

Modelling particle collisions in STRs

- **Physical characteristic values to describe collision mechanisms** The use of the experimental data obtained via various experimental techniques described above have, over the years, led to the development of empirical and numerical models to determine the amount of collisions that particles undergo with each other in agitated conditions. The evaluation of these collisions have a wide range of applications including understanding the aggregation of solid particles in floculation and / or sedimentation, bubble coalescence in liquid and gas dispersions, and crystal nucleation (reviewed in [328]). The most common collision mechanisms are listed in Table 1.9, and typically depend on physical characteristic constants including the Stokes number St and the smallest scales of turbulence (Kolmogorov length scale) λ_k (see Equation 1.5). Briefly, the presence of concentration gradients is partly related to the particle inertia, characterized by the Stokes number (Equation 1.10). This number evaluates the ratio between the particle relaxation time τ_p (Equation 1.11) and the characteristic Kolmogorov time scale τ_K (Equation 1.12). If this number is smaller than 1, particles will have trajectories close to that of the liquid flow, and thus will be more easily dispersed. On the contrary, if the Stokes number is greater than 1, the particles will not have time to adjust to sudden flow changes and thus, concentration gradients can appear [329]. For further information on the models and characteristic length and time scales readers are advised to refer to the extensive literature on the subject which has been reviewed in [328]. Specifically, the amount of particle-particle collisions will typically depend on the the level of fluid turbulence as well as particle characteristics (size, density, shape *etc.*). For example, in a laminar regime and for sufficiently small particles, the perkinetic model predicts that particle-particle collisions will arise from the random motion of particles due to Brownian motion. When increasing turbulence, particle collisions will become more organized, either by following the flow streamline (in the case of sufficiently small or light particles) or through sedimentation (if particles are sufficiently heavy). Lastly, further increasing turbulence will lead to the development of turbulent eddies in the flow and particle size is expected to determine the mechanisms causing particle collisions. In the case of microcarrier suspension in Stirred Tank Reactors, the last mechanisms will typically be taking place *i.e.* either particles collide due to deviations from turbulent eddies, or due to independent motion of the particles if the particles are sufficiently large. The next few paragraphs will discuss simple models and characteristics which can be used to determine these particle-particle collisions. Much more complex and thorough accelerative (correlated and uncorrelated) models have been reviewed in [328].

$$St = \frac{\tau_p}{\tau_K} \tag{1.10}$$

$$\tau_p = \frac{\rho_s d_p^2}{18\mu} \tag{1.11}$$

$$\tau_K = \left(\frac{\nu}{\varepsilon}\right)^{0.5} \tag{1.12}$$

Table 1.9: Modes of collisions (adapted from [328])

Mechanism	**Description**	**Continuous phase flow regime**	**Flow hydrodynamics of the dispersed phase and conditions**
Brownian motion (perkinetic)	Particle collision due to random Brownian motion of particles	Laminar	Particles are small, less than 1 μm
Shear (arthokinetic)	Particles follow streamlines and collide due to different positions within the shear flow field	Laminar and turbulent	Various length scales : St ≤ 1
Differential sedimentation	Particles of different sizes exhibit different settling velocities leading to collisions	Laminar	Various length scales λ_k, various particle relaxation times τ_p
Accelerative - correlated	Particles deviate from streamline and collide. Particle and carrier fluid velocities are correlated or partially correlated	Turbulent	Intermediate particle size; various particle relaxation times τ_p
Accelerative - independent	Particles are thrown randomly from eddy to eddy and collide. Particle and carrier fluid velocities are uncorrelated	highly turbulent	Particles are larger than viscous dissipation eddies; St ≥ 10

- **Average inter-particle distance** To begin with, a first approach consists of a theoretical statistical collisional model based on particle size, concentration and the surrounding fluid behaviour [330]. In this context, the collision frequency should be correlated with the space between microcarriers (*i.e.* inter-particle distance from edge to edge). Considering a homogeneous hexagonal particle distribution, the maximum compacity for spherical objects corresponds to a state where particles are touching and is obtained at a volume fraction α_{max} of 52 % [331]. When decreasing particle concentration below the packing limit, the distance between particles h can be given by Equation 1.13 and ultimately depends on the particle diameter d_p and particle solid hold-up α. From a statistical perspective, the collisional frequency and force of individual collisions should depend on this inter particle distance, $\langle h \rangle$ (*i.e.* a greater average distance between particles implies a decreased collisional frequency). The advantage of using such macroscopic descriptors is their easy calculation based on simple parameters which are available. It can be noted however that many studies have shown that there are significant particle concentration gradients which can be observed in stirred tank reactors (STR) and that such simplistic approaches do not take into account these variations. As a result, they provide easy, average and overall estimations of elements

which can be correlated to average microcarrier-microcarrier collisions but more complex studies regarding local particle velocities and gradients are inevitable to decipher the complex picture and understand the actual stresses that cells may be undergoing during an expansion process on microcarriers.

$$\langle h \rangle = d_p \left[\left(\frac{\alpha_{max}}{\alpha} \right)^{1/3} - 1 \right] \tag{1.13}$$

- **Collision frequency (CF)** In the case of microcarriers in an agitated bioreactor, the mean particle velocity at a given point can be considered as equal to the mean liquid velocity surrounding it, if the particles are big enough to not be caught up in turbulent eddies but small and light enough to follow liquid streamlines (*i.e.* Stokes number smaller than 1, see Equation 1.10). In a holistic approach, the collision frequency between particles CF can be extrapolated using Equation 1.14 which indicates a direct correlation between the agitation rate N and the collision frequency and takes into account parameters such as the flow number N_Q (to account for agitator geometry), the amount of particles n_p and their diameter d_p and the liquid volume V. To finish, another existing model concerning particle collisions in an agitated tank could be the one proposed by Cherry and Papoutsakis (Equation 1.15) [332] which correlates particle collision frequency with the volumetric dissipated power $\langle \varepsilon \rangle$. This dissipated power can be estimated by the product of N^3 and D^2. As a result, this model estimates that particle-particle collision frequency should ultimately depend on the agitator speed and agitator diameter.

$$CF = \frac{\sqrt{2}}{2} \pi d_p^2 \left(\frac{n_p}{V} \right)^2 \times N \times N_Q \tag{1.14}$$

$$CF = \frac{(\nu \times \langle \varepsilon \rangle)^{1/4} \times \alpha^2}{d_p^4} \tag{1.15}$$

- **Turbulent collision severity (TCS)** A common description of the amount of collisions and forces that cells may be undergoing during cell culture is proposed by Cherry and Papoutsakis using the Turbulent Collision Severity index, defined by the product of the average collision kinetic energy, its frequency per element of volume and the total amount of particles. This indicator defines a collision energy per bead per time and depends on the mass m, diameter d_p, and density ρ_p of beads, on their relative velocity $\langle u \rangle$, and on the volume fraction they occupy α (Equation 1.16, [333]). Accordingly, having a sufficiently detailed description of the solid particles, the amount of collisions that cells grown on microcarriers would undergo should be easily calculated if elements characterizing particle ve-

locities are available. However, to date, this remains a complex task that can be tackled with various approaches. To begin with, certain authors have supposed that particle velocities can be approximated to the speed of the smallest turbulent eddies since microcarriers have approximately the same density and size as these eddies (*i.e.* $\langle u \rangle = (\epsilon\nu)^{1/4}$). As a result this leads to a simpler representation of the TCS per bead as described in Equation 1.17 [333]. However, if the turbulent eddies are much larger than beads, the relative bead velocities are not well described using this assumption and other models can be used such as those introduced in [333]. In this case, authors propose to use Kolmogorov scale comparison and, in particular to calculate the ratio between an eddy TCS and a shear TCS. However, in the case of microcarrier-based systems, a ratio between bead and eddy sizes close to 1 is often assumed.

$$TCS = \frac{m \cdot \langle u \rangle}{2} \times \frac{\sqrt{\langle u \rangle} \cdot \alpha^2}{d_p^4} \Bigg/ \frac{\alpha}{\frac{\pi}{6} \cdot d_p^3} = \langle u \rangle^{3/2} \left(\frac{\pi^2 \rho_p d_p^2 \alpha}{72} \right) \tag{1.16}$$

$$TCS = (\nu \times \langle \varepsilon \rangle)^{3/4} \times \frac{\rho_p \pi^2 d_p^2 \alpha}{72} \tag{1.17}$$

1.4.5 Section summary

Understanding how cells perceive the stresses generated throughout cell culture could be an asset towards the development of these processes. These major stresses are composed of (i) tensile forces caused by surface material distortion and rigidity or shear stress and (ii) pressure forces which are, in majority caused by microcarrier - microcarrier interactions and by interactions between microcarriers and elements of the cell culture system (*i.e.* impeller, bioreactor wall, online probes). It can be seen that there are fundamentally different theoretical approaches to estimate particle collisions using known parameters such as agitation rate and agitator diameter. As a result, having experimental approaches to determine the most viable and interesting model for specific systems and microcarriers may be crucial to further understand these particle collision characteristics. Lastly, the review of literature to determine particle collision models specifically applied to microcarriers in different stirred tank reactors (STRs) shows that there is limited documentation characterizing the fundamental physical mechanisms at stake in such systems. This concerns microcarrier solid phases in STRs and specifically physical constraints with regard to human cells (which have specific responses to shear and pressure forces).

1.5 Thesis aims and objectives

1.5.1 State of the art - concluding remarks

The scalable manufacturing of cell and gene therapeutic products are currently ongoing great progress and development. For this, **large efforts can be seen from both public and private entities worldwide to develop technologies and scientific understanding of process engineering** and ensure these new therapeutic products can safely be delivered to patients and continue to be used to address a wide range of clinical applications. **Elements of context of where these efforts have been focused on were essentially the object of Paragraph 1.1**. In addition, broad consortiums such as the international society for cell and gene therapy (ISCT) have tackled crucial bottlenecks by for example providing minimal elements to define and characterize stem cells or providing partnerships between international regulatory bodies, industry, clinicians and academia. These global efforts ensure that research and development of these types of therapies can be performed within a globally similar environment and provides initial elements of standardization.

However, reviewing how stem cell research is currently being performed, in small scale and simplified 2-dimensional systems (T-Flasks) indicated that **large heterogeneities persist within the scientific community regarding the best process parameters for small scale studies as can be seen in Paragraph 1.2**. Lab-specific protocols remain within individual research teams working with similar cells. In addition, diverging conclusions of the impact of certain process parameters on other defined output parameters are widely present in the literature. As a result, it seems that cross-dependence between process parameters is present in what may seem like simple culture systems and should be kept in mind for future process development. **In more complex systems such as cell culture on microcarriers in stirred tank reactors (STRs), lessons learned from the pharmaceutical industry of vaccines and antibodies bring precious elements concerning equipment design and monitoring but are not sufficient to tackle specific issues of cell therapeutic products as introduced in Paragraph 1.3**. In the case of MSC expansion on microcarriers, specific challenges including adherent viable cell count monitoring, adhesion and detachment protocols, or how to optimize the way microcarriers are suspended have not yet been fully elicited.

In this complex context of microcarrier-based expansion processes in bioreactors, one of many parameters to consider is the way that the solid phase will be suspended via the agitator and how the solid phase interacts with one another (friction and/or shocks between microcarriers). **In this context, Paragraph 1.4 presented elements of description to evaluate the quantity and eventual intensity of collisions that cells grown on microcarriers may perceive in STRs.** Both theoretical and experimental approaches can be used to determine these collisions.

1.5.2 Thesis objectives and overview

To date, bottlenecks persist concerning deep scientific understanding of how various process parameters will impact the cell production process. Specifically applied to microcarrier-based expansion processes of WJ-MSCs, very little information is available to characterize the impact of microcarrier concentration on MSC growth and death rates or on critical quality attributes which may have crucial and possibly dangerous clinical impacts. As a result, the following proposes to rationally describe the impact of particle concentration on MSC growth through a pluri-disciplinary characterization of microcarrier-microcarrier interactions in agitated conditions. In order to do so the biological and physical aspects of this work will be presented and are summarized in Figure 1.29.

To begin with, **Chapter 2 will present a quantitative approach to estimate cell death caused by microcarrier-microcarrier collisions in two cell culture geometries and scales : Erlenmeyer Flasks and Spinner Flasks. For this, cells were grown at various microcarrier concentrations using two microcarrier types : Cytodex-1 and Synthemax II**. Complementary cultures were performed by adding various concentrations of particles with the same size and density as microcarriers in view of providing specific information on how additional particles may impact MSC growth on microcarriers. In addition, elements of MSC characterization were performed for these experiments to understand not only the impact of microcarrier-microcarrier interactions on growth but also on defined elements of cell quality.

In order to estimate the amount and intensity of microcarrier-microcarrier collisions in a specific tank geometry, experiments were performed using both the attenuation of light by Cytodex-1 microcarriers (to estimate local microcarrier concentration) and the acoustic signal which comes from particles colliding with a hydrophone (to estimate microcarrier-sensor collision frequency and intensity). **These experiments provided elements to estimate the amount of particle collisions that MSCs may perceive during suspension and steady phases of cell culture in STRs and will be the object of Chapter 3**.

Lastly, **Chapter 4 will present a bioreactor-based approach to MSC manufacturing and biological aspects on how particle concentration and agitation impacts MSC growth and quality attributes**. For this, various MSC cultures were performed in STRs with varying particle concentrations and agitation strategies. The MSCs produced in these conditions were then characterized to define if certain critical quality attributes could be affected by parameters such as microcarrier concentration and/or agitation.

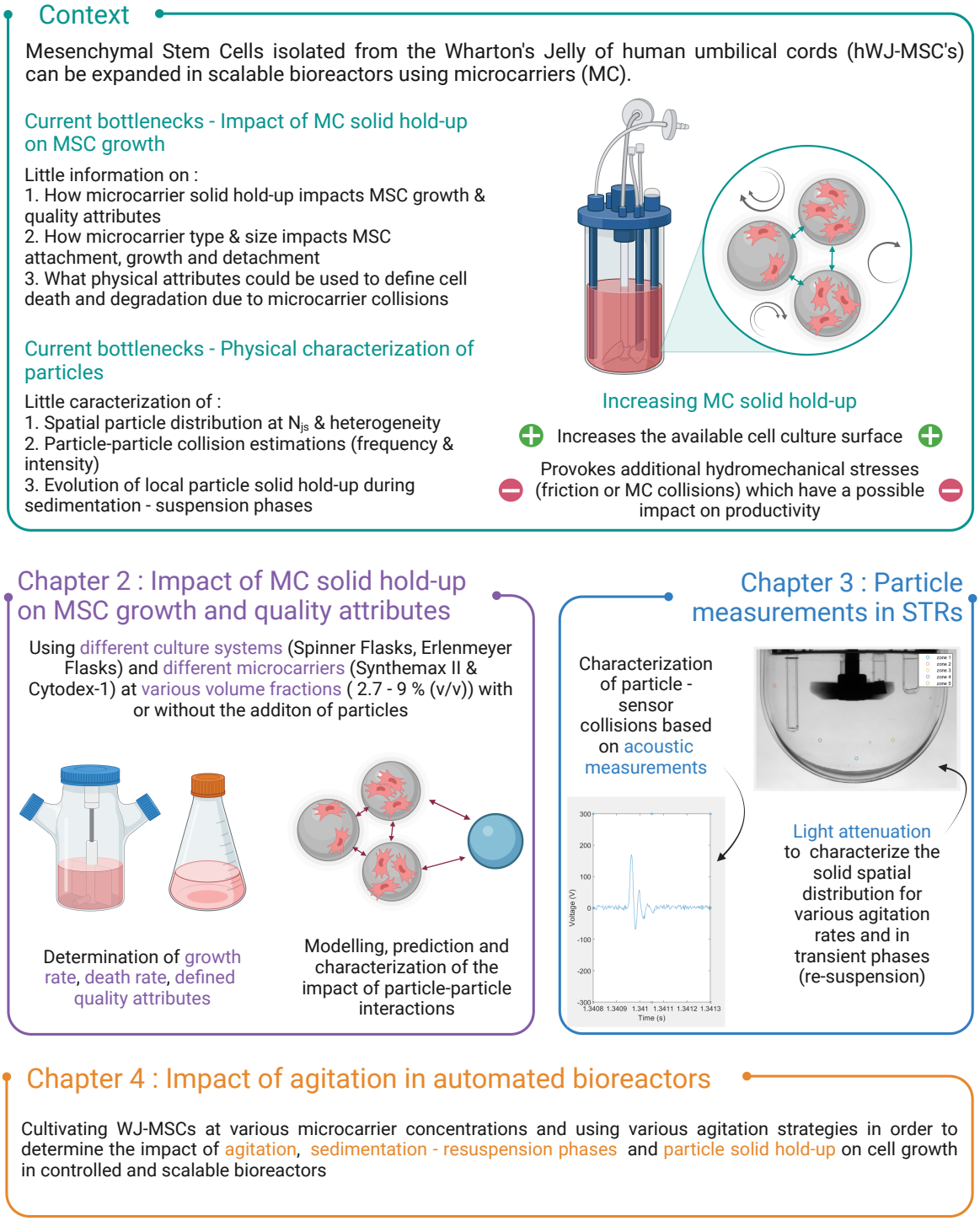

Figure 1.29: Graphical overview of the thesis structure and axis.

Bibliography

[1] L. Yount. Antoni van leeuwenhoek: First to see microscopic life. *Enslow Publishers, Inc.*, 2008.

[2] D. Ribatti. An historical note on the cell theory. *Experimental Cell Research*, 364(1):1–4, 2018.

[3] R. Virchow. Cellular pathology as based upon physiological and pathological histology. *JB Lippincott*, 1863.

[4] E. Haeckel. Natürliche schöpfungsgeschichte: Gemeinverständliche wissenschaftliche vorträge über die entwickelungslehre im allgemeinen und diejenige von darwin. *Reimer Publishers*, page 610, 1868.

[5] A.-H. Maehle. Ambiguous cells: the emergence of the stem cell concept in the nineteenth and twentieth centuries. *Notes and Records of the Royal Society*, 65(4):359–378, 2011.

[6] J. Gurdon. The developmental capacity of nuclei taken from differentiating endoderm cells of xenopus laevis. *Journal of embryology and experimental morphology*, 8:505–26, 1961.

[7] J. E. Till and E. A. McCulloch. A direct measurement of the radiation sensitivity of normal mouse bone marrow cells. *Radiation Research*, 14(2):213–222, 1961.

[8] D. Evered and S. Harnett. Cell and molecular biology of vertebrate hard tissues. *John Wiley & Sons*, 2008.

[9] M. J. Evans and M. H. Kaufman. Establishment in culture of pluripotential cells from mouse embryos. *Nature*, 292(5819):154–156, 1981.

[10] V. Murugan. Stem cell issue: Embryonic stem cell research: A decade of debate from bush to obama. *The Yale journal of biology and medicine*, 82(3):101, 2009.

[11] M. Dominici, K. Le Blanc, I. Mueller, I. Slaper-Cortenbach, F. Marini, D. Krause, R. Deans, A. Keating, D. Prockop, and E. Horwitz. Minimal criteria for defining multipotent mesenchymal stromal cells. the international society for cellular therapy position statement. *Cytotherapy*, 8:315–317, 2006.

[12] D. Baksh, J. E. Davies, and P. W. Zandstra. Adult human bone marrow–derived mesenchymal progenitor cells are capable of adhesion-independent survival and expansion. *Experimental hematology*, 31(8):723–732, 2003.

[13] G. J. Jimenez-Puerta, J. A. Marchal, E. López-Ruiz, and P. Gálvez-Martín. Role of mesenchymal stromal cells as therapeutic agents: Potential mechanisms of action and implications in their clinical use. *Journal of Clinical Medicine*, 9(2):445, 2020.

[14] R. Berebichez-Fridman and P. R. Montero-Olvera. Sources and clinical applications of mesenchymal stem cells. *Sultan Qaboos University Medical Journal*, 18(3):e264–e277, 2018.

[15] E. Horwitz, K. Le Blanc, M. Dominici, I. Mueller, I. Slaper-Cortenbach, F. Marini, R. Deans, D. Krause, and A. Keating. Clarification of the nomenclature for MSC: The international society for cellular therapy position statement. *Cytotherapy*, 7(5):393–395, 2005.

[16] R. G. Rowe and G. Q. Daley. Induced pluripotent stem cells in disease modelling and drug discovery. *Nature reviews. Genetics*, 20(7):377–388, 2019.

[17] P. S. Cho, D. J. Messina, E. L. Hirsh, N. Chi, S. N. Goldman, D. P. Lo, I. R. Harris, S. H. Popma, D. H. Sachs, and C. A. Huang. Immunogenicity of umbilical cord tissue–derived cells. *Blood*, 111(1):430–438, 2008.

[18] A. K. Batsali, M.-C. Kastrinaki, H. A. Papadaki, and C. Pontikoglou. Mesenchymal stem cells derived from whartons jelly of the umbilical cord: Biological properties and emerging clinical applications. *Current Stem Cell Research & Therapy*, 8(2):144–155, 2013.

[19] K. Seshareddy, D. Troyer, and M. L. Weiss. Method to isolate mesenchymal-like cells from wharton's jelly of umbilical cord. *Methods in Cell Biology*, 86:101–119, 2008.

[20] J. E. Davies, J. T. Walker, and A. Keating. Concise review: Whartons jelly: The rich, but enigmatic, source of mesenchymal stromal cells. *Stem Cells Translational Medicine*, 6(7):1620–1630, 2017.

[21] W. global health observatory. Disease burden and mortality estimates. *World Health Organisation*, 2020.

[22] D. E. Rodriguez-Fuentes, L. E. Fernandez-Garza, J. A. Samia-Meza, S. A. Barrera-Barrera, A. I. Caplan, and H. A. Barrera-Saldana. Mesenchymal stem cells current clinical applications: a systematic review. *Archives of Medical Research*, 52(1):93–101, 2021.

[23] D. Jovic, Y. Yu, D. Wang, K. Wang, H. Li, F. Xu, C. Liu, J. Liu, and Y. Luo. A brief overview of global trends in msc-based cell therapy. *Stem Cell Reviews and Reports*, pages 1–21, 2022.

[24] E. Özmert and U. Arslan. Management of retinitis pigmentosa by wharton's jelly-derived mesenchymal stem cells: prospective analysis of 1-year results. *Stem Cell Research & Therapy*, 11(1):1–17, 2020.

[25] J. Panés, D. García-Olmo, G. Van Assche, J. F. Colombel, W. Reinisch, D. C. Baumgart, A. Dignass, M. Nachury, M. Ferrante, L. Kazemi-Shirazi, et al. Expanded allogeneic adipose-derived mesenchymal stem cells for complex perianal fistulas in crohn's disease: a phase 3 randomised, double-blind controlled trial. *The Lancet*, 388(10051):1281–1290, 2016.

[26] C. Ikebe and K. Suzuki. Mesenchymal stem cells for regenerative therapy: optimization of cell preparation protocols. *Biomedical Research International*, 2014:11, 2014.

[27] M. E. Bateman, A. L. Strong, J. M. Gimble, and B. A. Bunnell. Concise review: using fat to fight disease: a systematic review of nonhomologous adipose-derived stromal/stem cell therapies. *Stem Cells*, 36:1311–1328, 2018.

[28] O. Ringden, M. Uzunel, I. Rasmusson, M. Remberger, B. Sundberg, H. Lennies, H.-U. Marschall, A. Dlugosz, A. Szakos, Z. Hassan, B. Omazic, J. Aschan, L. Barkholt, and K. Le Blanc. Mesenchymal stem cells for treatment

of therapy-resistant graft-versus-host disease:. *Transplantation*, 81:1390–1397, 2006.

[29] M. Di Nicola, C. Carlo-Stella, M. Magni, M. Milanesi, P. D. Longoni, P. Matteucci, S. Grisanti, and A. M. Gianni. Human bone marrow stromal cells suppress T-lymphocyte proliferation induced by cellular or nonspecific mitogenic stimuli. *Blood*, 99:3838–3843, 2002.

[30] L. Fouillard, A. Chapel, D. Bories, S. Bouchet, J.-M. Costa, H. Rouard, P. Herve, P. Gourmelon, D. Thierry, M. Lopez, and N. C. Gorin. Infusion of allogeneic-related HLA mismatched mesenchymal stem cells for the treatment of incomplete engraftment following autologous haematopoietic stem cell transplantation. *Leukemia*, 21:568–570, 2007.

[31] M. Gnecchi, H. He, O. D. Liang, L. G. Melo, F. Morello, H. Mu, N. Noiseux, L. Zhang, R. E. Pratt, J. S. Ingwall, et al. Paracrine action accounts for marked protection of ischemic heart by akt-modified mesenchymal stem cells. *Nature medicine*, 11(4):367–368, 2005.

[32] V. Sengupta, S. Sengupta, A. Lazo, P. Woods, A. Nolan, and N. Bremer. Exosomes derived from bone marrow mesenchymal stem cells as treatment for severe covid-19. *Stem cells and development*, 29(12):747–754, 2020.

[33] A. Trounson, R. G. Thakar, G. Lomax, and D. Gibbons. Clinical trials for stem cell therapies. *BMC Medicine*, 9:52, 2011.

[34] A. Trounson and C. McDonald. Stem cell therapies in clinical trials: progress and challenges. *Cell Stem Cell*, 17:11–22, 2015.

[35] B. Parekkadan and J. M. Milwid. Mesenchymal stem cells as therapeutics. *Annual Review of Biomedical Engineering*, 12:87–117, 2010.

[36] L. Sensebé, M. Gadelorge, and S. Fleury-Cappellesso. Production of mesenchymal stromal/stem cells according to good manufacturing practices: a review. *Stem Cell Research & Therapy*, 4:66, 2013.

[37] M. Mousaei Ghasroldasht, J. Seok, H.-S. Park, F. B. Liakath Ali, and A. Al-Hendy. Stem cell therapy: From idea to clinical practice. *International Journal of Molecular Sciences*, 23(5):2850, 2022.

[38] M. H. Amer, F. R. Rose, K. M. Shakesheff, M. Modo, and L. J. White. Translational considerations in injectable cell-based therapeutics for neurological applications: concepts, progress and challenges. *NPJ Regenerative medicine*, 2:13, 2017.

[39] R. H. Lee, A. A. Pulin, M. J. Seo, D. J. Kota, J. Ylostalo, B. L. Larson, L. Semprun-Prieto, P. Delafontaine, and D. J. Prockop. Intravenous hMSCs improve myocardial infarction in mice because cells embolized in lung are activated to secrete the anti-inflammatory protein TSG-6. *Cell stem cell*, 5:54–63, 2009.

[40] L. Zangi, R. Margalit, S. Reich-Zeliger, E. Bachar-Lustig, A. Beilhack, R. Negrin, and Y. Reisner. Direct imaging of immune rejection and memory induction by allogeneic mesenchymal stromal cells. *Stem Cells*, 27:2865–2874, 2009.

[41] K. English. Mechanisms of mesenchymal stromal cell immunomodulation. *Immunology & Cell Biology*, 91(1):19–26, 2013.

[42] H. Yagi, A. Soto-Gutierrez, B. Parekkadan, Y. Kitagawa, R. G. Tompkins, N. Kobayashi, and M. L. Yarmush. Mesenchymal stem cells: Mechanisms of immunomodulation and homing. *Cell Transplantation*, 19(6):667–679, 2010.

[43] M. Honczarenko, Y. Le, M. Swierkowski, I. Ghiran, A. M. Glodek, and L. E. Silberstein. Human bone marrow stromal cells express a distinct set of biologically functional chemokine receptors. *Stem Cells*, 24(4):1030–1041, 2006.

[44] G. Ren, L. Zhang, X. Zhao, G. Xu, Y. Zhang, A. I. Roberts, R. C. Zhao, and Y. Shi. Mesenchymal stem cell-mediated immunosuppression occurs via concerted action of chemokines and nitric oxide. *Cell Stem Cell*, 2(2):141–150, 2008.

[45] A. M. Betancourt. New cell-based therapy paradigm: induction of bone marrow-derived multipotent mesenchymal stromal cells into pro-inflammatory msc1 and anti-inflammatory msc2 phenotypes. *Mesenchymal Stem Cells-Basics and Clinical Application II*, pages 163–197, 2012.

[46] D. S. Harburger and D. A. Calderwood. Integrin signalling at a glance. *Journal of cell science*, 122(2):159–163, 2009.

[47] D. E. Discher, P. Janmey, and Y.-l. Wang. Tissue cells feel and respond to the stiffness of their substrate. *Science*, 310(5751):1139–1143, 2005.

[48] G. Yourek, S. M. McCormick, J. J. Mao, and G. C. Reilly. Shear stress induces osteogenic differentiation of human mesenchymal stem cells. *Regenerative medicine*, 5(5):713–724, 2010.

[49] V. Vogel and M. Sheetz. Local force and geometry sensing regulate cell functions. *Nature reviews Molecular cell biology*, 7(4):265–275, 2006.

[50] V. Bassaneze, V. G. Barauna, C. Lavini-Ramos, J. Kalil, I. T. Schettert, A. A. Miyakawa, and J. E. Krieger. Shear stress induces nitric oxide–mediated vascular endothelial growth factor production in human adipose tissue mesenchymal stem cells. *Stem cells and development*, 19(3):371–378, 2010.

[51] V. Frank, S. Kaufmann, R. Wright, P. Horn, H. Y. Yoshikawa, P. Wuchter, J. Madsen, A. L. Lewis, S. P. Armes, A. D. Ho, et al. Frequent mechanical stress suppresses proliferation of mesenchymal stem cells from human bone marrow without loss of multipotency. *Scientific reports*, 6(1):1–12, 2016.

[52] I.-C. Lee, J.-H. Wang, Y.-T. Lee, and T.-H. Young. The differentiation of mesenchymal stem cells by mechanical stress or/and co-culture system. *Biochemical and biophysical research communications*, 352(1):147–152, 2007.

[53] F. Pauwels. A new theory concerning the influence of mechanical stimuli on the differentiation of the supporting tissues. In *Biomechanics of the locomotor apparatus*, pages 375–407. Springer, 1980.

[54] P. R. Blenman, D. R. Carter, and G. S. Beaupre. Role of mechanical loading in the progressive ossification of a fracture callus. *Journal of Orthopaedic Research*, 7(3):398–407, 1989.

[55] D. R. Carter, G. S. Beaupré, N. J. Giori, and J. A. Helms. Mechanobiology of skeletal regeneration. *Clinical Orthopaedics and Related Research*, 355:S41–S55, 1998.

[56] M. Jagodzinski, A. Breitbart, M. Wehmeier, E. Hesse, C. Haasper, C. Krettek, J. Zeichen, and S. Hankemeier. Influence of perfusion and cyclic compression on proliferation and differentiation of bone marrow stromal cells in 3-dimensional culture. *Journal of Biomechanics*, 41(9):1885–1891, 2008.

[57] D. Pelaez, N. Arita, and H. S. Cheung. Extracellular signal-regulated kinase (erk) dictates osteogenic and/or chondrogenic lineage commitment of mesenchymal stem cells under dynamic compression. *Biochemical and biophysical research communications*, 417(4):1286–1291, 2012.

[58] D. R. Wagner, D. P. Lindsey, K. W. Li, P. Tummala, S. E. Chandran, R. L. Smith, M. T. Longaker, D. R. Carter, and G. S. Beaupre. Hydrostatic pressure enhances chondrogenic differentiation of human bone marrow stromal cells in osteochondrogenic medium. *Annals of biomedical engineering*, 36(5):813–820, 2008.

[59] D. A. Lee, M. M. Knight, J. J. Campbell, and D. L. Bader. Stem cell mechanobiology. *Journal of Cellular Biochemistry*, 112(1):1–9, 2011.

[60] F. Song, D. Jiang, T. Wang, Y. Wang, Y. Lou, Y. Zhang, H. Ma, and Y. Kang. Mechanical stress regulates osteogenesis and adipogenesis of rat mesenchymal stem cells through PI3k/akt/GSK-3b/b-catenin signaling pathway. *Biomedical Research International*, 2017, 2017.

[61] C. Mason, D. A. Brindley, E. J. Culme-Seymour, and N. L. Davie. Cell therapy industry: billion dollar global business with unlimited potential. *Regenerative medicine*, 6(3):265–272, 2011.

[62] T. R. Olsen, K. S. Ng, L. T. Lock, T. Ahsan, and J. A. Rowley. Peak msc — are we there yet? *Frontiers in medicine*, 5:178, 2018.

[63] A. S. Simaria, S. Hassan, H. Varadaraju, J. Rowley, K. Warren, P. Vanek, and S. S. Farid. Allogeneic cell therapy bioprocess economics and optimization: Single-use cell expansion technologies. *Biotechnology and bioengineering*, 111(1):69–83, 2014.

[64] C. Maillot, C. Sion, N. De Isla, D. Toye, and E. Olmos. Quality by design to define critical process parameters for mesenchymal stem cell expansion. *Biotechnology Advances*, 50:107765, 2021.

[65] S. Metcalfe. Mesenchymal stem cells and management of covid-19 pneumonia. *Medicine in drug discovery*, 5:100019, 2020.

[66] G. Moll, N. Drzeniek, J. Kamhieh-Milz, S. Geissler, H.-D. Volk, and P. Reinke. MSC therapies for COVID-19: importance of patient coagulopathy, thromboprophylaxis, cell product quality and mode of delivery for treatment safety and efficacy. *Frontiers in Immunology*, 11:1091, 2020.

[67] R. M. Ten Ham, J. Hoekman, A. M. Hövels, A. W. Broekmans, H. G. Leufkens, and O. H. Klungel. Challenges in advanced therapy medicinal product development: a survey among companies in europe. *Molecular Therapy-Methods & Clinical Development*, 11:121–130, 2018.

[68] A. S. Rathore and H. Winkle. Quality by design for biopharmaceuticals. *Nature Biotechnology*, 27:9, 2009.

[69] S. C. Gad. *Pharmaceutical manufacturing handbook*. Wiley-Interscience, John Wiley and Sons, Inc., Hoboken, New Jersey, 2008.

[70] L. X. Yu, G. Amidon, M. A. Khan, S. W. Hoag, J. Polli, G. Raju, and J. Woodcock. Understanding pharmaceutical quality by design. *The AAPS journal*, 16(4):771–783, 2014.

[71] N. Xiao, H.-Z. Huang, Y. Li, L. He, and T. Jin. Multiple failure modes analysis and weighted risk priority number evaluation in FMEA. *Engineering Failure Analysis*, 18:1162–1170, 2011.

[72] P. K. Sellappan N. Modified prioritization methodology for risk priority number in failure mode and effects analysis. *International Journal Applied Science and Technology*, 3:11, 2013.

[73] A. Certa, M. Enea, G. M. Galante, and C. M. La Fata. Electre tri-based approach to the failure modes classification on the basis of risk parameters: an alternative to the risk priority number. *Computers and Industrial Engineering*, 108:100–110, 2017.

[74] A. Khandagade, V. Kale, and R. Sinha. Critical quality risk analysis of process parameters of fluid bed coating technology. *International Journal Industrial Engineering and Technology*, 3:10, 2013.

[75] J. Harms, X. Wang, T. Kim, X. Yang, and A. S. Rathore. Defining process design space for biotech products: case study of pichia pastoris fermentation. *Biotechnolgy Progress*, 24:655–662, 2008.

[76] R. Seely and J. Haury. Applications of failure modes and effects analysis to biotechnology manufacturing processes. In *Process validation in manufacturing of biopharmaceuticals*, chapter 2. Addison-Wesley, Boca Raton, FL, 2005.

[77] C. B. W. Group. A Mab: a case study in bioprocess development version 2.1. *CMC Biotech Working Group*, page 278, 2009.

[78] M. Mitchell. Determining criticality—process parameters and quality attributes part II; design of experiments

and data-driven criticality. *BioPharmaceutical International*, page 9, 2014.

[79] R. R. Sharma, K. Pollock, A. Hubel, and D. McKenna. Mesenchymal stem or stromal cells: a review of clinical applications and manufacturing practices. *Transfusion*, 54:1418–1437, 2014.

[80] Y. Y. Lipsitz, N. E. Timmins, and P. W. Zandstra. Quality cell therapy manufacturing by design. *Nature Biotechnology*, 34:393–400, 2016.

[81] A. S. Rathore. Roadmap for implementation of quality by design (QbD) for biotechnology products. *Trends Biotechnology*, 27:546–553, 2009.

[82] E. Spaeth, A. Klopp, J. Dembinski, M. Andreeff, and F. Marini. Inflammation and tumor microenvironments: defining the migratory itinerary of mesenchymal stem cells. *Gene Therapies*, 15:730–738, 2008.

[83] E. Eggenhofer and M. J. Hoogduijn. Mesenchymal stem cell-educated macrophages. *Transplantation Researc-hearch*, 1:12, 2012.

[84] A. I. Caplan and D. Correa. The MSC: an injury drugstore. *Cell Stem Cell*, 9:11–15, 2011.

[85] A. Corcione, F. Benvenuto, E. Ferretti, D. Giunti, V. Cappiello, F. Cazzanti, M. Risso, F. Gualandi, G. L. Mancardi, V. Pistoia, and A. Uccelli. Human mesenchymal stem cells modulate B-cell functions. *Blood*, 107:367–372, 2006.

[86] G. M. Spaggiari, A. Capobianco, S. Becchetti, M. C. Mingari, and L. Moretta. Mesenchymal stem cell-natural killer cell interactions: evidence that activated NK cells are capable of killing MSCs, whereas MSCs can inhibit IL-2-induced NK-cell proliferation. *Blood*, 107:1484–1490, 2006.

[87] Y. Han, X. Li, Y. Zhang, Y. Han, F. Chang, and J. Ding. Mesenchymal stem cells for regenerative medicine. *Cells*, 8:32, 2019.

[88] N. Amariglio, A. Hirshberg, B. W. Scheithauer, Y. Cohen, R. Loewenthal, L. Trakhtenbrot, N. Paz, M. Koren-Michowitz, D. Waldman, L. Leider-Trejo, A. Toren, S. Constantini, and G. Rechavi. Donor-derived brain tumor following neural stem cell transplantation in an ataxia telangiectasia patient. *PLoS Medicine*, 6:0221–0231, 2009.

[89] W. Li, G. Ren, Y. Huang, J. Su, Y. Han, J. Li, X. Chen, K. Cao, Q. Chen, P. Shou, L. Zhang, Z.-R. Yuan, A. I. Roberts, S. Shi, A. D. Le, and Y. Shi. Mesenchymal stem cells: a double-edged sword in regulating immune responses. *Cell Death Differentiation*, 19:1505–1513, 2012.

[90] G. Agmon and K. L. Christman. Controlling stem cell behavior with decellularized extracellular matrix scaffolds. *Current Opinion Solid State and Materials*, 20:193–201, 2016.

[91] A. I. Caplan. Adult mesenchymal stem cells for tissue engineering versus regenerative medicine. *Journal of cellular physiology*, 213:341–347, 2007.

[92] C. Martin, É. Olmos, M.-L. Collignon, N. De Isla, F. Blanchard, I. Chevalot, A. Marc, and E. Guedon. Revisiting MSC expansion from critical quality attributes to critical culture process parameters. *Process Biochemistry*, 59:231–243, 2017.

[93] A. M. Billing, H. Ben Hamidane, S. S. Dib, R. J. Cotton, A. M. Bhagwat, P. Kumar, S. Hayat, N. A. Yousri, N. Goswami, K. Suhre, A. Rafii, and J. Graumann. Comprehensive transcriptomic and proteomic characterization of human mesenchymal stem cells reveals source specific cellular markers. *Scientific reports*, 6:1–15, 2016.

[94] S. T. Mindaye, M. Ra, J. L. Lo Surdo, S. R. Bauer, and M. A. Alterman. Global proteomic signature of undifferentiated human bone marrow stromal cells: Evidence for donor-to-donor proteome heterogeneity. *Stem Cell Research*, 11:793–805, 2013.

[95] M. Mendicino, A. M. Bailey, K. Wonnacott, R. K. Puri, and S. R. Bauer. MSC-based product characterization for clinical trials: an FDA perspective. *Cell Stem Cell*, 14:141–145, 2014.

[96] R. Vishnubalaji, M. Al-Nbaheen, B. Kadalmani, A. Aldahmash, and T. Ramesh. Comparative investigation of the differentiation capability of bone-marrow- and adipose-derived mesenchymal stem cells by qualitative and quantitative analysis. *Cell and Tissue Research*, 347:419–427, 2012.

[97] L. Hayflick. The limited in vitro lifetime of human diploid cell strains. *Experimental Cell Research*, 37:614–636, 1964.

[98] S. Sethe, A. Scutt, and A. Stolzing. Aging of mesenchymal stem cells. *Ageing Research Review*, 5:91–116, 2006.

[99] D. Kletsas, H. Pratsinis, G. Mariatos, P. Zacharatos, and V. G. Gorgoulis. The proinflammatory phenotype of senescent cells: the p53-mediated ICAM-1 expression. *Annual New York Academy of Science*, 1019:330–332, 2004.

[100] A. Krtolica and J. Campisi. Integrating epithelial cancer, aging stroma and cellular senescence. *Advanced Gerontology*, 11:109–116, 2003.

[101] H. J. Kim and J.-S. Park. Usage of human mesenchymal stem cells in cell-based therapy: advantages and disadvantages. *Development and Reproduction*, (1):1–10, 2017.

[102] T. Vazin and W. J. Freed. Human embryonic stem cells: derivation, culture, and differentiation: a review. *Restorative neurology and neuroscience*, 28:589–603, 2010.

[103] S. A. Steigman, M. Armant, L. Bayer, G. S. Kao, L. Silberstein, J. Ritz, and D. O. Fauza. Preclinical regulatory validation of a 3-stage amniotic mesenchymal stem cell manufacturing protocol. *Journal of Pediatric Surgery*, 43:1164–1169, 2008.

[104] D. Belotti, G. Gaipa, B. Bassetti, B. Cabiati, G. Spaltro, E. Biagi, M. Parma, A. Biondi, L. Cavallotti, E. Gambini,

and G. Pompilio. Full GMP-compliant validation of bone marrow-derived human CD133+ cells as advanced therapy medicinal product for refractory ischemic cardiomyopathy. *Biomedical Research International*, 2015:10, 2015.

[105] A. J. Nauta and W. E. Fibbe. Immunomodulatory properties of mesenchymal stromal cells. *Blood, The Journal of the American Society of Hematology*, 110(10):3499–3506, 2007.

[106] S. Shi, S. Gronthos, S. Chen, A. Reddi, C. M. Counter, P. G. Robey, and C.-Y. Wang. Bone formation by human postnatal bone marrow stromal stem cells is enhanced by telomerase expression. *Nature Biotechnology*, 20:587–591, 2002.

[107] D. P. Lennon, S. E. Haynesworth, D. M. Arm, M. A. Baber, and A. I. Caplan. Dilution of human mesenchymal stem cells with dermal fibroblasts and the effects on in vitro and in vivo osteochondrogenesis. *Development Dynamics*, 219:50–62, 2000.

[108] T. Margossian, L. Reppel, N. Makdissy, J.-F. Stoltz, D. Bensoussan, and C. Huselstein. Mesenchymal stem cells derived from wharton's jelly: comparative phenotype analysis between tissue and in vitro expansion. *Bio-Medical Material Engineering*, 22:243–254, 2012.

[109] L. Aust, B. Devlin, S. Foster, Y. Halvorsen, K. Hicok, T. Du Laney, A. Sen, G. Willingmyre, and J. Gimble. Yield of human adipose-derived adult stem cells from liposuction aspirates. *Cytotherapy*, 6(1):7–14, 2004.

[110] K.-T. Guo, R. Schafer, A. Paul, A. Gerber, G. Ziemer, and H. P. Wendel. A new technique for the isolation and surface immobilization of mesenchymal stem cells from whole bone marrow using high-specific DNA aptamers. *Stem Cells*, 24:2220–2231, 2006.

[111] C. K. Tong, S. Vellasamy, B. Chong Tan, M. Abdullah, S. Vidyadaran, H. Fong Seow, and R. Ramasamy. Generation of mesenchymal stem cell from human umbilical cord tissue using a combination enzymatic and mechanical disassociation method. *Cell Biology International*, 35:221–226, 2011.

[112] M. Oedayrajsingh-Varma, S. Van Ham, M. Knippenberg, M. Helder, J. Klein-Nulend, T. Schouten, M. Ritt, and F. Van Milligen. Adipose tissue-derived mesenchymal stem cell yield and growth characteristics are affected by the tissue-harvesting procedure. *Cytotherapy*, 8(2):166–177, 2006.

[113] T. Gentry, S. Foster, L. Winstead, E. Deibert, M. Fiordalisi, and A. Balber. Simultaneous isolation of human BM hematopoietic, endothelial and mesenchymal progenitor cells by flow sorting based on aldehyde dehydrogenase activity: implications for cell therapy. *Cytotherapy*, 9:259–274, 2007.

[114] D. A. De Ugarte, K. Morizono, A. Elbarbary, Z. Alfonso, P. A. Zuk, M. Zhu, J. L. Dragoo, P. Ashjian, B. Thomas, P. Benhaim, I. Chen, J. Fraser, and M. H. Hedrick. Comparison of multi-lineage cells from human adipose tissue and bone marrow. *Cells Tissues Organs*, 174:101–109, 2003.

[115] H. J. Yang, K.-J. Kim, M. K. Kim, S. J. Lee, Y. H. Ryu, B. F. Seo, D.-Y. Oh, S.-T. Ahn, H. Y. Lee, and J. W. Rhie. The stem cell potential and multipotency of human adipose tissue-derived stem cells vary by cell donor and are different from those of other types of stem cells. *Cells Tissues Organs*, 199:373–383, 2014.

[116] V. Planat-Benard, C. Menard, M. Andre, M. Puceat, A. Perez, J.-M. Garcia-Verdugo, L. Penicaud, and L. Casteilla. Spontaneous cardiomyocyte differentiation from adipose tissue stroma cells. *Circulation research*, 94(2):223–229, 2004.

[117] B. Christ, M. Franquesa, M. Najimi, L. J. W. van der Laan, and M. H. Dahlke. Cellular and molecular mechanisms of mesenchymal stem cell actions. *Stem Cells International*, 2017:1–2, 2017.

[118] D. G. Phinney. Functional heterogeneity of mesenchymal stem cells: implications for cell therapy. *Journal of Cell Biochemistry*, 113:2806–2812, 2012.

[119] C. T. Vangsness, H. Sternberg, and L. Harris. Umbilical cord tissue offers the greatest number of harvestable mesenchymal stem cells for research and clinical application: a literature review of different harvest sites. *Arthroscopy*, 31:1836–1843, 2015.

[120] C. W. Group. Donation of starting material for cell-based advanced therapies: a SaBTO review. *Advisory Committee on the Safety of Blood, Tissues and Organs*, 2014:141, 2014.

[121] N. Baker, L. B. Boyette, and R. S. Tuan. Characterization of bone marrow-derived mesenchymal stem cells in aging. *Bone*, 70:37–47, 2015.

[122] J. D. Kretlow, Y.-Q. Jin, W. Liu, W. Zhang, T.-H. Hong, G. Zhou, L. S. Baggett, A. G. Mikos, and Y. Cao. Donor age and cell passage affects differentiation potential of murine bone marrow-derived stem cells. *BMC Cell Biology*, 9:60, 2008.

[123] A. Stolzing, E. Jones, D. McGonagle, and A. Scutt. Age-related changes in human bone marrow-derived mesenchymal stem cells: consequences for cell therapies. *Mechanisms of Ageing and Development*, 129:163–173, 2008.

[124] P. Meunier, J. Aaron, C. Edouard, and G. Vignon. Osteoporosis and the replacement of cell populations of the marrow by adipose tissue. a quantitative study of 84 iliac bone biopsies. *Clinical Orthopaedic Related Research*, 80:147–154, 1971.

[125] M. A. Baxter, R. F. Wynn, S. N. Jowitt, J. E. Wraith, L. J. Fairbairn, and I. Bellantuono. Study of telomere length reveals rapid aging of human marrow stromal cells following in vitro expansion. *Stem Cells*, 22:675–682, 2004.

[126] M. S. Choudhery, M. Badowski, A. Muise, J. Pierce, and D. T. Harris. Donor age negatively impacts adipose tissue-derived mesenchymal stem cell expansion and differentiation. *Journal Translational Medicine*, 12:8, 2014.

[127] M. Zaim, S. Karaman, G. Cetin, and S. Isik. Donor age and long-term culture affect differentiation and proliferation of human bone marrow mesenchymal stem cells. *Annual Hematology*, 91:1175–1186, 2012.

[128] L. Pierdomenico. Diabetes mellitus during pregnancy interferes with the biological characteristics of wharton's jelly mesenchymal stem cells. *Open Tissue Engineering Regenerative Medicine Journal*, 4:103–111, 2011.

[129] M. Tencerova, M. Frost, F. Figeac, T. K. Nielsen, D. Ali, J.-J. L. Lauterlein, T. L. Andersen, A. K. Haakonsson, A. Rauch, J. S. Madsen, C. Ejersted, K. Højlund, and M. Kassem. Obesity-associated hypermetabolism and accelerated senescence of bone marrow stromal stem cells suggest a potential mechanism for bone fragility. *Cell Reports*, 27(7):2050–2062, 2019.

[130] S. R. A. Chen and S. Oh. Application of human mesenchymal and pluripotent stem cell microcarrier cultures in cellular therapy: achievements and future direction. *Biotechnol Adv*, 31:1032–1046, 2013.

[131] N. Fekete, M. T. Rojewski, D. Fürst, L. Kreja, A. Ignatius, J. Dausend, and H. Schrezenmeier. GMP-compliant isolation and large-scale expansion of bone marrow-derived MSC. *PLoS One*, 7:e43255, 2012.

[132] R. J. Thomas, A. Chandra, Y. Liu, P. C. Hourd, P. P. Conway, and D. J. Williams. Manufacture of a human mesenchymal stem cell population using an automated cell culture platform. *Cytotechnology*, 55:31–39, 2007.

[133] P. J. Hanley, Z. Mei, A. G. Durett, M. d. G. Cabreira-Harrison, M. Klis, W. Li, Y. Zhao, B. Yang, K. Parsha, O. Mir, F. Vahidy, D. Bloom, R. B. Rice, P. Hematti, S. I. Savitz, and A. P. Gee. Efficient manufacturing of therapeutic mesenchymal stromal cells using the quantum cell expansion system. *Cytotherapy*, 16:1048–1058, 2014.

[134] C. Zanini, F. Severina, G. Lando, C. Fanizza, E. Cesana, D. Desidera, and M. Bonifacio. Good design practices for an integrated containment and production system for advanced therapies. *Biotechnology Bioengineering*, 117:2319–2330, 2020.

[135] E. J. Caterson, L. J. Nesti, K. G. Danielson, and R. S. Tuan. Human marrow-derived mesenchymal progenitor cells. *Molecular Biotechnology*, 20:245–256, 2002.

[136] K. Schallmoser, C. Bartmann, E. Rohde, A. Reinisch, K. Kashofer, E. Stadelmeyer, C. Drexler, G. Lanzer, W. Linkesch, and D. Strunk. Human platelet lysate can replace fetal bovine serum for clinical-scale expansion of functional mesenchymal stromal cells. *Transfusion*, 47:1436–1446, 2007.

[137] S. A. Kuznetsov, M. H. Mankani, and P. G. Robey. Effect of serum on human bone marrow stromal cells: ex vivo expansion and in vivo bone formation. *Transplantation*, 70:1780–1787, 2000.

[138] H. Abdelrazik, G. M. Spaggiari, L. Chiossone, and L. Moretta. Mesenchymal stem cells expanded in human platelet lysate display a decreased inhibitory capacity on T- and NK-cell proliferation and function. *European Journal of Immunology*, 41:3281–3290, 2011.

[139] M. E. Bernardo. *Human mesenchymal stromal cells: biological characterization and clinical application*. PhD thesis, Leiden University, 2010.

[140] A. Nasef, N. Mathieu, A. Chapel, J. Frick, S. Francois, C. Mazurier, A. Boutarfa, S. Bouchet, N.-C. Gorin, D. Thierry, and L. Fouillard. Immunosuppressive effects of mesenchymal stem cells: involvement of HLA-G. *Transplantation*, 84:231–237, 2007.

[141] W. Wagner, S. Bork, G. Lepperdinger, S. Joussen, N. Ma, D. Strunk, and C. Koch. How to track cellular aging of mesenchymal stromal cells? *Aging*, 2:224–230, 2010.

[142] W. Wagner, S. Bork, P. Horn, D. Krunic, T. Walenda, A. Diehlmann, V. Benes, J. Blake, F.-X. Huber, V. Eckstein, P. Boukamp, and A. D. Ho. Aging and replicative senescence have related effects on human stem and progenitor cells. *PLoS One*, 4:5846, 2009.

[143] W. J. C. Rombouts and R. E. Ploemacher. Primary murine MSC show highly efficient homing to the bone marrow but lose homing ability following culture. *Leukemia*, 17:160–170, 2003.

[144] K. Schallmoser, C. Bartmann, E. Rohde, S. Bork, C. Guelly, A. C. Obenauf, A. Reinisch, P. Horn, A. D. Ho, D. Strunk, and W. Wagner. Replicative senescence-associated gene expression changes in mesenchymal stromal cells are similar under different culture conditions. *Haematologica*, 95:867–874, 2010.

[145] P. Charbord, E. Livne, G. Gross, T. Häupl, N. M. Neves, P. Marie, P. Bianco, and C. Jorgensen. Human bone marrow mesenchymal stem cells: a systematic reappraisal via the genostem experience. *Stem Cell Review*, 7:32–42, 2011.

[146] M. M. Bonab, K. Alimoghaddam, F. Talebian, S. H. Ghaffari, A. Ghavamzadeh, and B. Nikbin. Aging of mesenchymal stem cell in vitro. *BMC Cell Biology*, 7:14, 2006.

[147] A. Noer, A. C. Boquest, and P. Collas. Dynamics of adipogenic promoter DNA methylation during clonal culture of human adipose stem cells to senescence. *BMC Cell Biology*, 8:18, 2007.

[148] J. Kim, J. W. Kang, J. H. Park, Y. Choi, K. S. Choi, K. D. Park, D. H. Baek, S. K. Seong, H.-K. Min, and H. S. Kim. Biological characterization of long-term cultured human mesenchymal stem cells. *Archive Pharmaceutical Research*, 32:117–126, 2009.

[149] W. Wagner, P. Horn, M. Castoldi, A. Diehlmann, S. Bork, R. Saffrich, V. Benes, J. Blake, S. Pfister, V. Eckstein, and A. D. Ho. Replicative senescence of mesenchymal stem cells: a continuous and organized process. *PLoS One*,

3:2213, 2008.

[150] A. Banfi, A. Muraglia, B. Dozin, M. Mastrogiacomo, R. Cancedda, and R. Quarto. Proliferation kinetics and differentiation potential of ex vivo expanded human bone marrow stromal cells: implications for their use in cell therapy. *Experimental Hematology*, 28:707–715, 2000.

[151] B. L. Larson, J. Ylöstalo, and D. J. Prockop. Human multipotent stromal cells undergo sharp transition from division to development in culture. *Stem Cells*, 26:193–201, 2008.

[152] D. C. Chow, L. A. Wenning, W. M. Miller, and E. T. Papoutsakis. Modeling pO2 distributions in the bone marrow hematopoietic compartment. II. modified kroghian models. *Biophysical journal*, 81:685–696, 2001.

[153] C. Fehrer, R. Brunauer, G. Laschober, H. Unterluggauer, S. Reitinger, F. Kloss, C. Gülly, R. Gaßner, and G. Lepperdinger. Reduced oxygen tension attenuates differentiation capacity of human mesenchymal stem cells and prolongs their lifespan. *Aging Cell*, 6:745–757, 2007.

[154] S.-P. Hung, J. H. Ho, Y.-R. V. Shih, T. Lo, and O. K. Lee. Hypoxia promotes proliferation and osteogenic differentiation potentials of human mesenchymal stem cells. *Journal Orthopaed Research*, 30:260–266, 2012.

[155] J. C. Estrada, C. Albo, A. Benguria, A. Dopazo, P. Lopez-Romero, L. Carrera-Quintanar, E. Roche, E. P. Clemente, J. A. Enriquez, A. Bernad, and E. Samper. Culture of human mesenchymal stem cells at low oxygen tension improves growth and genetic stability by activating glycolysis. *Cell Death Differentiation*, 19:743–755, 2012.

[156] S. Zhou, S. Lechpammer, J. S. Greenberger, and J. Glowacki. Hypoxia inhibition of adipocytogenesis in human bone marrow stromal cells requires transforming growth factor-β/Smad3 signaling. *Journal of Biology and Chemistry*, 280:22688–22696, 2005.

[157] T.-S. Li and E. Marbán. Physiological levels of reactive oxygen species are required to maintain genomic stability in stem cells. *Stem Cells*, 28:1178–1185, 2010.

[158] M. Csete. Oxygen in the cultivation of stem cells. *Annual New York Acadademy of Science*, 1049:1–8, 2005.

[159] J. A. Rowley. Peak MSC—are we there yet? *Frontiers Medicine*, 5:14, 2018.

[160] O.-W. Merten. Advances in cell culture: anchorage dependence. *Philosophical Transactions of the Royal Society Biological Sciences*, 370(1661):20140040, 2015.

[161] P. Godara, C. D. McFarland, and R. E. Nordon. Design of bioreactors for mesenchymal stem cell tissue engineering. *Journal of Chemical Technology & Biotechnology: International Research in Process, Environmental & Clean Technology*, 83(4):408–420, 2008.

[162] A. Hoch and J. Leach. Concise review: optimizing expansion of bone marrow mesenchymal stem/stromal cells for clinical applications. *Stem Cell Translational Medicine*, 3:643–652, 2014.

[163] W. R. Prather, A. Toren, M. Meiron, R. Ofir, C. Tschope, and E. M. Horwitz. The role of placental-derived adherent stromal cell (PLX-PAD) in the treatment of critical limb ischemia. *Cytotherapy*, 11(4):427–434, 2009.

[164] T. A. Wyrobnik, A. Ducci, and M. Micheletti. Advances in human mesenchymal stromal cell-based therapies – Towards an integrated biological and engineering approach. *Stem Cell Research*, 47:101888, 2020.

[165] S. Kern, H. Eichler, J. Stoeve, H. Kluter, and K. Bieback. Comparative analysis of mesenchymal stem cells from bone marrow, umbilical cord blood, or adipose tissue. *Stem Cells*, 24:1294–1301, 2006.

[166] H.-S. Wang, S.-C. Hung, S.-T. Peng, C.-C. Huang, H.-M. Wei, Y.-J. Guo, Y.-S. Fu, M.-C. Lai, and C.-C. Chen. Mesenchymal stem cells in the wharton's jelly of the human umbilical cord. *Stem Cells*, 22:1330–1337, 2004.

[167] P. A. Zuk, M. Zhu, P. Ashjian, D. A. De Ugarte, J. I. Huang, H. Mizuno, Z. C. Alfonso, J. K. Fraser, P. Benhaim, and M. H. Hedrick. Human adipose tissue is a source of multipotent stem cells. *Molecular biology of the cell*, 13(12):4279–4295, 2002.

[168] K. Bieback, S. Kern, H. Klüter, and H. Eichler. Critical parameters for the isolation of mesenchymal stem cells from umbilical cord blood. *Stem Cells*, 22:625–634, 2004.

[169] S. Gronthos, A. C. Zannettino, S. J. Hay, S. Shi, S. E. Graves, A. Kortesidis, and P. J. Simmons. Molecular and cellular characterisation of highly purified stromal stem cells derived from human bone marrow. *Journal of cell science*, 116(9):1827–1835, 2003.

[170] P. A. Zuk, M. Zhu, H. Mizuno, J. Huang, J. W. Futrell, A. J. Katz, P. Benhaim, H. P. Lorenz, and M. H. Hedrick. Multilineage cclls from human adipose tissue: implications for cell-based therapies. *Tissue Engineering*, 7:211–228, 2001.

[171] D. G. Phinney, G. Kopen, W. Righter, S. Webster, N. Tremain, and D. J. Prockop. Donor variation in the growth properties and osteogenic potential of human marrow stromal cells. *Journal Cell Biochemistry*, 75:424–436, 1999.

[172] H. Dimitriou, E. Linardakis, G. Martimianaki, E. Stiakaki, C. H. Perdikogianni, P. Charbord, and M. Kalmanti. Properties and potential of bone marrow mesenchymal stromal cells from children with hematologic diseases. *Cytotherapy*, 10:125–133, 2008.

[173] Rauscher Frederick M., Goldschmidt-Clermont Pascal J., Davis Bryce H., Wang Tao, Gregg David, Ramaswami Priya, Pippen Anne M., Annex Brian H., Dong Chunming, and Taylor Doris A. Aging, progenitor cell exhaustion, and atherosclerosis. *Circulation*, 108:457–463, 2003.

[174] M. R. Dressler, D. L. Butler, and G. P. Boivin. Effects of age on the repair ability of mesenchymal stem cells in rabbit tendon. *Journal Orthopaedic Research*, 23:287–293, 2005.

[175] F. Bruna, D. Contador, P. Conget, B. Erranz, C. L. Sossa, and M. L. Arango-Rodriguez. Regenerative potential of mesenchymal stromal cells: age-related changes. *Stem Cells International*, 2016:15, 2016.

[176] S. Golpanian, J. El-Khorazaty, A. Mendizabal, D. L. DiFede, V. Suncion, V. Karantalis, J. E. Fishman, E. Ghersin, W. Balkan, and J. M. Hare. Effect of aging on human mesenchymal stem cell therapy in ischemic cardiomyopathy patients. *Journal American Colledge Cardiology*, 65:125–132, 2015.

[177] K. Stenderup, J. Justesen, E. F. Eriksen, S. I. S. Rattan, and M. Kassem. Number and proliferative capacity of osteogenic stem cells are maintained during aging and in patients with osteoporosis. *Journal Bone Mineral Research*, 16:1120–1129, 2001.

[178] C. Wan, Q. He, M. McCaigue, D. Marsh, and G. Li. Nonadherent cell population of human marrow culture is a complementary source of mesenchymal stem cells (MSCs). *Journal Orthopaedic Research*, 24:21–28, 2006.

[179] P. A. Sotiropoulou, S. A. Perez, M. Salagianni, C. N. Baxevanis, and M. Papamichail. Characterization of the optimal culture conditions for clinical scale production of human mesenchymal stem cells. *Stem Cells*, 24:462–471, 2006.

[180] I. Pountos, D. Corscadden, P. Emery, and P. V. Giannoudis. Mesenchymal stem cell tissue engineering: techniques for isolation, expansion and application. *Injury*, 38:S23–S33, 2007.

[181] P. Simmons and B. Torok-Storb. Identification of stromal cell precursors in human bone marrow by a novel monoclonal antibody, stro-1. *Blood*, 78:55–62, 1991.

[182] N. Kotobuki, M. Hirose, Y. Takakura, and H. Ohgushi. Cultured autologous human cells for hard tissue regeneration: preparation and characterization of mesenchymal stem cells from bone marrow. *Artificial Organs*, 28:33–39, 2004.

[183] M. François, I. B. Copland, S. Yuan, R. Romieu-Mourez, E. K. Waller, and J. Galipeau. Cryopreserved mesenchymal stromal cells display impaired immunosuppressive properties as a result of heat-shock response and impaired interferon-γ licensing. *Cytotherapy*, 14:147–152, 2012.

[184] P. A. Sotiropoulou, S. A. Perez, A. D. Gritzapis, C. N. Baxevanis, and M. Papamichail. Interactions between human mesenchymal stem cells and natural killer cells. *Stem Cells*, 24:74–85, 2006.

[185] M. F. Pera, B. Reubinoff, and A. Trounson. Human embryonic stem cells. *Journal Cell Science*, 113:5–10, 2000.

[186] C. Lange, F. Cakiroglu, A.-N. Spiess, H. Cappallo-Obermann, J. Dierlamm, and A. R. Zander. Accelerated and safe expansion of human mesenchymal stromal cells in animal serum-free medium for transplantation and regenerative medicine. *Journal of cellular physiology*, 213:18–26, 2007.

[187] C. M. Kong, H. D. Lin, A. Biswas, A. Bongso, and C.-Y. Fong. Manufacturing of human wharton's jelly stem cells for clinical use: selection of serum is important. *Cytotherapy*, 21(4):483–495, 2019.

[188] C. Doucet, I. Ernou, Y. Zhang, J.-R. Llense, L. Begot, X. Holy, and J.-J. Lataillade. Platelet lysates promote mesenchymal stem cell expansion: a safety substitute for animal serum in cell-based therapy applications. *Journal of Cellular Physiology*, 205:228–236, 2005.

[189] D. C. Colter, R. Class, C. M. DiGirolamo, and D. J. Prockop. Rapid expansion of recycling stem cells in cultures of plastic-adherent cells from human bone marrow. *Proceedings of the National Academy of Sciences*, 97(7):3213–3218, 2000.

[190] I. Sekiya, B. L. Larson, J. R. Smith, R. Pochampally, J.-G. Cui, and D. J. Prockop. Expansion of human adult stem cells from bone marrow stroma: conditions that maximize the yields of early progenitors and evaluate their quality. *Stem Cells*, 20:530–541, 2002.

[191] T. Fink, L. Abildtrup, K. Fogd, B. M. Abdallah, M. Kassem, P. Ebbesen, and V. Zachar. Induction of adipocyte-like phenotype in human mesenchymal stem cells by hypoxia. *Stem Cells*, 22:1346–1355, 2004.

[192] P. A. Conget and J. J. Minguell. Phenotypical and functional properties of human bone marrow mesenchymal progenitor cells. *Journal of cellular physiology*, 181(1):67–73, 1999.

[193] S. Bork, S. Pfister, H. Witt, P. Horn, B. Korn, A. D. Ho, and W. Wagner. DNA methylation pattern changes upon long-term culture and aging of human mesenchymal stromal cells. *Aging Cell*, 9:54–63, 2010.

[194] I. M. Bjørge, C. R. Correia, and J. F. Mano. Hipster microcarriers: exploring geometrical and topographical cues of non-spherical microcarriers in biomedical applications. *Materials Horizons*, 9(3):908–933, 2022.

[195] C. McKee and R. Chaudhry. Advances and challenges in stem cell culture. *Colloids and Surfaces*, 159:62–77, 2017.

[196] O. Yang, S. Prabhu, and M. Ierapetritou. Comparison between batch and continuous monoclonal antibody production and economic analysis. *Industrial & Engineering Chemistry Research*, 58(15):5851–5863, 2019.

[197] F. M. Wurm. Production of recombinant protein therapeutics in cultivated mammalian cells. *Nature biotechnology*, 22(11):1393–1398, 2004.

[198] S. S. Farid. Process economics of industrial monoclonal antibody manufacture. *Journal of Chromatography Biology*, 848(1):8–18, 2007.

[199] B. Kelley. Very large scale monoclonal antibody purification: the case for conventional unit operations. *Biotechnology progress*, 23(5):995–1008, 2007.

[200] I. Jyothilekshmi and N. Jayaprakash. Trends in monoclonal antibody production using various bioreactor systems. 2021.

[201] S. Palombella, C. Perucca Orfei, G. Castellini, S. Gianola, S. Lopa, M. Mastrogiacomo, M. Moretti, and L. de Girolamo. Systematic review and meta-analysis on the use of human platelet lysate for mesenchymal stem cell cultures: comparison with fetal bovine serum and considerations on the production protocol. *Stem cell research & therapy*, 13(1):1–31, 2022.

[202] F. Dos Santos, P. Z. Andrade, J. S. Boura, M. M. Abecasis, C. L. Da Silva, and J. M. Cabral. Ex vivo expansion of human mesenchymal stem cells: a more effective cell proliferation kinetics and metabolism under hypoxia. *Journal of cellular physiology*, 223(1):27–35, 2010.

[203] J. M. Ryu, M. Y. Lee, S. P. Yun, and H. J. Han. High glucose regulates cyclin d1/e of human mesenchymal stem cells through tgf-β1 expression via ca2+/pkc/mapks and pi3k/akt/mtor signal pathways. *Journal of cellular physiology*, 224(1):59–70, 2010.

[204] T. Lo, J. H. Ho, M.-H. Yang, and O. K. Lee. Glucose reduction prevents replicative senescence and increases mitochondrial respiration in human mesenchymal stem cells. *Cell transplantation*, 20(6):813–826, 2011.

[205] G. Pattappa, H. K. Heywood, J. D. De Bruijn, and D. A. Lee. The metabolism of human mesenchymal stem cells during proliferation and differentiation. *Journal of cellular physiology*, 226(10):2562–2570, 2011.

[206] D. Schop, F. W. Janssen, L. D. van Rijn, H. Fernandes, R. M. Bloem, J. D. de Bruijn, and R. van Dijkhuizen-Radersma. Growth, metabolism, and growth inhibitors of mesenchymal stem cells. *Tissue Engineering*, 15:1877–1886, 2009.

[207] P.-O. Carlsson, E. Schwarcz, O. Korsgren, and K. Le Blanc. Preserved β-cell function in type 1 diabetes by mesenchymal stromal cells. *Diabetes*, 64:587–592, 2015.

[208] J. G. Carmelo, A. Fernandes-Platzgummer, M. M. Diogo, C. L. da Silva, and J. M. Cabral. A xeno-free microcarrier-based stirred culture system for the scalable expansion of human mesenchymal stem/stromal cells isolated from bone marrow and adipose tissue. *Biotechnology journal*, 10(8):1235–1247, 2015.

[209] S. Y. Lunt and M. G. Vander Heiden. Aerobic glycolysis: meeting the metabolic requirements of cell proliferation. *Annual Reviews*, 2011.

[210] C.-T. Chen, Y.-R. V. Shih, T. K. Kuo, O. K. Lee, and Y.-H. Wei. Coordinated changes of mitochondrial biogenesis and antioxidant enzymes during osteogenic differentiation of human mesenchymal stem cells. *Stem cells*, 26(4):960–968, 2008.

[211] H. Li, H. Dai, and J. Li. Immunomodulatory properties of mesenchymal stromal/stem cells: the link with metabolism. *Journal of Advanced Research*, 2022.

[212] M. G. Vander Heiden, L. C. Cantley, and C. B. Thompson. Understanding the warburg effect: the metabolic requirements of cell proliferation. *Science*, 324(5930):1029–1033, 2009.

[213] G. Tritsch and G. Moore. Spontaneous decomposition of glutamine in cell culture media. *Experimental cell research*, 28(2):360–364, 1962.

[214] Y. Yu, H. Newman, L. Shen, D. Sharma, G. Hu, A. J. Mirando, H. Zhang, E. Knudsen, G.-F. Zhang, M. J. Hilton, et al. Glutamine metabolism regulates proliferation and lineage allocation in skeletal stem cells. *Cell metabolism*, 29(4):966–978, 2019.

[215] G. G. Dos Santos, A. A. Hastreiter, T. Sartori, P. Borelli, and R. A. Fock. L-glutamine in vitro modulates some immunomodulatory properties of bone marrow mesenchymal stem cells. *Stem Cell Reviews and Reports*, 13(4):482–490, 2017.

[216] X. Chen, A. Chen, T. L. Woo, A. B. Choo, S. Reuveny, and S. K. Oh. Investigations into the metabolism of two-dimensional colony and suspended microcarrier cultures of human embryonic stem cells in serum-free media. *Stem Cells and Development*, 19(11):1781–1792, 2010.

[217] K. G. Chen, B. S. Mallon, R. D. McKay, and P. G. Robey. Human pluripotent stem cell culture: considerations for maintenance, expansion, and therapeutics. *Cell stem cell*, 14(1):13–26, 2014.

[218] M. M. Hunt, G. Meng, D. E. Rancourt, I. D. Gates, and M. S. Kallos. Factorial experimental design for the culture of human embryonic stem cells as aggregates in stirred suspension bioreactors reveals the potential for interaction effects between bioprocess parameters. *Tissue Engineering Part C: Methods*, 20(1):76–89, 2014.

[219] J. Hupfeld, I. H. Gorr, C. Schwald, N. Beaucamp, K. Wiechmann, K. Kuentzer, R. Huss, B. Rieger, M. Neubauer, and H. Wegmeyer. Modulation of mesenchymal stromal cell characteristics by microcarrier culture in bioreactors. *Biotechnology and Bioengineering*, 111(11):2290–2302, 2014.

[220] A. Mizukami, A. Fernandes-Platzgummer, J. G. Carmelo, K. Swiech, D. T. Covas, J. M. S. Cabral, and C. L. d. Silva. Stirred tank bioreactor culture combined with serum-/xenogeneic-free culture medium enables an efficient expansion of umbilical cord-derived mesenchymal stem/stromal cells. *Biotechnology Journal*, 11(8):1048–1059, 2016.

[221] D. de Sousa Pinto, C. Bandeiras, M. de Almeida Fuzeta, C. A. Rodrigues, S. Jung, Y. Hashimura, R.-J. Tseng, W. Milligan, B. Lee, F. C. Ferreira, et al. Scalable manufacturing of human mesenchymal stromal cells in the vertical-wheel bioreactor system: an experimental and economic approach. *Biotechnology journal*, 14(8):1800716, 2019.

[222] G. Eibes, F. dos Santos, P. Z. Andrade, J. S. Boura, M. M. Abecasis, C. L. da Silva, and J. M. Cabral. Maximizing the ex vivo expansion of human mesenchymal stem cells using a microcarrier-based stirred culture system. *Journal*

of biotechnology, 146(4):194–197, 2010.

[223] F. Dos Santos, A. Campbell, A. Fernandes-Platzgummer, P. Z. Andrade, J. M. Gimble, Y. Wen, S. Boucher, M. C. Vemuri, C. L. da Silva, and J. M. Cabral. A xenogeneic-free bioreactor system for the clinical-scale expansion of human mesenchymal stem/stromal cells. *Biotechnology and bioengineering*, 111(6):1116–1127, 2014.

[224] T. R. Heathman, A. Stolzing, C. Fabian, Q. A. Rafiq, K. Coopman, A. W. Nienow, B. Kara, and C. J. Hewitt. Scalability and process transfer of mesenchymal stromal cell production from monolayer to microcarrier culture using human platelet lysate. *Cytotherapy*, 18(4):523–535, 2016.

[225] T. R. Heathman, A. Stolzing, C. Fabian, Q. A. Rafiq, K. Coopman, A. W. Nienow, B. Kara, and C. J. Hewitt. Serum-free process development: improving the yield and consistency of human mesenchymal stromal cell production. *Cytotherapy*, 17(11):1524–1535, 2015.

[226] M. Hervy, J. L. Weber, M. Pecheul, P. Dolley-Sonneville, D. Henry, Y. Zhou, and Z. Melkoumian. Long term expansion of bone marrow-derived hmscs on novel synthetic microcarriers in xeno-free, defined conditions. *PLoS One*, 9(3):e92120, 2014.

[227] S. Kaiser, V. Jossen, C. Schirmaier, D. Eibl, S. Brill, C. van den Bos, and R. Eibl. Fluid flow and cell proliferation of mesenchymal adipose-derived stem cells in small-scale, stirred, single-use bioreactors. *Chemie Ingenieur Technik*, 85(1-2):95–102, 2013.

[228] A. T.-L. Lam, J. Li, J. P.-W. Toh, E. J.-H. Sim, A. K.-L. Chen, J. K.-Y. Chan, M. Choolani, S. Reuveny, W. R. Birch, and S. K.-W. Oh. Biodegradable poly-ε-caprolactone microcarriers for efficient production of human mesenchymal stromal cells and secreted cytokines in batch and fed-batch bioreactors. *Cytotherapy*, 19(3):419–432, 2017.

[229] K. C. A. Nienow, Q. Rafiq and C.-J. Hewitt. A potentially scalable method for the harvesting of hmscs from microcarriers. *Biochemical Engineering Journal*, 85:79–88, 2014.

[230] Q. Rafiq. *Developing a standardised manufacturing process for the clinical-scale production of human mesenchymal stem cells*. thesis, Loughborough University, 2013.

[231] F. d. Santos, P. Z. Andrade, M. M. Abecasis, J. M. Gimble, L. G. Chase, A. M. Campbell, S. Boucher, M. C. Vemuri, C. L. d. Silva, and J. M. Cabral. Toward a clinical-grade expansion of mesenchymal stem cells from human sources: a microcarrier-based culture system under xeno-free conditions. *Tissue Engineering Part C: Methods*, 17(12):1201–1210, 2011.

[232] J. Lembong, R. Kirian, J. D. Takacs, T. R. Olsen, L. T. Lock, J. A. Rowley, and T. Ahsan. Bioreactor parameters for microcarrier-based human msc expansion under xeno-free conditions in a vertical-wheel system. *Bioengineering*, 7(3):73, 2020.

[233] J. Leber, J. Barekzai, M. Blumenstock, B. Pospisil, D. Salzig, and P. Czermak. Microcarrier choice and bead-to-bead transfer for human mesenchymal stem cells in serum-containing and chemically defined media. *Process Biochemistry*, 59:255–265, 2017.

[234] G. Catapano, P. Czermak, R. Eibl, D. Eibl, and R. Pörtner. Bioreactor design and scale-up. In *Cell and tissue reaction engineering*, pages 173–259. Springer, 2009.

[235] M. A. MacDonald, M. Nöbel, D. Roche Recinos, V. S. Martínez, B. L. Schulz, C. B. Howard, K. Baker, E. Shave, Y. Y. Lee, E. Marcellin, et al. Perfusion culture of chinese hamster ovary cells for bioprocessing applications. *Critical Reviews in Biotechnology*, pages 1–17, 2021.

[236] B. Cunha, T. Aguiar, M. M. Silva, R. J. Silva, M. F. Sousa, E. Pineda, C. Peixoto, M. J. Carrondo, M. Serra, and P. M. Alves. Exploring continuous and integrated strategies for the up-and downstream processing of human mesenchymal stem cells. *Journal of biotechnology*, 213:97–108, 2015.

[237] C. Sion, D. Ghannoum, B. Ebel, F. Gallo, N. de Isla, E. Guedon, I. Chevalot, and E. Olmos. A new perfusion mode of culture for wj-mscs expansion in a stirred and online monitored bioreactor. *Biotechnology and Bioengineering*, 118(11):4453–4464, 2021.

[238] T. Mitaka. Reconstruction of hepatic organoid by hepatic stem cells. *Journal of hepato-biliary-pancreatic surgery*, 9(6):697–703, 2002.

[239] D. Grimm, M. Egli, M. Krüger, S. Riwaldt, T. J. Corydon, S. Kopp, M. Wehland, P. Wise, M. Infanger, V. Mann, et al. Tissue engineering under microgravity conditions–use of stem cells and specialized cells. *Stem Cells and Development*, 27(12):787–804, 2018.

[240] S. Li, Z. Ma, Z. Niu, H. Qian, D. Xuan, R. Hou, and L. Ni. Nasa-approved rotary bioreactor enhances proliferation and osteogenesis of human periodontal ligament stem cells. *Stem Cells and Development*, 18(9):1273–1282, 2009.

[241] J. d. S. da Silva, A. Mizukami, L. V. G. Gil, J. V. de Campos, O. B. Assis, D. T. Covas, K. Swiech, and C. A. T. Suazo. Improving wave-induced motion bioreactor performance for human mesenchymal stromal cell expansion. *Process Biochemistry*, 84:143–152, 2019.

[242] B. David, D. Bonnefont-Rousselot, K. Oudina, M.-C. Degat, M. Deschepper, V. Viateau, M. Bensidhoum, C. Oddou, and H. Petite. A perfusion bioreactor for engineering bone constructs: an in vitro and in vivo study. *Tissue Engineering Part C: Methods*, 17(5):505–516, 2011.

[243] M. N. F. B. Hassan, M. D. Yazid, M. H. M. Yunus, S. R. Chowdhury, Y. Lokanathan, R. B. H. Idrus, A. M. H. Ng, and J. X. Law. Large-scale expansion of human mesenchymal stem cells. *Stem Cells International*, 2020.

[244] C. Lobato da Silva, R. Goncalves, F. Lemos, M. Lemos, E. Zanjani, G. Almeida-Porada, and J. Cabral. Modelling of ex vivo expansion/maintenance of hematopoietic stem cells. *Bioprocess and Biosystems Engineering*, 25(6):365–369, 2003.

[245] D. C. Kirouac, G. J. Madlambayan, M. Yu, E. A. Sykes, C. Ito, and P. W. Zandstra. Cell–cell interaction networks regulate blood stem and progenitor cell fate. *Molecular systems biology*, 5(1):293, 2009.

[246] D. Cadena-Herrera, J. E. Esparza-De Lara, N. D. Ramírez-Ibañez, C. A. López-Morales, N. O. Pérez, L. F. Flores-Ortiz, and E. Medina-Rivero. Validation of three viable-cell counting methods: Manual, semi-automated, and automated. *Biotechnology Reports*, 7:9–16, 2015.

[247] C. Loubière, C. Sion, N. De Isla, L. Reppel, E. Guedon, I. Chevalot, and E. Olmos. Impact of the type of microcarrier and agitation modes on the expansion performances of mesenchymal stem cells derived from umbilical cord. *Biotechnology Progress*, 35(6):e2887, 2019.

[248] C. Schirmaier, V. Jossen, S. C. Kaiser, F. Jüngerkes, S. Brill, A. Safavi-Nab, A. Siehoff, C. van den Bos, D. Eibl, and R. Eibl. Scale-up of adipose tissue-derived mesenchymal stem cell production in stirred single-use bioreactors under low-serum conditions. *Engineering in Life Sciences*, 14(3):292–303, 2014.

[249] A.-C. Tsai and T. Ma. Expansion of human mesenchymal stem cells in a microcarrier bioreactor. In *Bioreactors in Stem Cell Biology*, pages 77–86. Springer, 2016.

[250] C. Justice, A. Brix, D. Freimark, M. Kraume, P. Pfromm, B. Eichenmueller, and P. Czermak. Process control in cell culture technology using dielectric spectroscopy. *Biotechnology advances*, 29(4):391–401, 2011.

[251] S. Rourou, S. Gaumon, and H. Kallel. On-line monitoring of vero cells cultures during the growth and rabies virus process using biomass spectrometer. In *Cells and Culture*, pages 829–832. Springer, 2010.

[252] A. Ron, N. Fishelson, N. Croitoriu, D. Benayahu, and Y. Shacham-Diamand. Theoretical examination of aggregation effect on the dielectric characteristics of spherical cellular suspension. *Biophysical chemistry*, 140(1-3):39–50, 2009.

[253] I. A. Isidro, P. Vicente, D. A. Pais, J. I. Almeida, M. Domingues, B. Abecasis, N. Zapata-Linares, J. R. Rodriguez-Madoz, F. Prosper, A. Aspegren, et al. Online monitoring of hipsc expansion and hepatic differentiation in 3d culture by dielectric spectroscopy. *Biotechnology and Bioengineering*, 118(9):3610–3617, 2021.

[254] P. O'Mara, A. Farrell, J. Bones, and K. Twomey. Staying alive! sensors used for monitoring cell health in bioreactors. *Talanta*, 176:130–139, 2018.

[255] J. C. Yee, M. S. Rehmann, G. Yao, S. W. Sowa, K. L. Aron, J. Tian, M. C. Borys, and Z. J. Li. Advances in process control strategies for mammalian fed-batch cultures. *Current opinion in chemical engineering*, 22:34–41, 2018.

[256] K. F. Reardon. Practical monitoring technologies for cells and substrates in biomanufacturing. *Current Opinion in Biotechnology*, 71:225–230, 2021.

[257] F. Ravera, E. Efeoglu, and H. J. Byrne. Vibrational spectroscopy for in vitro monitoring stem cell differentiation. *Molecules*, 25(23):5554, 2020.

[258] A.-C. Tsai, R. Jeske, X. Chen, X. Yuan, and Y. Li. Influence of microenvironment on mesenchymal stem cell therapeutic potency: from planar culture to microcarriers. *Frontiers in Bioengineering and Biotechnology*, 8:640, 2020.

[259] C. Sion, C. Loubière, M. Wlodarczyk-Biegun, N. Davoudi, C. Müller-Renno, E. Guedon, I. Chevalot, and E. Olmos. Effects of microcarriers addition and mixing on wj-msc culture in bioreactors. *Biochemical Engineering Journal*, 157:107521, 2020.

[260] F. G. Teixeira, K. M. Panchalingam, S. I. Anjo, B. Manadas, R. Pereira, N. Sousa, A. J. Salgado, and L. A. Behie. Do hypoxia/normoxia culturing conditions change the neuroregulatory profile of wharton jelly mesenchymal stem cell secretome? *Stem Cell Research & Therapy*, 6(1):133.

[261] R. A. Haraszti, R. Miller, M. Stoppato, Y. Y. Sere, A. Coles, M.-C. Didiot, R. Wollacott, E. Sapp, M. L. Dubuke, X. Li, S. A. Shaffer, M. DiFiglia, Y. Wang, N. Aronin, and A. Khvorova. Exosomes produced from 3d cultures of MSCs by tangential flow filtration show higher yield and improved activity. *Molecular Therapy*, 26(12):2838–2847, 2018.

[262] C. Xu, J. Zhao, Q. Li, L. Hou, Y. Wang, S. Li, F. Jiang, Z. Zhu, and L. Tian. Exosomes derived from three-dimensional cultured human umbilical cord mesenchymal stem cells ameliorate pulmonary fibrosis in a mouse silicosis model. *Stem Cell Research & Therapy*, 11.

[263] F. Petry, J. R. Smith, J. Leber, D. Salzig, P. Czermak, and M. L. Weiss. Manufacturing of human umbilical cord mesenchymal stromal cells on microcarriers in a dynamic system for clinical use. *Stem Cells International*, 2016.

[264] A. M. d. Soure, A. Fernandes-Platzgummer, F. Moreira, C. Lilaia, S.-H. Liu, C.-P. Ku, Y.-F. Huang, W. Milligan, J. M. S. Cabral, and C. L. d. Silva. Integrated culture platform based on a human platelet lysate supplement for the isolation and scalable manufacturing of umbilical cord matrix-derived mesenchymal stem/stromal cells. *Journal of Tissue Engineering and Regenerative Medicine*, 11(5):1630–1640, 2017.

[265] C. Li, Y. Qian, S. Zhao, Y. Yin, and J. Li. Alginate/PEG based microcarriers with cleavable crosslinkage for expansion and non-invasive harvest of human umbilical cord blood mesenchymal stem cells. *Materials Science and Engineering: C*, 64:43–53, 2016.

[266] H. Kurogi, A. Takahashi, M. Isogai, M. Sakumoto, T. Takijiri, A. Hori, T. Furuno, T. Koike, T. Yamada, T. Nagamura-Inoue, and M. Sakaki-Yumoto. Umbilical cord derived mesenchymal stromal cells in microcarrier based industrial scale culture sustain the immune regulatory functions. *Biotechnology Journal*, 16(6):2000558, 2021.

[267] P. A. Tozetti, S. R. Caruso, A. Mizukami, T. R. Fernandes, F. B. d. Silva, F. Traina, D. T. Covas, M. D. Orellana, and K. Swiech. Expansion strategies for human mesenchymal stromal cells culture under xeno-free conditions. *Biotechnology Progress*, 33(5):1358–1367, 2017.

[268] M. de Almeida Fuzeta, N. Bernardes, F. D. Oliveira, A. C. Costa, A. Fernandes-Platzgummer, J. P. Farinha, C. A. V. Rodrigues, S. Jung, R.-J. Tseng, W. Milligan, B. Lee, M. A. R. B. Castanho, D. Gaspar, J. M. S. Cabral, and C. L. da Silva. Scalable production of human mesenchymal stromal cell-derived extracellular vesicles under serum-/xeno-free conditions in a microcarrier-based bioreactor culture system. *Frontiers in Cell and Developmental Biology*, 8, 2020.

[269] H. Tavassoli, S. N. Alhosseini, A. Tay, P. P. Chan, S. K. W. Oh, and M. E. Warkiani. Large-scale production of stem cells utilizing microcarriers: a biomaterials engineering perspective from academic research to commercialized products. *Biomaterials*, 181:333–346, 2018.

[270] S. Sart, A. Errachid, Y.-J. Schneider, and S. N. Agathos. Modulation of mesenchymal stem cell actin organization on conventional microcarriers for proliferation and differentiation in stirred bioreactors. *Journal of tissue engineering and regenerative medicine*, 7(7):537–551, 2013.

[271] H. Delanoe-Ayari, R. Al Kurdi, M. Vallade, D. Gulino-Debrac, and D. Riveline. Membrane and acto-myosin tension promote clustering of adhesion proteins. *Proceedings of the National Academy of Sciences*, 101(8):2229–2234, 2004.

[272] D. Riveline, E. Zamir, N. Q. Balaban, U. S. Schwarz, T. Ishizaki, S. Narumiya, Z. Kam, B. Geiger, and A. D. Bershadsky. Focal contacts as mechanosensors: externally applied local mechanical force induces growth of focal contacts by an mdia1-dependent and rock-independent mechanism. *The Journal of cell biology*, 153(6):1175–1186, 2001.

[273] P. Wysotzki, A. Sancho, J. Gimsa, and J. Groll. A comparative analysis of detachment forces and energies in initial and mature cell-material interaction. *Colloids and Surfaces B: Biointerfaces*, 190:110894, 2020.

[274] D. Le Guillou-Buffello, M. Gindre, P. Johnson, P. Laugier, and V. Migonney. An alternative quantitative acoustical and electrical method for detection of cell adhesion process in real-time. *Biotechnology and bioengineering*, 108(4):947–962, 2011.

[275] J. M. Atienza, J. Zhu, X. Wang, X. Xu, and Y. Abassi. Dynamic monitoring of cell adhesion and spreading on microelectronic sensor arrays. *Journal of biomolecular screening*, 10(8):795–805, 2005.

[276] D. M. Gryte, M. D. Ward, and W. S. Hu. Real-time measurement of anchorage-dependent cell adhesion using a quartz crystal microbalance. *Biotechnology progress*, 9(1):105–108, 1993.

[277] S. Derakhti, S. H. Safiabadi-Tali, G. Amoabediny, and M. Sheikhpour. Attachment and detachment strategies in microcarrier-based cell culture technology: A comprehensive review. *Materials Science and Engineering: C*, 103:109782, 2019.

[278] N. Shiragami, M. Hakoda, A. Enomoto, and T. Hoshino. Hydrodynamic effect on cell attachment to microcarriers at initial stage of microcarrier culture. *Bioprocess Engineering*, 16(6):399–401, 1997.

[279] C. J. Hewitt, K. Lee, A. W. Nienow, R. J. Thomas, M. Smith, and C. R. Thomas. Expansion of human mesenchymal stem cells on microcarriers. *Biotechnology letters*, 33(11):2325–2335, 2011.

[280] S. Frauenschuh, E. Reichmann, Y. Ibold, P. M. Goetz, M. Sittinger, and J. Ringe. A microcarrier-based cultivation system for expansion of primary mesenchymal stem cells. *Biotechnology progress*, 23(1):187–193, 2007.

[281] Y. Yuan, M. S. Kallos, C. Hunter, and A. Sen. Improved expansion of human bone marrow-derived mesenchymal stem cells in microcarrier-based suspension culture. *Journal of tissue engineering and regenerative medicine*, 8(3):210–225, 2014.

[282] X. Yuan, A.-C. Tsai, I. Farrance, J. A. Rowley, and T. Ma. Aggregation of culture expanded human mesenchymal stem cells in microcarrier-based bioreactor. *Biochemical engineering journal*, 131:39–46, 2018.

[283] M. António, A. Fernandes-Platzgummer, C. L. da Silva, and J. M. Cabral. Scalable microcarrier-based manufacturing of mesenchymal stem/stromal cells. *Journal of biotechnology*, 236:88–109, 2016.

[284] K. Y. Tan, S. Reuveny, and S. K. W. Oh. Recent advances in serum-free microcarrier expansion of mesenchymal stromal cells: Parameters to be optimized. *Biochemical and biophysical research communications*, 473(3):769–773, 2016.

[285] A. T.-L. Lam, J. Li, A. K.-L. Chen, S. Reuveny, S. K.-W. Oh, and W. R. Birch. Cationic surface charge combined with either vitronectin or laminin dictates the evolution of human embryonic stem cells/microcarrier aggregates and cell growth in agitated cultures. *Stem cells and development*, 23(14):1688–1703, 2014.

[286] K. M. Panchalingam, S. Jung, L. Rosenberg, and L. A. Behie. Bioprocessing strategies for the large-scale production of human mesenchymal stem cells: a review. *Stem cell research & therapy*, 6(1):1–10, 2015.

[287] C. Ferrari, F. Balandras, E. Guedon, E. Olmos, I. Chevalot, and A. Marc. Limiting cell aggregation during mesenchymal stem cell expansion on microcarriers. *Biotechnology progress*, 28(3):780–787, 2012.

[288] D. Schop, R. van Dijkhuizen-Radersma, E. Borgart, F. Janssen, H. Rozemuller, H.-J. Prins, and J. De Bruijn. Expansion of human mesenchymal stromal cells on microcarriers: growth and metabolism. *Journal of tissue engineering and regenerative medicine*, 4(2):131–140, 2010.

[289] V. Jossen, C. Schirmer, D. Mostafa Sindi, R. Eibl, M. Kraume, R. Pörtner, and D. Eibl. Theoretical and practical issues that are relevant when scaling up hmsc microcarrier production processes. *Stem cells international*, 2016, 2016.

[290] Q. A. Rafiq, S. Ruck, M. P. Hanga, T. R. Heathman, K. Coopman, A. W. Nienow, D. J. Williams, and C. J. Hewitt. Qualitative and quantitative demonstration of bead-to-bead transfer with bone marrow-derived human mesenchymal stem cells on microcarriers: Utilising the phenomenon to improve culture performance. *Biochemical engineering journal*, 135:11–21, 2018.

[291] A. W. Nienow. Reactor engineering in large scale animal cell culture. *Cytotechnology*, 50(1):9–33, 2006.

[292] S. R. Caruso, M. D. Orellana, A. Mizukami, T. R. Fernandes, A. M. Fontes, C. A. Suazo, V. C. Oliveira, D. T. Covas, and K. Swiech. Growth and functional harvesting of human mesenchymal stromal cells cultured on a microcarrier-based system. *Biotechnology progress*, 30(4):889–895, 2014.

[293] R. Friedman, M. Betancur, L. Boissel, H. Tuncer, C. Cetrulo, and H. Klingemann. Umbilical cord mesenchymal stem cells: adjuvants for human cell transplantation. *Biology of Blood and Marrow Transplantation*, 13(12):1477–1486, 2007.

[294] A. Shekaran, E. Sim, K. Y. Tan, J. K. Y. Chan, M. Choolani, S. Reuveny, and S. Oh. Enhanced in vitro osteogenic differentiation of human fetal mscs attached to 3d microcarriers versus harvested from 2d monolayers. *BMC biotechnology*, 15(1):1–13, 2015.

[295] C. Sion. *Development of an optimized perfused-continuous process of culture of human umbilical cord mesenchymal stem cells (hMSC) grown on innovative adhesion supports*. PhD thesis, Université de Lorraine, 2020.

[296] P. S. Couto, M. Rotondi, A. Bersenev, C. Hewitt, A. Nienow, F. Verter, and Q. Rafiq. Expansion of human mesenchymal stem/stromal cells (hmscs) in bioreactors using microcarriers: lessons learnt and what the future holds. *Biotechnology Advances*, 45:107636, 2020.

[297] M. S. Croughan, J.-F. P. Hamel, and D. I. Wang. Effects of microcarrier concentration in animal cell culture. *Biotechnology and bioengineering*, 32(8):975–982, 1988.

[298] W. Hu, J. Meier, and D. Wang. A mechanistic analysis of the inoculum requirement for the cultivation of mammalian cells on microcarriers. *Biotechnology and bioengineering*, 27(5):585–595, 1985.

[299] A. K.-L. Chen, Y. K. Chew, H. Y. Tan, S. Reuveny, and S. K. W. Oh. Increasing efficiency of human mesenchymal stromal cell culture by optimization of microcarrier concentration and design of medium feed. *Cytotherapy*, 17(2):163–173, 2015.

[300] M. S. Croughan. *Hydrodynamic effects on animal cells in microcarrier bioreactors*. PhD thesis, Massachusetts Institute of Technology, 1988.

[301] P. Mishra and F. Ein-Mozaffari. Critical review of different aspects of liquid-solid mixing operations. *Reviews in Chemical Engineering*, 36(5):555–592, 2020.

[302] E. T. Papoutsakis. Fluid-mechanical damage of animal cells in bioreactors. *Trends in Biotechnology*, 9(1):427–437, 1991.

[303] S. Stolberg and K. E. McCloskey. Can shear stress direct stem cell fate? *Biotechnology progress*, 25(1):10–19, 2009.

[304] T. Zwietering. Suspending of solid particles in liquid by agitators. *Chemical Engineering Science*, 8(3):244–253, 1958.

[305] R. Jafari, J. Chaouki, and P. A. Tanguy. A comprehensive review of just suspended speed in liquid-solid and gas-liquid-solid stirred tank reactors. *International Journal of Chemical Reactor Engineering*, 10(1), 2012.

[306] C. Loubière, A. Delafosse, E. Guedon, I. Chevalot, D. Toye, and E. Olmos. Dimensional analysis and cfd simulations of microcarrier 'just-suspended'state in mesenchymal stromal cells bioreactors. *Chemical Engineering Science*, 203:464–474, 2019.

[307] C. Loubière. *Characterization and impact of the hydrodynamics on the performance of umbilical-cord derived stem cells culture in stirred tank bioreactors*. PhD thesis, Université de Lorraine, 2018.

[308] T. R. Heathman, A. W. Nienow, Q. A. Rafiq, K. Coopman, B. Kara, and C. J. Hewitt. Agitation and aeration of stirred-bioreactors for the microcarrier culture of human mesenchymal stem cells and potential implications for large-scale bioprocess development. *Biochemical Engineering Journal*, 136:9–17, 2018.

[309] A. W. Nienow, C. J. Hewitt, T. R. Heathman, V. A. Glyn, G. N. Fonte, M. P. Hanga, K. Coopman, and Q. A. Rafiq. Agitation conditions for the culture and detachment of hmscs from microcarriers in multiple bioreactor platforms. *Biochemical Engineering Journal*, 108:24–29, 2016.

[310] C. Buurman, G. Resoort, and A. Plaschkes. Scaling-up rules for solids suspension in stirred vessels. *Chemical engineering science*, 41(11):2865–2871, 1986.

[311] A. Barresi and G. Baldi. Solid dispersion in an agitated vessel. *Chemical Engineering Science*, 42(12):2949–2956, 1987.

[312] J. Godfrey and Z. Zhu. Measurement of particle-liquid profiles in agitated tanks. In *AIChE Symposium Series*,

volume 90, pages 181–185. New York, NY: American Institute of Chemical Engineers, 1971-c2002., 1994.

[313] A. Tamburini, A. Cipollina, G. Micale, A. Brucato, and M. Ciofalo. Cfd simulations of dense solid–liquid suspensions in baffled stirred tanks: Prediction of suspension curves. *Chemical Engineering Journal*, 178:324–341, 2011.

[314] M. Lassaigne, B. Blais, L. Fradette, and F. Bertrand. Experimental investigation of the mixing of viscous liquids and non-dilute concentrations of particles in a stirred tank. *Chemical Engineering Research and Design*, 108:55–68, 2016.

[315] R. Jafari, P. A. Tanguy, and J. Chaouki. Characterization of minimum impeller speed for suspension of solids in liquid at high solid concentration, using gamma-ray densitometry. *International journal of chemical engineering*, 2012, 2012.

[316] I. Pieralisi, G. Rodriguez, M. Micheletti, A. Paglianti, and A. Ducci. Microcarriers' suspension and flow dynamics in orbitally shaken bioreactors. *Chemical Engineering Research and Design*, 108:198–209, 2016.

[317] A. Delafosse, C. Loubière, S. Calvo, D. Toye, and E. Olmos. Solid-liquid suspension of microcarriers in stirred tank bioreactor–experimental and numerical analysis. *Chemical Engineering Science*, 180:52–63, 2018.

[318] R. Angst and M. Kraume. Experimental investigations of stirred solid/liquid systems in three different scales: Particle distribution and power consumption. *Chemical Engineering Science*, 61(9):2864–2870, 2006.

[319] P. Sessiecq, P. Mier, F. Gruy, and M. Cournil. Solid particles concentration profiles in an agitated vessel. *Chemical Engineering Research and Design*, 77(8):741–746, 1999.

[320] R. Congjing, J. Xiaojing, W. Jingdai, Y. Yongrong, and Z. Xiaohuan. Determination of critical speed for complete solid suspension using acoustic emission method based on multiscale analysis in stirred tank. *Industrial & engineering chemistry research*, 47(15):5323–5327, 2008.

[321] M. V. Sardeshpande, V. Juvekar, and V. V. Ranade. Solid suspension in stirred tanks: Uvp measurements and cfd simulations. *The Canadian Journal of Chemical Engineering*, 89(5):1112–1121, 2011.

[322] M. Del Pozo, C. Briens, and G. Wild. Particle—particle collisions in liquid—solid and gas—liquid—solid fluidized beds. *Chemical engineering science*, 48(18):3313–3319, 1993.

[323] A. Aguilar-Corona, R. Zenit, and O. Masbernat. Collisions in a liquid fluidized bed. *International journal of multiphase flow*, 37(7):695–705, 2011.

[324] W. A. Al-Masry, E. M. Ali, and M. N. Al-Kalbani. Prediction of regime transitions in bubble columns using acoustic and differential pressure signals. *Chemical Engineering Journal*, 133(1-3):139–149, 2007.

[325] W. A. Al-Masry and E. M. Ali. Identification of hydrodynamics characteristics in bubble columns through analysis of acoustic sound measurements—influence of the liquid phase properties. *Chemical Engineering and Processing: Process Intensification*, 46(2):127–138, 2007.

[326] Y. Zhou, L. Yang, Y. Lu, X. Hu, X. Luo, and H. Chen. Flow regime identification in gas-solid two-phase fluidization via acoustic emission technique. *Chemical Engineering Journal*, 334:1484–1492, 2018.

[327] N. Salehi-Nik, R. Sotudeh-Gharebagh, N. Mostoufi, R. Zarghami, and M. Mahjoob. Determination of hydrodynamic behavior of gas–solid fluidized beds using statistical analysis of acoustic emissions. *International Journal of Multiphase Flow*, 35(11):1011–1016, 2009.

[328] C. Meyer and D. Deglon. Particle collision modeling–a review. *Minerals Engineering*, 24(8):719–730, 2011.

[329] M. Micheletti, L. Nikiforaki, K. C. Lee, and M. Yianneskis. Particle concentration and mixing characteristics of moderate-to-dense solid- liquid suspensions. *Industrial & engineering chemistry research*, 42(24):6236–6249, 2003.

[330] P. Buffière and R. Moletta. Collision frequency and collisional particle pressure in three-phase fluidized beds. *Chemical Engineering Science*, 55(22):5555–5563, 2000.

[331] R. Mishra, J. Militky, V. Baheti, J. Huang, B. Kale, M. Venkataraman, V. Bele, V. Arumugam, G. Zhu, and Y. Wang. The production, characterization and applications of nanoparticles in the textile industry. *Textile Progress*, 46(2):133–226, 2014.

[332] R. Cherry and E. Papoutsakis. Hydrodynamic effects on cells in agitated tissue culture reactors. *Bioprocess Engineering*, 1(1):29–41, 1986.

[333] R. Cherry and E. Papoutsakis. Growth and death rates of bovine embryonic kidney cells in turbulent microcarrier bioreactors. *Bioprocess Engineering*, 4(2):81–89, 1989.

Chapter 2

Impact of microcarrier concentration on MSC growth, death and phenotypical attributes

Contents

2.1 Impact of microcarrier concentration on MSC growth and death

In view of understanding the impact of microcarrier-microcarrier collisions on MSC growth and certain defined quality attributes, MSC expansion were performed in Erlenmeyer Flasks and Spinner Flasks and using two different microcarrier types (Cytodex 1 and Synthemax II). The results of these experiments were published as a scientific article in the Biotechnology Bioengineering journal [1].

Impact of microcarrier concentration on mesenchymal stem cell growth and death : experiments and modelling - Biotechnology Bioengineering, 2022 - C. Maillot, N. De Isla, C. Loubiere, D. Toye, E. Olmos

2.1.1 Publication abstract

Mesenchymal stem cell products are promising therapeutic candidates to treat a wide range of pathologies. The successful commercialization of these cell therapies will however depend on the development of reproducible cell production processes. For this, using microcarriers as growth supports within controlled conditions may be a viable process option. Although increasing microcarrier concentration may be associated with greater productivity due to the increased available culture surface, additional friction or shocks between microcarriers are likely to lead to undesired cell death. However, data detailing the impact of microcarriers collisions on MSC growth remains scarce. The following work demonstrates that MSC growth on microcarriers is greatly influenced by particle concentration even when little impact is observed on the apparent growth rate. It is suggested that the apparent growth rate may result in a equilibrium between growth and death kinetics which are independently affected by particle concentration and that certain MSCs quality attributes may be progressively degraded in parallel. In addition, the theoretical reduction of MSC growth rate was modelled according to the ratio between the average inter-particle distance and the Kolmogorov scale. This study is an original contribution towards understanding the hydrodynamic effects in microcarrier-based stem cell cultures.

2.1.2 Introduction

Since the beginning of the 21st century, the discovery and development of various Advanced Therapy Medicinal Products (ATMPs) has triggered an increasing number of clinical trials using human cells. Carried by this movement, Mesenchymal Stem Cells (MSCs) have been gradually used as cell therapies to address a wide range of pathologies

including neuro-degenerative or respiratory diseases [2, 3], but also as raw materials for tissue reconstruction, for example in view of grafting epithelial and skeletal assemblies [4, 5]. More recently, the discovery of therapeutic bioactive products secreted by MSCs have resulted in the development of processes for which the production of MSCs is no longer performed for the cells themselves but rather the molecules they produce [6]. Regardless of how the cells are used, most therapeutic applications require around 1 to 1 000 million cells per patient per dose [2, 7], exceeding the amount of cells which can be extracted from a single donor. As a result, an *ex-vivo* expansion phase is usually required, traditionally performed using monolayer or multilayer tissue flasks of different sizes [8]. Although this method of expansion is well documented in literature, it is labour intensive and introduces contamination risks due to the required manual cell passaging between different containers. In addition, controversies persist between research teams concerning optimal process parameters to use during the expansion process and their impact on the final cell product [9]. Various lead clinical trials using MSCs produced this way have either failed to meet the requirements for phase progression or undergone early termination [10], indicating that important bottlenecks still remain to successfully commercialize these therapies.

In order to scale-up the manufacturing of high-quality stem cell products, a shift to 3D cultures using bioreactors may be required [11, 12]. For this, adherent MSC's are no longer cultured in planar conditions but using embryoid bodies (small aggregates of cells in suspension), micro capsules containing the cells, or microcarriers (small particles in suspension on which adherent stem cells expand). Using 3D culture brings flexibility to the process, enables high density cell expansion in conditions which can easily be monitored, reduces the risk of contamination [13], and significantly reduces the cost and space required for GMP manufacturing [14]. However, to our knowledge, out of the 10 353 clinical trials involving MSC's in 2021, only 2 clinical studies have been completed using a bioreactor-based MSC expansion strategy (laryngo-tracheal engineered tissue transplantation NCT01997437 and placenta derived mesenchymal-like stem cells expanded in PluriXTM 3D bioreactors for intramuscular injections NCT00919958). None of the clinical trials seem to involve a microcarrier-based approach, possibly indicating the need to continue fundamental research on these processes, in particular to understand how both solid and liquid phases interact and impact MSC expansion.

In this mindset, optimizing microcarrier concentration may prove to be critical. While pioneering work using human fibroblasts showed no significant impact of increasing Sephadex (particle diameter $\approx$ 180 µm) microcarrier concentration from 5 to 15 g L^{-1} [15], successive studies showed that increasing Cytodex 1 (particle diameter $\approx$ 190 µm) microcarrier concentration above a threshold of approximately 1 g L^{-1} was associated with a decreased observed specific growth rate [16]. More recently, similar results have shown a deleterious effect of increasing microcarrier concentration from 3000 to 7500 Cytodex 3 microcarriers per mL (particle diameter $\approx$ 175 µm) dur-

ing MSC growth [17] while other studies showed this negative impact of increasing Cytodex 3 microcarrier concentration only after a certain threshold of 8 g L^{-1} [18]. Although a certain heterogeneity persists in literature, an overall consensus tends to show that increasing microcarrier concentration is, in general (and sometimes after a certain threshold), associated with a negative impact on growth. In addition, cell damage typically may occur in agitated conditions due to (1) collisions between cells on microcarriers and the impeller or culture vessel, (2) collisions between microcarriers and/or (3) interactions with turbulent flow eddies approximately the same size as the microcarriers on which cells are grown [19]. Consequently, the negative impact of microcarrier concentration on growth is often attributed to microcarrier-microcarrier interactions without, to our knowledge, a robust scientific demonstration for MSCs.

The aim of the present study is to provide a detailed description of the impact of microcarrier concentration on human MSC growth by testing a wider range of microcarrier concentrations (α), using microcarriers of different sizes, and through different agitation systems. Supplementary cultures to which various concentrations of plastic particles (β) were added also contributed to further describe the impact of repeated mechanical constraints on human MSC expansion dynamic parameters (Figure 2.1). Adding these plastic particles, on which cells cannot adhere and were found to not grow, provoked particle-microcarrier collisions without providing additional cell culture surface. Combining both sets of experiments was then used to evaluate the theoretical real growth rate in each system. In addition, immmunophenotyping was performed on MSCs after their growth on microcarriers to define the potential impact of microcarrier concentration on cell phenotype.

2.1.3 Experimental approach

Cell extraction, primary cultures and cell culture medium

Human mesenchymal stem cells (hMSC's) were extracted from the Wharton's Jelly of umbilical cords from just-born babies (Centre Hospitalier Universitaire de Nancy, France) and expanded and cryopreserved according to methods previously described [20, 21]. A primary expansion was performed after thawing individual cryovessels onto standard T-Flasks for 5 to 10 days. At least two independent donor cell banks were used for each set of experiments. All cultures were performed in a CO_2 incubator (Sanyo, MCO 215Lit) (37 °C, 5 % CO_2) and α-MEM medium (Thermo fisher scientific, 11590606) supplemented with 5 % human platelet lysate (HPL) (Macopharma, BC0190020 or Sexton biotechnologies, PL-NH-500), 1 $\%_{v/v}$ antibiotic antimycotic solution (Sigma aldrich, A5955) and 4 mM glutamine (Sigma aldrich, G7513). In cultures performed using the HPL supplied by Macopharma, a mechanical defibrination of the medium was performed in order to limit the development of a gel-like matrix during agitated cultures [22] and primary cultures were performed with the addition of 2 IU

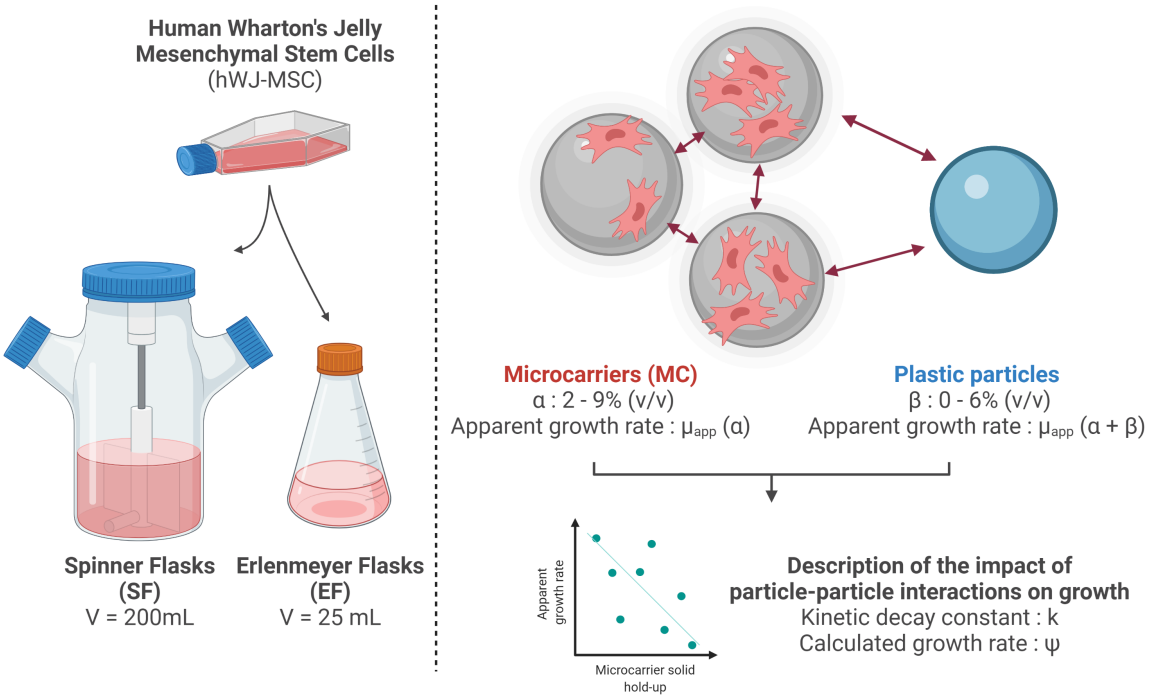

Figure 2.1: Experimental approach used to determine the impact of microcarrier interactions on human Wharton's Jelly Mesenchymal Stem Cell (hWJ-MSC) growth. MSCs were grown at various microcarrier concentrations (α) and with various added particle concentrations (β) in both Spinner Flasks (SF) and Erlenmeyer Flasks (EF). The apparent growth rate in each condition could then be calculated (μ_{app}). Figure created with biorender.com.

mL^{-1} heparin (Sigma aldrich, H3149). For each set of experiments, the same HPL supplier was used throughout all cell culture stages.

Microcarrier-based cultures protocols in Erlenmeyer Flasks (EF) or Spinner Flasks (SF)

After having previously prepared either Cytodex 1 microcarriers (Cytiva lifesciences, 17044802) or Synthemax II Dissolvable microcarriers (Corning, 7290) according to the manufacturers' instructions, hMSCs were inoculated during 4 hours in either Erlenmeyer Flasks (EF) (Thermo fisher scientific, PVB125) or Spinner Flasks (SF) (Schott bottles agitated with Duran GL 45 stirred reactor agitators, Merck, Z680788-1KT) at an initial concentration of 7500 cells cm^{-2} which was previously defined as optimal [23]. The initial adhesion phase was performed without HPL in half of the final working volume and either in static conditions (EF) or using intermittent agitation cycles of 5 minutes every 30 minutes for 2 hours followed by cycles of 5 minutes every 60 minutes for 2 hours (SF). These conditions were found to increase the initial attachment yield compared to a 4 hour static adhesion phase in medium containing HPL. After cell adhesion, the medium was completed to the final volume and HPL was added. Half of the culture supernatant was replaced every 3-4 days by fresh medium in order to limit the accumulation of by-products and feed the cell culture.

A range of microcarrier concentrations were used for cell culture (4.4 to 9.0 $\%_{v/v}$ (EF) or 2.7 to 6.6 $\%_{v/v}$ (SF)). In certain experiments, a constant microcarrier concentration was used (4.4 $\%_{v/v}$ (EF) or 2.7 $\%_{v/v}$ (SF)) to which a range of plastic particles (Pall Solohill, P102-1521) were added on which cell growth was not observed and has been shown to be negligible [24]. These particles have a similar size and density as the microcarriers used for cell growth and, as a result, provoke additional collision forces during cell culture without increasing the available cell culture surface. The microcarrier concentrations in Spinner Flasks and Erlenmeyer Flasks in the control conditions were chosen as have previously been shown to successfully support cell growth in these agitation systems [23]. Agitation conditions were fixed at the particle just suspended state $N = N_{js} \approx 70$ rpm (EF) or $N = N_{js} = 40$ rpm (SF). We can note that the impact of particle concentration on the agitation rate required to maintain particles in suspension was found to be negligible for the particle concentrations used, according to the well-known Zwietering equation [25]. The complete suspension of particles in each condition was also visually verified.

Characterization of kinetic parameters during MSC cell expansion on microcarriers

Cell growth characterization. Cell counting of the total amount of live cells on microcarriers X was performed at least daily in all experiments by analyzing a homogeneous 500 µl sample of the cell culture. For Cytodex 1 experiments, attached cells were counted by automatic recognition of fluorescent nuclei attached to microcarriers after DAPI-Methanol staining. By using methods previously described, the average number of cells per microcarrier can be obtained from at least 6 different microscopic observations [24]. Cells counted directly on the microcarriers were presumed to be live cells. For Synthemax II experiments, microcarriers were left to sediment and the pellet was dissolved by using a trypsin-pectinase solution according to manufacturers' recommendations. After dissolution, the cell suspension solution was filtered (100 µm mesh) and counted using an automatic cell counter (Beckman coulter, Vicell-XR). Regardless of the microcarrier type, only the cells which were attached on the microcarriers were counted. In addition, the theoretical initial viable cell concentration attached on microcarriers X_i was calculated by multiplying the amount of cells initially seeded by the average inoculation yield in each system. This value was preferred over the measured initial cell concentration in order to smooth the impact of counting variability which can be imprecise at the beginning of the cell culture due to low initial cell concentrations and an inoculation yield which could also be variable between conditions. Subsequently, the apparent growth rate μ_{app} was determined by fitting Equation 2.1 to the experimental data points during the exponential growth phase.

$$X(t) = X_i \times e^{\mu_{app} \cdot t} \tag{2.1}$$

Apparent cell growth determination. The apparent MSC growth rate was determined at various microcarrier concentrations α. For each microcarrier concentration, experiments were performed in duplicate or triplicate analysis. Theoretically, the apparent growth rate at a given microcarrier concentration $\mu_{app}(\alpha)$ is affected by both cell growth and death kinetic decay constants. Accordingly, MSCs would theoretically have a growth rate $\Psi(\alpha)$ if microcarrier-microcarrier interactions were absent and did not cause additional mortality. We should note that in all experiments, a constant seeding cell density was applied of 7500 cells per cm^2. As a result, increasing microcarrier concentration and cell culture surface also induces higher volumetric cell concentrations throughout the cell cultures. It is supposed that the theoretical growth rate $\Psi(\alpha)$ may be dependent on microcarrier concentration due to different levels of secreted growth factors or toxic metabolic by-products which can enhance or inhibit growth [16]. In addition, the negative impact of particle-particle interactions on cell growth is presumed to follow a first order kinetic model according to microcarrier concentration α [16]. As a result, performing experiments at various microcarrier concentrations gives important information how growth is impacted and can be modelled by Equation 2.2. However, these experiments alone are not sufficient to determine the kinetic decay constant k nor the MSC growth rate in the system which would occur without microcarrier-microcarrier interactions $\Psi(\alpha)$.

$$\mu_{app}(\alpha) = \Psi(\alpha) - k \times \alpha \tag{2.2}$$

Kinetic decay constant. In order to obtain the kinetic decay constant k, a separate set of experiments was performed by adding plastic particles after the initial cell attachment phase, on which cells did not attach nor grow. These plastic particles were added at various concentrations β while the microcarrier concentration α was kept constant. It is noteworthy that although it has been observed that cells grow on plastic microcarriers (with very low growth and attachment rates, [24]), this was not found to be the case in the concomitant presence of Cytodex-1 or Synthemax II microcarriers. Daily DAPI staining of cells in all of the Cytodex-1 experiments showed no attachment or growth on these particles which were therefore considered as not providing additional adherence surfaces. For each microcarrier concentration, experiments were performed in duplicate or triplicate analysis except for experiments performed using Synthemax II microcarriers in Erlenmeyer Flasks. For this last experiment, the experimental error was estimated based on the mean experimental variability measured in Erlenmeyer Flasks and Cytodex 1 microcarriers. Subsequently, Equation 2.2 was used to describe the apparent growth rate $\mu_{app}(\alpha + \beta)$ according to both growth and

death constants. Firstly, the theoretical growth rate which would occur in the system if microcarrier-microcarrier interactions were absent $\Psi(\alpha)$ is considered as constant in these set of experiments, since the microcarrier concentration is not modified and growth on the plastic microcarriers is absent (*i.e.* $\Psi(\alpha+\beta) \approx \Psi(\alpha)$). Secondly, this growth rate should be reduced by microcarrier-microcarrier interactions according to a first order kinetic model represented by the constant k. Lastly, the impact of particle-microcarrier interactions can be supposed as having a kinetic decay constant of $k/2$ since, on average, a microcarrier containing cells meets a plastic particle twice less frequently since only half of the interacting particles have cells. Solving Equation 2.3 with various particle concentrations β allowed us to determine two critical system constants : the MSC growth rate which would occur without microcarrier interactions at the control microcarrier concentration $\Psi(\alpha)$; and the kinetic decay constant due to microcarrier and particle interactions k.

$$\mu_{app}(\alpha + \beta/2) = \Psi(\alpha) - k \times \left(\alpha + \frac{\beta}{2}\right) \tag{2.3}$$

Finally, combining the results obtained at various microcarrier concentrations and the results obtained with the addition of plastic particles allowed us to solve Equation 2.2 after having determined k with Equation 2.3. These results shed new light on how the growth rate in microcarrier-based cell culture systems is impacted by microcarrier concentration.

Metabolite analysis. Glucose and lactate concentrations were measured daily using an offline analyzer (Thermo Fisher Scientific, Gallery multi-parametric analyzer) and used to calculate the specific glucose consumption rates $q_{Gluc/X}$ and specific lactate production rates $q_{Lac/X}$ over the exponential growth phase $\Delta t_{i->f}$ (Equation 2.4 and Equation 2.5). For this, the initial i and final f metabolite concentrations were used as well as the variation in metabolite concentration during medium changes $\Delta Gluc$ or ΔLac. Lastly, the transformation yield of glucose to lactate during the exponential phase was calculated (Equation 2.6). Considering the low volumes of experiments in Erlenmeyer Flasks and detachment yields on Cytodex 1 microcarriers, this analysis was limited to Spinner Flask experiments using Synthemax II microcarriers.

$$q_{Gluc/X} = \frac{Gluc_i - Gluc_f + \Delta Gluc}{X_f - X_i} \times \frac{1}{\Delta t_{i->f}} \tag{2.4}$$

$$q_{Lac/X} = \frac{Lac_f - Lac_i + \Delta Lac}{X_f - X_i} \times \frac{1}{\Delta t_{i->f}} \tag{2.5}$$

$$Y_{Lac/Gluc} = \frac{q_{Lac/X}}{q_{Gluc/X}} \tag{2.6}$$

Immunophenotyping. MSCs expanded on Synthemax II microcarriers in SF were detached at the end of the exponential growth phase and cryopreserved at a concentration of 5×10^6 cells mL^{-1}. These cells were then thawed and cultured for 3 days before characterization according to the general guidelines provided by the International Society for Cellular Therapy (ISCT) [26]. Plastic adhesion was verified at this stage. For cytometry, approximately 1×10^5 cells were resuspended in 100 µL phosphate buffer saline (PBS) supplemented with bovine serum albumin (BSA) and incubated with specific antibodies for 1 hour at room temperature. After incubation, MSCs were washed with PBS, centrifuged at 300 g for 5 minutes and resuspended in 250 µL of 1% paraformaldehyde (PFA) until analysis by FACS flow cytometry (Beckman Coulter, Gallios) according to methods and specific antibodies previously described [27].

Cell death characterization. In order to further characterize live and dead cell populations at the end of the cell culture, a detailed analysis was performed on cells which were grown in Spinner Flasks (SF) on Synthemax II microcarriers. These conditions were chosen since the larger volume of the spinner flasks allowed a greater sampling capacity and since cells grown on Synthemax II were shown to have the greatest cell detachment yield. Live and dead cells attached to the Synthemax II microcarriers were quantified after microcarrier dissolution using an offline cell analyzer (Vi-cell, Beckman coulter). This quantification was performed on three independent 500 µL homogeneous samples. In addition, cell lysis was quantified through supernatant Lactate DeHydrogenase (LDH) concentration which was measured at the start and end of the cell culture using an offline analyzer (Thermo Fisher Scientific, Gallery multi-parametric analyzer). This technique was calibrated by measuring the LDH concentration before and after 4 freeze-thaw cycles of five MSC cell dilutions. Measuring cell concentration after these cycles showed no more live cells indicating all cells had undergone lysis during these cycles. The conversion factor of 1 IU LDH to 2.1×10^6 lysed cells was used to determine cell death during the cell culture.

2.1.4 Results and discussion

Observed cell growth during microcarrier-based cell culture

The first set of experiments were performed at various Cytodex 1 and Synthemax II microcarrier concentrations using both Erlenmeyer Flasks (EF) and Spinner Flasks (SF). To begin with, the impact of microcarrier concentration on the capacity of cells to effectively colonize each microcarrier surface was evaluated. For this, the maximum cell concentration was measured at the end of the exponential growth phase (Figure 2.2, left). As a reference, the initial seeding cell concentration in all conditions was of 7500 cells per cm^2. This would be the initial cell concentration if the attachment yield was of 100 %. The measured average inoculation yields in each condition is also presented in

Appendix 1. It can be noted that, in general, seeding was found to be more efficient in Spinner Flasks due to the greater volume and more reproducible agitation conditions during the initial attachment phase. Lastly, no significant trends were observed in the seeding efficiency when increasing particle concentration.

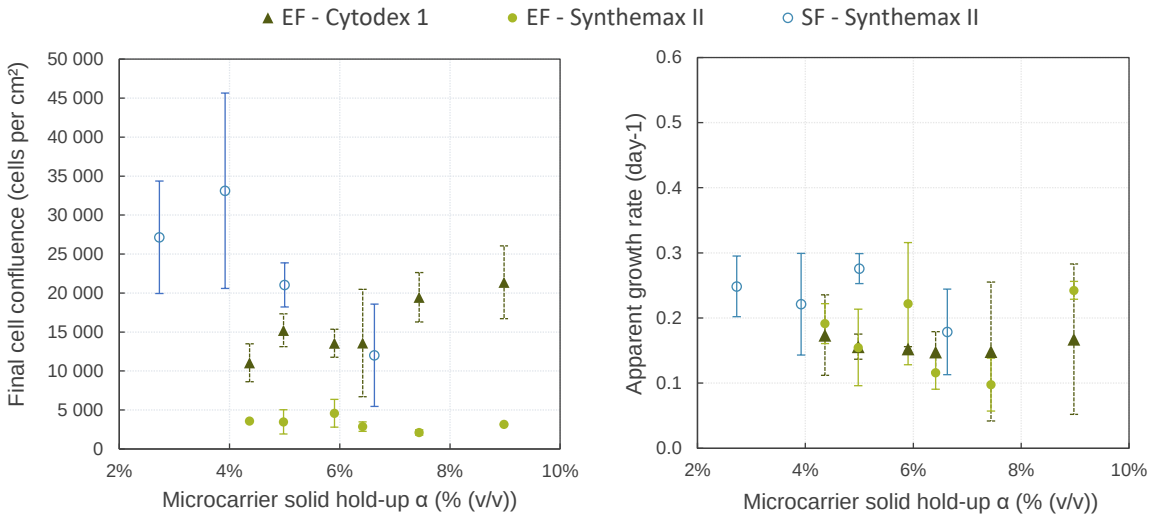

Figure 2.2: Left : Maximum cell surface concentration observed at the end of the exponential growth phase of hWJ-MSCs grown on either Cytodex 1 or Synthemax II in either Spinner Flasks (SF) or Erlenmeyer Flasks (EF) at various solid hold-up concentrations (α). Right : Apparent growth rate ($\mu_{app}(\alpha)$) measured at various microcarrier solid hold-up concentrations (α). Error bars correspond to the standard deviation measured between different cultures performed in duplicate or triplicate analysis.

In Spinner Flasks (SF) using Synthemax II microcarriers, similar levels of confluence were observed at the end of the exponential growth phase for cell cultures performed between 2.7 $\%_{v/v}$ and 5 $\%_{v/v}$ (for comparison, the average length of the exponential growth phases observed in these conditions can be found in Table 2.1). However, increasing microcarrier concentration past 5 $\%_{v/v}$ was found to reduce microcarrier colonization. These results indicate that certain factors in high microcarrier concentrations (possibly microcarrier-microcarrier interactions) may be limiting cells from achieving confluence through either increased cell death or by mechanical factors which cause cells to detach from microcarriers. In the case of Erlenmeyer Flasks however, little impact of microcarrier concentration on cell colonization was observed in both Cytodex 1 and Synthemax II microcarrier cell cultures, indicating that cells are reaching similar confluence levels in all conditions regardless of microcarrier concentration. Notably, the final cell surface concentration was found to be lower than the theoretical initial seeded cell concentration when using Synthemax II microcarriers. This may be caused by the fact that the inoculation yield was lower in these conditions (only approximately 20 % of the inoculated cells adhered to the microcarriers). In addition, the speed at which cells reached confluence was obtained by fitting experimental data to known growth models. No notable impact of microcarrier concentration on the observed growth rate was observed in Erlenmeyer Flasks (EF) or Spinner Flasks (SF) and regardless of the

microcarrier used (Figure 2.2, right). In all of the conditions observed, the apparent growth rate $\mu_{app}(\alpha)$ remained within typical process variability (obtained by calculating the standard deviation of the results obtained in duplicate or triplicate analysis).

Table 2.1: Average exponential growth phase duration for experiments presented in Figure 2.2.

	Exponential growth phase duration					
Total solid hold-up	**4.4 %$_{v/v}$**	**5.0 %$_{v/v}$**	**5.9 %$_{v/v}$**	**6.4 %$_{v/v}$**	**7.4 %$_{v/v}$**	**9.0 %$_{v/v}$**
EF - Cytodex-1	2.8 days	4.4 days	4.2 days	4.9 days	9.0 days	7.8 days
EF - Synthemax II	7.5 days	8.1 days	7.5 days	7.5 days	6.9 days	7.3 days
Total solid hold-up	**2.7 %$_{v/v}$**	**3.9 %$_{v/v}$**	**5.0 %$_{v/v}$**	**6.6 %$_{v/v}$**		
SF - Synthemax II	7.0 days	7.9 days	6.5 days	6.8 days		

Kinetic decay constant during microcarrier-based cell culture

In order to further understand how microcarrier-microcarrier interactions affect MSC growth when increasing microcarrier concentration, separate experiments were performed with a constant concentration of either Cytodex 1 or Synthemax II microcarriers in SF (2.7 $\%_{v/v}$ and EF 4.4 $\%_{v/v}$. These concentrations were chosen since the growth of WJ-MSCs has previously been demonstrated as successful in both agitation systems in these conditions [23]. Plastic particles were added at various concentrations (β) after the initial attachment phase. Cell growth was not observed on the added plastic particles.

To begin with, analysis of growth data seemed to indicate that cells grown with added plastic particles had a slower apparent growth rate and that the effect was increased the more plastic particles were added. For instance, the growth kinetics of 3 conditions among 12 and modelled growth curves can be observed in Figure 2.3, left and indicates this trend. Notably, in cases where high particle concentrations were added ($\beta/2 > 3\ \%_{v/v}$), the apparent growth rate was negative, indicating a higher death rate than real growth rate. Fitting exponential growth models to the experimental data observed was then used to determine the apparent growth rate at various plastic particle concentrations and using both Cytodex I and Synthemax II microcarriers. Regardless of the agitation system or the microcarrier used, a linear decrease in the MSC apparent growth rate was observed when increasing the total particle concentration (Figure 2.3, right). Similar results have previously been observed for human FS-4 fibroblast growth on Cytodex 1 microcarriers [16] to which various concentrations of particles were added. Similarly to the hypothesis proposed, the decrease in MSC growth rate observed may be caused by repeated mechanical constraints caused by the additional particles added, as it has been shown that frequent mechanical stresses suppress the proliferation of human MSCs [28].

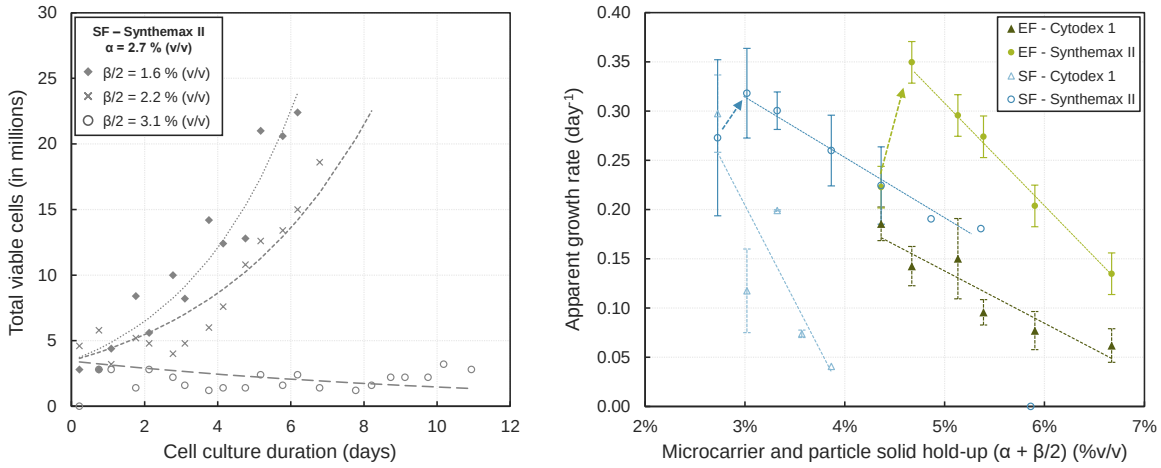

Figure 2.3: Left : MSC cell growth on Synthemax II microcarriers (MC) ($\alpha = 2.7\ \%_{v/v}$) in Spinner Flaks (SF) with the addition of plastic particles ($\beta\ /\ 2$). Right : Apparent MSC growth rate for constant Cytodex 1 or Synthemax II concentrations (α) and various concentrations of plastic particles ($\beta\ /\ 2$) in Erlenmeyer Flasks (EF) and Spinner flasks (SF). Error bars correspond to the standard deviation measured between different cultures performed in duplicate or triplicate analysis except for experiments performed using Synthemax II microcarriers in Erlenmeyer Flasks. For this last experiment, the experimental error was estimated based on the mean experimental variability measured in Erlenmeyer Flasks and Cytodex 1 microcarriers.

These linear fitting of these experimental results was then used to identify the kinetic decay constant k caused by microcarrier-particle interactions using Equation 2.3 for each agitation system (Table 2.2). Interestingly, this constant was found to depend on the microcarrier type used, possibly due to the different physical characteristics of each microcarrier. To begin with, microcarrier size typically impacts the frequency and force which occur during the collisions between two particles. For a same solid hold-up, smaller particles will have a higher collisions frequency but of a lower intensity. In addition, the difference in material surface elasticity impacts how the collision force will be transmitted to the cell as an elastic surface may absorb part of the collision force [29]. In addition, the choice of agitation system was also found to have an impact on how these added particles impact cell growth. As a result, it is possible that for a given solid hold-up, different mechanisms exist in either Spinner Flasks or Erlenmeyer Flasks, possibly due to differences in the spacial distribution of microcarriers caused by the agitation system. The use of an external agitation method in Erlenmeyer Flasks typically concentrates particles in the middle of the flask which may lead to an increased frequency of collisions and/or friction between particles in these systems and thus affect cell growth in a different manner than in cell cultures for which microcarriers are suspended using an impeller [30]. Interestingly, the impact of adding plastic particles was found to be most significant in Erlenmeyer Flasks using Synthemax II microcarriers and in Spinner Flasks using Cytodex 1 microcarriers which may seem to indicate that both the agitation system (ie particle suspension and homogeneity) and the type of microcarrier used (ie size, elasticity) affect the way these microcarrier interactions

affect cell growth.

In addition, fitting the observed growth rate with Equation 2.3 was then used to determine the growth rate the control condition which would theoretically be obtained if particle-particle interactions were absent $\Psi(\alpha)$. This growth rate can then be compared to the apparent growth rate in the control condition $\mu_{app}(\alpha)$. Results indicate, in all conditions, that the measured growth rate in the system may largely underestimate the growth rate without these added mechanical constraints. These results may indicate that growing cells under different mechanical constraints may also have an impact on the quality of the cells obtained at the end of the cell culture (cells may be undergoing more divisions than measured or have altered phenotypical characteristics and as a result may be reaching senescent states earlier than they would in static conditions).

Lastly, interesting results were observed for cells grown on Synthemax II microcarriers in both Erlenmeyer and Spinner Flasks. In these cases, adding small amounts of plastic microcarriers to the cell culture was found to have a beneficial impact on the apparent growth rate as represented by the arrows in Figure 2.3. As a result, the linear fitting was performed by excluding the results obtained in the control conditions for a more accurate calculation of the mechanical decay kinetic constant in these conditions. The increase in the apparent growth rate in these conditions may be explained by a reduced aggregation between cells and microcarriers since the plastics particles may break these cell-microcarrier aggregates and create greater homogeneity in the systems but additional experiments should be performed in this range of plastic particle concentration to confirm the possible positive effect at very small concentrations.

Table 2.2: Growth kinetic parameters calculated for MSC cultures grown on Synthemax II and Cytodex 1 microcarriers in Erlenmeyer Flasks (EF) and Spinner Flasks (SF).

Culture System (Microcarrier)	**Control apparent growth rate** $\mu_{app}(\alpha)$ (day^{-1})	**Control growth rate without mechanical constraints** $\Psi(\alpha)$ (day^{-1})	**Kinetic decay constant** k (day^{-1})
EF (Cytodex 1)	0.19	0.40	5.3
EF (Synthemax II)	0.22	0.85	10.9
SF (Cytodex 1)	0.30	0.79	19.6
SF (Synthemax II)	0.27	0.61	9.3

Observed cell death at the end of microcarrier cell culture

As suggested above, increasing particle concentration during MSC cell culture on microcarriers seems to have a significant impact on cell growth. Notably, the apparent cell growth rate was found to decrease with increasing added plastic particle concentration. In order to determine if this decreased apparent growth rate was due to an overall slower cell growth, or due to an increased amount of cell death in the system, the quantity of live and dead cells at the end of MSC cell cultures grown on Synthemax

II microcarriers was measured in Spinner Flasks (Figure 2.4). These conditions were chosen since they provided the greatest sampling capacity and since cells were most easily detached from the microcarriers for analysis.

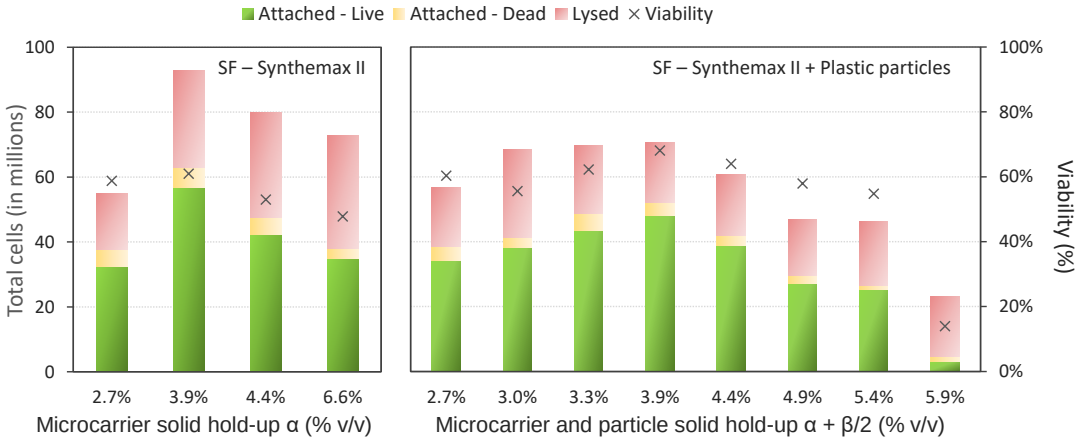

Figure 2.4: Live and dead cell populations counted at the end of the exponential growth phase of MSC cell cultures grown on Synthemax II microcarriers in Spinner Flasks (SF). Left : cells were grown at various microcarrier concentrations (α). Right : Cells were grown at a constant microcarrier concentration ($\alpha = 2.7\ \%_{v/v}$) to which plastic particles were added (β).

To begin with, the amount of live cells at the end of the cell culture was found to slightly increase with increasing microcarrier concentration or when increasing the amount of plastic particles added until a threshold of approximately 4 $\%_{v/v}$ in both cases. Afterwards, the amount of live cells decreased when increasing microcarrier concentration. These results are similar to results previously obtained concerning human fibroblast cell growth on Cytodex 1 microcarriers and may indicate that deleterious effects of particle concentration may only impact microcarrier confluence after a certain threshold. Determining the cell viability in the system showed that, apart from extremely high particle concentrations of about 5.9 %, viability at the end of the cell culture remained stable around approximately 50 to 60 % which seems to indicate that the decreased growth rate observed above should be correlated with an slower cell growth rather than an increased cell death.

Metabolite analysis

In addition metabolic data was analyzed for cell cultures performed in Spinner flasks with Synthemax II microcarriers. Glucose plays a central role in MSC cell metabolism as it is the primary energy source used through either oxidative phosphorylation or glycolysis. In all experiments, the average transformation yield from glucose to lactate was found to stay stable around 2 mol / mol indicating a preferential glycolysis metabolism in all cell cultures. Furthermore, in experiments with added plastic particles, the average glucose consumption rate and lactate production rate was also found to stay

stable regardless of the particle concentration added (Figure 2.5, right). These results indicate that cells have, on average, similar metabolic activities since similar quantities of glucose were consumed per cell per day on average during the exponential growth phase. Lastly, in experiments performed at various Synthemax II microcarrier concentrations, a slight increase in metabolic activity was found when increasing microcarrier concentration which may indicate that certain secondary metabolic pathways may be activated when increasing microcarrier concentration (Figure 2.5, Light). Notably, it may be possible that cells respond to stresses identified by membrane mechanosensors by activating internal contractile or tension forces through, for example myosin motors coupled with receptor-associated actin filaments [31]. Due to the experimental restrictions presented above, the results of Figure 2.5 were restricted to Spinner cultures with Synthemax II microcarriers. These results provide indications of possible general trends, but additional experiments would be necessary to confirm them.

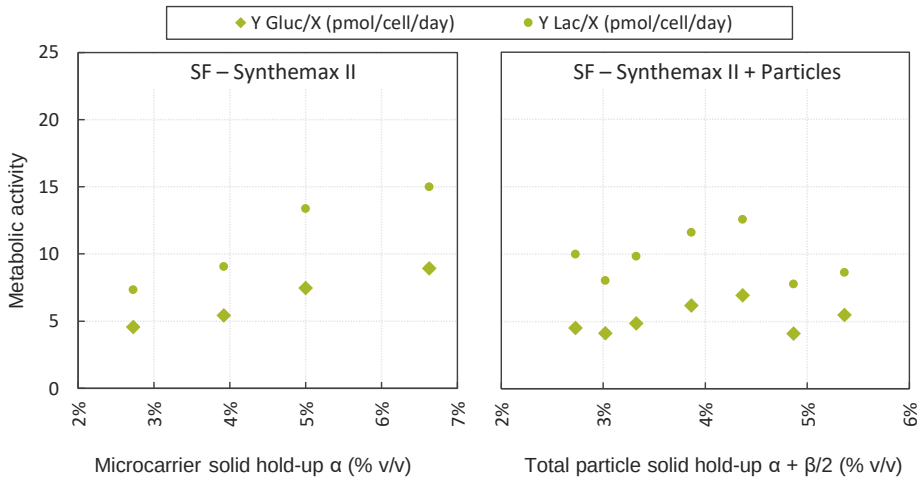

Figure 2.5: Kinetic metabolic parameters during MSC exponential growth at various Synthemax II MC concentrations in Spinner Flasks (SF). Cells were either grown at various MC concentrations (α) (left) or at a fixed MC concentration (α) with the addition of Plastic particles at various concentrations β (right).

Immunophenotyping

Immunophenotyping results tend to indicate a progressive degradation of MSC cell marker expression with a significant impact at high microcarrier concentrations (> 5 $\%_{v/v}$) for which the criteria proposed by the ISCT (> 95 %) are no longer verified for CD44 and CD73 markers which have been reported to be associated with cell proliferation and MSC homing (Figure 2.6). We should note, however, that the expression of these cell markers remain high (> 90 %) and that all other cell markers showed no sign of degradation. In addition, a significant over expression of the CD106 marker has been observed for cells cultivated with increasing mechanical constraints through

the addition of plastic particles during cell culture possibly indicating a progressive cell engagement towards certain vascular lineages as well as a slight under expression of CD44, CD73 and CD166 surface markers. These results indicate the degradation of MSCs when grown under high mechanical stress conditions through increasing particle concentration, particularly at high microcarrier concentrations ($> 5\ \%_{v/v}$).

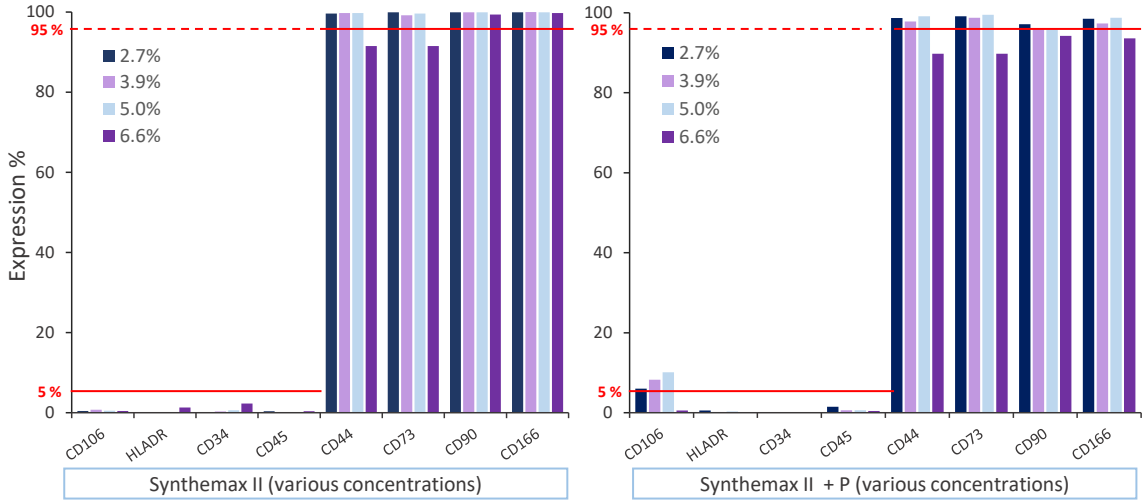

Figure 2.6: Percentage of cells expressing surface markers after expansion with various solid hold-up concentrations of Synthemax II microcarriers (left) or Synthemax II microcarriers and Plastic particles ($\alpha + \beta$).

Calculated real cell growth rates during microcarrier-based cell cultures

Evidence above seems to indicate that there may be fundamental underlying variations at stake when increasing microcarrier concentration in agitated conditions, even when no significant variation is observed when looking at the apparent growth rate in these cultures (Figure 2.2). To begin with, the kinetic decay constants due to microcarrier-microcarrier concentration were used to gain additional information on the theoretical growth rate which could occur without mechanical constraints in the cultures for which only the apparent growth rate could be observed (Figure 2.7). A theoretical growth rate much higher than the observed growth rate was found in experiments performed in Erlenmeyer Flasks using Synthemax II microcarriers for which the real growth rate was estimated as high as 1.2 day^{-1} in high microcarrier concentrations. These results indicate that the increased mechanical constraints in these conditions affect cell growth and, combined with metabolic data, may indicate that a higher metabolic activity per cell is required for cell maintenance.

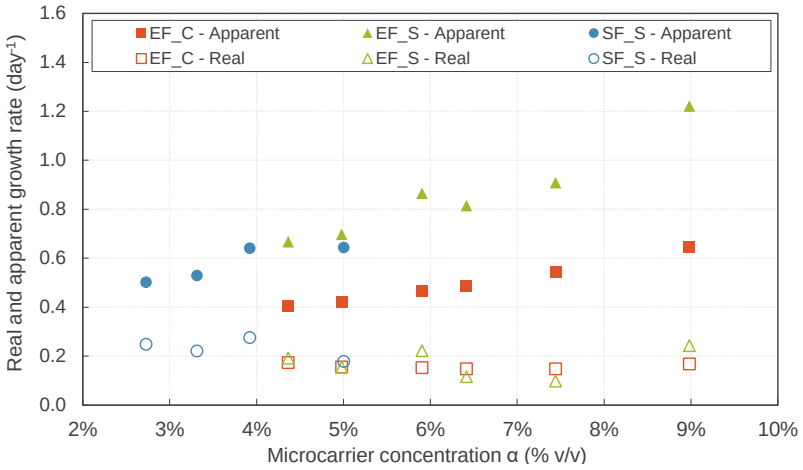

Figure 2.7: Apparent and calculated MSC growth rate at various microcarrier concentrations α in Erlenmeyer Flasks (EF) or Spinner Flasks (SF) and with either Cytodex 1 (C) or Synthemax II (S) microcarriers.

Calculating hydro-mechanical parameters

As suggested previously in extensive work performed on FS-4 cells grown on microcarriers, microcarrier collisions may arise through the action of turbulence in the fluid, and cell damage primarily occurs when the size of these turbulent eddies are comparable or smaller than the spacing between microcarriers [32]. In this mindset, the average inter-particle distance in each system h was calculated according to Equation 2.7 (presuming particles are spherical with mean sauter diameter D_{32}, homogeneously organized, and arranged in space in cubic order). This distance depends on the microcarrier and particle concentrations in each system as well as the packing limit α_m when particle distance reached 0 which was considered as 52% [33].

$$h = D_{32}\left[\left(\frac{\alpha_m}{\alpha}\right)^{1/3} - 1\right] \tag{2.7}$$

Lastly, the average Kolmogorov microscale of turbulence λ_k was calculated for each system and particle concentrations according to the method described in Appendix 2 using an approach previously described [23]. As previously described in literature, the impact of microcarrier interactions on cell growth typically begins to have an effect when the average distance between particles h is smaller than the size average smallest turbulent eddies in the system λ_k [16]. Since previous results indicate that a linear decrease in growth rate is observed when increasing microcarrier solid hold-up [32], we propose a linear model based on a volumetric approach to this ratio h/λ_k, a constant representing collisions within each experimental setup $k_{collision}$ and the minimal theoretical growth rate which could be observed when the particle concentration reaches the packing limit $\mu_{app_{lim}}$ (Equation 2.8). Consequently, the theoretical reduction in growth rate caused by microcarrier-microcarrier interactions may be theoretically calculated for a given microcarrier concentration if the microcarrier size distribution and

the agitation system chosen are sufficiently characterized.

$$\mu_{app}(\alpha) = k_{collision} \times \left(\frac{h}{\lambda_k}\right)^3 + \mu_{app_{lim}} \tag{2.8}$$

Modelling growth according to hydro-mechanical parameters

The data obtained with the addition of plastic particles is presented in Figure 2.8, left. A linear decrease in the standardized growth rate is observed when decreasing this ratio, and therefore when the inter-particle distance becomes closer to the size of the smallest turbulent eddies in the system. The model proposed (Equation 2.8) can be used to predict the MSC growth rate reduction (Figure 2.8, right and Table 2.3) and represents, to our knowledge, the first results predicting MSC growth rate reduction on microcarriers using a model based on the physical characteristics of the cell culture system. These results suggest that, in each geometrical setup, the decreased growth rate due to particle interactions will depend on the limit theoretical growth rate obtained when the particle concentration reaches the packing limit $\mu_{app_{lim}}$ and a constant representing these collisions within this experimental setup $k_{collision}$.

Table 2.3: Model parameters calculated to determine the impact of microcarrier-microcarrier interactions at various particle concentrations.

Culture System	**Collision constant** $k_{collision}$ (h^{-1})	**Theoretical standardized growth rate when at packing limit** $\mu_{app_{lim}}$ (h^{-1})
Erlenmeyer Flasks	0.03	0.31
Spinner Flasks	0.14	0.50

Conclusion

MSC cell culture on microcarriers performed with increasing quantities of plastic particles brought to light the fact that increasing the total particle concentration seemed to have a negative impact on growth. Results obtained with MSCs were found to be similar to previous studies performed with human fibroblasts grown on microcarriers with the addition of other particles : a linear relationship seems to exist between the observed apparent growth rate and the quantity of added particles [16]. Data concerning LDH secreted in the media throughout the exponential growth phase was used to notice that cell death was not significantly up-regulated to account for the decreased apparent growth rate. As a result, the most likely hypothesis may be that MSC mechanosensors can detect the increased mechanical constraints in these conditions (due to the added repeated friction and shocks caused by the added particles). Consequently, secondary metabolic pathways may be activated in response (thoroughly reviewed in [34]). For example myosin motors which can be activated to increase cell rigidity and counter

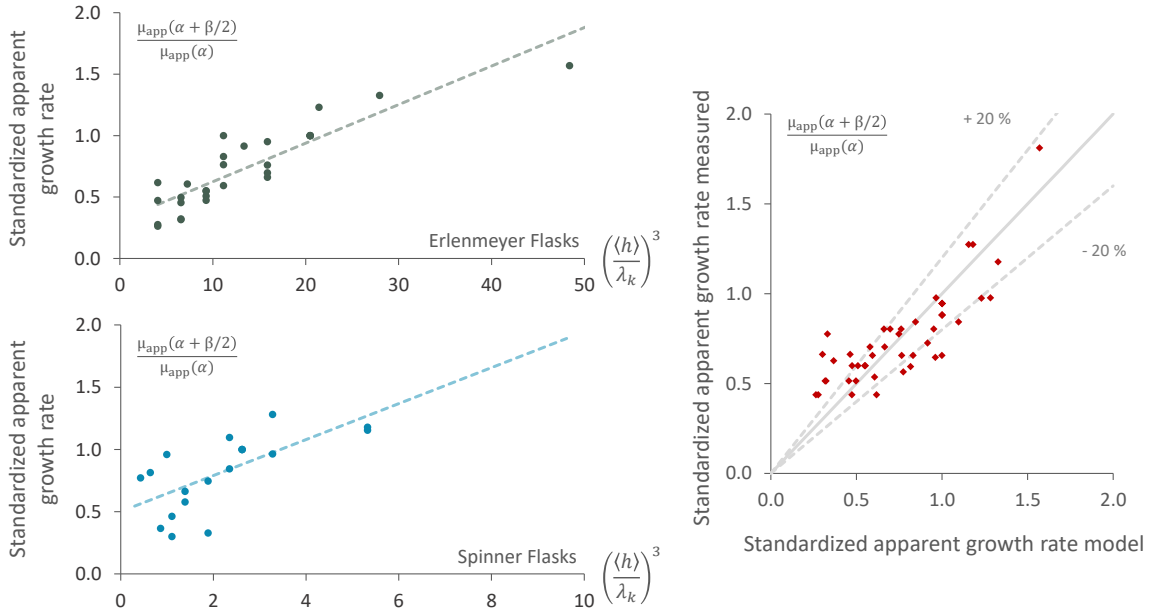

Figure 2.8: Apparent cell growth rate observed on Synthemax II and Cytodex 1 microcarriers in Erlenmeyer Flasks (EF) ($\alpha = 4.4\ \%_{v/v}$) or Spinner Flasks (SF) ($\alpha = 2.7\ \%_{v/v}$) and added Plastic particles (β) (left). Results are presented according to the average distance between particles calculated in each condition normalized to the average Kolmogorov turbulence microscale in each individual system. Linear fitting was then performed on the experimental data (right).

these mechanical constraints [31]. Cells may also be undergoing morphological changes to adapt to the environment generated with repeated mechanical stresses as it has been shown that the hydromechanical environment (such as extracellular matrix rigidity for example) maintains stem and progenitor cell pools in adult epidermal niches [35], or on the contrary, induces differentiation [36, 37]. Results indicating that similar levels of glucose were consumed per cell per day for a slower apparent growth seems to corroborate these results : the slower apparent cell growth indicates cells are dividing less fast and associated with gradual changes in secondary metabolisms. Notably, cells maintained high levels of MSC surface marker expression. However, a progressive degradation of CD44 and CD73 expression was observed in cultures performed with high particle concentrations. In addition, experiments performed with microcarriers of different sizes and rigidities, as well as different cell culture volumes and agitation systems seem to indicate that the impact of these mechanical constraints depend on these characteristics.

In parallel, experiments were performed at various microcarrier concentrations. In these experiments, little impact of the particle concentration was observed on the MSC apparent growth rate. However, information obtained above indicates that underlying cell mechano-transduction signals are possibly taking place with increasing particle concentration without being identifiable by simply observing the apparent growth rate. As a result, the theoretical real growth rate in the system is possibly significantly higher

than observed. In addition, a gradual degradation of the MSCs produced was observed, as well as a gradual increase in cell senescence and replicative inhibition (data not shown) even if the MSCs produced met the common MSC criterion suggested by the ISCT [26].

Lastly, we present first steps towards modelling and predicting growth reduction based on known physical properties of the cell cultures. Previous authors suggest that the increased death rate due to microcarrier interactions typically begins to have an effect when the average distance between particles h is smaller than the size average smallest turbulent eddies in the system λ_k [16]. The model we propose therefore takes into account the ratio between these physical characteristics and quite accurately allows us to predict the growth rate reduction based on these ratios.

2.1.5 Appendices

Appendix 1 : Average inoculation yield for experiments performed in Spinner and Erlenmeyer Flasks

Erlenmeyer Flasks						
Total solid hold-up	**4.4 %$_{v/v}$**	**5.0 %$_{v/v}$**	**5.9 %$_{v/v}$**	**6.4 %$_{v/v}$**	**7.4 %$_{v/v}$**	**9.0 %$_{v/v}$**
Cytodex-1 (no particles)	0.14	0.25	0.12	0.08	0.09	0.13
Cytodex-1 (particles)	0.52	0.67	0.46	0.41	0.45	0.60
Synthemax II (no particles)	0.15	0.12	0.09	0.10	0.14	0.11
Synthemax II (particles)	0.18	0.23	0.15	0.11	0.08	0.08
Spinner Flasks						
Total solid hold-up (%v/v)	**2.7 %$_{v/v}$**	**3.3 %$_{v/v}$**	**3.9 %$_{v/v}$**	**4.4 %$_{v/v}$**	**5.0 %$_{v/v}$**	**6.0 %$_{v/v}$**
Cytodex-1 (no particles)	N/A	N/A	N/A	N/A	N/A	N/A
Cytodex-1 (particles)	0.53	0.52	0.42	0.76	0.41	N/A
Synthemax II (no particles)	0.73	N/A	0.47	N/A	0.58	0.45
Synthemax II (particles)	0.55	0.51	0.36	0.42	N/A	0.30

Appendix 2 : Supplementary material and methods for the determination of hydrodynamic characteristics

Various studies have described bioreactor hydrodynamics [16, 38, 39] and the impact of cell interactions with turbulent eddies in conditions at or close to the just suspended state N_{js} (i.e. when all particles are in suspension and stay restless close to the bottom of the tank for only a few seconds) [40]. For this, the Kolmogorov microscale of turbulence (λ) can be calculated according to Equation 2.9 for which ν is the kinematic viscosity of the medium ($m^2\ s^{-1}$) and $\langle\ \varepsilon\ \rangle$ is the average local specific energy dissipation rate ($W\ kg^{-1}$). The kinematic viscosity of the medium was calculated for each microcarrier solid hold-up value (α) supposing homogeneously distributed spherical particles according to Equation 2.10 [41], a liquid viscosity (μ_{liq}) of 0.0007 Pas s^{-1}, and a liquid density (ρ_{liq}) of 993 kg m $^{-3}$.

$$\lambda = \left(\frac{\nu^3}{\langle\varepsilon\rangle}\right)^{1/4} \tag{2.9}$$

$$\nu(\alpha) = \frac{\mu(\alpha)}{\rho_{liq}} = \frac{\mu_{liq} \times (1 + 2.5\alpha + 5.2\alpha^2)}{\rho_{liq}} \tag{2.10}$$

In Erlenmeyer Flasks, the the average local specific energy dissipation rate $\langle\ \varepsilon_{EF}\ \rangle$ was calculated according to Equation 2.11 using the Newton number (Ne), agitation rate (N = 1.2 rps), flask diameter (d = 0.066 m) and liquid volume (V_L = 25 10$^-$6 m^3).

$$\langle\varepsilon_{EF}\rangle = \mathrm{Ne} \times N^3 \times d^4 \times V_L^{-2/3} \tag{2.11}$$

$$\mathrm{Ne} = 70\mathrm{Re}^{-1} + 25\mathrm{Re}^{-0.6} + 1.5\mathrm{Re}^{-0.2} \tag{2.12}$$

In Spinner flasks, Equation 2.15 was used to calculate $\langle\ \varepsilon_{SF}\ \rangle$ taking into account the impeller power number (N_p = 0.6), agitator diameter (d = 0.05 m) and liquid volume (V_L = 200 10$^-$6 m^3). We should note that an estimation of the power number in spinner flasks was performed via Computational Fluid Dynamics simulation of the specific geometrical setup.

CFD simulation was performed using the commercial finite solver ANSYS Fluent (ANSYS Inc., version 19.3). The steady-state with a pseudo-transient approach and the Moving Reference Frame (MRF) approach were used to model the impeller rotation, with an agitation rate set at 40 rpm. The Reynolds stress tensor was modelled by the standard k-epsilon turbulence model, completed by a Scalable wall function for the near-wall treatment. A wall boundary condition, i.e. zero-velocity, was applied for both vessel and impeller boundaries, while a symmetry condition was applied at the fluid surface. The mass and momentum conservation equations (Eq. (1) and (2)) were solved for the liquid phase supposing water properties at 37°C (density ρ = 993.3 kg m^{-3} and dynamic viscosity μ = 6.92 $\times 10^{-4}$ Pa s), with $\mathbf{v}$ is the fluid velocity, p the pressure and $\mathbf{g}$ the acceleration due to gravity.

$$\nabla \cdot (v) = 0 \tag{2.13}$$

$$\nabla \cdot (\rho\mathbf{v}\mathbf{v}) = -\nabla p^{-}\nabla \cdot \tau + \rho\mathbf{g} \tag{2.14}$$

The calculation domain consisted in 330,000 polyhedral meshes approximately. Pressure-velocity coupling was solved using a coupled method and pressure, momentum, turbulent kinetic energy and turbulent dissipation rate transport equations were discretized using 2nd order schemes. Convergence of the simulations was supposed when equation residuals were less than 10^{-5} and when steady-state liquid velocities

were stabilized. The volume averaged turbulent dissipation rate within the spinner flask was obtained using the following equation:

$$\langle \varepsilon_{SF} \rangle = N_p \times N^3 \times d^5 \times V_L^{-1} \tag{2.15}$$

2.1.6 Section summary

The experiments presented above provide elements which aimed at quantitatively describing the impact of microcarrier concentration on MSC growth and death kinetics, metabolism, and certain cell attributes. The study aimed at providing physical elements to explain the impact of increasing microcarrier concentration on defined output parameters in view of defining if the simple models provided could be adapter to larger equipment volumes in a regulated environment. For the experiments presented, modelling was shown to accurately predict the reduction of growth based on the average inter-particle distance in the system and the average Kolmogorov microscale of turbulence. Although the study was performed over a wide range of microcarrier concentrations, with two different modes of agitation and two microcarrier types, it is unclear to what extent these small scale studies can be extrapolated to larger stirred tank reactors. In addition, the characterization of the cells produced after their culture in these various conditions was not performed in detail. In order to further understand what mechanisms may be at stake when increasing hydro-mechanical constraints, the following paragraph will focus on defined quality attributes to determine if increasing microcarrier concentration could have an impact on the quality of the cells produced. The results of the paragraphs in this chapter will then be used in comparison with results obtained in larger STRs which will be the object of Chapter 4.

2.2 Impact of microcarrier concentration on MSC phenotypical attributes

2.2.1 Introduction

The aim of the present study is to provide a more precise description of the impact of microcarrier concentration on human MSC defined quality attributes. In this mindset, cells which were cultivated in the conditions described in the previous sub-chapter were used for a more through characterisation (including elements of genetic expression, senescence *etc.*). The cells analyzed were obtained at the end of the exponential phase of cultures performed on Synthemax II microcarriers in Spinner Flasks at different microcarrier concentrations and with or without the addition of various concentrations of plastic particles (as described in the previous chapter). In order to define the duration of the exponential growth phase, two experiments were performed in identical conditions beforehand and were grown until the stationary and death phases were achieved. Whereas previous results indicated that MSC growth was impacted by the addition of particles, and that certain elements of metabolism were also impacted as well a reduced expression of certain surface markers including CD44 and CD73 ; the following paragraphs will present complementary data concerning differentiation, genetic expression of certain differentiation precursor genes, clonogenicity and senescence.

2.2.2 Experimental approach

Cell extraction and expansion

The methods used to extract and expand MSCs are presented in the previous sub-chapter. Briefly, human mesenchymal stem cells (hMSC's) were extracted from the Wharton's Jelly of umbilical cords, expanded on standard T-Flasks for 5 to 10 days and then expanded on various concentrations of Synthemax II Dissolvable microcarriers (Corning, 7290) in Spinner Flasks (Schott bottles agitated at $N_{js} = 40$ rpm with Duran GL 45 stirred reactor agitators, Merck, Z680788-1KT). A range of microcarrier concentrations were used for cell culture (2.7 to 6.6 $\%_{v/v}$). The initial seeding density was kept constant at 7500 cells cm^{-2} regardless of the microcarrier concentration. In a separate set of experiments, a constant microcarrier concentration was used (2.7 $\%_{v/v}$) to which a range of plastic particles (Pall Solohill, P102-1521) were added on which cell growth was not observed and has been shown to be negligible [24].

MSC characterization after expansion on microcarriers

MSCs expanded on Synthemax II MCs in SF (highest final cell concentration obtained) were detached from microcarriers at the end of the exponential growth phase and cryopreserved at a concentration of $5{\times}10^6$ cells mL^{-1}. These cells were then thawed and

cultured for 3 days before characterization according to the general guidelines provided by the International Society for Cellular Therapy (ISCT) [26]. Plastic adhesion was verified at this stage. It should be kept in mind that it is likely that these quality attributes are not sufficient to guarantee therapeutic potency [42], but results impacting these criteria should be carefully taken into consideration. Complementary criteria were also evaluated in view of further characterizing the produced cells (summarized in Table 2.4).

Table 2.4: MSC quality attributes used for cell characterization after culture on Synthemax II microcarriers in spinner flasks (SF). Quality testing was performed at the end of the exponential phase of MSC culture after cryopreservation of the produced cells.

	Criteria	**Method evaluated in the present work**
Minimal criteria [42]	Adherence to plastic	Growth on standard T-Flasks
	Specific surface marker expression	Flow cytometry (Gallios, Beckman coulter and specific antibodies) ($\geqslant$ 95%)
	Differentiation capacity	Growth in standard differentiation medium followed by microscopic observation and photo analysis
Complementary criteria	Growth	Modelling experimental data, metabolic analysis
	Stemness	CFU-F quantification
	Senescence	β-galactosidase staining, RT-qPCR of specific genes
	Genetic expression profiles	Pre-differentiation quantification towards certain lineages through RT-qPCR

Surface Marker Expression. Approximately 1×10^5 cells were re-suspended in 100 μL phosphate buffer saline (PBS) supplemented with bovine serum albumin (BSA) and incubated with specific antibodies (Table 2.5) for 1 hour at room temperature. After incubation, MSCs were washed with PBS, centrifuged at 300 g for 5 minutes and resuspended in 250 μL of 1% paraformaldehyde (PFA) until analysis by FACS flow cytometry (Beckman Coulter, Gallios) according to methods previously described [27].

Differentiation tests. 48-well tissue culture treated flat bottom plates (Eppendorf, 1403) were seeded in triplicate wells according to kit specifications (Thermo Fisher scientific, A1007001, A1007101 and A1007201) and grown in specific differentiation media which was changed every 2-3 days per kit recommendations for the recommended culture duration. Samples were then fixed with 4 $\%_{v/v}$ paraformaldehyde (PFA) at room temperature. Adipocytes were stained with 1 $\%_{v/v}$ Oil Red O solution, Osteoblasts were stained with 0.5 $\%_{v/v}$ Alizarin Red solution, Chondrocytes were stained with 1 $\%_{v/v}$ Alician Blue solution. Samples were photographed in triplicate analysis during light microscopy observation (magnification $\times$ 200). The surface occupied by differentiated cells was then quantified using the the imageJ software and the ratio of colored

Table 2.5: Specific antibodies used for cytometric analysis of MSCs expanded and description of the Cluster Differentiation (CD) targets.

Antibody	Description	Supplier	Clone
CD-106-PE	Vascular cell adhesion molecule-1 (VCAM-1), mediates adhesion and signal transduction [43]	BD Pharmingen, 555647	51-10C9
HLADR-FITC	MHC class II cell surface receptor	Beckman coulter, IM0463U	B8.12.2
CD34-PE	Cell surface glycoprotein and cell adhesion factor, regulates cell proliferation and differentiation [44]	BD Pharmingen, 555822	581
CD45-FITC	Transmembrane protein tyrosine phosphatase, regulates lymphocyte maturation stages, marker of hematopoietic lineages [45]	DAKO, F0861	T29/33
CD44-FITC	Homing cell adhesion molecule (HCAM), cell adhesion, migration, homing, proliferation and apoptosis of stem cells [46]	Beckman Coulter, IM1219U	J.173
CD73-PE	Ecto-5-nucleotidase enzyme asoociated with cell proliferation	BD Pharmingen, 550257	AD2
CD90-FITC	Thy-1 cell surface glycoprotein, role in cell-cell and cell-matrix interactions and cell motility [47]	Beckman Coulter, IM1839U	2G5 F15-426165
CD166-PE	ALCAM adhesion protein, role in tight cell-to-cell interaction and regulation of stem cell differentiation [48]	Beckman Coulter, A22361	3A6

cells was calculated compared to the control conditions (cells which had not been cultivated on microcarriers).

Clonogenicity. Tissue culture treated plates (Thermo Fisher scientific, nuclon surface 140675) were inoculated at a concentration of 2 cells per cm^2. After 14 days of culture in the complete medium used for cell culture on microcarriers, colonies were revealed through Crystal violet staining 3 $\%_{w/v}$ (CAS 548-62-9) and colonies were manually counted. The percentage of cells which formed colonies was then calculated for each condition.

Genetic expression profiles measured by RT-qPCR. Total RNAs were extracted from each cell sample using the RNeasy Mini Kit (Qiagen, 74104) and quantified by absorbance measurement (Thermo Fisher scientific, nanoDrop 2000). Subsequently, 1 μg of the DNA sample was used for cDNA synthesis using the QuantiTect Reverse Transcription kit (Qiagen 205311). Genes were amplified by qPCR (Thermo Fisher scientific, pikoREAL) using a Maxima SYBR Green qPCR Master mix (Thermo Fisher scientific, 11873913, specific primers (Table 2.6 provided by Eurogentech). A negative control was performed in the absence of RNA matrix to validate the absence of contamination of the reagents used. Results were analyzed by comparing genetic expression with the expression of the housekeeping gene *EEF1A1* and Equations 2.16, 2.17 and 2.18 (Thermo Fisher scientific, pikoReal Software 2.1). The amplicon size and purity was verified by comparing the amplicon melting temperature to the theoretical melting temperature calculated.

$$R = 2^{-\Delta\Delta C_q} \quad \text{with} \quad \Delta\Delta C_q = \Delta C_{q_{gene}} - \Delta C_{q_{EEF1A1}} \tag{2.16}$$

$$\Delta C_{q_{gene}} = C_{q_{gene(sample)}} - C_{q_{gene(reference)}} \tag{2.17}$$

$$\Delta C_{q_{EEF1A1}} = C_{q_{EEF1A1(sample)}} - C_{q_{EEF1A1(reference)}} \tag{2.18}$$

Table 2.6: Primers used for RT-qPCR quantification MSC gene expression

Information	**Gene**	**Primers used**	**Amplicon size**
Housekeeping gene	*EEF1A1*	F ACACGGCTCACATTGCATGC R ACAGCAAAGCGACCCAAAGG	187
p21 protein (proliferation inhibition)	*CDKN1A*	F GCATGACAGATTTCTACCACTCC R GACTAAGGCAGAAGATGTAGAGC	133
Adipocyte fatty acid binding protein	*FABP4*	F TGGGCCAGGAATTTGACGAAG R TCAACGTCCCTTGGCTTATGC	215
Transcription Factor (osteoblasts)	*RUNX2*	F CCCGTGGCCTTCAAGGT R CGTTACCCGCCATGACAGTA	73
Transcription Factor (chondroblasts)	*SOX9*	F GAGCAGACGCACATCTC R CCTGGGATTGCCCCGA	133

Senescence characterization.

- *β-galactosidase staining.* 48-well tissue culture treated plates (Eppendorf, 1403) were inoculated at a concentration of 3000 cells per cm^2 in complete growth medium used for cell culture on microcarriers. Cells were then revealed according to the staining kit (Thermo Fisher scientific, 75707). Briefly, cells were fixed with a 1 % PFA solution and then incubated with β-galactosidase assay regent and observed under light microscopy (magnification × 200). 5 independent photos were taken and colored cells were counted using the ImageJ software. Results are expressed as an over expression of β-galactosidase cell percentage compared to cells which have not undergone microcarrier culture.

- *p21 protein expression.* Cell expression of p21 protein was quantified by RT-qPCR (*EEF1A1* gene) according to the method described above and primers in Table 2.6. The expression of p21 has typically been associated with increased senescent MSC profiles which typically have reduced cell proliferation capacities [49].

2.2.3 Results and discussion

Plastic Adherence and Surface marker expression

The capacity of cells to maintain their plastic adherence was verified in all conditions apart from extremely high particle concentrations for which a significant impact on this quality attribute was observed (> 5 %). As a result, the other characteristics were no longer verified for this condition. Results tend to indicate a progressive degradation of MSC cell marker expression with a significant impact at high microcarrier concentrations ($> 5\ \%_{v/v}$) for which the criteria proposed by the ISCT (> 95 %) are no longer verified for CD44 and CD73 markers which have been reported to be associated with cell proliferation and MSC homing (see paragraph 2.1.4 for results and further details). It is important to note that the expression of the MSC surface markers remained high in all of the conditions tested but rather that the expression of certain markers gradually decreases with increasing mechanical constraints. Accordingly, and considering the results obtained on growth and death kinetic constants, the impact of microcarrier-microcarrier collisions seems to progressively increase with increasing microcarrier concentration.

Cell Differentiation Potential

Cells grown on only Synthemax II microcarriers had a greater ability to differentiate into osteocytes when grown at high microcarrier concentrations while their capacity to differentiate into adipocytes seemed to be inhibited (Figure 2.9). In all of the conditions studied, the ability of MSCs to develop a pellet when in presence of medium for chondrocyte differentiation medium was demonstrated but chondrocyte staining was not performed successfully and chondrogenic potential was not quantified. However for both other cell types and in all conditions, the differentiation potential seemed to be lower than in the control conditions which had not undergone growth on microcarriers, indicating a possible degradation of stemness during their culture in agitated conditions. In addition, cell cultures grown with increasing plastic particle concentrations seemed to have a reduced osteocyte and adipocyte differentiation potential indicating a significant impact of microcarrier collisions on WJ-MSC attributes (Figure 2.9). It can be noted that the increased osteogenic differentiation in cases of low hydrostatic pressures has previously be noted in literature [50, 51] as well as an increased chondrogenic potential and a decreased adipogenic potential. The results obtained seem to correlate well with the literature although additional testing would be required to validate this hypothesis, as well as information on MSC chondrogenic potential.

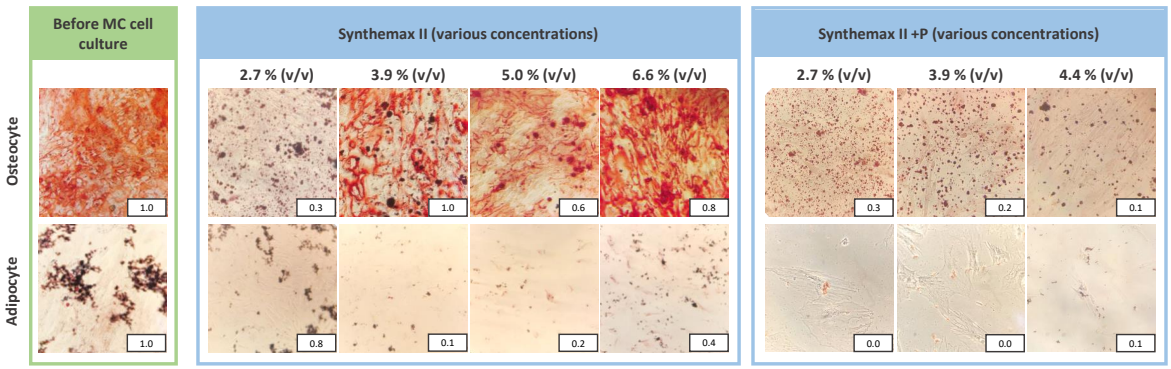

Figure 2.9: Cell differentiation into osteocytes and adipocytes depending on MC concentration. Cells were grown in specific differentiation media and then stained accordingly. The colored surface was then calculated using the ImageJ software and the percentage of colored pixels standardized to the control condition was then calculated (indicated on the bottom right of each image).

Genetic expression profiles

In order to gain further information on activated gene expression during MSC cultures, the expression of three differentiation genes was quantified by RT-qPCR. Accordingly, the expression of *FABP4* (adipocyte fatty acid binding protein), *RUNX2* (Osteoblast transcription factor) and *SOX9* (Chrondroblast transcription factor) was measured to define if MSC cell culture at different microcarrier concentrations activated the expression of certain of these genes, which would indicate that the MSCs produced may have triggered their differentiation towards one or several differentiated lineages due to varying levels of mechanical stresses.

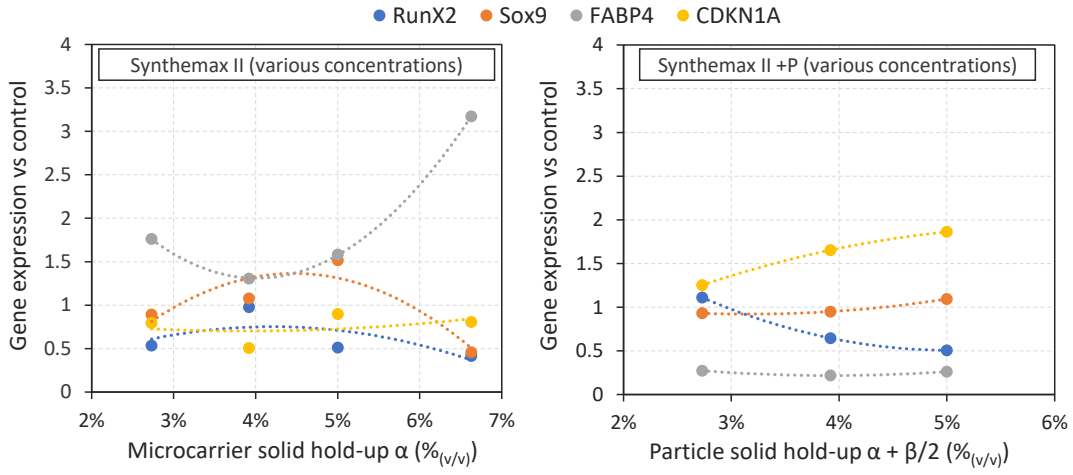

Figure 2.10: Expression of pre-differentiation and senescence genes after growth on microcarriers (measured by RT-qPCR). Gene expression was normalized according to the expression of reference cell genetic expression (cells which have not undergone microcarrier expansion) and the housekeeping gene *EEF1A1*.

In cell cultures performed on Synthemax II microcarriers at various concentrations, no significant evolution of the expression of either *RunX2* or *Sox9* were observed and

expression of these genes were found to be slightly under expressed compared to the control cells which had not undergone cell growth on microcarriers (expression varied between 0.5 and 1.5 times the expression in the control cells (Figure 2.10, left)). Expression of the *FABP4* gene was found to be over expressed in all microcarrier conditions with a general trend in over-expression when the microcarrier concentration was increased, possibly indicating that cells may be undergoing differentiation in these conditions oriented towards adipocyte lineages. An over-expression by a factor of 3 compared to the control condition was observed for this gene in the highest microcarrier concentration. In parallel, characterization of genetic expression of cells grown on Synthemax II microcarriers with various concentrations of plastic particles seems to indicate a decrease in *RunX2* expression with increasing microcarrier concentration (Osteoblast transcription factor) and an under-expression of the *FABP4* gene compared to the control cells (Figure 2.10, right). These results are controversial when considering existing literature on the impact of mechanical stimuli on genetic expression. For example, an over-expression of the *RunX2* gene has been observed in BM-MSCs grown with low levels of mechanical stimuli throughout cell culture [52]. Interestingly, it can be noted that the trends observed with the addition of plastic particles do not follow the trends observed when only increasing microcarrier concentration (for example concerning the *FABP4* gene). These results may indicate that, physiologically, cells may not respond in the same manner to mechanical stresses caused by the addition of particles compared to mechanical stresses caused by increasing microcarrier concentration. Complementary data would be required to further understand the physiological mechanisms in these conditions.

Clonogenicity

The ability of cells to generate colonies from single cells (clonogenicity) was verified in all conditions (*i.e.* colonies were observed in all conditions). Quantitatively, no specific trend on the clonogenicity was observed by varying the microcarrier concentration or adding plastic particles to the cell culture. In all experiments, the percentage of cells which formed colonies remained similar to the control condition indicating cells had maintained their capacity to form colonies after microcarrier cell culture (Figure 2.11). It can be noted that a slightly higher clonogenic capacity was observed for cells grown on microcarriers with varying levels of Plastic particles but it is not yet clear if the difference observed is significant. The fact that this attribute was verified in all conditions is however important to state that the MSCs produced remained viable, dividing and clonogenic.

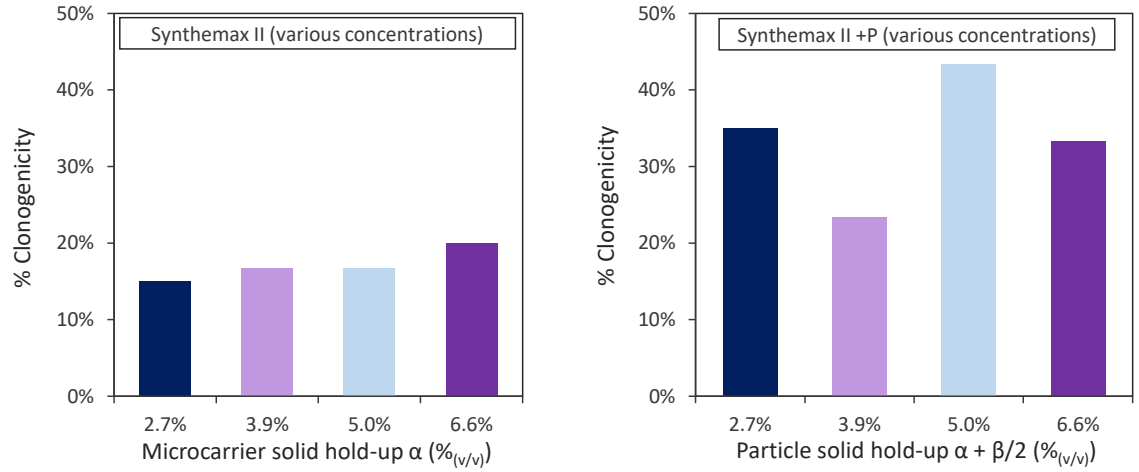

Figure 2.11: MSC clonogenicity after growth on microcarriers.

Senescence Characterization

Senescence was characterized using two orthogonal methods (RT-qPCR) of the genetic expression of the p21 protein which is typically associated with an inhibition of proliferation (*CDKN1A* gene) and β-Galactosidase staining. Results tend to indicate no significant cell senescence in cultures which have been expanded on microcarriers compared to the control cells which have not undergone cell culture on microcarriers (Figure 2.12) at the exception of high microcarrier concentrations ($> 5\ \%_{v/v}$). On the other hand, a significant impact of microcarrier collisions was found in cultures which were performed with various concentrations of plastic particles added for which the *CDKN1A* gene was found to be over expressed compared to the control cells and which express significantly higher β-Galactosidase staining compared to cells which had only been cultivated in static cultures. These elements may indicate that increasing mechanical stresses caused by the addition of Plastic particles may cause premature senescent phenotypes.

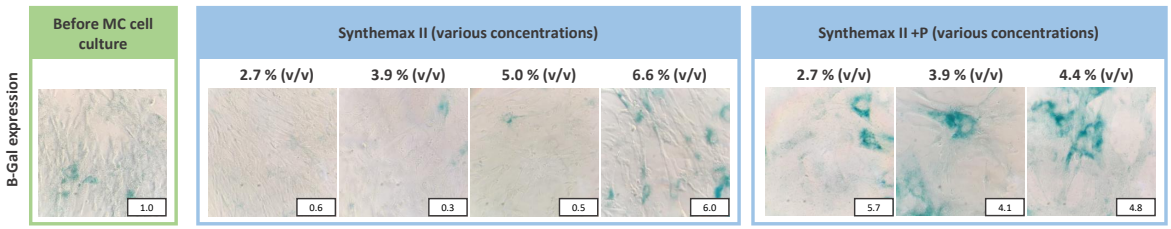

Figure 2.12: Cell senescence characterization through β-galactosidase staining of cells cultured in standard T-Flasks. The colored surface was then calculated using the ImageJ software and the percentage of colored pixels standardized to the control condition was then calculated (indicated on the bottom right of each image).

2.2.4 Section summary

The results presented above provide complementary information on how microcarrier and particle concentration can impact certain MSC attributes. Although the results should be taken with careful consideration since determining specific cell quality was not the object of this work (considering the complexity of such a task), they provide a basis on which other studies may be built upon. Notably, results tend to indicate a progressive degradation of MSC quality with increasing mechanical constraints (increasing senescent phenotypes, reduced differentiation capacity, over-expression of certain genes indicating early stages of differentiation towards osteogenic lineage *etc*) caused by microcarrier concentration increase. As a result, this should be kept in mind when developing novel processes to expand MSCs on microcarriers. The specific impact of micorcarrier concentration may also need to be evaluated independently if another microcarrier type is used.

2.3 Chapter overview

The aim of this chapter was to define, at small scales and for a wide range of microcarrier concentrations, what may be the impact of increasing microcarrier concentration on MSC dynamic parameters such as growth rate, death rate, metabolism *etc.* but also final cell attributes such as senescence, viability, clonogenicity, stemness *etc.* To begin with, MSC apparent growth was measured in Erlenmeyer Flasks and in Spinner Flasks when cells were grown on various concentrations of Cytodex 1 microcarriers or Synthemax II microcarriers. These experiments indicated that little impact of increasing microcarrier concentration was observed on the apparent growth rate. However, parallel experiments performed with increasing concentrations of plastic particles on which MSCs could not expand indicated a linear decrease in the apparent growth rate according to the added particle concentration. Accordingly, the results suggest that there may be underlying mechanisms ongoing during MSC expansion when the cells are subject to hydro-mechanical constraints such as microcarrier-microcarrier collisions. In parallel, conditions where either (A) no particles were added but MSCs were cultivated in increasing microcarrier concentrations or (B) MSCs grown on microcarriers and particles were added to increase mechanical stresses; a progressive degradation of certain cell attributes were noted, also indicating that underlying mechanisms may be at stake. Although the experiments were performed at small scales, the wide range of parameters tested provided information which could be of use when further developing MSC expansion processes. In addition, the work presented in this chapter was used as a basis to the work which will be presented in Chapter 4 concerning MSC expansion on microcarriers in bioreactors.

Bibliography

[1] C. Maillot, N. De Isla, C. Loubiere, D. Toye, and E. Olmos. Impact of microcarrier concentration on mesenchymal stem cell growth and death: Experiments and modelling. *Biotechnology and Bioengineering*, 2022.

[2] D. E. Rodriguez-Fuentes, L. E. Fernandez-Garza, J. A. Samia-Meza, S. A. Barrera-Barrera, A. I. Caplan, and H. A. Barrera-Saldana. Mesenchymal stem cells current clinical applications: a systematic review. *Archives of Medical Research*, 52(1):93–101, 2021.

[3] A. Trounson and C. McDonald. Stem cell therapies in clinical trials: progress and challenges. *Cell Stem Cell*, 17:11–22, 2015.

[4] P. Bianco and P. G. Robey. Stem cells in tissue engineering. *Nature*, 414:4, 2001.

[5] J. Ringe, C. Kaps, G.-R. Burmester, and M. Sittinger. Stem cells for regenerative medicine: advances in the engineering of tissues and organs. *Naturwissenschaften*, 89(8):338–351, 2002.

[6] M. Riazifar, E. J. Pone, J. Lötvall, and W. Zhao. Stem cell extracellular vesicles: extended messages of regeneration. *Annual Review Pharmacology*, 57:125–154, 2017.

[7] A. K.-L. Chen, S. Reuveny, and S. K. W. Oh. Application of human mesenchymal and pluripotent stem cell microcarrier cultures in cellular therapy: achievements and future direction. *Biotechnology advances*, 31(7):1032–1046, 2013.

[8] C. Ikebe and K. Suzuki. Mesenchymal stem cells for regenerative therapy: optimization of cell preparation protocols. *BioMed research international*, 2014, 2014.

[9] C. Maillot, C. Sion, N. De Isla, D. Toye, and E. Olmos. Quality by design to define critical process parameters for mesenchymal stem cell expansion. *Biotechnology Advances*, 50:107765, 2021.

[10] B. Parekkadan and J. M. Milwid. Mesenchymal stem cells as therapeutics. *Annual review of biomedical engineering*, 12:87, 2010.

[11] P. Godara, C. D. McFarland, and R. E. Nordon. Design of bioreactors for mesenchymal stem cell tissue engineering. *J Chem Tech Biotechnol*, 83:408–420, 2008.

[12] A. I. Hoch and J. K. Leach. Concise review: optimizing expansion of bone marrow mesenchymal stem/stromal cells for clinical applications. *Stem Cell Translational Medicine*, 3:643–652, 2014.

[13] C. McKee and G. R. Chaudhry. Advances and challenges in stem cell culture. *Colloids and Surfaces B: Biointerfaces*, 159:62–77, 2017.

[14] A. L. Russell, R. C. Lefavor, and A. C. Zubair. Characterization and cost–benefit analysis of automated bioreactor-expanded mesenchymal stem cells for clinical applications. *Transfusion*, 58(10):2374–2382, 2018.

[15] W. Hu, J. Meier, and D. Wang. A mechanistic analysis of the inoculum requirement for the cultivation of mammalian cells on microcarriers. *Biotechnology and bioengineering*, 27(5):585–595, 1985.

[16] M. S. Croughan, J.-F. P. Hamel, and D. I. Wang. Effects of microcarrier concentration in animal cell culture. *Biotechnology and bioengineering*, 32(8):975–982, 1988.

[17] C. J. Hewitt, K. Lee, A. W. Nienow, R. J. Thomas, M. Smith, and C. R. Thomas. Expansion of human mesenchymal stem cells on microcarriers. *Biotechnology Letters*, page 31, 2011.

[18] A. K.-L. Chen, Y. K. Chew, H. Y. Tan, S. Reuveny, and S. K. W. Oh. Increasing efficiency of human mesenchymal stromal cell culture by optimization of microcarrier concentration and design of medium feed. *Cytotherapy*, 17(2):163–173, 2015.

[19] R. S. Cherry and E. T. Papoutsakis. Physical mechanisms of cell damage in microcarrier cell culture bioreactors. *Biotechnology and bioengineering*, 32(8):1001–1014, 1988.

[20] L. Reppel. *Potentialité des cellules stromales de la gelée de Wharton en ingénierie du cartillage*. PhD thesis, Universite de Lorraine, 2014.

[21] C. Martin. *Étude des procédés d'amplification de cellules souches mésenchymateuses humaines*. PhD thesis, Universite de Lorraine, 2017.

[22] S. Laner-Plamberger, T. Lener, D. Schmid, D. A. Streif, T. Salzer, M. Öller, C. Hauser-Kronberger, T. Fischer, V. R. Jacobs, K. Schallmoser, et al. Mechanical fibrinogen-depletion supports heparin-free mesenchymal stem cell propagation in human platelet lysate. *Journal of translational medicine*, 13(1):1–10, 2015.

[23] C. Sion, C. Loubière, M. K. Wlodarczyk-Biegun, N. Davoudi, C. Muller-Renno, E. Guedon, I. Chevalot, and E. Olmos. Effects of microcarriers addition and mixing on WJ-MSC culture in bioreactors. *Biochemical Engineering Journal*, 157:107521, 2020.

[24] C. Loubière, C. Sion, N. De Isla, L. Reppel, E. Guedon, I. Chevalot, and E. Olmos. Impact of the type of microcarrier and agitation modes on the expansion performances of mesenchymal stem cells derived from umbilical cord. *Biotechnology progress*, 35(6):e2887, 2019.

[25] T. N. Zwietering. Suspending of solid particles in liquid by agitators. *Chemical engineering science*, 8(3-4):244–253, 1958.

[26] M. Dominici, K. Le Blanc, I. Mueller, I. Slaper-Cortenbach, F. Marini, D. Krause, R. Deans, A. Keating, D. Prockop, and E. Horwitz. Minimal criteria for defining multipotent mesenchymal stromal cells. the international society for cellular therapy position statement. *Cytotherapy*, 8:315–317, 2006.

[27] C. Sion, D. Ghannoum, B. Ebel, F. Gallo, N. de Isla, E. Guedon, I. Chevalot, and E. Olmos. A new perfusion mode

of culture for wj-mscs expansion in a stirred and online monitored bioreactor. *Biotechnology and Bioengineering*, 118(11):4453–4464, 2021.

[28] V. Frank, S. Kaufmann, R. Wright, P. Horn, H. Y. Yoshikawa, P. Wuchter, J. Madsen, A. L. Lewis, S. P. Armes, A. D. Ho, et al. Frequent mechanical stress suppresses proliferation of mesenchymal stem cells from human bone marrow without loss of multipotency. *Scientific reports*, 6(1):1–12, 2016.

[29] R. S. Cherry and E. T. Papoutsakis. Hydrodynamic effects on cells in agitated tissue culture reactors. *Bioprocess engineering*, 1(1), 1986.

[30] A. A. Öncül. *Simulation of interacting populations in inhomogeneous flows using reduced models*. PhD thesis, Magdeburg, University, 2010.

[31] P. Romani, L. Valcarcel-Jimenez, C. Frezza, and S. Dupont. Crosstalk between mechanotransduction and metabolism. *Nature Reviews Molecular Cell Biology*, 22(1):22–38, 2021.

[32] M. S. Croughan. *Hydrodynamic effects on animal cells in microcarrier bioreactors*. PhD thesis, Massachusetts Institute of Technology, 1988.

[33] R. Mishra, J. Militky, V. Baheti, J. Huang, B. Kale, M. Venkataraman, V. Bele, V. Arumugam, G. Zhu, and Y. Wang. The production, characterization and applications of nanoparticles in the textile industry. *Textile Progress*, 46(2):133–226, 2014.

[34] K. H. Vining and D. J. Mooney. Mechanical forces direct stem cell behaviour in development and regeneration. *Nature reviews Molecular cell biology*, 18(12):728–742, 2017.

[35] A. J. Zhu, I. Haase, and F. M. Watt. Signaling via β1 integrins and mitogen-activated protein kinase determines human epidermal stem cell fate in vitro. *Proceedings of the National Academy of Sciences*, 96(12):6728–6733, 1999.

[36] N. Huebsch, P. R. Arany, A. S. Mao, D. Shvartsman, O. A. Ali, S. A. Bencherif, J. Rivera-Feliciano, and D. J. Mooney. Harnessing traction-mediated manipulation of the cell/matrix interface to control stem-cell fate. *Nature materials*, 9(6):518–526, 2010.

[37] A. J. Engler, S. Sen, H. L. Sweeney, and D. E. Discher. Matrix elasticity directs stem cell lineage specification. *Cell*, 126(4):677–689, 2006.

[38] H. W. Leung, A. Chen, A. B. Choo, S. Reuveny, and S. K. Oh. Agitation can induce differentiation of human pluripotent stem cells in microcarrier cultures. *Tissue Engineering Part C: Methods*, 17:165–172, 2010.

[39] A. Delafosse, C. Loubière, S. Calvo, D. Toye, and E. Olmos. Solid-liquid suspension of microcarriers in stirred tank bioreactor – experimental and numerical analysis. *Chemical Engineering Science*, 180:52–63, 2018.

[40] A.-C. Tsai, R. Jeske, X. Chen, X. Yuan, and Y. Li. Influence of microenvironment on mesenchymal stem cell therapeutic potency: From planar culture to microcarriers. *Frontiers in Bioengineering and Biotechnology*, 8:640, 2020.

[41] G. K. Batchelor and J. T. Green. The determination of the bulk stress in a suspension of spherical particles to order c2. *Journal of Fluid Mechanics*, 56(3):401–427, 1972.

[42] M. Mendicino, A. M. Bailey, K. Wonnacott, R. K. Puri, and S. R. Bauer. MSC-based product characterization for clinical trials: an FDA perspective. *Cell Stem Cell*, 14:141–145, 2014.

[43] B. Pepinsky, C. Hession, L. Chen, P. Moy, L. Burkly, A. Jakubowski, E. Chow, C. Benjamin, G. Chi-Rosso, and S. Luhowskyj. Structure/function studies on vascular cell adhesion molecule-1. *Journal of Biological Chemistry*, 267(25):17820–17826, 1992.

[44] L. E. Sidney, M. J. Branch, S. E. Dunphy, H. S. Dua, and A. Hopkinson. Concise review: Evidence for CD34 as a common marker for diverse progenitors. *Stem Cells*, 32:1380–1389, 2014.

[45] S. Shivtiel, O. Kollet, K. Lapid, A. Schajnovitz, P. Goichberg, A. Kalinkovich, E. Shezen, M. Tesio, N. Netzer, I. Petit, A. Sharir, and T. Lapidot. Cd45 regulates retention, motility, and numbers of hematopoietic progenitors, and affects osteoclast remodeling of metaphyseal trabecules. *Journal of Experimental Medicine*, 205:2381–2395, 2008.

[46] M. Schieker, C. Pautke, K. Reitz, I. Hemraj, P. Neth, W. Mutschler, and S. Milz. The use of four-colour immunofluorescence techniques to identify mesenchymal stem cells. *Journal of Anatomy*, 204(2):133–139, 2004.

[47] T. A. Rege and J. S. Hagood. Thy-1 as a regulator of cell-cell and cell-matrix interactions in axon regeneration, apoptosis, adhesion, migration, cancer, and fibrosis. *The FASEB Journal*, 20:1045–1054, 2006.

[48] O. Ohneda, K. Ohneda, F. Arai, J. Lee, T. Miyamoto, Y. Fukushima, D. Dowbenko, L. A. Lasky, and T. Suda. ALCAM (CD166): its role in hematopoietic and endothelial development. *Blood*, 98:2134–2142, 2001.

[49] Long noncoding RNA-p21 modulates cellular senescence via the wnt/beta-catenin signaling pathway in mesenchymal stem cells. 16:7039–7047.

[50] P. R. Blenman, D. R. Carter, and G. S. Beaupre. Role of mechanical loading in the progressive ossification of a fracture callus. *Journal of Orthopaedic Research*, 7(3):398–407, 1989.

[51] D. R. Carter, G. S. Beaupré, N. J. Giori, and J. A. Helms. Mechanobiology of skeletal regeneration. *Clinical Orthopaedics and Related Research (1976-2007)*, 355:S41–S55, 1998.

[52] F. Song, D. Jiang, T. Wang, Y. Wang, Y. Lou, Y. Zhang, H. Ma, and Y. Kang. Mechanical stress regulates osteogenesis and adipogenesis of rat mesenchymal stem cells through pi3k/akt/gsk-3 beta-catenin signaling pathway. *BioMed research international*, 2017, 2017.

Chapter 3

Characterizing particle distributions and collisions using light attenuation & acoustic measurements

Contents

3.1 Introduction

3.1.1 Chapter overview

The aim of this chapter is to present experimental approaches to estimate particle distributions and collisions in a Stirred Tank Reactor (STR). For this, both the frequency with which particles collide and the intensity of these collisions are important from a process perspective in view of determining, *in fine*, the stress that Mesenchymal Stem Cells (MSCs) may perceive during their culture on microcarriers (MCs). To begin with, the bioreactor used will be described as well as a characterization of the liquid phase hydrodynamics. This preliminary work was performed by simulating the expected distribution of physical liquid phase characteristics including velocity or the Kolmogorov microscale of turbulence λ_k. In addition, a similar description of the solid phase was performed by calculating, for example, the minimal agitation required to suspend particles N_{js}, or the distribution of local Stokes number St.

Subsequently, **local particle concentration gradients within the STR were determined by measuring the attenuation of light by Cytodex-1 microcarriers in suspension**. As the frequency with which particles collide should depend on local particle concentration, having information on particle distribution may be used to predict elements of particle-particle collision probabilities. Particular consideration was accorded to **particle suspension dynamics (*i.e.* suspension of the particle bed from the bottom of the STR into a steady state where all of the particles are in suspension)**. Accordingly, the evolution of particle concentration spatial distribution during suspension was described. In addition, the spatial distribution of a characteristic suspension time τ_{95}, as well as the temporal evolution of a homogenization index σ, were obtained from these measurements. Experiments were performed for a range of concentrations of 1 to 30 g L^{-1} and for suspension performed at N_{js} and above N_{js}. Lastly, it is expected that cell death would be diminished by minimizing the time that MSCs are subjected to friction and/or microcarrier collisions. Accordingly, this work proposes to identify local over-concentration through a factor Γ. Describing the spatial distribution and evolution over time of Γ should help when comparing different suspension processes with one another, keeping in mind that minimizing Γ may, in theory, benefit MSC proliferation. Microcarrier suspension dynamics in STRs remains a domain which substantially lacks fundamental research applied to mammalian cell cultures. The approach presented in this chapter thus provides original results and perspectives which take into account the specificities of microcarrier solid phases applied to a geometry used for MSC cell culture.

In parallel **acoustic signals generated by particle - sensor collisions were analyzed to evaluate the frequency and force of these collisions**. For this, specific tracer particles with properties close to those of microcarriers (*ie.* same size or same density)

were used to provide a proof of concept that acoustic techniques could be used to detect individual particle collisions. In addition, individual particle-sensor collisions were measured in various experimental conditions (changing impeller size, geometry and particle numbers). A model predicting particle - sensor collision frequencies and intensities according to geometrical aspects was proposed. Although the work which will be presented is still in early stages of development and would require further experiments to prove robustness, the techniques and results obtained remain compelling.

3.1.2 Bioreactor equipment and geometry

In order to ensure coherency in the work proposed, the numerical and experimental approaches were all performed in the same experimental setup used for MSC expansion. Considering the technical, theoretical and experimental knowledge accumulated with the Pierre Guerin Tryton tank in the research laboratories at both the Universities of Liège and Lorraine, this tank was used for all the following work. Briefly, the tank is a cylindrical container with a diameter T of 12 cm and a hemispherical bottom. The maximal working volume of the tank is of 1.12 L but the following description will concern a working volume of 700 mL, ensuring coherence with the work presented in Chapter 4. The solid phase was composed of Cytodex 1 microcarriers which have a hydrated diameter of 180 μm. In addition, the bioreactor used for cell culture is equipped with 4 online probes allowing the monitoring of temperature, pH, dissolved oxygen and viable cells. The localization of these probes can be found in Figure 3.1 (elements presented in green). The number of plunging elements as well as their size, depth and localization was kept similar in all studies later described in order to ensure similar flow patterns in all systems. Lastly, the bioreactor setup required the regulation of parameters including pH, dissolved oxygen and nutrient concentrations. The localization of the ports used to add gasses and / or media are noted in Figure 3.1, A.

Unless specified otherwise, liquid homogenization and particle suspension was ensured by a down-pumping HTPG impeller with a diameter D of 6 cm and an off-bottom clearance C of 6 cm (Figure 3.1, B). Accordingly the ratios D/T and C/T were equal to 0.5 unless specified otherwise. In these conditions, the minimal agitation required to suspend these particles was found to be of 70 rpm (determined visually). The choice of the HTPG impeller was based on past experiments performed by Dr. Sion at the University of Lorraine which provided a proof of concept that MSCs could be efficiently expanded with this impeller [1].

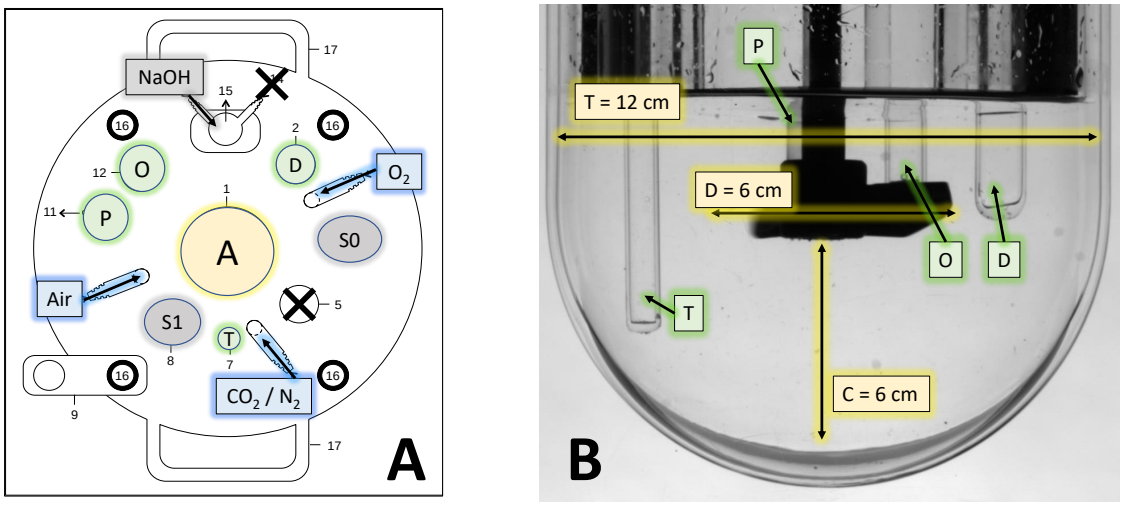

Figure 3.1: Description of the Pierre Guerin bioreactor setup. (A) Experimental setup for MSC expansion on MCs in a volume of 0.7 L. A - (yellow element) Agitator, P - O - D (green elements, plunging) pH, Dissolved Oxygen and Dielectric probes respectively, S0 - S1 - NaOH (grey elements, not plunging) sampling port, plunging cane and sodium hydroxide addition ports respectively, Air - O_2 - CO_2/N_2 (blue elements, not plunging) gas inlets. (B) Photography of the plunging elements present in the experimental setup (green probes) and elements of geometry (yellow).

3.1.3 Characteristics of bioreactor hydrodynamics

Characterization of fluid velocities

After having defined the geometrical aspects of the tank and operating conditions, the liquid flow in the system was characterized by Computational Fluid Dynamics (CFD) simulations (performed by Dr. Loubière at the Laboratoire Réactions et Génie des Procédés, Nancy, France according to methods previously described [2]). Briefly, the flow of a single phase fluid system (water, 37 °C) of 0.7 L was simulated in the Tryton bioreactor with a diameter ($C/T = 0.5$; $D/T = 0.5$). The agitation rate was set to 70 rpm (N_{js}) and 120 rpm (greater than N_{js}). For these simulations, water density was considered as $\rho = 993.3$ kg m^{-3} and dynamic viscosity was considered as $\mu = 6.92 \times 10^{-4}$ Pa s^{-1}. **In these conditions, 90 % of the STR fluid volume was found to have a local velocity below 0.075 m s^{-1} when the tank was agitated at** N_{js} as shown in Figure 3.2. The mean velocity at N_{js} was calculated as 0.05 m s^{-1}. In parallel, simulations performed above N_{js} (at 120 rpm) indicated higher fluid velocities for which 90 percent of the STR fluid volume was found to have a local velocity below 0.135 m s^{-1} and for which the average fluid velocity was calculated as 0.10 m s^{-1}. In addition, for both conditions at 70 and 120 rpm, large macroscopic fluid structures previously reported in literature were observed. The fluid was found to be pushed downwards by the impeller and subsequently pushed back up along the tank edges [2].

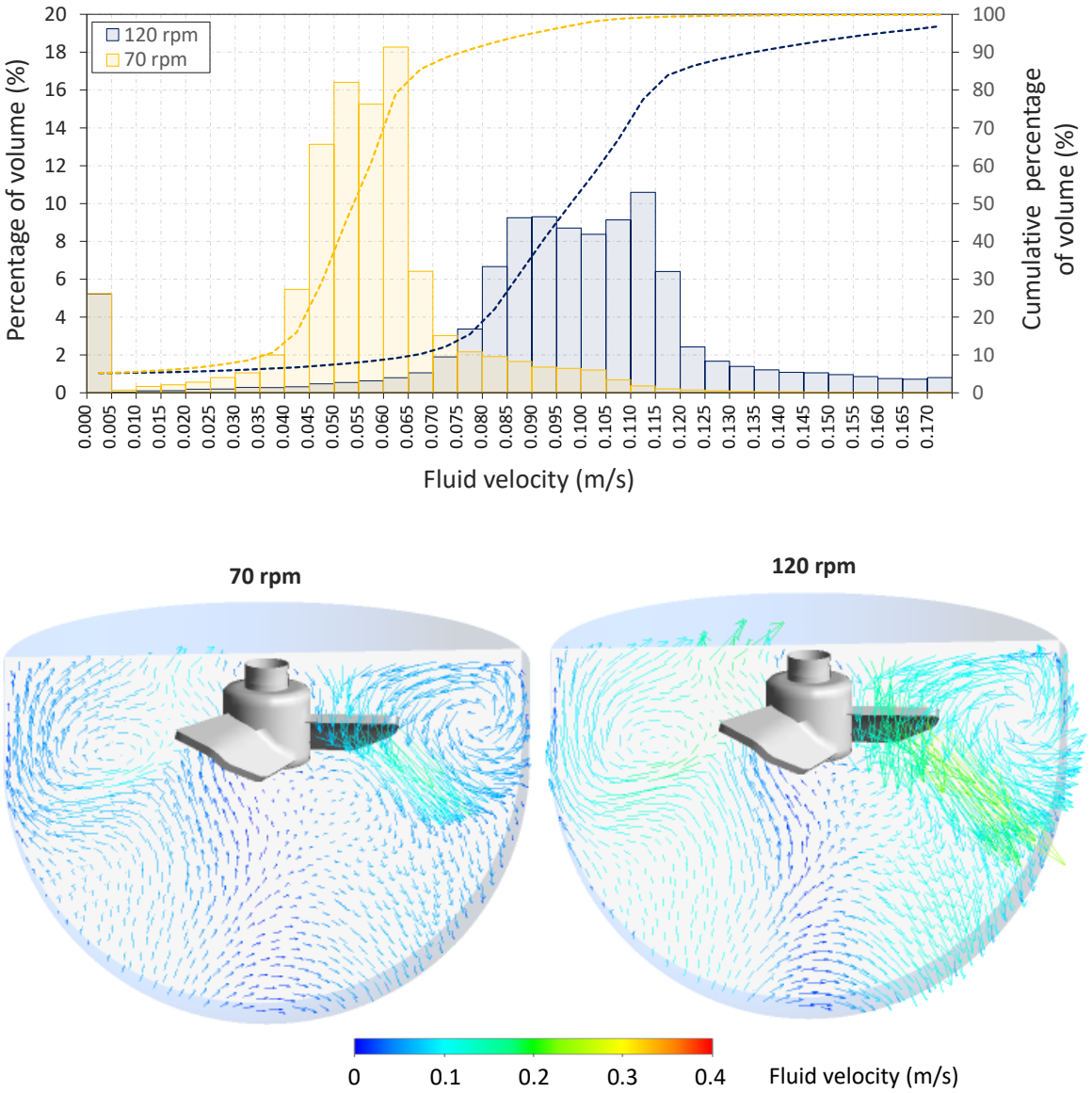

Figure 3.2: CFD simulations of fluid velocities in a Tryton STR equipped with a HTPGd impeller at 70 rpm and 120 rpm at 37 degrees in water (single phase flow). Top : Distribution of velocity magnitudes in the STR at 70 and 120 rpm. Bottom : local fluid velocity vectors at 70 rpm (left) and 120 rpm (right) per element of volume. Simulations performed by Dr. Loubière at the Laboratoire Réactions et Génie des Procédés, Nancy according methods thoroughly described in [2]).

Determination of the impeller power number

The volumetric power input P/V was determined as 0.88 W m^{-3} with an agitation of 70 rpm while it was determined as 4.2 W m^{-3} at 120 rpm. These values were obtained via the CFD software which reported the torque in the impeller shaft C_W (Equation 3.1). In addition, these simulations were used to estimate the power number of the HTPG impeller N_p at N_{js} in these conditions ($N_{p,HTPGd,70rpm}$ **= 0.50**) according to Equation 3.2 based on the fluid density ρ_L, agitation rate N, and agitator diameter D. It can be noted that a slightly lower agitator power number was calculated $N_{p,HTPGd,120rpm}$ = 0.48 with the higher agitation rate above N_{js}, but the difference was found to be

negligible. For the rest of this chapter, the impeller power number of 0.5 was used.

$$P = 2\pi N C_W \tag{3.1}$$

$$\langle \varepsilon \rangle = \frac{1}{\rho_L} \cdot \frac{P}{V} = \frac{N_p N^3 D^5}{V} \quad \text{and} \quad N_p = \frac{V}{\rho_L N^3 D^5} \cdot \frac{P}{V} \tag{3.2}$$

Characterizing elements of turbulence

The agitation power generated by the impeller will generate fluid flow patterns which will depend on fluid characteristics. Accordingly, the ratio of inertial forces to viscous forces within a fluid can be calculated according to Equation 3.3 and defined as the Reynolds number Re. At low Reynolds numbers, flows tend to be dominated by laminar flow regimes, while turbulent regimes are obtained at high Reynolds numbers. The high average Reynolds number in the experimental setup (Re **= 6027**) indicates that a turbulent flow regime occurred in the bioreactor.

$$Re = \frac{\rho N D^2}{\mu} \tag{3.3}$$

In addition, microscale characteristics of the fluid flow can be described by using Kolmogorov's theory of turbulence. The minimal eddy length scale can be calculated according to Equation 3.4, based on the average turbulent energy dissipation rate in the tank $\langle \varepsilon \rangle$ simulated above and the kinematic viscosity of the fluid ν. The values calculated indicated an average Kolmogorov microscale of turbulence of ($\langle \lambda_k \rangle$ **= 140 µm**), while this value was decreased to 70 µm at 120 rpm. Specifically, the distribution of λ_k was simulated by CFD and represented in Figure 3.3. Important variations in this microscale was observed for both agitation rates using local values of ε. To begin with, when agitation was set to 70 rpm, a large variation in λ_k was observed between ranges of 90 µm and 260 µm. The largest values of λ_k were observed around the bottom of the tank while the lowest values of λ_k were observed around the impeller region. Similar distributions were observed in conditions with higher agitation rates but in these cases, the distributions varied between 65 µm and 160 µm and the distribution was less spread-out. The Kolmogorov microscale is typically an important fluid characteristic concerning microcarrier-based cell cultures since studies have shown that the largest impact of shear stress on cells typically occur when the size of the microcarrier approaches the local value of λ_k. Specifically applied to MSC cultures, an impact on growth is expected for microcarrier sizes between 0.25 and 0.5 times λ_k (although not robustly demonstrated) [3, 4].

$$\langle \lambda_k \rangle = \left(\frac{\nu^3}{\langle \varepsilon \rangle} \right)^{1/4} \tag{3.4}$$

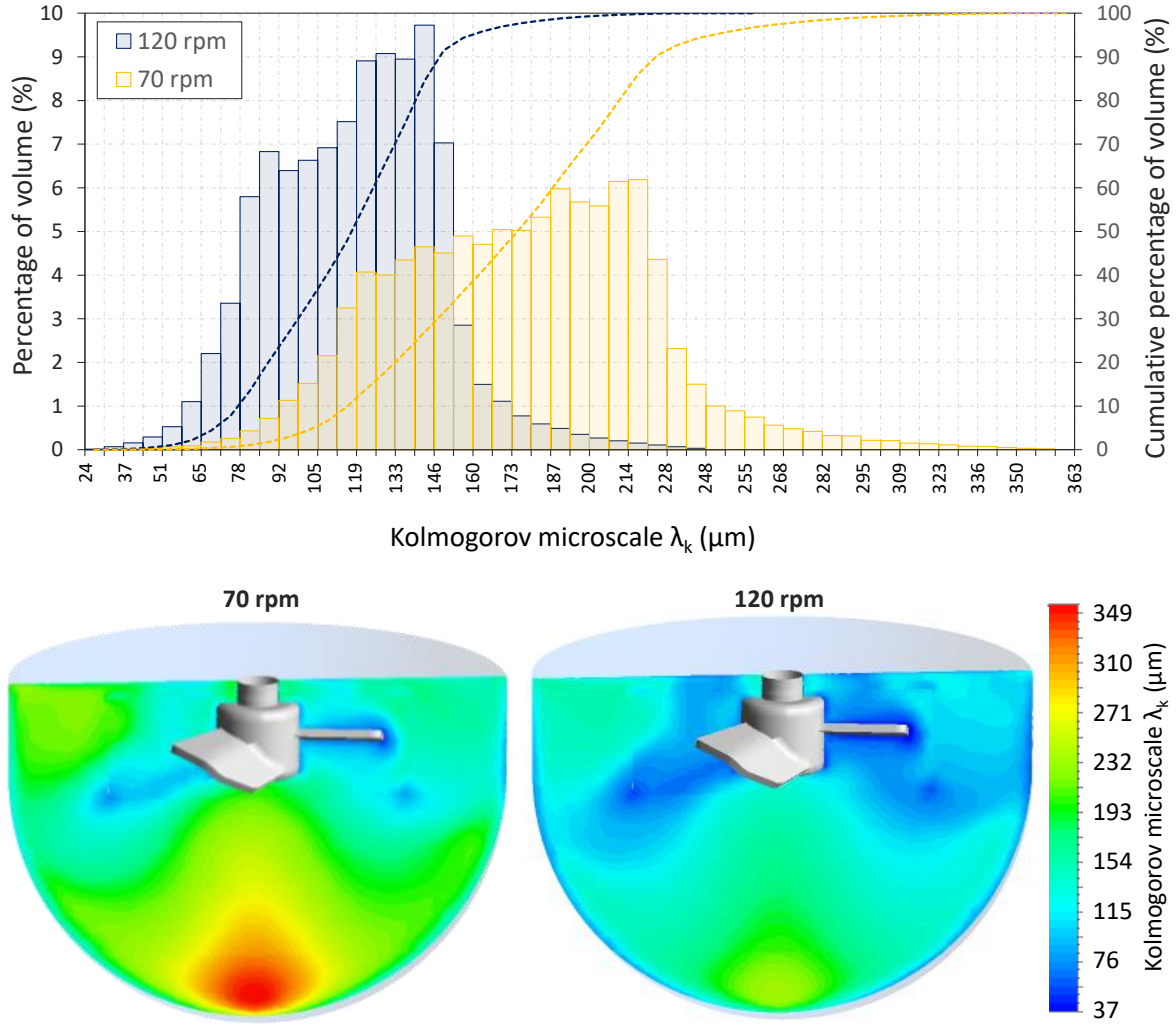

Figure 3.3: CFD simulations of the local kolmogorov microscale of turbulence λ_k in a Tryton STR equipped with a HTPGd impeller at 70 rpm and 120 rpm at 37 degrees in water (monophasic system). Top : Distribution of λ_k in the STR at 70 and 120 rpm per element of volume. Bottom : Spatial distribution of λ_k at 70 rpm (left) and 120 rpm (right). Simulations performed by Dr. Loubière at the Laboratoire Réactions et Génie des Procédés, Nancy according methods thoroughly described in [2]).

Average parameters in the STR

Comprehensively, average bioreactor fluid characteristics at the just-suspended state N_{js} are presented in Table 3.1. The previous simulations indicate that these average values are quite reductive since significant variations are to be expected. Regardless, they allow the easy comparison of various systems with each other as well as orders of magnitude which likely represent the fluid behaviours and flow regime.

Table 3.1: Characteristic constants of the fluid flow in the Tryton STR at N_{js}.

Working Volume	**Impeller power number**	**Impeller diameter**	**Agitation rate**	**Energy dissipation**	**Kinematic viscosity**	**Reynolds number**	**Average kolmogorov length**
V (L)	N_p (-)	D (m)	N (rps)	ε (W kg^{-1})	ν (m^2 s^{-1})	Re (-)	$\langle\lambda_k\rangle$ (µm)
0.7	0.50	$6 \cdot 10^{-2}$	1.2	$0.89 \cdot 10^{-3}$	$6.97 \cdot 10^{-7}$	6027	140

3.1.4 Calculating characteristic data of particle suspension

Minimal agitation to attain a just-suspended state

Macroscopic constants can also be calculated to globally characterize particle suspension, dispersion and trajectories. To begin with, the minimal agitation required to obtain a just-suspended state N_{js} is an essential parameter for cell culture on microcarriers. In the experimental setup, N_{js} was first calculated according to the Zwietering equation (Equation 3.5) for a total solid hold-up concentration α of 2.73 $\%_{v/v}$ (corresponding to a solid hold-up mass ratio X_p of 0.14 $\%_{g/g}$). A S factor of 11.1 was used to calculate the just-suspended agitation since previously estimated in the same system specifically for Cytodex-1 particles and a HTPGd impeller in this tank. However, the theoretical results obtained (N_{js} = 34 rpm) were significantly different from experimental results observed. As a result, **the Zwietering correlation was found unsuitable to predict N_{js} for our experimental setup**, in agreement with the work of Loubière et al [5].

$$N_{js} = S \cdot \nu_L^{0.1} \cdot \left(\frac{g(\rho_p - \rho_L)}{\rho_L}\right) \cdot X_p^{0.13} \cdot d_p^{0.2} \cdot D^{-0.85} \tag{3.5}$$

It is important to note that Cytodex-1 microcarriers have a high swelling factor (20 mL g^{-1}) and that their hydrated density is close to that of the liquid in which they will be hydrated. Due to these quite unique particle properties, it is possible that the Zwietring correlation proposed not be adapted to these particle characteristics. For this reason, a separate approach to estimate N_{js} was performed. The model proposed by Loubiere et al specifically developed for the Tryton tank and Cytodex-1 microcarriers was found to provide a much better estimation of N_{js} [5]. Accordingly, the Reynolds number at N_{js} was estimated by Equation 3.6 (Re_{js} **= 6889**) using factors $K = 8.2$ and $A = 0.07$. Subsequently, **the agitation rate at this Reynolds number was calculated according to Equation 3.7 and indicated a theoretical N_{js} of 80 rpm. The close correlation between this calculated value of N_{js} and both the observed N_{js} in the previous work of Loubiere et al. [5] and the observed N_{js} during MSC cultures performed in the same tank validated the use of this model for the calculation of N_{js}.**

$$Re_{js} = K \cdot \alpha_s^A \cdot \left(\frac{C}{T}\right)^{1/3} \cdot \left(\frac{D}{T}\right)^{0.6} \cdot \left(\frac{d_p}{D}\right)^{-0.4} \cdot \left(\frac{\mu_L}{(\rho_P - \rho_L) \cdot g^{0.5} \cdot T^{1.5}}\right)^{-28/45} \tag{3.6}$$

$$Re_{js} = \frac{\rho_L N_{js} D^2}{\mu} \tag{3.7}$$

Stokes number

In addition, to compare the simulated fluid trajectories with expected particle trajectories, particle Stokes number was calculated. This dimensionless number characterizes the behavior of particles suspended in a fluid flow by comparing the value of a characteristic particle relaxation time τ_p to a characteristic time of the flow τ_k (Equation 3.9). While the particle relaxation time characterizes the time required for a particle to adjust or "relax" its velocity to a new environment or condition of forces (and typically depends on particle mass and mechanical mobility), the characteristic time of the flow is impacted by elements of fluid viscosity and energy dissipation. Accordingly, a particle with a low Stokes number follows fluid streamlines, while a particle with a large Stokes number is dominated by its inertia and continues along its initial trajectory. **In the case of microcarriers, the small particle size and small Stokes number ($\langle St \rangle = 0.10$) calculated according to Equation 3.8 seem to indicate that, at $N = 70$ rpm (slightly below the theoretical N_{js} calculated), particles, on average, follow fluid streamlines and thus collide due to their relative positions within the flow field** [6].

$$\langle St \rangle = \frac{\tau_p}{\langle \tau_K \rangle} \tag{3.8}$$

$$\tau_p = \frac{\rho_p d_p^2}{18\mu} \quad \text{and} \quad \langle \tau_K \rangle = \left(\frac{\nu}{\langle \varepsilon \rangle} \right)^{0.5} \tag{3.9}$$

In addition, having a local description of the Stokes number could also be interesting to define possible heterogeneous particle behaviours. The distribution of St in the STR volume is presented in Figure 3.4 for agitation rates at and above N_{js}. To begin with, the Stokes number calculated was found to have similar distributions at 70 and 120 rpm. However, larger Stokes numbers were observed when increasing agitation, indicating that particles should tend to, to a lesser extent, exhibit movements correlated with fluid movements. This is possibly due to the smallest eddies in higher agitation conditions and the fact that the particles are unable to follow the turbulent fluctuations of the fluid.

When observing the spatial distribution of Stokes, it was found that highest Stokes numbers were observed around the impeller region for both agitation rates. The regions around the impeller were also found to be those with the smallest Kolmogrov length scales λ_k (and specifically zones where λ_k were smaller than the particle size of 180 µm). In addition, these zones were also subject to the largest fluid velocities. As a result, the high turbulence in these regions may cause particle inertia to have a greater impact in particle motion compared to other zones for which particle movement should rather follow fluid streamlines. In addition, for both agitation rates, the Stokes number was found to be below 0.3 in over 95% of the tank volume. Considering the fact that

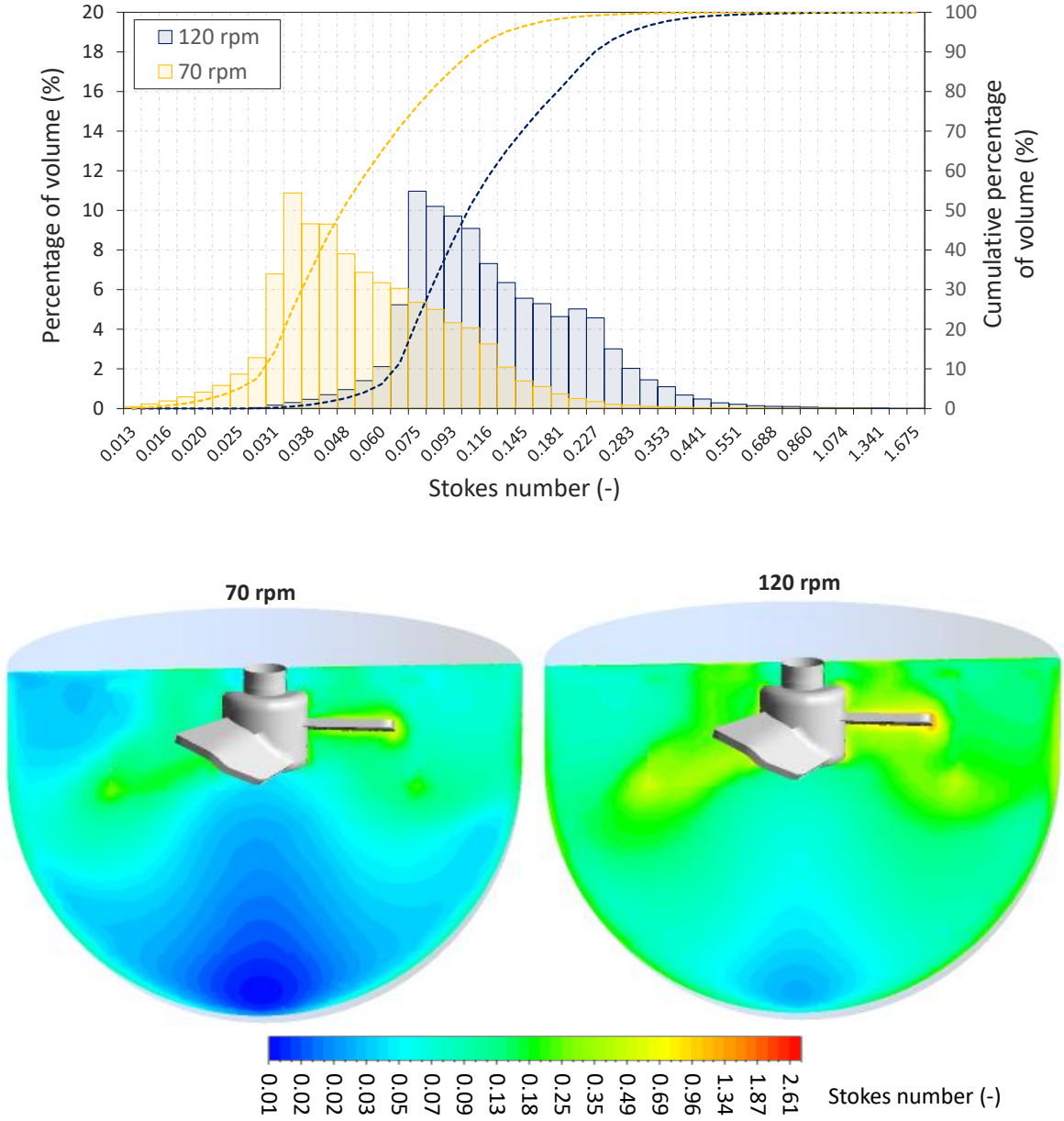

Figure 3.4: CFD simulations of the local Stokes number St in a Tryton STR equipped with a HTPGd impeller at 70 rpm and 120 rpm at 37 degrees in water (mono-phasic system). Top : Distribution of St in the STR at 70 and 120 rpm per element of volume. Bottom : Spatial distribution of St at 70 rpm (left) and 120 rpm (right). Simulations performed by Dr. Loubière at the Laboratoire Réactions et Génie des Procédés, Nancy according methods thoroughly described in [2]).

the Stokes distribution in the STR is less than 0.2 at $N = N_{js}$ and 0.5 at $N = 120$ rpm in the vast majority of the STR volume, the hypothesis that collisional mechanisms should be caused by the fluid flow can be maintained.

3.1.5 Section Summary

The introductory study characterizes both the liquid and solid phases in the geometrical setup used for MSC cell cultures in STRs (700 mL working volume in a STR agitated at 70 rpm with a HTPGd impeller of 6 cm). The same setup was used for the measurement of particle concentrations and particle collisions. A summary of the key constants characterizing the solid phase can be found in Table 3.2.

Table 3.2: Characteristic parameters of the solid phase in the Tryton STR.

MC	**MC density**	**Solid hold-up**	**MC diameter**	**Minimal agitation**	**Relaxation time**	**Averaged turbulent time**	**Averaged Stokes number**
-	ρ_p (kg m^{-3})	X ($\%_{(v/v)}$)	d_p (µm)	N_{js} (rpm)	τ_p (s)	$\langle \tau_k \rangle$ (s)	$\langle St \rangle$ (-)
Cytodex 1	1019	2.73	170	70	2.4 10^{-3}	27.98 10^{-3}	0.09

The preliminary data brings important overview information concerning fluid velocities and the fact that, the bioreactor hydrodynamics is globally turbulent. In addition, the low Stokes number calculated in the system indicates that, on average, the particle velocities and trajectories will be mediated by the fluid characteristics. However, it is important to keep in mind that the elements presented above provide a general overview what goes on in the tank and spatial heterogeneities should be expected including :

- Varying levels of turbulence and fluid velocities in the tank due to the dissipation of the impeller power in the fluid. The local hydrodynamic fluid behaviour may vary, for example through varying scales of turbulence λ_k.
- Varying particle concentrations for which the impact on the apparent liquid velocity should not be ignored. For example, greater local particle concentrations will increase the local density and viscosity.

As a result, the work presented in the following paragraphs will aim at providing additional elements characterizing the solid phase in these conditions taking into account the possible spatial heterogenities expected even when the system has attained an apparent stationary state.

3.2 Measurement of local particle concentrations using light attenuation

3.2.1 Introduction

Statistically, the amount of particle-particle collisions that take place in agitated conditions depend on local particle concentrations. As a result, experimental techniques which can be used to measure local particle concentrations provide indirect measures to estimate local particle collision frequency. For this, optical techniques have the advantage of determining local particle concentrations throughout the bioreactor with non-invasive measures, and are therefore not limited to a local environment, as certain invasive measures may be. **In the case of microcarriers, local particle concentrations can be measured through the attenuation of light passing through the STR as previously described [7]**. Briefly, a LED back-light can be used to illuminate a tank which is placed in a cubic aquarium filled with water (to minimize optical deformation). The light attenuated by the bioreactor and particles can then be measured by a CMOS camera and analyzed offline. The work which will be presented is the object of a future publication *Dynamic measurement of local microcarrier concentration using light attenuation during particle suspension.*

3.2.2 Experimental setup : light attenuation measures

First, experiments were performed at Cytodex 1 microcarrier concentrations ranging from 0 to 37.5 g L^{-1} for calibration. Agitation was set to 120 rpm (1.5 times the estimated N_{js}) to ensure a homogeneous suspension of the particles during calibration (suspension was verified visually). For each microcarrier concentration, a video was acquired for 30 seconds at an acquisition frequency of 2.5 Hz. All of the controls were performed after ensuring that the system was in a steady state. Post-treatment of the data was performed via Matlab as described later.

Back-light stability

The first control which was put in place for all videos was to ensure that there was no significant variation of the back-light intensity over time and between experiments. For this, the evolution of the average light intensity A measured by the sensor in three zones outside the bioreactor were evaluated in all of the experiments used for the calibration at 120 rpm (Zones A, B and C in Figure 3.5, right). No significant variation in the back-light was observed in the three zones defined, ensuring comparability between experiments. Complementary experiments were performed with a lower agitation rate of 70 rpm and are also presented for comparability (these videos were not used for the calibration but were used for dynamic analysis and therefore required the verification of

back-light stability). The data presented in this figure fully covers all of the experiments performed and presented in this sub-chapter.

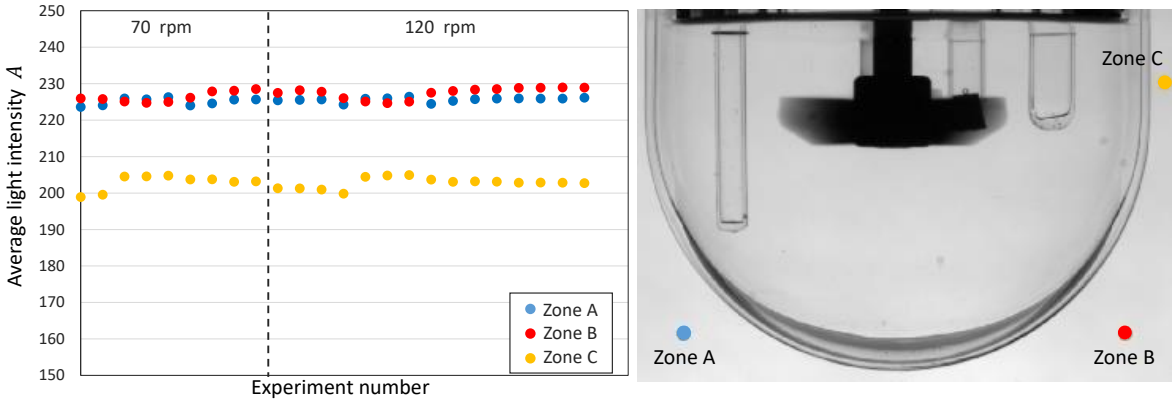

Figure 3.5: Control of back-light intensity over all experiments in 3 defined zones outside the tank. Left : Average light attenuation measures in the defined zone after video post-treatment. Right : Photograph of the defined zones.

Calibration for a concentration range from 0 to 37.5 g L^{-1}

The next step consisted in measuring the spatial distribution of light attenuation inside the bioreactor when increasing particle concentration. Particle concentrations between 0 and 37.5 g L^{-1} were used. To begin with, the raw video data obtained over the 30 seconds for each concentration during calibration was averaged over time. For each point (video pixel), a 3^{rd} degree polynomial model was fit to calibrate the measured concentration C based on the logarithm of the measured light intensity in this point A (Equation 3.10). This calibration in every point of the bioreactor was required (fitting K_1, K_2, K_3 and K_4 coefficients) due to the difference in length between optical paths at various areas of the bioreactor (typically, the light passes through a lower distance at the bottom of the tank due to the hemispherical bottom and as a result, this must be accounted for during calibration), the fact that the tank envelope is not perfectly homogeneous, and possible spatial variations in back light intensity.

$$C = K_1 \times log(A)^3 + K_2 \times log(A)^2 + K_3 \times log(A) + K_4 \tag{3.10}$$

After calculating the individual polynomial coefficients for every pixel, a verification was performed in 6 defined zones of interest inside the bioreactor (Zones 1 - 6 in Figure 3.6, right). This verification also visually illustrates the calibration method. The average light intensity measured in the different zones was plotted against the theoretical concentration and the 3^{rd} degree polynomial models represented in Figure 3.6, left. The good agreement between the light intensity values and the theoretical concentration indicates that the fitting performed by the Matlab script was coherent with the measured data (Figure 3.6, left).

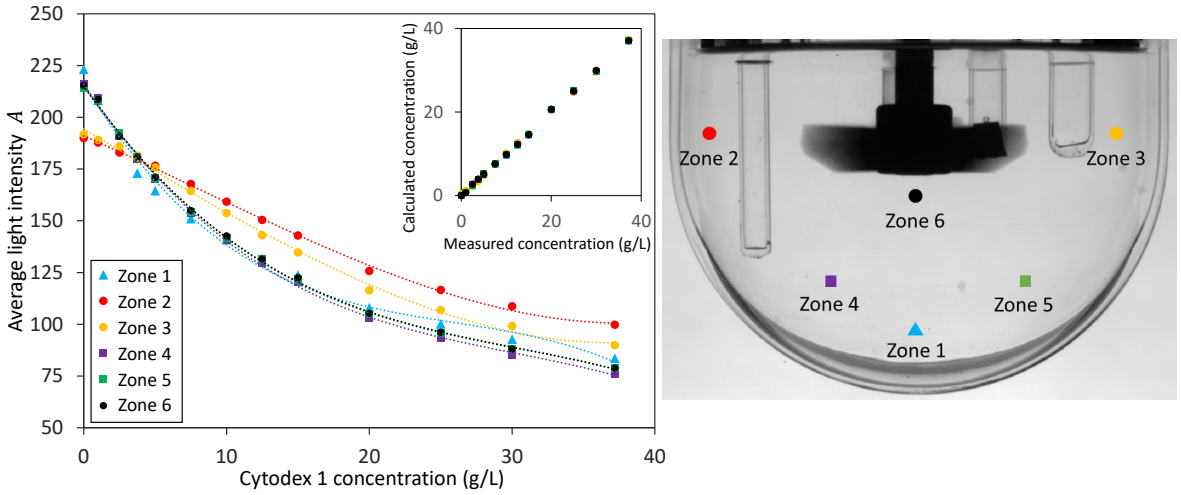

Figure 3.6: Calibration visualization for 6 defined zones of interest at 120 rpm for particle concentrations between 0 and 37.2 g L^{-1}.

Concentration spatial distribution

Building upon the results presented for 6 defined zones in the tank, it is important to define if the calibration can be used to correctly estimate particle concentration in all of the tank (certain zones near the impeller, near the bottom of the tank or near online probes may be more difficult to calibrate). Accordingly, the calibration matrix defined above was used to recalculate the local concentration for each pixel and for each concentration tested. Results indicate little heterogeneity in particle concentration when using this calibration method via this type of visualizations (Figure 3.7). The only zones which were found to be difficult to predict were those around the probes introduced in the tank (specifically for small particle concentrations). However, a measurement of relative calibration errors are required to evaluate with more precision the method variability.

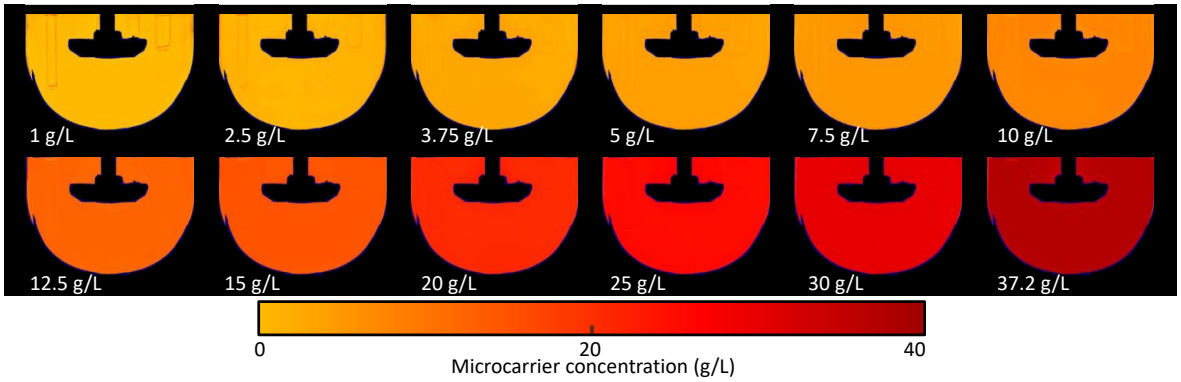

Figure 3.7: Control of the spatial distribution of microcarrier concentration during calibration (heatmap).

Evaluating the mean error of the calibration method δ

In order to asses a global estimation of the error of calibration, the average mean error per pixel δ was determined for each calibrated concentration according to Equation 3.11. Accordingly, for each pixel of the measurement, the absolute difference between the calibrated concentration $C(x, y)$ and the average concentration in the system C_f was calculated and normalized according to C_f. The sum of these local errors was calculated and divided by the number of pixels on which the calibration was performed N_{pixels}. Results are presented in Table 3.3. It can be observed that larger values of δ were observed for low particle concentrations (C_f of 1 and 2.5 g L^{-1}). These errors can be explained by the fact that measuring a precise concentration for low values of C_f are limited by the experimental setup which may be disturbed by variations in back-light intensity, room light intensity, or sensor sensibility. These variations in the environment may have a greater impact than small variations in attenuation caused by the increased particle concentration. Accordingly, caution will be kept in mind when analyzing data obtained for small particles concentrations (approximately 1 g L^{-1}). Further work at these small concentrations may require particular attention during the experimental acquisition of the videos and possibly a separate calibration specific to these small particle concentrations.

$$\delta = \sum_{(x=1,y=1)}^{(x=x_F,y=y_F)} \frac{|C(x,y) - C_f|}{C_f} \times \frac{1}{N_{pixels}} \tag{3.11}$$

Table 3.3: Standardized calibration error per concentration condition C_f.

Average concentration C_f (g L^{-1})	**1**	**2.5**	**3.75**	**5**	**7.5**	**10**	**12.5**	**15**	**20**	**25**	**30**
Error δ (%)	58.1	19.2	10.8	7.9	4.6	4.0	3.5	4.5	4.8	1.7	1.7

Concentration evolution over time

The polynomial relations were then used to evaluate the evolution of particle concentration locally over time in the calibration conditions to ensure that there was no drift of this measure. As an example, results over time in Zone 1 (defined in 3.6 are presented in Figure 3.8. No significant drift over time was observed for the 13 calibration conditions tested apart from a slightly higher calculated concentration during the first few seconds of the calibration at 20 g L^{-1} (possibly due to an incomplete homogenization at the beginning of the experiment). However, this small drift was found to have little impact on the overall calibration and the full data set for this concentration was maintained. Concentration drift over time was found to be negligible in all 6 zones (data not shown) indicating that particle suspension had in fact reached a steady state before the start of the videos.

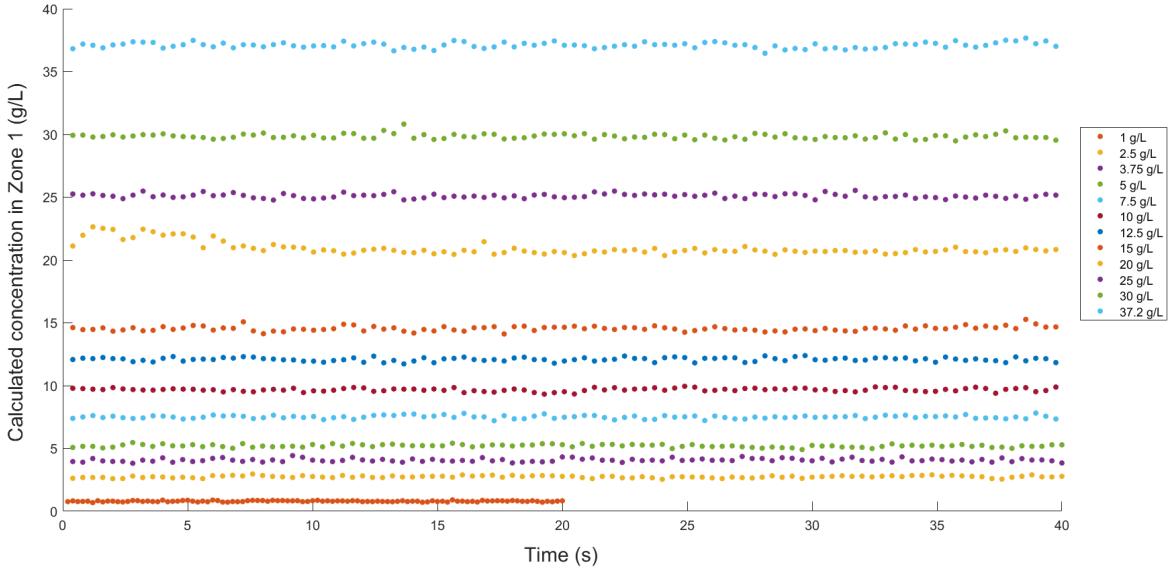

Figure 3.8: Evolution of the average calculated concentration in Zone 1 (defined in Figure 3.6) over time for the calibration concentrations between 1 and 37.2 g L^{-1}.

3.2.3 Results and discussion

Local concentration distribution evolution over time $C(x, y, t)$

According to the defined calibration, videos of the same experimental setup were performed at various concentrations during the suspension of these particles. For this, a given quantity of microcarriers were added in such a way as to reach varying average microcarrier concentration in the tank C_f. Starting from a fully settled particle bed, agitation was then turned on at either 70 or 120 rpm and recording was started in identical conditions than those performed for the calibration. Concentration spatial distribution data were obtained frame by frame $C(x, y, t)$ according to the calibration matrix and analyzed via Matlab. It should be kept in mind that the calibration was performed for concentrations between 0 and 37.2 g L^{-1}L. Consequently, all of the data points which were found to have measured concentrations outside this range were estimated by extrapolating the polynomial relations defined within the range. As a result, the system may have significant errors for microcarrier concentrations which are far outside this range (for example, concentration of certain zones at the bottom of the tank were found to have concentrations greater than 50 g L^{-1} at the beginning of the re-suspension when the average concentration in the tank was of 15 g L^{-1}). Keeping this in mind and for means of comparison, all of the data calculated will be presented.

An example of the concentration distributions obtained at 3 different times during suspension can be observed in Figure 3.9. As shown in the left part of this figure, initially, microcarriers are settled at the bottom of the tank. After approximately 40 seconds of suspension, the microcarriers were found to amass near the bottom of the STR and after approximately 80 seconds start to diffuse within the tank volume. These visual approaches can be used to qualitatively appreciate microcarrier suspension over

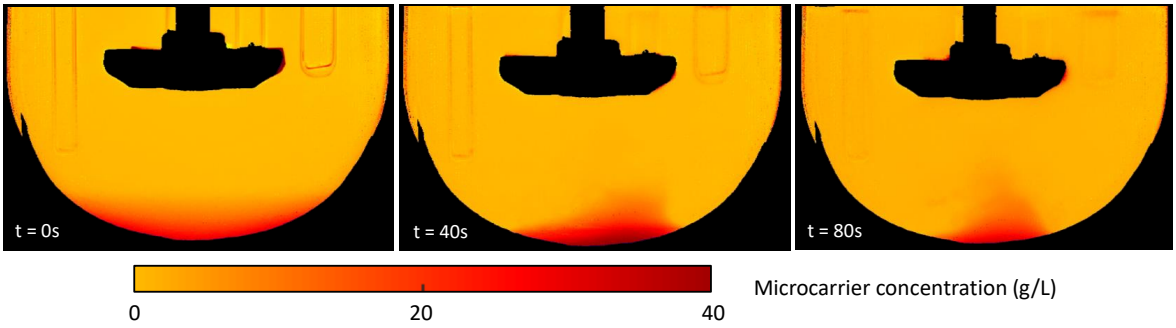

Figure 3.9: Concentration distribution obtained at 70 rpm after 0, 40 and 80 seconds of agitation. Microcarrier average concentration was 2.5 g L^{-1}.

time but remain limited when comparing many experimental conditions between each other.

Local concentration evolution over time in 6 defined zones of interest

Qualitatively, observing how microcarrier concentration evolves over time in certain defined STR zones (such as the 6 Zones defined in Figure 3.6) can be a good indicator of particle suspension characteristics. For example, this visual representation led to the identification of different suspension steps and kinetics depending on the local zone observed and on microcarrier average concentration C_f. As an illustration, curves which present the evolution of particle concentration in Zones 1 and 6 (defined in Figure 3.6) for average particle concentrations C_f of 2.5 and 10 g L^{-1} are presented in Figure 3.10.

- To begin with, several steps during re-suspension were observed for small particle concentrations in zones very close to the bottom of the tank (Zone 1, C_f of 2.5 g L^{-1}). Initially, microcarrier concentration in these zones remained constant and higher than the average microcarrier concentration in the system (*i.e.* microcarriers are settled at the bottom of the tank and local solid concentration is higher than in suspended conditions). Once the agitation is turned on, a densification phase is observed, possibly due to fluid movements generated downwards by the impeller. It can be noted that the over-concentrations at this stage can be significant (reaching approximately 10 times the average concentration in the system during approximately 1 - 2 minutes for C_f of 2.5 g L^{-1}). Lastly, in these zones, particles eventually progressively diffuse in the tank and a gradual decrease in particle concentration is observed until a stationary regime is obtained (for which the local concentration reaches the average concentration in the system C_f). As it can be seen with the results presented for Zone 1, the time it takes to fully homogenize the system increased with microcarrier concentration (while it seemed to take approximately 100 seconds to homogenize Zone 1 for microcarrier concentrations of 2.5 g L^{-1}, it took over 400 seconds for microcarrier concentrations of 10 g L^{-1}).

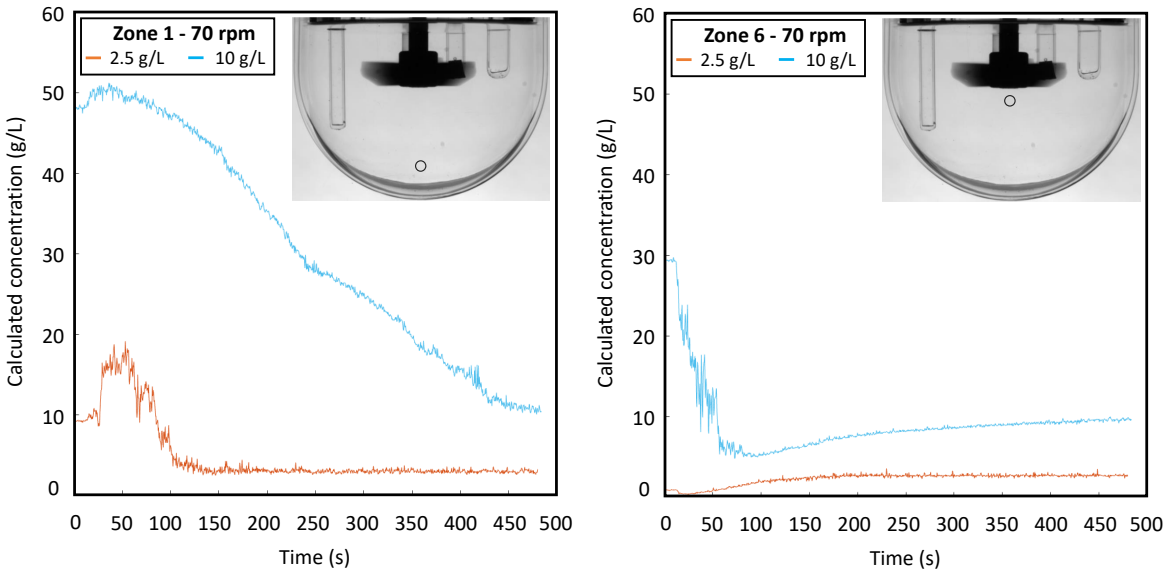

Figure 3.10: Evolution of concentration in Zones 1 and 6 (defined in Figure 3.6) for average concentrations of 2.5 and 10 g L^{-1} during suspension at 70 rpm.

- A second suspension trend was observed in zones which are situated below the impeller, but less close to the bottom wall than Zone 1 as to not be subject to forces caused by the downwards liquid flow. For high enough particle concentrations, these zones are situated in the bed of particles at the beginning of the experiment. Zone 6 ($C_f = 10$ g L^{-1}) illustrates this trend (Figure 3.10, right). An initial phase was observed with particle concentrations higher than the average concentration (due to the fact that these zones are observing regions inside the initial particle bed), followed by a second stage where the particle concentration gradually decreased during homogenization until reaching the average concentration in the system C_f. It can be noted at this stage that this zone attained degrees of homogenization much quicker than the previously described Zone 1 for the concentration of 10 g L^{-1} (concentration of Zone 6 was close to C_f after approximately 200 seconds while Zone 1 reached these concentrations after approximately 400 seconds).

- The last suspension trend concerns zones which are not initially in the microcarrier bed (Zone 6 for a concentration of 2.5 g L^{-1}). In these cases, particle concentration gradually increases from 0 (*i.e.* clear liquid) to the average concentration C_f. The homogenization of this Zone was found to take approximately the same time as the presented Zone 1 at the same microcarrier concentration of 2.5 g L^{-1} (approximately 100 seconds). However, much lower concentration variations were reported during this time (concentration range stayed within 0 and 2.5 g L^{-1} in Zone 6 while varied between 2.5 and 20 g L^{-1} in Zone 1).

The time evolutions of particle concentrations in 6 zones of interested defined in Figure 3.6 are presented in Figure 3.11. Concentration ranged from 2.5 to 15 g L^{-1} and

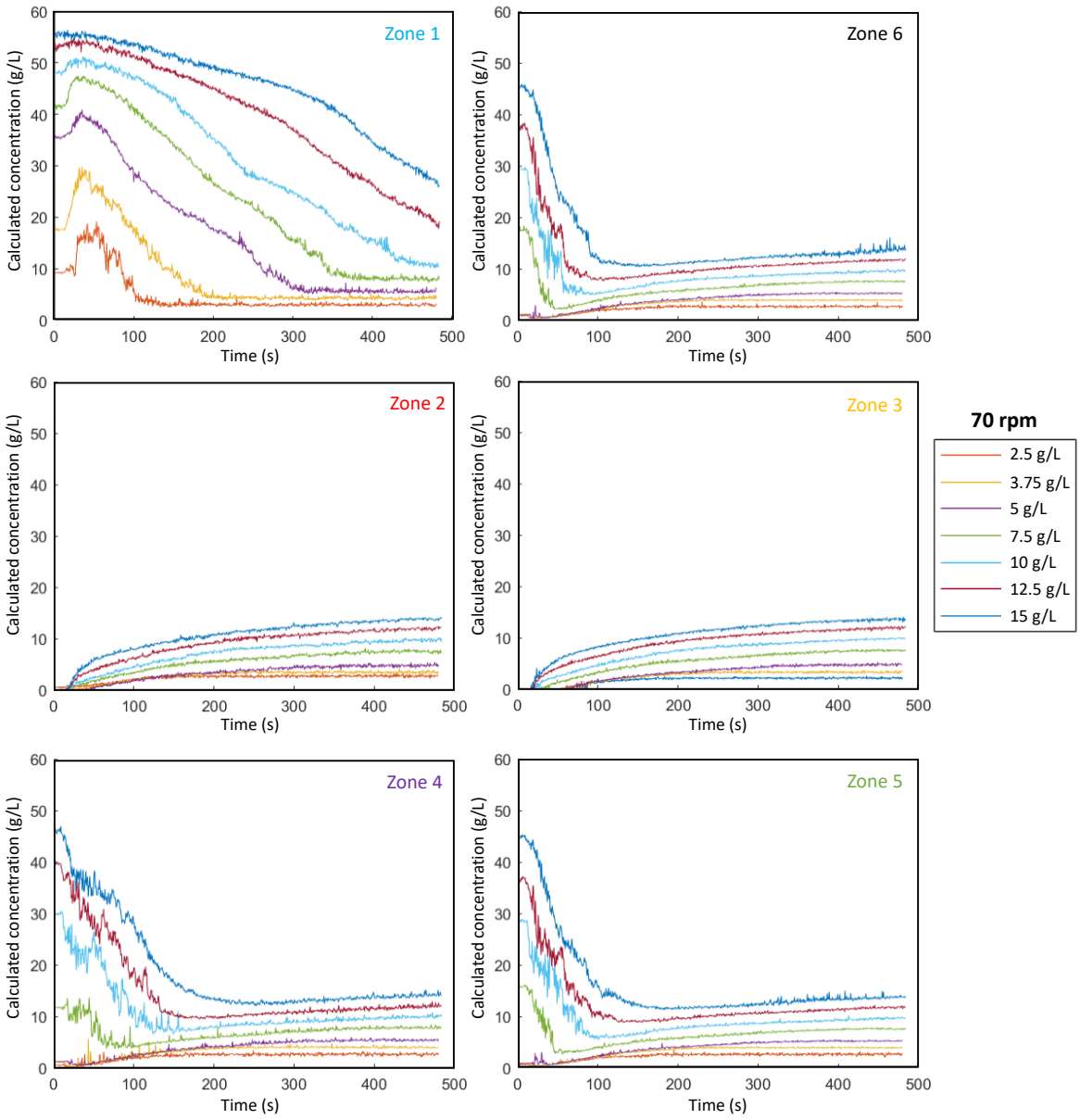

Figure 3.11: Temporal evolution of concentrations in Zones 1 to 6 (defined in Figure 3.6) during suspension at N = 70 rpm.

agitation was kept constant at 70 rpm. This agitation rate was chosen since similar to agitation rates used for MSC cell cultures on microcarriers. All of the observed trends correspond to one of the three profiles described previously. In addition, similar profiles were obtained between Zones 2 and 3 and between Zones 4 and 5 which are symmetrically opposite zones in the tank for all tested concentrations. Lastly, the observed profiles within each zone was found to depend on the average microcarrier concentration in the system, specifically concerning the time to achieve an apparent steady state. The impact of particle concentration was the most pronounced in Zone 1 near the bottom of the tank where significant variations in homogenization time were observed as reported in the previous paragraphs. It is interesting to note that the time it took for the first particles to reach the highest zones near the top of the STR (Zones

2 and 3) typically depended on microcarrier concentration, probably since conditions with high microcarrier concentrations have a higher bed, reducing the time for particles to reach the top of the bioreactor.

The results presented above indicated that the temporal evolution of particle concentration will have different profiles depending on the tank region. Specifically, **the duration required to attain homogenization, as well as the maximal local concentration attained during suspension, seemed to depend on the local zone studied. Importantly, certain zones such as Zone 1 may be subject to significantly higher concentrations (up to a factor of 10) than the final average concentration for approximately 1 - 2 minutes due to an initial phase of compression generated by the impeller**. Since the physical friction and or shocks that cells grown on microcarriers will be subject to ultimately depends on the time spent in specific high-concentration or low-concentration zones, it is important to further quantify these phenomena.

Local heterogeneity index spatial distribution over time $\sigma(x, y, t)$

The concentration evolution results were then extrapolated into a heterogeneity index $\sigma(x, y, t)$ which represents, for each pixel (x, y) and for each time step t, the difference between the measured concentration $C(x, y, t)$ and the average final concentration C_f. Results were normalized according to C_f in order to easily compare experiments performed at various concentrations with one-another according to Equation 3.12. Theoretically, the evolution of this factor should ultimately tend towards 0 while the system tends towards a theoretically homogeneous state for which the concentration in every pixel tends towards the average concentration in the system C_f.

$$\sigma(x, y, t) = \frac{|C(x, y, t) - C_f|}{C_f} \tag{3.12}$$

The spatial distribution of the heterogeneity index after 40, 80 and 160 seconds of re-suspension with an average concentration C_f of 2.5 g L^{-1} and with an agitation of 70 rpm are reported in Figure 3.12. These results can be compared to Figure 3.9 for which the same data is used and only the measured concentration is represented. It can be observed that large portions of the reactor have a heterogeneity index after 40 and 80 seconds of suspension between 0 and 1. This indicates that, in the majority of the STR, the concentration remains with a range of 0 and 2 times C_f. However, notable zones were found to have concentrations which were measured as high as over 5 times C_f. These zones typically correspond to zones at the bottom of the STR in the hemispherical bottom. The heterogeneity index was found to be quite uniformly distributed and close to 0 after 160 seconds of suspension at 70 rpm.

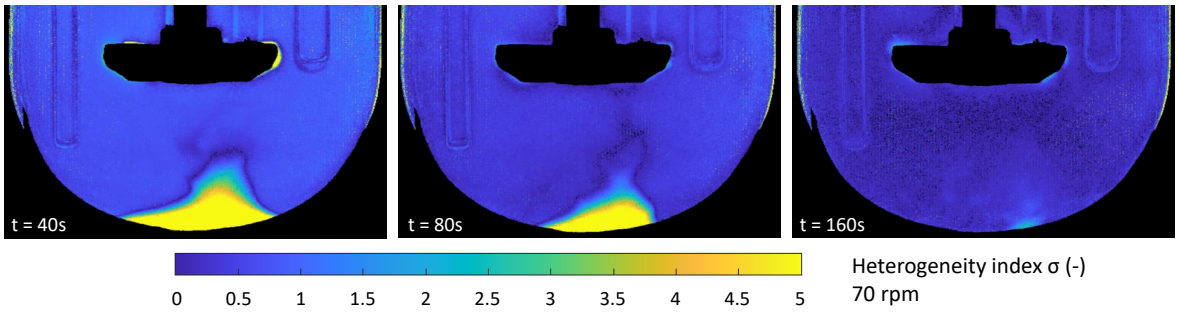

Figure 3.12: Heterogeneity index distribution evolution over time with a microcarrier concentration of 2.5 g L^{-1} and agitation set to 70 rpm. The distribution are presented after 0, 40 and 80 seconds of agitation.

Lastly, the same results obtained with an agitation of 120 rpm were also obtained in parallel and can be found in Figure 3.13. Contrary to the results obtained at N_{js}, agitating at 120 rpm indicated, as expected, a much quicker homogenization of particles. In the presented experiment at a C_f of 2.5 g L^{-1}, almost the entire tank was found to be homogenized after only 40 seconds, whereas this degree of homogenization was only achieved after 160 seconds when agitating at 70 rpm. The zones which were found to take the longest time to achieve the target concentration were near the bottom of the tank under the impeller. It can also be noted that, at 120 rpm, the tank seemed to achieve a constant degree of homogenization after approximately 80 seconds (the distribution of $\sigma(x, y, t)$ was not found to significantly change between 80 and 160 seconds indicating a steady regime).

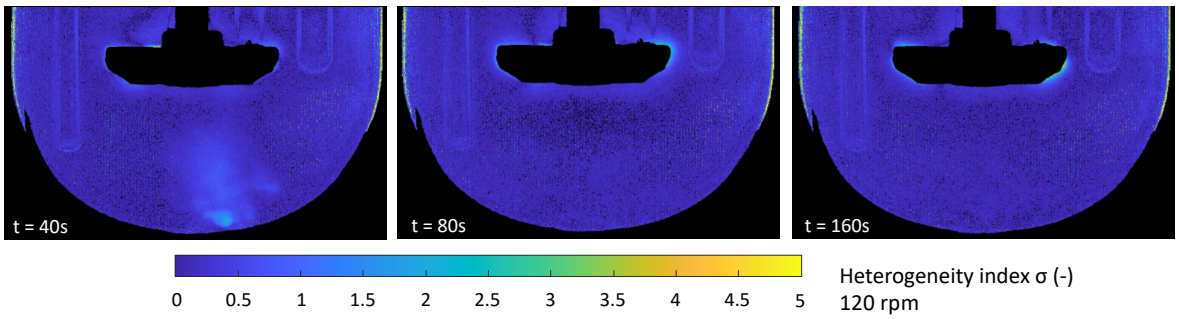

Figure 3.13: Heterogeneity index distribution evolution over time with a microcarrier concentration of 2.5 g L^{-1} and agitation set to 120 rpm. The distribution are presented after 0, 40 and 80 seconds of agitation.

Average heterogeneity index evolution over time $\langle\sigma(t)\rangle$

For each time step t, the average value of $\sigma(x, y)$ was calculated as an average over all of the pixels in the bioreactor N_{pixel}. Accordingly, the average heterogeneity index $\langle\sigma(t)\rangle$ was calculated using Equation 3.13.

$$\langle\sigma(t)\rangle = \sum_{(x,y)=(1,1)}^{(x,y)=(x_f,y_f)} \frac{\sigma(x, y, t)}{N_{pixel}} \tag{3.13}$$

Results concerning this homogeneity index are presented in Figure 3.14 for both agitation rates at N_{js} of 70 rpm (left) and above N_{js} at 120 rpm (right). To begin with, increasing the average microcarrier concentration while maintaining the same agitation rate led to similar homogenization profiles but with different kinetic behaviours. For example, the time required to achieve a stable level of homogenization was found to be approximately 200 seconds with C_f of 2.5 g L^{-1} whereas this duration gradually increased with concentration to achieve around 700 seconds when the C_f concentration was of 15 g L^{-1}. Interestingly however, when increasing the agitation rate to 120 rpm, the homogenization time in all concentrations remained stable around 50 seconds. It seems that, for the range of concentrations tested, increasing the agitation rate to 120 rpm generated the un-correlation of agitation from particle concentration, or at least that this variation is not detected. Lastly, in both agitation conditions (70 and 120 rpm), $\langle\sigma\rangle$ seemed to also vary depending on the concentration when the system achieved a steady state. Particularly for low microcarrier concentrations (C_f of 2.5 or 3.75 g L^{-1}), $\langle\sigma\rangle$ stabilized around 0.1 while an expected theoretical index in steady state would be of 0. It is possible that for these low microcarrier concentrations, the resolution of the experimental setup led to an accumulation of errors when calculating this factor and could explain these differences. These low concentrations were found to be the conditions for which the largest errors were observed during calibration.

Local homogenization duration $\tau(x, y)$

The level of homogeneity in heterogeneous systems can be evaluated via various methods. A simple method consists in describing the time that it takes for a given system (or area) to achieve a certain level of homogeneity. For this, in each data point, the ratio between the measured concentration C and the average concentration C_f can be calculated. The time it takes the system to achieve a degree of homogenization, or local homogenisation time $\tau(x, y)$, can then be obtained from the data as an indicator to compare systems between each other (as reviewed in [8]). This parameter was obtained by determining the time point following which the local concentration stayed within the method variability for each concentration defined in Table 3.3 to which an error δ_5 of 5% was added. Accordingly, the value of error used to define the homogeneous state according to the average concentration C_f can be found in Table 3.4. The system was

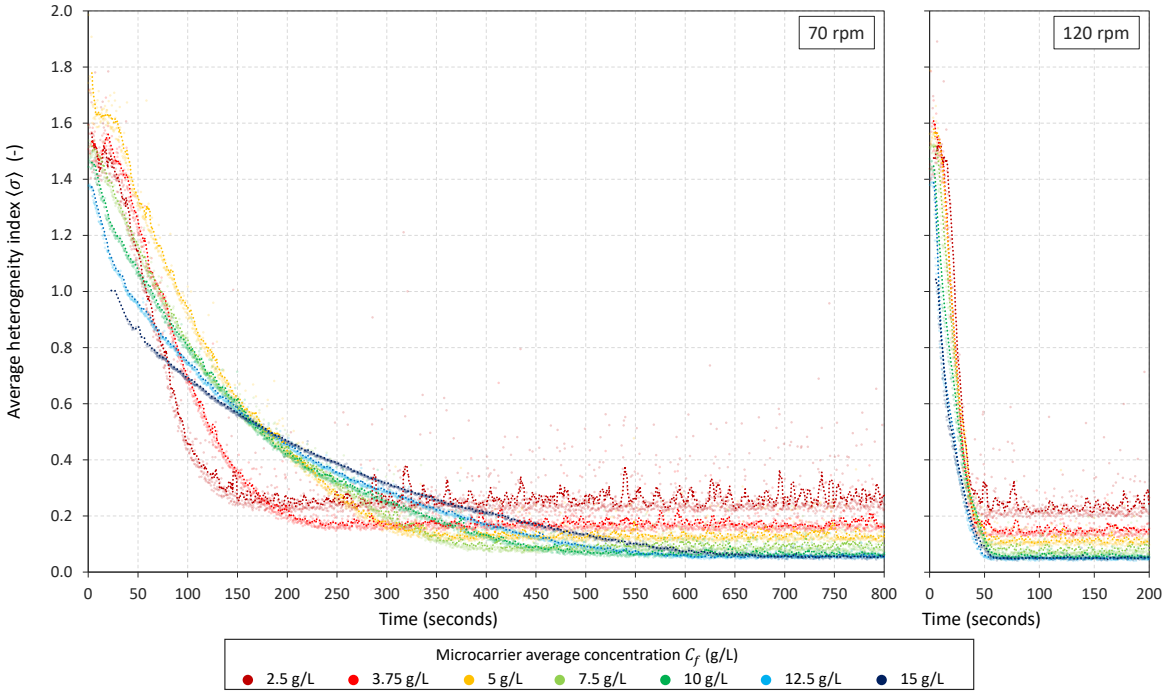

Figure 3.14: Evolution of the average heterogeneity index evolution over time $\langle\sigma(t)\rangle$ at and above N_{js} and concentrations between 2.5 and 15 g L^{-1}.

considered as homogeneous in a given pixel when the measured concentration stayed within a range of (1 - δ_5) to (1 + δ_5) times C_f for a minimum of 60 seconds (or 150 frames). This setpoint corresponds to the limit of detection of the method for each concentration and the STR was assumed to be homogenized at this time-point. To ensure results can be compared with one another, the first frame for which the agitator was found to move was manually determined in each condition and used to initialize the time variable. In addition, in order to easily visualize the spatial distribution of τ, the local homogenization time was calculated for each point in the bioreactor. Results for concentrations ranging from 2.5 to 12.5 g L^{-1} with an agitation rate of 70 rpm are presented in Figure 3.15.

Table 3.4: Standardized calibration errorδ_5 per concentration condition C_f.

Average concentration C_f (g L^{-1})	**2.5**	**3.75**	**5**	**7.5**	**10**	**12.5**	**15**	**20**	**25**	**30**
Error δ_5 (%)	24.2	15.8	12.9	9.6	9.0	8.5	9.5	9.8	6.7	6.7

First, it can be observed that there is a spatial gradient within the tank concerning the duration to achieve the target concentration C_f, regardless of the concentration in the tank. Typically, zones near the bottom of the tank were found to take longer to achieve the average concentration (represented in yellow and green). A gradient in homogenization duration is observed for all microcarrier concentrations, with durations lasting from nearly 0 to over 1000 seconds depending on microcarrier average concentration in the tank. For low microcarrier concentrations (2.5 g L^{-1}), most of

the STR volume had homogenization durations between 0 and 200 seconds and quickly reached the target concentrations. This indicates that for these particle concentrations, agitating at 70 rpm for approximately 5 minutes (300 seconds) could ensure that the majority of the tank volume achieved the target concentration. However, when increasing microcarrier concentration over 5 g L^{-1}, most of the tank volume had values of τ above 300 seconds, and notable zones which were difficult to homogenize at the bottom of the tank. In these cases, a homogenization of 5 minutes at 70 rpm would be insufficient to successfully suspend the particles. Homogenization durations may take up to 15 minutes in these cases. Globally, methods to estimate a sufficient homogenization duration to consider microcarriers as having attained an apparent steady state are important to correctly dimension homogenization processes.

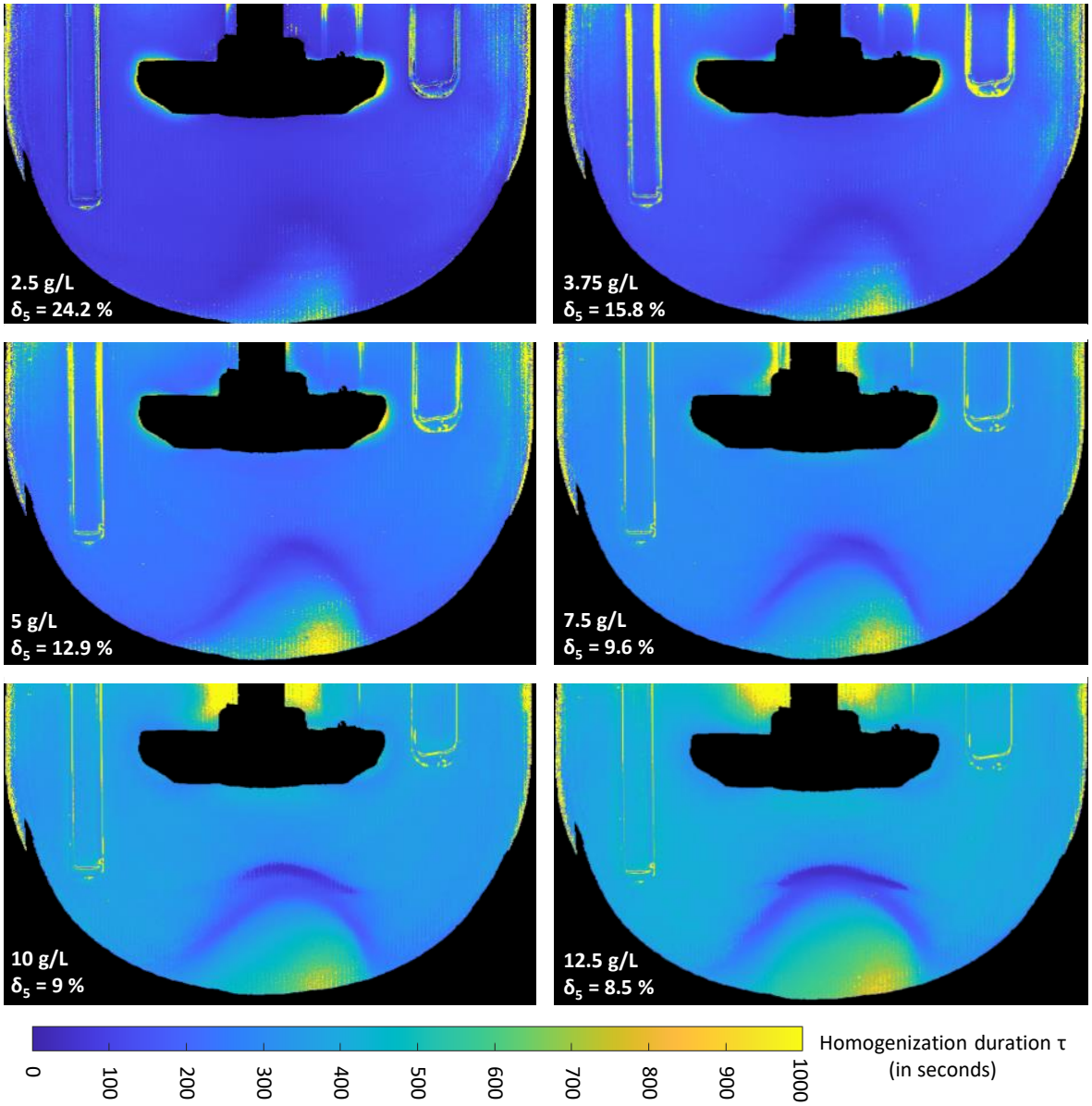

Figure 3.15: Local homogenization time $\tau(x, y)$ calculated for various average microcarrier concentrations during suspension at 70 rpm. The values represent the time to achieve a stable value of $C_f \pm \delta_5$.

Statistic distribution of the homogenization duration τ

Globally, the distribution of τ in the tank in each condition can be used to quickly compare systems and agitation kinetics between each other and help to size agitation processes. To begin with, the distribution of τ was observed at N_{js} according to the average concentration in the tank (Figure 3.16). An increase in τ with increasing concentration which was observed spatially in the previous paragraph is also observed in the distribution plots of τ. Whereas the median duration to achieve a 'homogeneous state' was of 112.8 seconds when C_f was 2.5 g L^{-1}, this value was multiplied by over a factor of three (446 seconds) with C_f of 15 g L^{-1}.

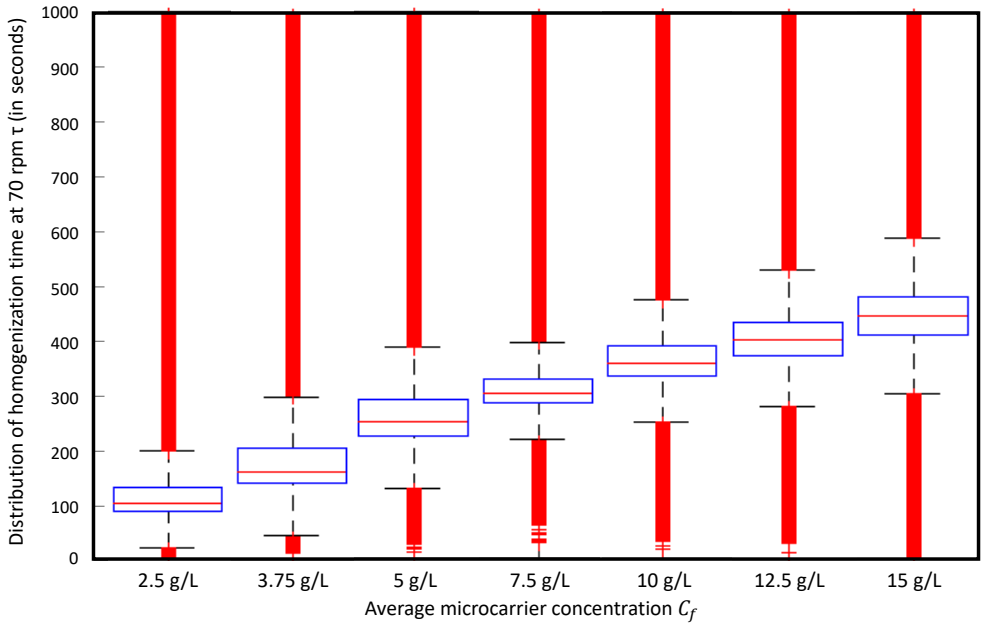

Figure 3.16: Statistic distribution of the homogenization time $\tau_{80\%}$ measured in the tank at different microcarrier concentrations for an agitation of N_{js} = 70 rpm.

In addition, the same experiments were performed at 120 rpm for which the homogenization time is represented according to the average concentration in the STR in Figure 3.17. When increasing the agitation in the tank, the average value of τ was not only found to be lower but also the distribution was found to be less disperse for all concentrations indicating that there may be less spatial heterogeneity during suspension when agitating particles at a higher agitation rate. Interestingly, these results also tend to demonstrate that the average homogenization duration in the STR becomes independent depend from microcarrier concentration when increasing agitation. **In order to minimize the duration of homogenization, it may be of use to increase the agitation rate above N_{js} to, as expected, limit homogenization time and interestingly limit spatial duration dispersion, particularly if particle concentrations are high**.

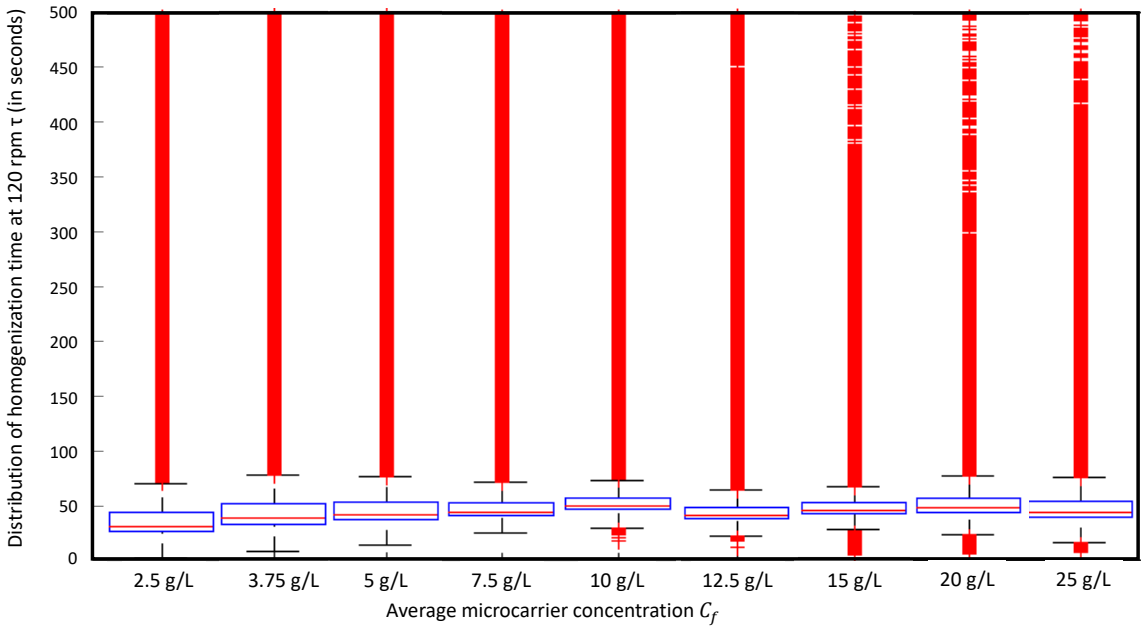

Figure 3.17: Statistic distribution of the homogenization time τ measured in the tank at different microcarrier concentrations for an agitation above N_{js}. Agitation was set to 120 rpm.

Local over-concentration index during particle re-suspension $\gamma(x, y, t)$

As described before, the local homogenisation time depends on the position in the bioreactor. In order to have information not only on the duration but also on local concentration ranges in the bioreactor, a separate analysis of the data was performed. For each pixel, the measured concentration in each frame $C(x, y, t)$ was compared to the average concentration C_f. In cases where the measured concentration was above the average concentration, local over concentration index $\gamma(x, y, t)$ was set to the level of over-concentration normalized according to C_f. If the measured local concentration was below the average concentration C_f, the over-concentration factor was set to 0 (Equation 3.14). Accordingly, $\gamma(x, y, t)$ represents, for each time-point, a measure of the local over-concentration which could be correlated with increased particle collision probabilities when compared to an average value C_f. An example of the evolution of the spatial distribution of $\gamma(x, y, t)$ for C_f of 2.5 g L^{-1} is presented in Figure 3.18 after 40, 80 and 160 seconds of agitation. As it could be expected, the zones which are overly concentrated during suspension concern zones near the bottom of the tank where particles were initially settled. In addition, as it has been described previously, certain zones near the reactor wall experience high particle concentration variations for which the local concentration can reach up to 10 times the average concentration in the system. These match previous observations where certain zones of the STR were found to be subject to certain levels of densification during suspension caused by the downwards fluid movement.

$$\begin{cases} \text{if} \quad C(x,y,t) > C(x,y,t) \quad \text{then} \quad \gamma(x,y) = \frac{C(x,y,t) - C_f}{C_f} \\ \text{if} \quad C(x,y,t) \leq C(x,y,t) \quad \text{then} \quad \gamma(x,y) = 0 \end{cases} \tag{3.14}$$

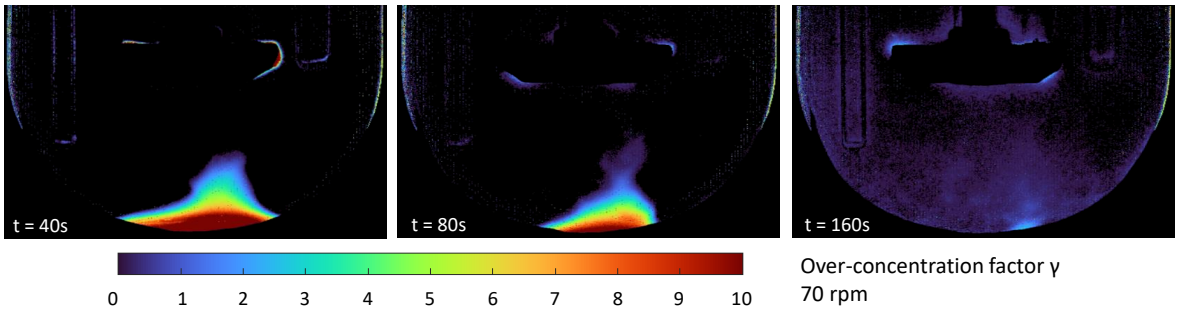

Figure 3.18: Over-concentration factor $\gamma(x,y,t)$ calculated for an average microcarrier concentration of 2.5 g L^{-1} at agitation rates of 70 rpm after 40, 80 and 160 seconds of suspension.

Average over-concentration index during particle re-suspension $\langle\gamma(t)\rangle$

From a global perspective, the integration of over-concentration factors $\gamma(x,y,t)$ can be calculated for all of the pixels in the reactor N_{pixels}. As a result, a global measure of the total over-concentration $\langle\gamma(t)\rangle$ present inside the STR can be estimated according to Equation 3.15 and the evolution of $\langle\gamma(t)\rangle$ can be observed over time to visualize the duration during which microcarriers will be subject to high levels of over-concentrations.

$$\langle\gamma(t)\rangle = \sum_{(x,y)=(1,1)}^{(x,y)=(x_f,y_f)} \frac{\gamma(x,y,t)}{N_{pixel}} \tag{3.15}$$

The evolution of $\langle\gamma(t)\rangle$ is presented in Figure 3.19 for agitations of 70 rpm (left) and 120 rpm (right). At agitation close to N_{js}, the time during which the STR is subject to important levels of over-concentration seems to be increased, possibly since homogenization takes longer. Interestingly however, the time during which zones of the reactor are subject to over-concentrations, as well as the levels of over-concentration, were found to be similar for all concentrations tested when agitating at 120 rpm. Accordingly, increasing agitation during suspension may be an interesting way to minimize the time during which over-concentrations are present in the STR (which may potentially damage cells).

Time-accumulated over-concentration during particle re-suspension Γ

The last step consisted in integrating the values of $\langle\gamma(t)\rangle$ in order to compare suspension profiles between each other. For this, the values of $\langle\gamma(t)\rangle$ were integrated until a steady state was manually observed in the STR. The duration to achieve a steady state can be found in Table 3.5. In order to compare results between each other, the

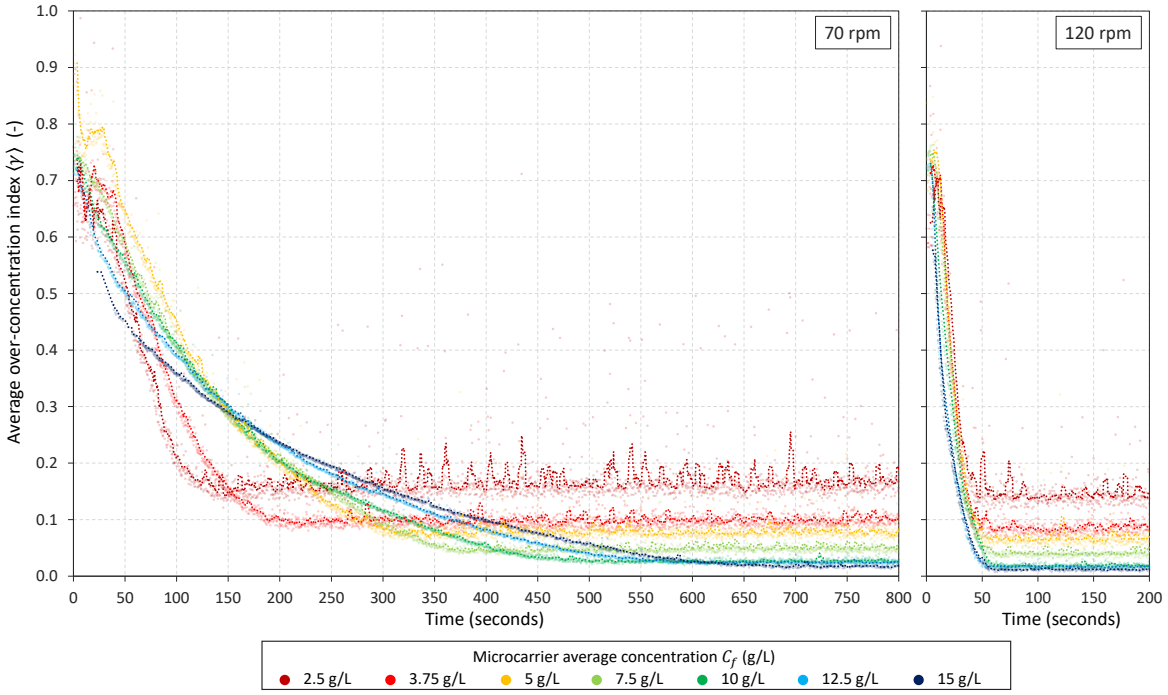

Figure 3.19: Average over-concentration index during particle re-suspension $\langle\gamma\rangle$ at 70 and 120 rpm and for microcarrier average concentrations C_f of 2.5 to 15 g L^{-1}.

average over-concentration factor at the steady state was subtracted from the measured over-concentration index and the overall over-concentration factor Γ was calculated according to Equation 3.16. The varying levels of over-concentration factor at a steady state $\langle\gamma(t_{steady})\rangle$ are expected to be caused by the varying levels of error depending on the concentration and not corresponding to a physical phenomena.

$$\Gamma = \sum_{t=0}^{t_{steady}} [\langle\gamma(t)\rangle - \langle\gamma(t_{steady})\rangle] \times t_{steady} \tag{3.16}$$

Table 3.5: Duration t_{steady} to achieve a steady value of $\langle\gamma(t)\rangle$ according to agitation and microcarrier concentration and corresponding steady state value $\langle\gamma(t_{steady})\rangle$ and calculated time-accumulated Γ factor.

Average concentration C_f (g L^{-1})	t_{steady} **at 70 rpm** (s)	$\langle\gamma(t_{steady})\rangle$ **at 70 rpm** (-)	Γ **at 70 rpm** (s)	t_{steady} **at 120 rpm** (s)	$\langle\gamma(t_{steady})\rangle$ **at 120 rpm** (-)	Γ **at 120 rpm** (s)
2.5	150	0.15	35.0	55	0.15	12.4
3.75	200	0.10	52.2	55	0.09	13.8
5	325	0.08	84.3	55	0.08	14.5
7.5	400	0.05	88.6	55	0.04	15.6
10	500	0.02	102.9	55	0.02	14.5
12.5	600	0.02	108.4	55	0.02	11.5
15	700	0.01	112.3	55	0.01	11.2

Results of the calculated Γ factor are presented in Table 3.5. To begin with, for an agitation rate of 70 rpm, Γ was found to increase with increasing microcarrier concentration indicating that the levels of over-concentration over time that high microcarrier concentration conditions are exposed to increase. This trend is not visible for an

agitation rate of 120 rpm, due to the fact that at this higher agitation rate, the homogenization time is much quicker and similar for all concentrations tested. Interestingly however, the Γ factors calculated were significantly lower for all of the concentrations tested with an agitation of 120 rpm. These results indicate that the duration during which microcarriers are over-concentrated and the level of over-concentration is much lower when increasing the agitation beyond N_{js}.

In addition, the severity of turbulent collisions can be related to the particles local kinetic energy, collision frequency, and volumetric solid fraction [9]. Considering that particles have a similar size to the Kolmogorov's microscale of turbulence λ_k, their local velocity v_p should be that of local turbulent eddies given by Equation 3.17.

$$v_p = (\nu\varepsilon)^{1/4} \quad \text{and} \quad E_C \propto v_p^2 \propto \varepsilon^{1/2} \tag{3.17}$$

It could also be considered that the agitator power number remains constant for the range of agitations and that the similitude $\frac{\varepsilon}{N^3D^2} \simeq 1$ is respected (Equation 3.18. In addition, based on the work of Cherry and Papoutsakis [9], particle collision frequency is expected to be proportional to particle velocity v_p (Equation 3.19).

$$E_C \propto N^{3/2} \tag{3.18}$$

$$CF \propto v_p \propto \varepsilon^{1/4} \propto N^{3/4} \tag{3.19}$$

Accordingly, collisions severity, during the suspension time, can be estimated via Equation 3.20. This type of approach integrates both collision intensities and an aspect of time during which cells will be exposed to such collisions. The comparison between the accumulated collision severity at 70 and 120 rpm during the suspension phase can be found in Figure 3.20. Results indicate that conditions with the smallest microcarrier concentrations had smallest TCS indices at 70 rpm. Above 3 g L^{-1}, a higher agitation rate (at 120 rpm) seems to diminish the accumulated collision severity during suspension.

$$TCS_{acc} \propto E_C \cdot CF \cdot \Gamma \propto N^{9/4}\Gamma \tag{3.20}$$

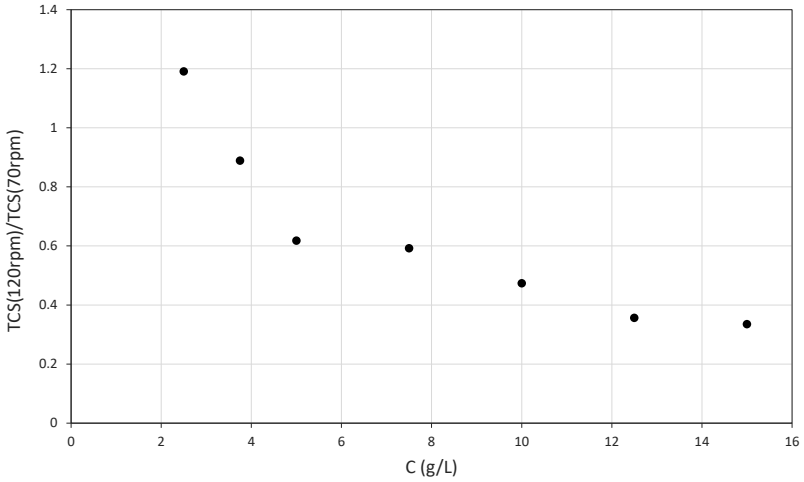

Figure 3.20: Evolution of TCSacc(120 rpm)/TCSacc(70 rpm) compared to microcarrier concentration

Discussion

Due to the adherent nature of MSCs and the fact that anchorage dependent mechanisms are expected to last between 5 and 20 minutes from a biological point of view [10], MSC expansion on microcarriers require an initial adhesion phase during which the MSCs and microcarriers settle at the bottom of the tank. In contrast, when cells have successfully adhered on the carriers, homogenization is preferred from a process perspective to limit aggregation, and reduce metabolic gradients including nutrient concentrations, metabolic by-products, but also to ensure sufficient aeration and pH controls. The nature of the process therefore results in an inevitable phase where microcarriers settled at the bottom of the tank are subsequently suspended. In addition, when microcarriers are fully colonized (typically after several days of expansion), it is possible to continue the expansion process by adding fresh microcarriers and using bead-to-bead cell transfers [11]. For the same reasons, the cell transfer from colonized microcarriers to fresh carriers require the sedimentation of the solid phase and a re-suspension after cells have successfully migrated. For these reasons, understanding mixing mechanisms during these stages is important to understand what stresses cells can be submitted to during these phases (which can occur several times during culture). Because mixing is a key process that determines bioreactor performance, a detailed analysis of how operational parameters such as concentration and agitation rate impact mixing efficiency and distribution is required for process optimization.

However, to date, few studies have characterised microcarrier mixing in STRs applied to microcarrier-based cell cultures. Mixing time in the Mobius CellReady bioreactor equipped with a marine impeller have been described for working volumes of 1 and 2.4 L with Solohill collagen-coated microcarriers (Pall Corp., USA) concentrations of 15 and 30 g L^{-1} [12]. In addition, mixing time in a vertical wheel system was deter-

mined for in comparison with STR [13]. Although these studies provide information on how mixing time is affected by parameters such as agitation, particle concentration and bioreactor size, the evaluation of mixing time and in particular concerning aspects of physical stresses that cells may perceive remain limited due to the difficulty of assessing particle concentration. To our knowledge, the evaluation of a local over-concentration factor applied to microcarrier suspension in STRs applied for MSC cell culture is quite unique and informative for this specific system.

In addition, the limits of the experimental method used should be kept in mind. To begin with, the calibration performed was found to have significant variations in measuring low concentration levels. This is possibly due to the calibration method, for which a separate and more detailed calibration may be required for low microcarrier concentrations. These should include repetitions during calibration to estimate the error of the experimental setup in itself including back light variation, sensor sensibility, light variation in the room *etc.* In addition, performing a calibration with specific low microcarrier concentrations between 0 and 5 g L^{-1} would be recommended to refine the calibration polynomial coefficients with those obtained for the large range of concentrations presented in the work above (for which attention was focused on over-concentration rather than measuring precisely low microcarrier concentration levels).

Lastly, the results presented above were performed for two agitation rates chosen at N_{js} and higher than N_{js}. Significant variations in the results obtained for these agitation rates were observed and would lead to the recommendation that agitating above N_{js} may minimize the stress that cells grown on microcarriers may perceive during suspension phases. However, defining the optimal agitation rate for this step would require the testing of a larger range of agitation rates for a given microcarrier concentration to evaluate levels of over-concentration (by calculating the Γ factor for example) and suspension time (by visualizing the homogenization index σ evolution over time). The decision of the agitation should also be based on the integration of hydrodynamic impacts of increasing agitation, for which the increased shear may also cause cell death. As a result, a compromise between minimizing mechanical stresses caused by overly concentrated zones in the STR and minimizing the shear stress that MSCs grown on microcarriers will perceive may be required. For this, further understanding the impact of both microcarrier-microcarrier collisions / friction and shear on MSC growth, death and quality attributes would be required.

3.3 Measuring particle collisions

3.3.1 Introduction

Particle-particle collision intensities may be a crucial parameter to monitor in processes using fragile solid phases and/or bioprocesses for which cells may be prone to damage. This notion of collision force is important from a physiological point of view since animal cells typically have specific responses when subject to high levels of hydro-mechanical stresses. Specifically, the influence of hydrostatic pressure and distortional strain was shown to impact MSC differentiation (for example, high levels of compressive hydrostatic stress may encourage chondrogenic differentiation while low hydrostatic stress may induce osteogenesis [14, 15]). As presented in Chapter 3.2, optical techniques can be used to determine particle concentration with high spatial resolution. However, these techniques are indirect measures of particle collisions for which intensity and frequency need to be extrapolated subsequently using theoretical models. For example, the local particle-particle collision frequency can indeed be related to local particle concentration measures since collision frequency is typically proportional to the particle number squared in a volume containing mono-dispersed particles. However, this probabilistic approach correlating particle collisions with concentration is limited and prone to errors. It is known that the modes of collisions between particles in a fluid should depend on both characteristics of the fluid (viscosity, turbulence *etc.*) and of the particle (inertia, size *etc.*). A detailed review of theoretical models and simulations of particle collision frequency (and historical assumptions) has been proposed by Meyer et al. who thoroughly explained the complex nature of particle collision modelling [16].

Physically, the collision intensity distribution in the bioreactors used for cell culture is expected to be correlated with the relative velocities of the colliding particles [17]. Accordingly, each local estimation of particle-particle collision frequency estimated via models described in [16] would be associated with a specific distribution of particles collision forces. An important pre-requisite to determine these forces seems to be modelling local relative particle velocities (which, in itself, is complex and difficult to measure and model in a dense liquid-solid suspension).

As a result, specific measures to directly detect, quantify and measure collisions could be used during process development to characterize elements pertinent to the solid phase but also as a tool to monitor these collisions during manufacturing and detect potentially critical deviations. The choice of acoustics as a detection method for the work presented in this sub-chapter was based on a literature review of particle-sensing technologies (individual particle detection was demonstrated in various experimental setups as described in Chapter 1.4). In the bioreactor geometry described previously, **the frequency of particle - sensor collisions was determined with impellers of different sizes and geometries through analysis of acoustic signals**. Subsequently, a model was

proposed to evaluate particle-sensor collision frequency according to parameters including the agitator type and diameter. An initial model was also proposed to estimate the average collision force which was measured for each collision by detecting variations in the acoustic signal intensity. In our study, the method proposed would require additional calibration to validate these results and should be considered as a proof of concept and methodology rather than definite and robust observations. The results presented are expected to mimic the possible collisions that particles could have with plunging and non-moving elements of the STR (and particularly how the collision force may vary depending on agitation and geometry). The work which will be presented is the object of a future publication *Using acoustics to measure particle-sensor collisions in bioreactors : a proof of concept study.* Lastly, optical endoscopic microscopic instruments were tested in view of determining if these types of equipments could also be used to detect microcarrier - microcarrier collisions.

3.3.2 Experimental setup : high frequency acoustic measures

Physical elements

The aim of the following work was to provide a prove of concept for the detection of particle-sensor collisions. All of the probes which would typically be used for MSC cell culture (pH, pO_2, temperature etc.) were placed as to have a similar geometry regarding plunging elements and thus similar liquid flows. The acoustic sensor was mounted in such a way as to take up the same volume as the dielectric probe and was inserted in the platform replacing this probe. **Consequently, results mimic typical collisions that cells grown on microcarriers may experience when hitting fixed plunging elements**.

The Reson TC4050 sensor provided by Teledyne Marine was noted as the most cited in the literature for particle detection. However, this particular sensor was no longer manufactured by the supplier and an equivalent model (Reson TC4013) was used. Advantages included the ability to measure a wide range of frequencies (from 1 to 170 kHz), a low detection level of -211 dB re 1V/µPa (relative unit used to specify the intensity of an underwater sound : to be able to compare relative intensities given in dB to one another, a standard reference pressure must always be used and is usually presented at 1 microPascal). This sensor was also expected to be sufficiently sensitive as to record collision signals with an estimated duration of 60 µs (expected duration of a collision according to similar work [18]). According to the Shannon-Niquist theory, the experimental setup (including acquisition system) should be capable of measuring frequencies at least as high as twice the expected signal. As a result, the acquisition card required for this experimental setup was chosen in order to meet these technical requirements (RedPitaya 40 MHz connectable STEMLab oscilloscope acquisition system). Lastly, a pre-amplification and physical filtration of unwanted parasitic frequencies was expected to be required. The Reson EC6081 pre-amplifier

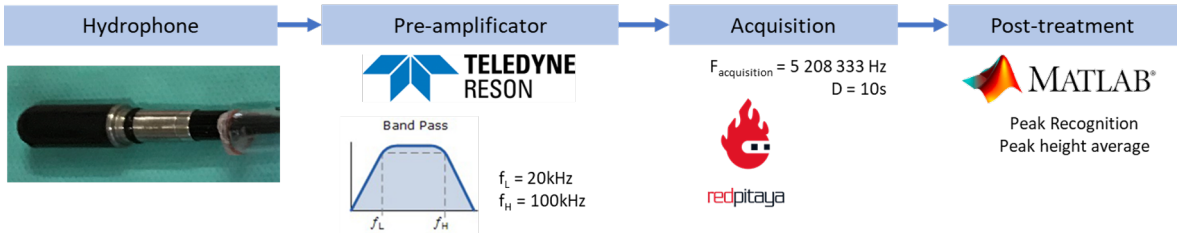

Figure 3.21: Schematic representation of the elements used for the acquisition of acoustic signals in the Tryton STR.

was chosen since it had a modulable High Pass filter (HP), Low Pass filter (LP) and output Gain (G) which could easily be adapted. A schematic representation of the different elements used for the acquisition can be found in Figure 3.21.

Particle description

Tracer particles (Tracer 1, reference : PSS-1.05 1.55 ± 0.05 mm, supplied by Cospheric) were used for initial proof of concept that the setup could detect individual particles (described in Table 3.6). They were chosen for their density close to that of microcarriers but the size of these particles was larger than the typical size of microcarriers by a factor of approximately 10. Accordingly, their physical characteristics would generate greater collision forces on the hydrophone and should therefore be easier to detect.

Table 3.6: Particle characteristics used for individual collision detection.

Particle	**Size range** (d_{95})	**Density**	**Material**	N_{js} (X = 2.73 $\%_{(v/v)}$)	τ_p	**St** (N = 70 rpm)
Cytodex 1	180 - 200 µm	1.03	Dextran	80 rpm	2.4 ms	0.10
Tracer 1	1500 - 1600 µm	1.05	Polystyrene	33 rpm	202.5 ms	8.41

For comparability, characteristic constants can be found in Table 3.6 which includes the minimal agitation rate to obtain a just-suspended state N_{js}. The value of N_{js} was calculated according to Equation 3.6 supposing a solid hold-up of 2.73 $\%_{(v/v)}$. It is important to note that due to the small size and low density of the particles, it is possible that the Zwietering correlation proposed not be adapted as reported in [5].

In addition, the Stokes number at 70 rpm was calculated according to Equation 3.8. As previously defined, the calculation of this dimensionless number characterizes the ratio between the characteristic response time of the fluid τ_p over a characteristic response time of the particles τ_k (corresponding to elements of inertia depending on particle characteristics). Accordingly, this ratio can be used to determine if particles will, or not, follow fluid streamlines. To calculate these constants, the characteristic turbulent time scale τ_k equal to 24.1 ms was used and the impeller power Number N_p of 0.5 (calculated in Paragraph 3.1.2 for an agitation of 70 rpm). The fact that the calculated Stokes number was found to be larger for the Tracer 1 particles (and

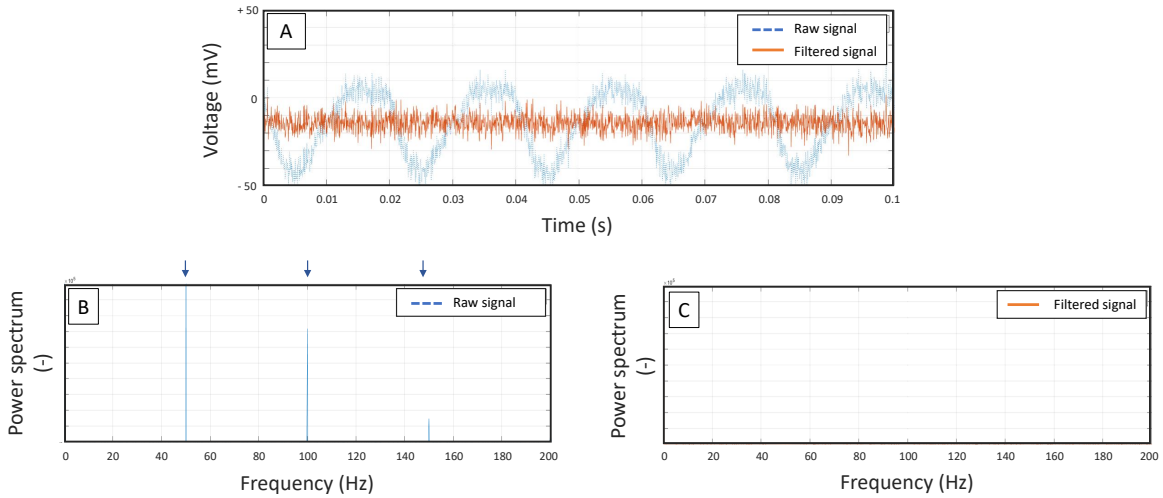

Figure 3.22: Post-treatment of the signal observed in the Tryton bioreactor filled with 700 mL of water without any agitation. (A) raw and filtered signal measured in the tank (B) Fast Fourier Transform (FFT) analysis of the raw signal. Arrows above the graph correspond to the parasitic harmonics of a 50 Hz signal (C) Fast Fourier Transform (FFT) analysis of the filtered signal. Results of FFT analysis are represented as a power spectrum for which the unities are relative to the measured voltage and have the same scale in (B) and (C).

greater than 1) indicates that these Tracer particles should, on average, not follow fluid streamlines due to their increased particle size.

Preliminary post-treatment signal analysis

Experiments were performed in water at various agitation rates to measure the acoustic signal without particles and set up acquisition parameters. As a preliminary experiment, high frequency acquisitions (20 kHz) of 5 seconds in 700 mL of Phosphate Buffer Saline (PBS) without any ongoing agitation were performed with the least restrictive settings on the pre-amplificator (LP filter of 10K Hz, HP filter of 1 Hz, Gain of 30 dB). PBS was used as it has a viscosity close to that of the culture medium used for microcarrier-based cell cultures and was also used for the light attenuation setup. Harmonics of a 50 Hz signal were detected after fast fourier transformation (FFT) of the measured signal as shown in Figure 3.22, B. The source of this signal is expected to be the alternative current used to power the electrical devices. These harmonic signals were eliminated by using specific band-pass filters (band width of 1 Hz) around the first 5 harmonics of a 50 Hz signal during post-treatment on Matlab. As it can be seen in sub-figures A and C, removing these harmonic signals led to a much lower overall amplitude of the blank signal and the absence of these harmonics in the power spectrum calculated by FFT.

Subsequent experiments were performed at increasing agitation conditions in order to understand the impact of the fluid movement caused by the agitator on the signal observed. Fast Fourrier Transformation of the data indicated that the sensor was detecting low frequency signals which were equal to three times the set agitation (Figure

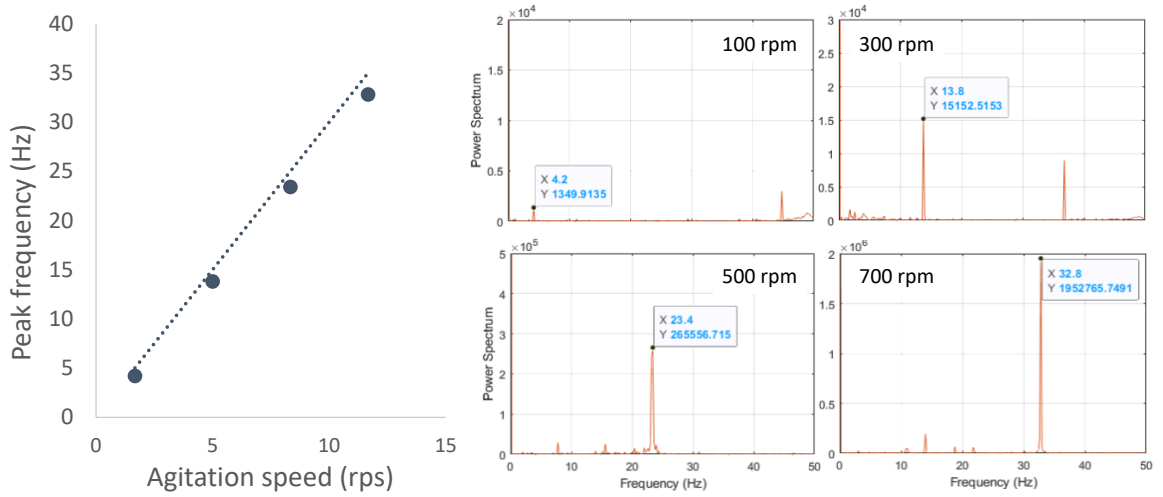

Figure 3.23: Low frequency signals observed when increasing agitation without particles. Left : Comparison between the frequency of FFT largest components and agitation. Dotted line represents a value of 3 times the agitation rate. Right : FFT transformation of acoustic signals observed with increasing agitation.

3.23). As the agitator chosen for these experiments was a down flow HTPG impeller with three blades, it was suspected that the hydrophone detected flow movements caused by the impeller movement. A post-treatment filter of 3 times the agitation rate with a bandwidth of 1 Hz was therefore implemented and applied when necessary.

These initial results were used to define the main sources of acoustic signals present in the STR without any particles. These were found to be (1) the alternative current used in the setup and (2) the hydrodynamic flow generated by the impeller blades with a periodic frequency equal to three times the agitation rate. For both identified signals, band-pass filters were setup during the post-treatment script via Matlab and contributed in reducing the experimental noise.

Effect of the acquisition format and frequency on the detection of particle-sensor collisions

Considering the preliminary results obtained in the liquid single phase flow, further experiments were set-up to detect how this signal would be modified in the presence of particles. All of the experiments described in this paragraph were performed with the maximum pre-amplifier gain (50 dB) and widest LP and HP filter combinations (1 Hz and 1 MHz respectively). Two compression formats of the raw data were tested (.TDMS and .wav) in order to determine the impact of compression on collision resolution. For this, particles were dropped from a height of approximately 3 cm on the sensor. Experiments were performed in PBS at room temperature. It was found that using the .wav format led to a Signal To Noise (SNT) ratio of approximately 30 while the .tdms format led to SNT ratios close to 90. As a result, the TDMS format was kept for

all further testing as was significantly more precise. The .wav format was also shown subsequently to not have sufficient temporal resolution to detect individual particle collisions.

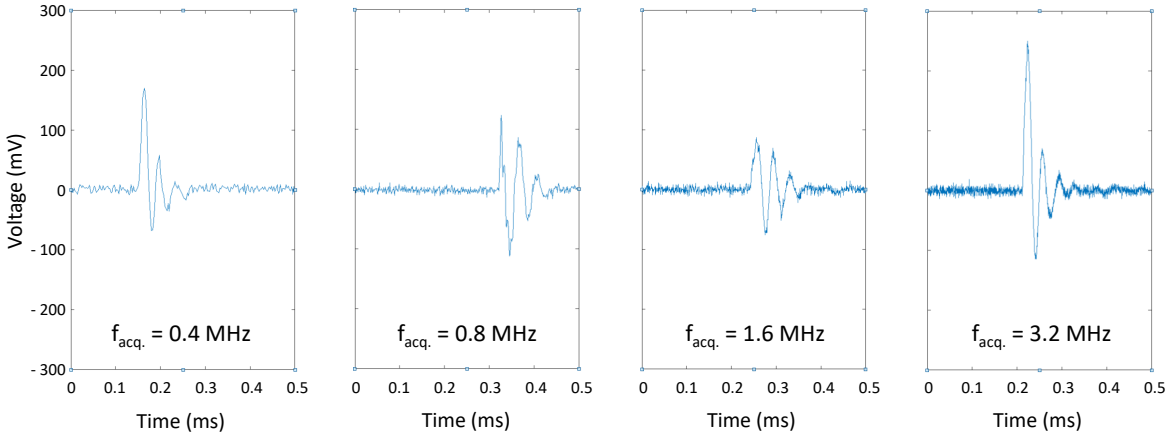

Figure 3.24: Impact of the acquisition frequency on the signal observed by dropping a glass particle of 5 mm from a height of approximately 3 cm in PBS.

Secondly, the impact of the acquisition frequency on the signal to noise ratio was evaluated by this time dropping large glass particles of an average diameter of 5 mm onto the sensor from a height of approximately 3 cm. This qualitative test indicated that the signal resolution was impacted by the acquisition frequency (Figure 3.24). Consequently, the highest acquisition frequency of 3.2 MHz was used for all subsequent measures as generated the highest signal to noise ratios in these conditions. It can be noted that the signal observed for a typical particle-sensor collision was found to last less than 0.2 milliseconds in total. The signal observed was composed of a sinusoidal signal which decreased in amplitude and for which an individual period lasted approximately 50 µs as it can be seen in Figure 3.24 with the highest acquisition frequency. It can be noted that the period of the signal measured corresponded with the period measured by Buffiere et al. [18] with a similar experimental setup (for which the individual period reported of a collision on an acoustic sensor was of 60 µs).

Automatic detection of particle-sensor collisions

Initial experiments were performed by modifying the pre-amplificator settings (*ie.* LP and HP filters as well as the pre-amplificator gain). The optimal setup conditions were found to be keeping the physical restrictions to a minimal on the low-pass and high-pass filters (*ie.* 1 Hz and 1 MHz respectively) and using the maximum gain (50 dB) on the pre-amplifier. Post-treatment of the data was performed by filtering the first 5 harmonics of the 50 Hz signal, applying a smoothing function (Savitsky Golay), and using an automatic peak detection function in Matlab with a threshold of 30 mV for peak detection and a set minimum distance between peaks t_p of 0.01 s. The threshold

value was set in such a way as to be significantly greater than typical filtered signal observed without beads and presented in Figure 3.22. The minimum distance between peaks was chosen to efficiently discriminate individual peaks from harmonics of a same signal (described further in the next paragraphs). An example of the types of signals analyzed after post-treatment can be found in Figure 3.25. The blue triangles above the peaks correspond to automatically detected peaks.

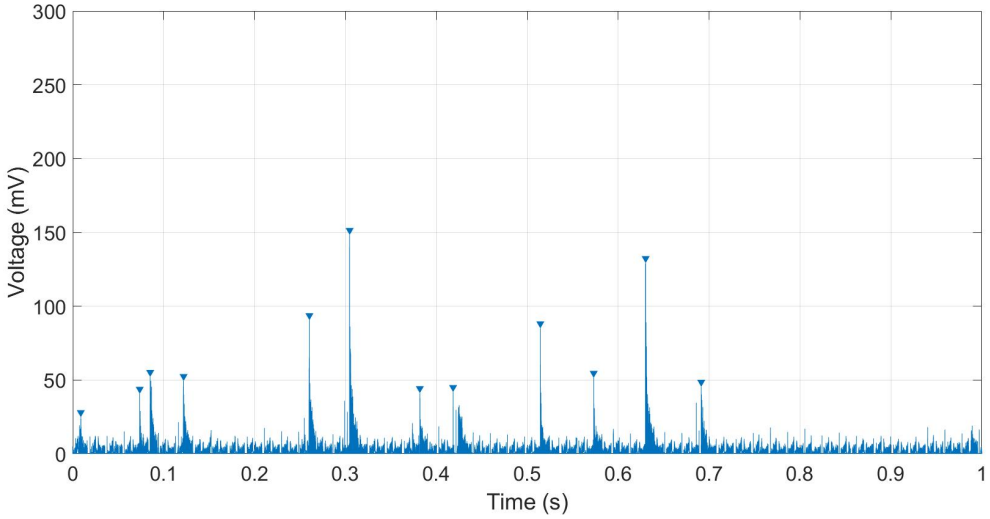

Figure 3.25: Example of detected particle-sensor collisions after Matlab post-treatment. Small triangles above the signal correspond to the automatic detection of peaks by Matlab script.

Sensor calibration

Once the individual collisions were detected by the Matlab script, the information concerning the intensity of the particle-sensor collisions could be estimated by integrating the observed individual peaks and through a correct calibration. For this, controls were performed by performing free falling experiments in the air and in water. Briefly, 0.5 mm glass particles (ρ_p = 2200 kg m^{-3}) were left to fall for 30 cm in water (ρ_l = 997 kg m^{-3}) and videos were taken to determine maximum particle velocity after image analysis and particle tracking. The particle velocity was also theoretically calculated for validation according to Equation 3.21. For this the fluid density ρ_L and viscosity η_L, particle diameter d_p and density ρ_p were used. The demonstration of the calculation of the terminal velocity by these equations can be found in the annex of Chapter 3.5. In both cases (video analysis of the free-fall experiments and theoretical calculation), the terminal velocity was calculated as 0.05 m s^{-1}. The area under the main peaks observed was then used to correlate particle kinetic energy at the time of the collisions E_c (Equation 3.22). For this, the peaks were considered as having a shape close to a triangular signal and the area was calculated by multiplying the peak height by the peak width at half of its maximum value. **The conversion ratio of 1 mV s^{-1} = 6.88**

10^{-7} J was applied for the analysis of peak intensities. An example of the signal observed during calibration can be found in Figure 3.26.

$$V_{lim} = g \times \tau \times (1 - \alpha) \quad with \quad \tau = \frac{2\rho_L (d_p/2)^2}{9\eta_L} \quad and \quad \alpha = \frac{\rho_L}{\rho_p} \tag{3.21}$$

$$E_{c,lim} = \frac{1}{2} \times m \times V_{lim}^2 = 2.55 \times 10^{-9} \quad J \tag{3.22}$$

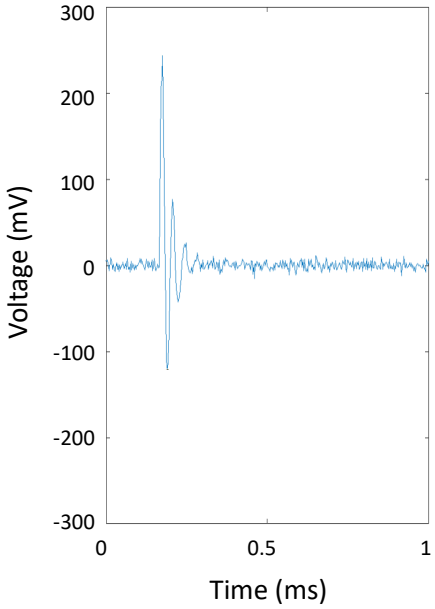

Figure 3.26: Example of an observed collision during the hydrophone calibration in free-fall experiments.

Defining the minimum time interval between peaks t_p by changing particle number

The first experiments were performed by changing the amount of tracer particles in the system. 100, 200 and 300 particles were respectively placed inside the bioreactor and collisions were automatically detected. It is possible that certain individual collisions be missed by the sensor when increasing the amount of particles due to an increased probability that a second particle collides with the sensor before the first signal is finished. It should be kept in mind that, in order to limit the detection of the same peak multiple times (in cases of strong collisions which may generate an oscillating signal which can last over 100 µs and led to several peaks), a minimal time interval between peaks t_p was set to 0.01 s (examples of raw data obtained over 1 second can be found in Figure 3.27 with 100, 200 and 300 particles, respectively A1, B1 and C1). In order to detect if certain collisions were missed by this setting, the same data was analyzed by decreasing the minimal time between peaks t_p to 0.0001 s or 100 µs (Figure 3.27 A2, B2 and C2). Both sets of experiments were performed with a HTPG impeller of 6 cm at 450 rpm (7.5 rps).

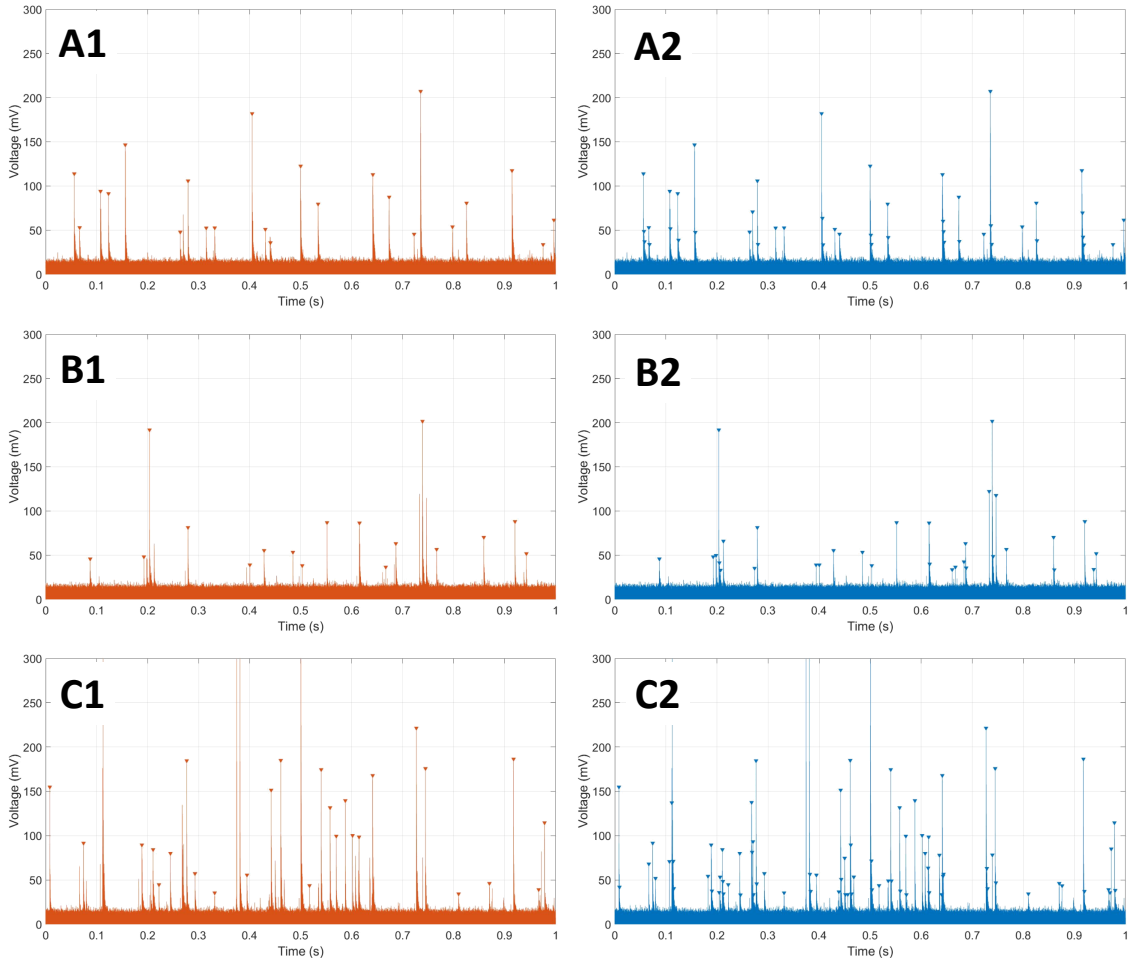

Figure 3.27: Automatic particle-sensor collision detection when increasing particle number and depending on t_p. Left, t_p was set to 0.01 s, right, t_p was set to 100 µs. 100, 200 and 300 particles were used respectively in experiments A, B and C.

Results concerning the statistics of the peaks detected in Figure 3.27 are presented in Table 3.7. As it can be seen, t_p greatly impacts the amount of collisions detected, particularly for high particle concentrations (301 peaks were detected for 300 particles when t_p was set to 0.01 s whereas 793 peaks were detected in the same conditions with a setting of 100 µs). A large difference in average peak width was also observed when increasing particle concentration from 100 to 200 particles when t_p was set to 0.01 s. This difference was reduced by setting t_p to 100 µs. Theoretically, it is expected that the average peak width should be independent of the number of particles in the system. As a result, the value of t_p was set to 0.0001 s or 100 µs for the rest of the work.

Table 3.7: Particle collision data over 10 s depending on the minimal time between peaks t_p of 0.01 s (left) and 100 µs (right) for a HTPGd impeller of 6 cm at an agitation rate of 450 rpm (7.5 rps).

Particle number (-)	**Nb. peaks** (-) t_p = 0.01 s	**Av. height** (mV) t_p = 0.01 s	**Av. width** (µs) t_p = 0.01 s	**Nb. peaks** (-) t_p = 100 µs	**Av. height** (mV) 100 µs	**Av. width** (µs) 100 µs
100	138	72.5	9	243	60.4	9
200	217	86.6	76	488	65.1	39
300	301	126.7	54	793	82.1	26

3.3.3 Results and discussion

Impact of particle number and agitator size on detected collision frequency and intensity

Experiments were subsequently performed by varying the amount of particles, the agitator diameter and the agitation rate in a same STR vessel. The minimum time between peaks t_p was kept constant at 100 µs which corresponds with a capacity of detecting 10 000 collisions per second. In addition, the raw data was pre-treated with a Savitsky Golay filter (order 3, frame-length 51) to smooth the data while keeping the major peaks of the signal. Downwards pumping HTPG agitators with diameters of 4 cm (HTPGd4), 5 cm (HTPGd5) and 6 cm (HTPGd6) were used for this experiment and results are presented in Figure 3.28. Data points are presented by agitator diameter. Accordingly, blue data points correspond to an agitator diameter of 6 cm, green data points were obtained with an agitator of 5 cm and orange data points with an agitator of 4 cm. The shades of each data point correspond with the amount of particles in the system (darkest colors correspond with experiments performed with the least amount of particles).

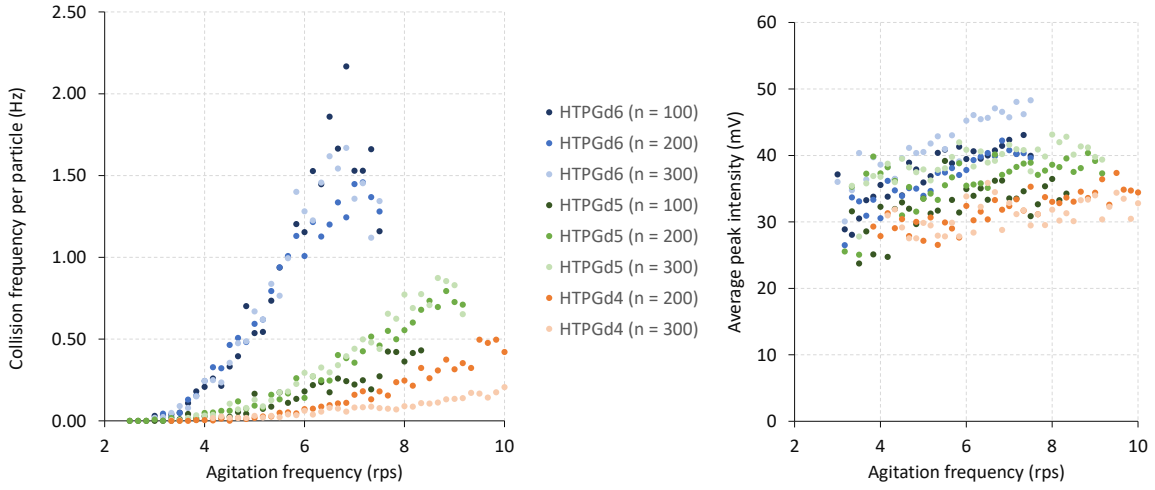

Figure 3.28: Automatic collision detection when increasing particle number and agitation rate with a minimum peak distance set to 100 µs. Left, collision frequency detected per particle ; right, average peak height.

To begin with, the collision frequency measured per particle according to the agitation rate when changing the agitator size can be observed in Figure 3.28, left and was found to be significantly impacted by agitator diameter. Collision frequencies obtained with the same agitator size (and are graphically represented by the same color) are impacted in a similar manner by agitation rate. In all cases, the collision frequency per particle was found to increase with agitation. A limit to this correlation was however observed for the largest agitator HTPGd6 (diameter of 6 cm). For this agitator, a threshold was observed for agitation rates at and above 6.5 rps. The measured collision frequencies in these conditions were found to be of approximately 1.5 collision per particle per second. In conditions with 100 particles, this corresponds to a 150 collisions detected every second, or a collision detected every 6 ms on average. Although these collisions are far from the limit imposed by the post-treatment algorithm (of a collision every 100 µs), it is possible that the distribution of the collisions in these conditions reach the experimental limit of detection and led to an under-estimation on the particle collision frequency. As a result, it should be kept in mind that high collision frequencies (above 150 collisions per second) may be underestimated. As a result, the data obtained over this threshold were excluded for the rest of this study. In addition, concerning the smaller impellers, the trends seem to suggest that there is an impact (although small) of particle number on the measured collision frequency per particle. For example, a higher collision frequency was reported for high agitation rates (above 7 rps) with the smallest agitator HTPGd4 with 200 particles compared to 300 particles (orange data spots). This trend was reversed for the HTPG5 impeller for which slightly larger collision frequencies per particle were observed with the least amount of particles (green data spots).

Lastly, a measure of collision intensity was carried out in these same experiments, presented as the mean peak height observed in mV. The mean peak height is expected to be correlated with the intensity with which the particles collide with the sensor. It seems that, globally, the average intensity with which the particles hit the sensor increases with agitation frequency and depends on the agitator size (Figure 3.28, right). For example, the increase in average peak intensity obtained for the largest agitator (HTPGd6, blue data points) was found to be more notable than the increase obtained for the smallest agitator (HTPGd4, orange data points).

Impact of impeller geometry and size on the observed N_{js} and collision frequency

For the three different agitator geometries tested (Elephant Ear (EE), HTPG and Rushton Tubine (RT)) and for the three agitator diameters tested (4, 5 and 6 cm), collisions were automatically detected during acquisitions at different agitation speeds with 300 particles. The minimal distance between peaks was kept constant at $t_p = 100$ µs. The results of the detected collision frequency according to the agitation frequency

applied are presented in Figure 3.29, left. In order to compare the different impellers, results are presented according to the agitation rate subtracted by N_{js}. This method to present results was chosen as it was supposed that for impellers of different geometries and of different sizes, the power required to homogenize particles P/V would be similar at N_{js} [5]. The acoustic measurement of N_{js} here corresponds with an agitation rate for which at least one particle collides with the sensor with sufficient force as to be detected within the acquisition time.

Table 3.8: Observed N_{js} for each impeller geometry and size and calculated value for HTPGd (300 Tracer-1 particles)

	HTPGd	**EE**	**RT4B**	**Calc. HTPGd**
D = 4 cm	3.19 rps	3.04 rps	4.22 rps	1.06 rps
D = 5 cm	3.81 rps	3.46 rps	3.60 rps	0.84 rps
D = 6 cm	4.29 rps	2.26 rps	3.14 rps	0.70 rps

Blue, red and green data points correspond to results obtained with HTPG, Rushton turbine and elephant ear impellers of different sizes respectively. Results tend to show that, for the three impellers tested and with 300 Tracer 1 particles, impeller geometry and impeller size had an impact on the amount of collisions detected by the sensor. The trends obtained for the three impellers of 6 cm (filled circles) were found to be extremely similar regardless of the impeller geometry. In all cases, reducing the impeller size led to a reduced amount of detected collisions but the reduced slope based on agitation frequency was found to depend on the agitator geometry.

Modelling collision frequency based on D/T

In order to reuse the work performed and understand the physical phenomena which may be detected by the acoustic sensor, a model was developed to explain the trends observed. To begin with, a linear fitting of all of the data sets with the agitation rate $(N-N_{js})$ was performed for each impeller size and showed a relatively good correlation. As a result, particle collision were suggested to occur at a rate proportional to the agitation rate, as previously reported by Buffiere et al [18]. The other parameters which were expected to impact the observed collision frequency include the agitator diameter D, tank diameter T and the amount of particles $N_{particles}$. For modelling, the amount of particles in the system was kept constant and equal to 300 particles. In addition, the geometry of the agitator was expected to impact the collision frequency (due to the differences in pumping number based on the agitator type at a given agitation rate). To take into account the geometrical aspects of the setup, a dimensionless S_{agit} factor is generally included in similar simulations [5, 19]. Taking into account these elements, the model presented in Equation 3.23 was proposed to estimate the collisions frequency CF based on these parameters and an a-dimensional factor A representing the power law observed on the ratio between the impeller diameter and the tank diameter.

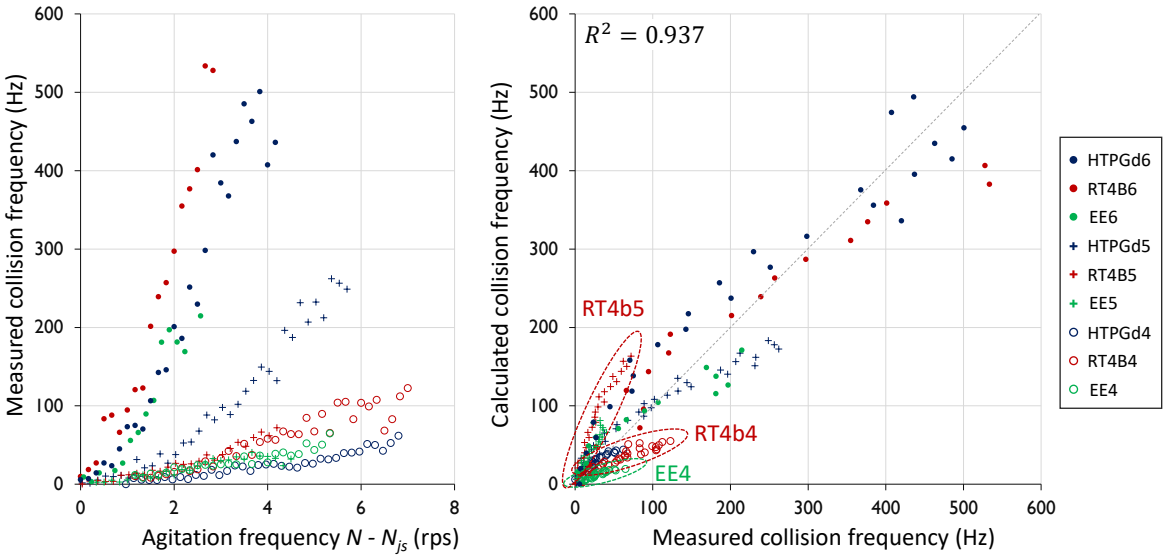

Figure 3.29: Automatic particle-sensor collision detection when changing agitator geometry and agitation rate. Left, collision frequency (Hz) observed with various impeller geometries and diameter ; right, comparison of modelled and experimental collision frequency based on the model of Equation 3.23 (parameters presented in Table 3.9). Results were obtained with $N_p = 300$ particles and t_p set to 100 µs.

$$CF = S_{agit} \times (N - N_{js}) \times \left(\frac{D}{T}\right)^{A} \times N_{particles} \tag{3.23}$$

The model proposed was solved by minimizing the root mean square of the difference between the modelled and measured data point susing a unique A parameter but different S_{agit} factors to account for geometrical aspects of the impellers. Calculated model parameters are presented in Table 3.9 and the comparison between the modelled and measured data can be found in Figure 3.29, right. Results show a good correlation between the measured and modelled data ($R^2 = 0.937$). However, plotting the results by type of impeller and diameter indicate that certain designs are more difficult to model (specifically small impellers which generate less collisions than the largest impellers). The most correctly predicted data was obtained for HTPGd impellers.

Table 3.9: Model characteristics solved depending on agitator type based on Equation 3.23. The A factor calculated was considered as constant for all agitators tested.

	HTPGd	**EE**	**RT4B**
$\mathbf{S}_{agit}$	56.4	31.7	68.3
A	7.2	7.2	7.2

The modelled factors show large variations in the S_{agit} factors calculated based on the type of agitator used. This was to be expected since the agitator geometry implies different macroscopic flows. While the Elephant Ear and HTPG impellers generate an axial flow leading to large re-circulation patterns in the tank, Rushton turbines generate a radial flow which leads to two smaller re-circulation flows below and above

the impeller as reported in [5]. In addition, little coherency with theoretical knowledge of collision frequency in agitated conditions was initially observed concerning the A exponent which was found to be close to 7. In order to further describe the trends observed by varying impeller diameter and shape, a separate approach based theoretical physical constants was applied.

Modelling collision frequency based on dimensionless numbers

As presented above, the model proposed was not found to be sufficiently coherent with known theoretical knowledge on what could occur in an agitated STR. As a result, the following approaches will rather correlate a standardized observed collision frequency with known dimensionless numbers. For this the ratio between the observed collision frequency (in Hz) and the agitation rate to which the value of N_{js} was subtracted was calculated. Accordingly, this dimensionless ratio was correlated with either the Reynolds number Re (Equation 3.24) or the Power number N_p (Equation 3.25) which are expected to theoretically intervene in particle collision frequency models. Accordingly, the collision frequency estimate should depend on the agitator diameter D, agitation frequency N, fluid density ρ, fluid viscosity μ, impeller generated power P and the gravity component g, which are expressed with three characteristic lengths (length $[m]$, mass $[kg]$ and time $[s]$).

$$Re = \frac{\rho \cdot N \cdot D^2}{\mu} \propto ND^2 \tag{3.24}$$

$$N_p = \frac{P}{\rho \cdot N^3 \cdot D^5} \Leftrightarrow P \propto N^3 D^5 \tag{3.25}$$

To begin with, the Reynolds number can be used to determine the flow regime according to Equation 3.24 and indicates a proportionality with the agitation frequency multiplied with the agitator diameter to the power of 2. Results between the measured and correlated data after solving for the different S_{agit} factors can be found in Figure 3.30. The solved factors can be found in this figure as well as the correlated equation. Overall, a high correlation ($R^2 = 0.985$) was observed between the observed and calculated collision values indicating that an approach based on the Reynolds number seems to correctly model the experimental data. The dispersion according to agitator types observed above were not observed with this model which defined individual S_{agit} factors based on both agitator type and size. It can be noted that slightly greater errors were noted for the smaller impellers (empty circles) as represented by a larger disparity compared to larger impellers (filled circles).

Lastly, a common indicator of mixing consists in using the power number N_p which is proportional to the power generated by the impeller P. This power can be a useful indicator and is proportional to the agitation rate to the power of 3 and the agitator

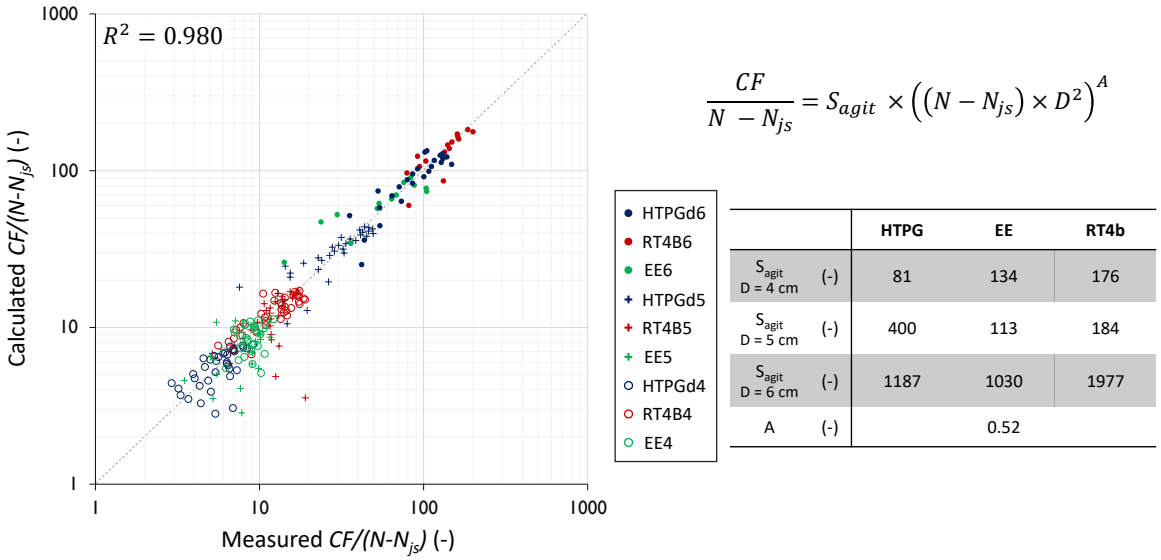

		HTPG	EE	RT4b
S_{agit} D = 4 cm	(-)	81	134	176
S_{agit} D = 5 cm	(-)	400	113	184
S_{agit} D = 6 cm	(-)	1187	1030	1977
A	(-)		0.52	

Figure 3.30: Comparison of modelled and experimental dimensionless collision frequency based on a correlation with the Reynolds number (Equation 3.24). Results were obtained with $N_p = 300$ particles and t_p set to 100 µs.

diameter to the power of 5 as indicated in Equation 3.25. The power number should typically depend on the agitator geometry. Results of the modelled data (correlated with P) compared to experimental data are presented in Figure 3.31 ($R^2 = 0.980$). The results presented here are extremely similar to those presented in Figure 3.30 and indicate that for both models, the dimensionless $CF/(N - N_{js})$ value correlates with $(N - N_{js})$ values to the power of approximately 0.5.

The approaches presented above present different modelling methods of the observed collision frequency based on two dimensionless numbers typically used to represent hydrodynamic and mixing characteristics. To begin with, the model proposed above can be compared to the model of Gjaltema et al which correlates particle collision frequency between two particle populations with the distance between the amount of each population, particle size and relative particle velocities [20]. The correlation assumes that the particles are larger than the turbulent microscales (like the experiments presented in this sub-chapter). In addition, Buffiere et al. used acoustic techniques in a three-phase fluidized bed to show the linear correlation between detected particle-sensor collisions and gas velocity [18]. As a result, it seems coherent that the measured collision frequency be related to $N - N_{js}$, as would be expected. Lastly, it can be observed that **calculating specific S_{agit} factors based on the agitator geometry and size greatly improved the coherency of the model proposed**. This is in accordance with physical models typically used to characterize mixing, for which correlation factors typically vary when geometric similitude is not maintained. For example, the well known Zwietering equation used to calculate N_{js} involves a similar S factor which has been proposed as depending on geometric ratios in the STR [5, 21].

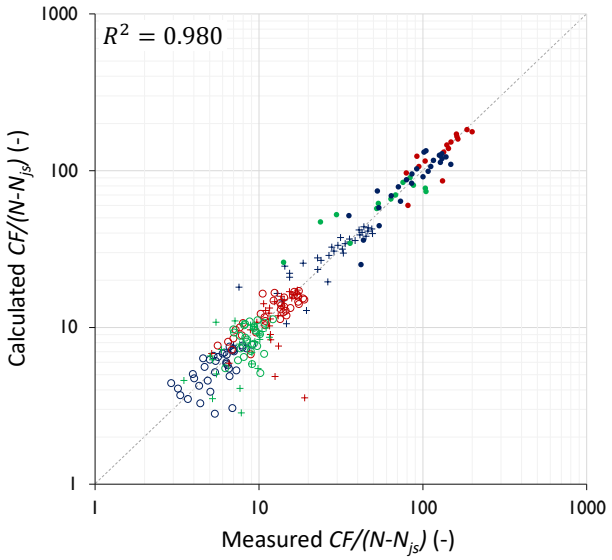

$$\frac{CF}{N - N_{js}} = S_{agit} \times \left(\left(N - N_{js} \right)^3 \times D^5 \right)^A$$

		HTPG	EE	RT4b
S_{agit} D = 4 cm	(-)	47	77	101
S_{agit} D = 5 cm	(-)	238	68	110
S_{agit} D = 6 cm	(-)	729	633	1215
A	(-)		0.17	

Figure 3.31: Comparison of modelled and experimental collision frequency based on the model on the Power number (Equation 3.25). Results were obtained with N_p = 300 particles and t_p set to 100 µs.

Impact of impeller geometry and size on collision intensity

The force with which particles collide with the sensor was also evaluated by determining the average peak height and width (results concerning the median height were found to less accurately represent the data and as a result the mean value was preferred). As previously reported [18], the force with which particles should collide with the sensor should be correlated with the area of the peak observed on the acoustic sensor. By assimilating the sinusoidal signal to a simple isosceles triangle, the average peak area can be assimilated as the product between the average peak height and the average width obtained at half of this height. These parameters were easily obtained and calculated in each condition via the *findpeaks* function in Matlab but results were found to be difficult to analyze due to important variations in the measured peak width. The area results were converted into a collision energy via the calibration value of 1 mV/s = 6.88 10^{-7} J but also results remained difficult to interpret.

As a result, the raw data of the average peak height was found to be the best indicator of an average collision energy that particles colliding with the sensor could have. Since, the initial calibration was not performed using the average peak height, only the raw data will be presented (Figure 3.32). A more thorough calibration of this technique would be required to further describe and measure collision forces, but the data obtained is extremely encouraging towards its feasibility. Results indicate that the average signal generated by particles colliding with the sensor seems to be relatively constant in each condition (Figure 3.32). A slight increase in this signal may be observed when increasing agitation and elements concerning impeller diameter may also impact this trend (smaller impellers were found to generate acoustic signals with a lower amplitude and had a lower impact of agitation as well). These results provide

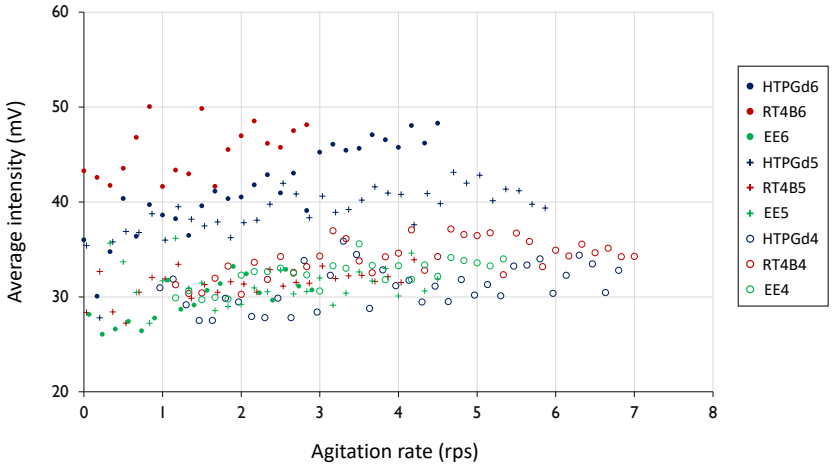

Figure 3.32: Average intensity of peaks (in mV) measured according to agitation characteristics (agitation rate, agitator diameter and agitator geometry). Results represent the average peak height value obtained of the peaks counted automatically and used for the collision frequency model (presented in Figure 3.29)

initial elements to characterize particle-sensor intensity quantification but would require a more thorough calibration (by using different particle weights for example) and also a more thorough description of these individual collisions (for which the experimental setup was found to have limitations concerning the collision frequency which could be detected).

A preliminary model based on the work of Zenit et al. [17] correlates particle pressure collisional force P_p with the local particle velocity u_0 squared according to Equation 3.26. For this the particle pressure should depend on the particle solid hold-up α, a function of this solid hold-up $F(\alpha)$ and liquid density ρ_L. These experiments were performed in experiments performed in a fluidized bed but results are expected to be similar in STRs when the probe is placed close to the tank wall. Accordingly, understanding the local particle velocities and local particle concentrations close to the localization of the probe would allow a local estimation of the particle pressure. In this experiment, integrating the signals obtained after a particle collided with the sensor allowed the measurement of P_p. Authors also compare their experimental results with other known models.

$$P_p = \alpha \cdot \rho_L \cdot F(\alpha) \cdot u_0^2 \tag{3.26}$$

In the present work, the estimation of the fluid velocity can be related to the agitation rate $(N - N_{js})$ and agitator diameter divided by the tank diameter D/T. As a result, a similar approach to that performed for collision frequency was applied to the measured collision intensities based on Equation 3.27 by considering that the fluid velocity was related to $N - N_{js}$ multiplied by D/T and by considering an independent value of particle pressure at N_{js} equal to $S_{agit_{P_0}}$. Results of the calculated and mea-

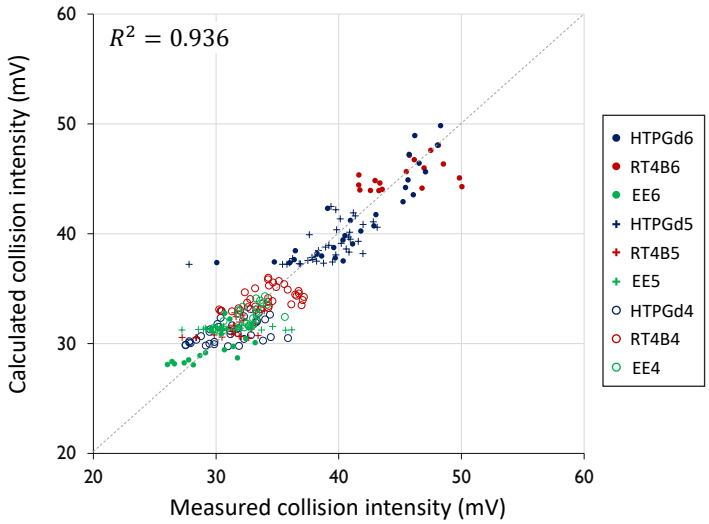

$$P_p = S_{agit,P} \times (N - N_{js})^2 \times \left(\frac{D}{T}\right)^2 + S_{agit,P_0}$$

$S_{agit\ P}$ (mV s²)	HTPG	EE	RT4b
$S_{agit\ P}$ D = 4 cm	0.67	1.04	0.58
$S_{agit\ P}$ D = 5 cm	0.88	0.11	0.81
$S_{agit\ P}$ D = 6 cm	2.46	2.23	3.01

$S_{agit\ P0}$ (mV)	HTPG	EE	RT4b
$S_{agit\ P0}$ D = 4 cm	0.17	0.37	0.34
$S_{agit\ P0}$ D = 5 cm	0.47	0.15	0.31
$S_{agit\ P0}$ D = 6 cm	0.97	1.86	3.01

Figure 3.33: Comparison of modelled and experimental collision intensities (in mV) depending on the agitator geometry and size and calculated S_{agit} coefficients.

sured collision intensity data (measured in mV) are presented in Figure 3.33. Results indicate a good correlation between the measured and calculated data. Similar experiments would be interesting with a more robust calibration of the method based on the integration of the signal obtained (as it has been described in literature) and possibly by calibrating the technique by using different bead properties.

$$P_p = S_{agit,P} \cdot \left((N - N_{js}) \cdot \frac{D}{T}\right)^2 + S_{agit_{P_0}} \tag{3.27}$$

Considering Equation 3.27, it is possible to discuss the effect of bioreactor scale on particle collisions intensity. If a geometric similarity is kept between two bioreactor scales (D/T = constant), the suspension of microcarriers is related to power dissipation per unit of volume (see [5]). This means that, in parallel, the tip velocity ND should decrease when the bioreactor scale is increased. However, the impact of bioreactor scale on the term $S_{agit_{P0}}$ is not clear and should be more precisely studied but, due to the decrease of N_{js} when T is increased, this term should also be lower. Consequently, for a constant P/V scale-up and a bioreactor operating at $N \approx N_{js}$, the collision intensity should be less intense at the larger scale.

Conclusion

The results presented above provide a proof of concept that using acoustic techniques can be efficiently used to detect individual particle collisions in a stirred tank reactor. The technique was efficiently used to detect a measure of N_{js}, defined in this study as the minimal agitation required to detect at least one particle collision during the acquisition time. Although the definition is not identical to the typical definition typically used in literature [19], the fact that the detection method is easy to put in place and

automated provides certain advantages. In addition, additional optimization of the technique could be used to detect similar aspects of N_{js} in conditions which could be difficult to detect using optical techniques, for example when using viscous solutions, using an opaque tank or opaque and concentrated particles.

In addition, for large particles, online measures of particle-sensor collision frequency was demonstrated and, with a sufficiently robust calibration, elements of collision intensities. A model was proposed to estimate collision frequency based on known parameters including agitation rate ($N - N_{js}$), and the ratio between the agitator diameter and the tank diameter D/T. Accordingly, defining a correlation factor which depended on the agitator diameter and type was found to provide a robust estimation of collision frequency with a correlation coefficient of 0.976. The most robust model was found to be based on an approach correlated with the Reynolds number and on the Power number. As a result, it would be recommended to follow this work with a larger range of agitators, in a different tank size and with different liquid viscosities to further characterize the physical phenomena observed.

Lastly, a measure of average collision intensity was estimated by measuring the average collision peak height measured by the acoustic sensor. Although the calibration of the setup to estimate the force with which the particles collided with the sensor (based on an integration of the measured peaks) was found to be insufficient, the results obtained remain interesting. They provide a methodology which could be applied with a more robust calibration technique to estimate particle-sensor collision intensities. By placing the sensor at different areas in the tank, this measure could bring additional information on possible spatial heterogeneities concerning particle-sensor collision intensities. In addition, by increasing the sensor sensibility and testing the experimental setup with smaller particles, it could be possible to gain more information on microcarrier collision-sensor intensities.

3.3.4 Identification of particle interactions using high resolution endoscopic probes

The results presented above provide interesting experimental data correlating collisions which can occur between particles and an online sensor. However, the acoustic signals measured were caused by direct collisions between the particles in the system and the sensor. Optical techniques may provide additional data. For example, collisions between calibrated 6 mm Pyrex beads in a solid-liquid fluidized flow were measured by particle tracking of colored tracers using a high speed camera equipped with a CMOS sensor (the acquisition frequency was set to 500 Hz) [22]. The technology was used to identify and track individual particles. However, these experiments concern

relatively large particles for which the Stokes number St is typically greater than 1, which does not accurately predict what could occur at smaller scales. Decreasing the scale of the measured particles (by a factor of 30 for example with microcarriers) is expected to significantly increase the complexity of the technology required for their measurement and may require bringing the sensor closer to the measured collisions by using endoscopic techniques. The following paragraphs will describe experimental elements evaluating the feasibility to detect local microcarrier-microcarrier collisions through high resolution endoscopic techniques.

High resolution endoscopic measures

High resolution endoscopic probe technologies have seen significant advances recently and been used to obtain information about bi-phasic systems (including local particle concentrations and collisions). For this, a sample is illuminated via a light source and the light diffused, reflected or scattered is then measured by a sensor. It can be noted that different illumination methods create individual optical scenes in the measuring volume of endoscopic probes. The way the sample is illuminated and how the light is then scattered and received can have a significant impact on the quality of the results obtained. For example, in the case of bubbles, the same bubble size distributions were measured by using reflection, transmission and transflection methods but with varying levels of resolution (photos of Figure 3.34, [23]). To begin with, transmission measures (which quantifies the amount of light transmitted through the medium and bubbles) were found to largely over-saturate the sensor and led to a difficult analysis of bubble numbers and size. Using sensors based on reflection (for which the amount of light reflected by the bubbles was quantified) decreased this contrast and led to photographs in which individual bubbles could be detected. However, the large amounts of reflection and shadows in this setup made it difficult to determine accurate bubble sizes. Lastly, transflection measures of these same bubbles, based on more complex optical paths through the sample, showed a high variability between direct and diffuse measures. As authors state, bubbles were much more difficult to detect in the direct transflection measures compared to the diffuse transflection method which provided the most accurate method to detect bubble size distributions. As it can be seen in this example, the choice of sensor and illumination methods can have significant impacts on the amount of information which can then be extracted from these experiments as well as their precision.

A review of manufacturers which provide the different endoscopic technologies described above was performed to perform experiments on microcarriers on which MSCs were grown. The probes provided by the SoPAT company were chosen since have already been used for the development and monitoring of pharmaceutical production processes including micro-encapsulation, active ingredient crystallization, extraction,

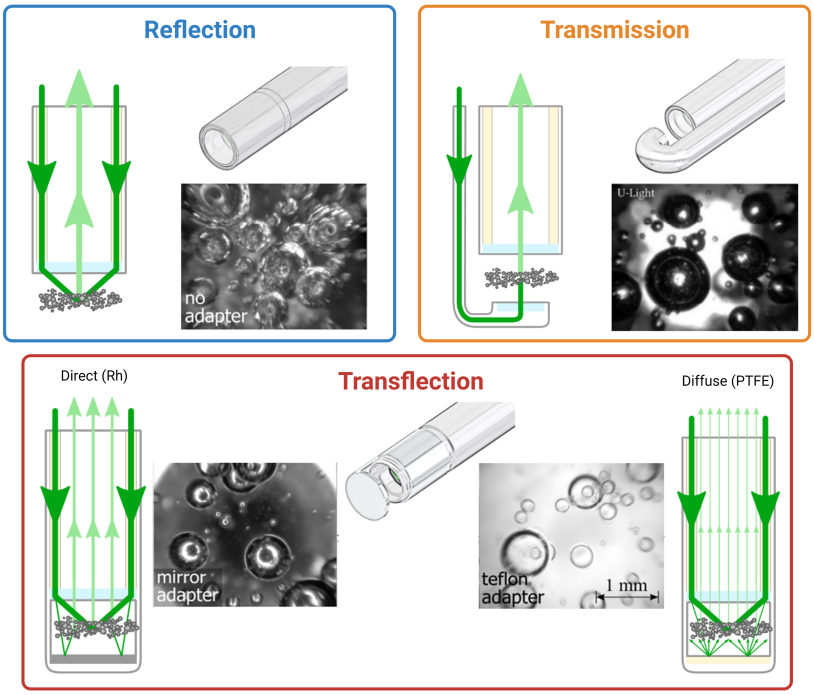

Figure 3.34: Description of various endoscopic sensors provided by SoPat. Photos correspond to air/water systems with 0.012 % PVA (polyvinyl alcohol) (Alcotex B72) as a surfactant (adapted from [23]).

granulation *etc.* For this, the fact that probes can be Cleaned In Place (CIP), Sterilized In Place (SIP) in an autoclave, as well as their 21-CFR certification is an asset for their use in a process-oriented research context and process monitoring. The technical specifications requested included the ability to (1) view individual particle collisions (for which we expect the collision duration be of approximately 60 µs [18]), (2) detect individual microcarriers (particle average diameter of 200 µm), and, if possible, (3) detect cell growth, confluence or shape on microcarriers. The last element is out of scope for collision detection but is an added benefit of using optical techniques compared to other collision detection methods. The probes used offered reflection, transmission and transflection measurement methods described in Figure 3.34. In the case of transflection, both direct (Rh) and diffuse (PTFE) transflection technologies were tested.

Since the acquisition frequency of all the probes capable of detecting particles of this size were set to 15 Hz by the manufacturer and could not be modified, the resolution of this technique for particle detection ultimately depends on local particle velocities around the sensor. Considering the low Stokes number of Cytodex 1 particles in the experimental setup, local particle velocities were estimated as being equal to local fluid velocities. The distribution of fluid velocities were estimated as less than 0.065 m s^{-1} in 90 % of the STR volume at 70 rpm and less than 0.14 m s^{-1} in 90 % of the STR volume at 120 rpm by the CFD simulation presented above (Figure 3.2). Supposing an average velocity of 0.1 m s^{-1}, with an acquisition frequency of 15 Hz, the particles would span around 6 600 µm between frames. Two similar endoscopic probes were

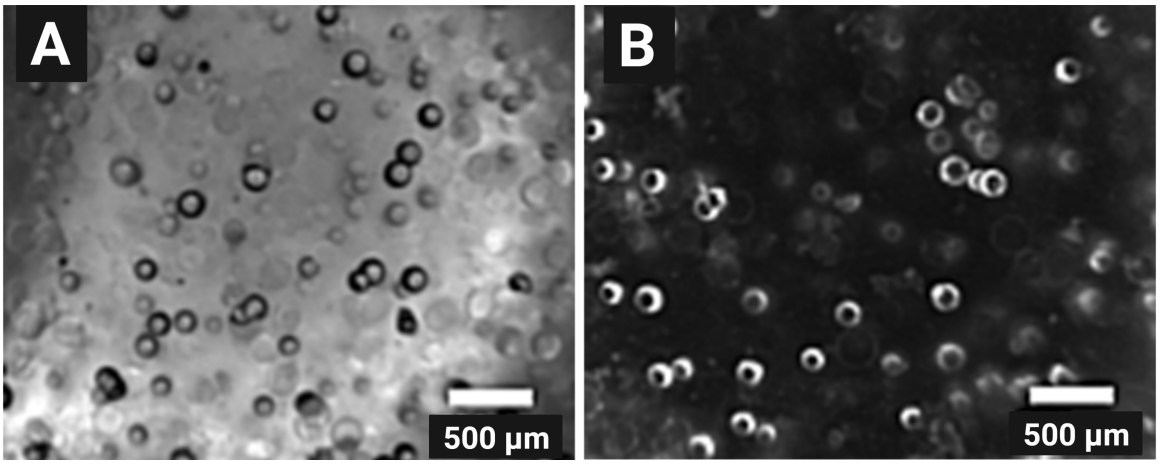

Figure 3.35: Optimized measurement of microcarriers with the SoPat Kr probe. A. Diffuse transflection (PTFE) measurement ; B. Direct transflection (Rh) measurement. Schematic representation of the optical paths are presented in Figure 3.34.

tested on cell-loaded microcarrier samples : the Sc probe and the Kr probe which has a larger field of view (see Table 3.10).

Table 3.10: Technical specifications of probes provided by SoPat to measure particles

Sensor Name	**Measurement Range [µm]**	**Field of View (diag.) [mm]**	**Frame Rate [Hz]**
Mesoscopic - Sc	9 - 1,100	2.6	15
Macroscopic - Kr	30 - 7,700	18	15

Preliminary results

The feasibility of using these optical endoscopic probes was evaluated by sending samples of MSCs grown on Cytodex-1 microcarriers to which a small amount of plastic particles were added. The objective was to identify if the sensor technology could detect the optical differences between these particles (Cytodex 1 microcarriers are transparent whereas Plastic particles are not), cell adherence on the microcarriers and essentially microcarrier collisions. To begin with, measures were performed with the Kr probe, which has the advantage of having a large reading frame and for which the measurements are performed using direct (Rh) and diffuse (PTFE) transflection technologies. A photographic example of the results obtained with this probe can be found in Figure 3.35 and indicate that in both PTFE and Rh measurements, optical differences were observed between the Cytodex-1 and plastic particles and that the Cytodex-1 particles were much harder to identify. In addition, the acquisition frequency and resolution of this probe was found to be insufficient to either detect particle-particle collisions or cells grown on microcarriers. As a result, the readings from this probe were found to be insufficient to continue using this probe in further experiments.

Results measured by the Sc probe which uses reflection and direct (Rh) or diffuse (PTFE) transflection optical paths are presented in Figure 3.36. The plastic particles

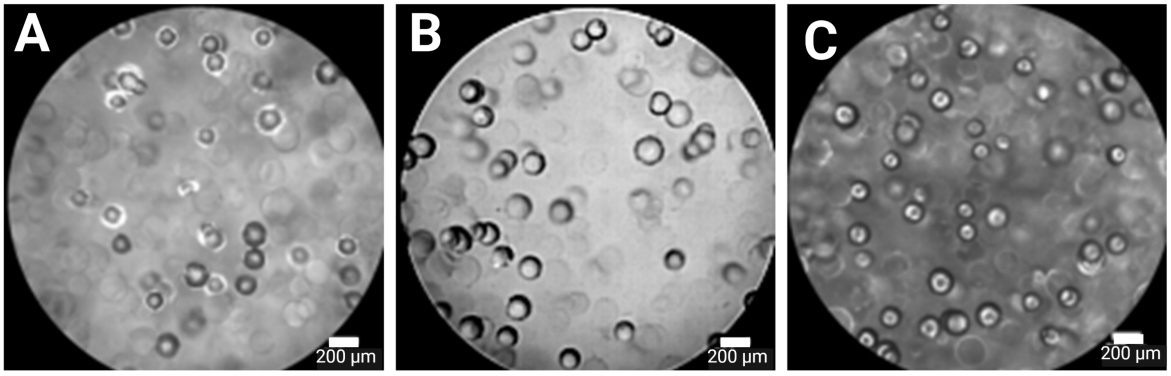

Figure 3.36: Endoscopic observation of microcarriers with the SoPat Sc probe. A. Reflection measurement ; B. Diffuse transflection (PTFE) measurement ; C. Direct transflection (Rh) measurement.

with a higher refractive index were easily detected by the probe and particle detection software, whereas cells and Cytodex-1 microcarriers were difficult to identify. The PTFE illumination settings were found to be the most promising for particle detection. However, when analyzing the videos obtained with the probe, the acquisition frequency was found to be insufficient to detect particle-particle collisions.

Additional measures were performed with the Sc probe in order to increase contrast and resolution for which photos are presented in Figure 3.35. In both Reflection and PTFE modes, cell colonization on the Cytodex-1 microcarriers was observed. In the reflection mode, a difference between the Cytodex-1 and the Plastic particles was observed indicating that this type of technology could be used to efficiently discriminate both microcarriers. It was however difficult to analyze these photographs and detect individual cells with this light profile. In contrast, the PTFE mode was found to be more efficient at detecting cell colonization on the Cytodex-1 microcarriers, but discriminating Plastic microcarriers from the added Plastic particles was found to be difficult.

Discussion

The brief results obtained above are a preliminary proof of concept that particle visualization by endoscopic microscopy can efficiently be used to detect individual Cytodex 1 microcarriers and Plastic particles and may be capable to detect elements of confluency on the microcarriers (with sufficiently precise and robust development). This preliminary proof of concept identified that, in the current state, the technologies provided by the supplier are lacking essential elements to detect particle-particle interactions (*i.e.* sufficient acquisition frequency which, ideally would need to resolve these collisions at the micro-second scale and sufficiently large acquisition frame in order to have the ability to use particle tracking algorithms in the flow conditions).

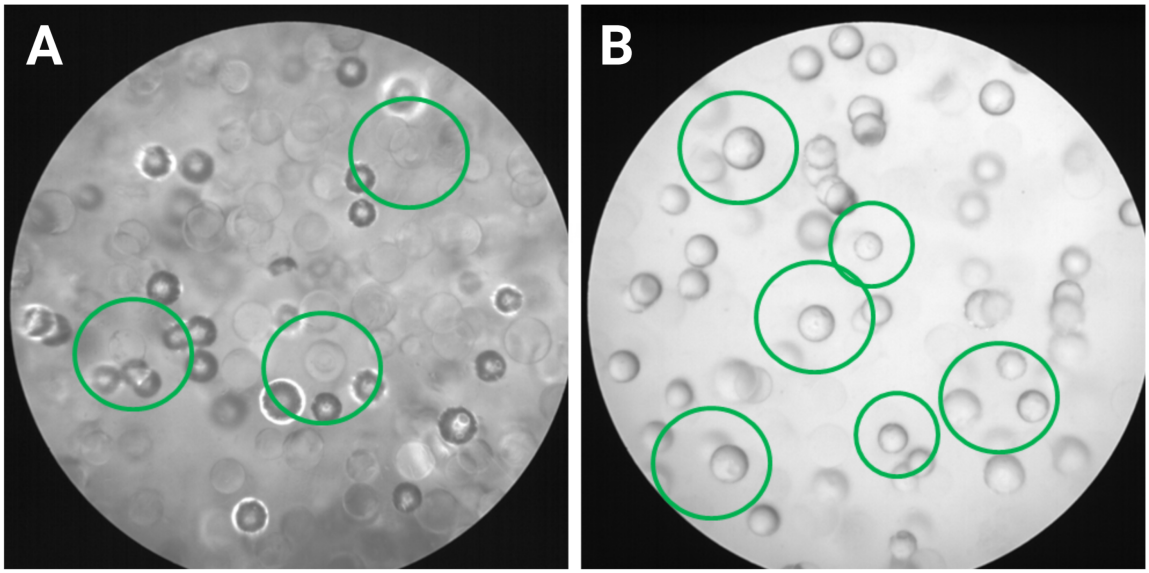

Figure 3.37: Optimized measurement of microcarriers with the SoPat Sc probe. A. Reflection measurement ; B. PTFE measurement. Green circles represent colonized Cytodex-1 microcarriers on which cells can be observed.

3.3.5 Section Summary

Acoustic and endoscopic measures were tested in this sub chapter to detect if they could be used for particle collision estimation. Only the acoustic measures were found to be sufficiently resolute to detect individual particle collisions. For this, **particle-sensor collisions were quantified by post-treatment of acoustic signals by using tracer particles which were approximately 8 times larger than microcarriers but had the same density. A method was proposed to estimate collision frequency according to the shape and size of the impeller and the agitation rate**. However, in this setup, the large particles used had a high Stokes number (St over 8) indicating that particles had movements, on average, independent of the fluid streamlines. This is not expected to be the case for microcarriers which have much smaller Stokes numbers. Considering the few experimental parameters tested and the large particles used, the work described above should rather be considered as a proof of concept and methodology proposal than a robust and demonstrated model.

In addition, it is still unclear which physical phenomena explains the collision frequency and intensity observed through the measured acoustic measures. In order to further discriminate between different models and further understand what mechanisms impact collision frequency with fixed elements in the STR, experiments with a wider range of experimental conditions would be recommended. These would include :

- performing experiments with different fluids. By changing the fluid viscosity, it would be easier to detect the impact of turbulence and define if the Reynolds number still accurately predicts collision frequency with the same S factors at

similar Reynolds numbers.

- performing experiments with different agitators. Using other impeller geometries for which power numbers in similar conditions are known and testing the HTPG and Elephant Ear impellers in upwards motion would bring more information on the correlation with mechanical power. In addition, since the macroscopic fluid motions are known to be significantly different depending on radial or axial impellers, the impact of these large fluid and particle circulation loops on the measures collision frequency would be interesting.

- performing experiments with different tank geometries. The model proposed assumes that the ratio between the agitator diameter and the tank diameter is the most important factor. However, it is unclear with the experiments performed if this is truly the case or if other parameters (such as the distance between the impeller tip and the acoustic probe, or the distance between the impeller tip and the tank wall) would represent this dimension more accurately. In a larger tank, measurements in different zones of the STR could be of use.

- setting up similar experiments with particles of different sizes. Notably, the fact that the tested particles presented above were significantly larger than the microcarriers makes results difficult to extrapolate to microcarriers which have different Stokes numbers and therefore should have significantly different movements within the fluid. This would require further design and implementation since the current setup was found to not have sufficient resolution to detect the smaller particles (even when testing glass particles which are significantly more dense then microcarriers). Detecting individual microcarrier collisions with the sensor may require a different piezoelectric technology. A frequency-based analysis of the signals obtained with the smaller particles could also be used if individual collisions cannot be isolated.

3.4 Chapter overview

As described above, the aim of this chapter was to estimate collisions that cells grown on microcarriers may perceive in view of determining if certain process parameters could reduce the mechanical stress that cells may be subject to. These collisions concern (1) microcarrier - microcarrier collisions, (2) microcarrier collisions with moving elements in the STR, for example the agitator and (3) microcarrier collisions with fixed elements of the STR such as the tank wall and plunging elements. The collision forces and / or frictional forces that a cell grown on a microcarrier may perceive during cell culture would be expected to be a combination of these three physical mechanisms.

To begin with, a local estimation of microcarrier concentration was obtained by measuring the attenuation of light generated by a back-light through a clear STR in which microcarriers were added. **The evolution of local particle concentrations over time was observed and factors including mixing index, homogenization duration and concentration factors were defined and measured. The results provide a quantitative measurement of mixing characteristics locally and over-time specifically applied to a STR routinely used for MSC expansion using Cytodex-1 microcarriers**. Interestingly, the quantification of microcarrier local concentration over time led to the identification of certain zones near the bottom of the tank which were subject to large levels of over-concentration (reaching up to 10 times the measured final concentration in the tank) for up to 10 minutes. These should be kept in mind when designing and implementing suspension protocols at large scale. The impact of these highly concentrated steps during suspension are, for now, unknown and may lead to a substantial degradation of the cells grown on microcarriers. Secondly, **agitating at 1.5 times the calculated N_{js} was found to reduce homogenization time, reduce over-concentration duration and reduce an overall estimation of over concentration (integrated in a factor Γ). Consequently, it would be recommended, in order to limit the physical constraints caused by microcarrier friction and or collisions, to agitate higher than N_{js} during particle suspension**. This should reduce the potential damaged caused to the cells grown on micorcarriers, but a compromise should also be investigated since agitating at a higher rate should also lead to a greater dissipated power in the tank, for which the generated shear stress may also damage cells. As a result, further work integrating both the physical knowledge on the liquid phase (obtained here by CFD simulations) and on the solid phase (described by local concentration measurements), would be extremely valuable.

Lastly, acoustic measures were used to detect particle-sensor collisions using tracer particles for which the diameter was approximately 8 times the average microcarrier diameter. **Individual particle-sensor collisions were successfully identified by a Mat-**

lab algorithm designed specifically for this application. Based on the detected data, different models were tested to correlate with the measured collision data. Considering the large size of the tracer particles and the few operating parameters tested, the acoustic measures provide a proof of concept and method description study as to how similar and more robust acoustic reading could be analyzed. For this, it would be advised to perform acoustic measures using different tank diameters, varying fluid velocity and by continuing the experimental proof of concept with smaller particles.

As a conclusion, it would be suggested to integrate the information obtained through numerical simulation, through optical light attenuation, and through acoustic signal analysis described in this chapter. All of the methods provide elements to quantify critical aspects of the liquid and solid phase but all cannot be grouped for the moment. For example, it would be interesting to use the concentration results obtained in the context of this study to validate certain hypotheses which would be required to perform numerical simulations with the solid phase. By using the data obtained for different agitation rates and at different microcarrier concentrations as a validation of numerical simulations, certain collisional measures may be estimated by CFD which could also be integrated to define holistic factors, such as Γ, numerically. In the case of the acoustic sensor, the large difference between the Stokes number of the particles used for these experiments and the Cytodex 1 microcarriers remains the main bottleneck. Currently, it is not clear how the acoustic data obtained for these large particles could correlate with what could occur with smaller particles.

Bibliography

[1] C. Sion. *Development of an optimized perfused-continuous process of culture of human umbilical cord mesenchymal stem cells (hMSC) grown on innovative adhesion supports.* PhD thesis, Université de Lorraine, 2020.

[2] C. Loubière. *Characterization and impact of the hydrodynamics on the performance of umbilical-cord derived stem cells culture in stirred tank bioreactors.* PhD thesis, Université de Lorraine, 2018.

[3] T. R. Heathman, A. W. Nienow, Q. A. Rafiq, K. Coopman, B. Kara, and C. J. Hewitt. Agitation and aeration of stirred-bioreactors for the microcarrier culture of human mesenchymal stem cells and potential implications for large-scale bioprocess development. *Biochemical Engineering Journal*, 136:9–17, 2018.

[4] A. W. Nienow, C. J. Hewitt, T. R. Heathman, V. A. Glyn, G. N. Fonte, M. P. Hanga, K. Coopman, and Q. A. Rafiq. Agitation conditions for the culture and detachment of hmscs from microcarriers in multiple bioreactor platforms. *Biochemical Engineering Journal*, 108:24–29, 2016.

[5] C. Loubière, A. Delafosse, E. Guedon, I. Chevalot, D. Toye, and E. Olmos. Dimensional analysis and cfd simulations of microcarrier 'just-suspended'state in mesenchymal stromal cells bioreactors. *Chemical Engineering Science*, 203:464–474, 2019.

[6] M. Micheletti, L. Nikiforaki, K. C. Lee, and M. Yianneskis. Particle concentration and mixing characteristics of moderate-to-dense solid- liquid suspensions. *Industrial & engineering chemistry research*, 42(24):6236–6249, 2003.

[7] A. Delafosse, C. Loubière, S. Calvo, D. Toye, and E. Olmos. Solid-liquid suspension of microcarriers in stirred tank bioreactor – experimental and numerical analysis. *Chemical Engineering Science*, 180:52–63, 2018.

[8] G. Ascanio. Mixing time in stirred vessels: A review of experimental techniques. *Chinese Journal of Chemical Engineering*, 23(7):1065–1076, 2015.

[9] R. S. Cherry and E. T. Papoutsakis. Physical mechanisms of cell damage in microcarrier cell culture bioreactors. *Biotechnology and bioengineering*, 32(8):1001–1014, 1988.

[10] P. Wysotzki, A. Sancho, J. Gimsa, and J. Groll. A comparative analysis of detachment forces and energies in initial and mature cell-material interaction. *Colloids and Surfaces B: Biointerfaces*, 190:110894, 2020.

[11] C. Sion, D. Ghannoum, B. Ebel, F. Gallo, N. de Isla, E. Guedon, I. Chevalot, and E. Olmos. A new perfusion mode of culture for wj-mscs expansion in a stirred and online monitored bioreactor. *Biotechnology and Bioengineering*, 118(11):4453–4464, 2021.

[12] T. A. Grein, J. Leber, M. Blumenstock, F. Petry, T. Weidner, D. Salzig, and P. Czermak. Multiphase mixing characteristics in a microcarrier-based stirred tank bioreactor suitable for human mesenchymal stem cell expansion. *Process Biochemistry*, 51(9):1109–1119, 2016.

[13] M. F. Sousa, M. M. Silva, D. Giroux, Y. Hashimura, R. Wesselschmidt, B. Lee, A. Roldão, M. J. Carrondo, P. M. Alves, and M. Serra. Production of oncolytic adenovirus and human mesenchymal stem cells in a single-use, vertical-wheel bioreactor system: impact of bioreactor design on performance of microcarrier-based cell culture processes. *Biotechnology progress*, 31(6):1600–1612, 2015.

[14] P. R. Blenman, D. R. Carter, and G. S. Beaupre. Role of mechanical loading in the progressive ossification of a fracture callus. *Journal of Orthopaedic Research*, 7(3):398–407, 1989.

[15] D. R. Carter, G. S. Beaupré, N. J. Giori, and J. A. Helms. Mechanobiology of skeletal regeneration. *Clinical Orthopaedics and Related Research (1976-2007)*, 355:S41–S55, 1998.

[16] C. Meyer and D. Deglon. Particle collision modeling–a review. *Minerals Engineering*, 24(8):719–730, 2011.

[17] R. Zenit, M. Hunt, and C. Brennen. Collisional particle pressure measurements in solid–liquid flows. *Journal of Fluid Mechanics*, 353:261–283, 1997.

[18] P. Buffière and R. Moletta. Collision frequency and collisional particle pressure in three-phase fluidized beds. *Chemical Engineering Science*, 55(22):5555–5563, 2000.

[19] T. Zwietering. Suspending of solid particles in liquid by agitators. *Chemical Engineering Science*, 8(3):244–253, 1958.

[20] A. Gjaltema, L. Tijhuis, M. Van Loosdrecht, and J. Heijnen. Detachment of biomass from suspended nongrowing spherical biofilms in airlift reactors. *Biotechnology and Bioengineering*, 46(3):258–269, 1995.

[21] I. Ayranci and S. M. Kresta. Critical analysis of zwietering correlation for solids suspension in stirred tanks. *Chemical Engineering Research and Design*, 92(3):413–422, 2014.

[22] A. Aguilar-Corona, R. Zenit, and O. Masbernat. Collisions in a liquid fluidized bed. *International journal of multiphase flow*, 37(7):695–705, 2011.

[23] J. Emmerich, Q. Tang, Y. Wang, P. Neubauer, S. Junne, and S. Maaß. Optical inline analysis and monitoring of particle size and shape distributions for multiple applications: Scientific and industrial relevance. *Chinese Journal of Chemical Engineering*, 27(2):257–277, 2019.

3.5 Annexes and supplementary material

Calculating particle free fall terminal velocity

A particle's terminal velocity during free fall experiments in a liquid can be calculated by solving Newton's second law of motion end defining the forces that will be applied to this particle when it has attained it's maximum velocity.

- **Archimedes' principle.** According to Archimedes' principle, an upwards force $\overrightarrow{P_A}$ is exerted on a body immersed in a fluid which is equal to the weight of the fluid moved by the body. It can be calculated according to Equation 3.28 taking into account the liquid density ρ_L, the particle volume V and the gravity downwards force $\overrightarrow{g}$.

$$\overrightarrow{P_A} = -\rho_L \times V \times \overrightarrow{g} \tag{3.28}$$

- **Particle weight.** During free fall, the particle is subject to it's weight for which the downwards force can be calculated according to Equation 3.29 by taking into account the particle density ρ_p, the particle volume V and the gravity downwards force $\overrightarrow{g}$.

$$\overrightarrow{P} = \rho_p \times V \times \overrightarrow{g} \tag{3.29}$$

- **Friction forces.** Friction forces apply when a particle moves within a fluid and is generated in the opposite direction of the particle movement. The types of friction that a particle can be subject to can be calculated with Equations 3.30 and 3.31 for which k is a constant which depends on the fluid viscosity η and the particle diameter d_p (Equation 3.32).

$$\overrightarrow{F_s} = k \times \overrightarrow{v} \tag{3.30}$$

$$\overrightarrow{F_s} = k \times \overrightarrow{v}^2 \tag{3.31}$$

$$k = -6\pi\eta \times \frac{d_p}{2} \tag{3.32}$$

These elements can then be used to solve Newton's second law of motion which states that the sum of forces applied to a solid will be equal to it's mass times the acceleration that this particle will be subject to. The differential equations solved for the y axis will depend on the frictional force mechanisms (Equations 3.33 and 3.34).

$$\frac{dv}{dt} + \frac{k}{\rho_p \times V_p} v = (1 - \frac{\rho_L}{\rho_p})g \tag{3.33}$$

$$\frac{dv}{dt} + \frac{k}{\rho_p \times V_p} v^2 = (1 - \frac{\rho_L}{\rho_p})g \tag{3.34}$$

By defining α according to the ratio of densities between the liquid and particles densities (Equation 3.35) and τ according to Equation 3.36, the differential equations solved for the y axis at the terminal particle velocity v_{lim} (for which the acceleration is equal to 0), give the solutions in Equation 3.37 if the friction forces are supposed as proportional to the particle speed and in Equation 3.38 if the friction forces are supposed as proportional to the square of the particle speed. For the calibration of the acoustic sensor above, the first model was assumed.

$$\alpha = \frac{\rho_L}{\rho_p} \tag{3.35}$$

$$\tau = \frac{\rho_p \times V_p}{k} \tag{3.36}$$

$$v_{lim} = g \times \tau \times (1 - \alpha) \tag{3.37}$$

$$v_{lim} = \sqrt{g \times \tau \times (1 - \alpha)} \tag{3.38}$$

Chapter 4

Impact of particle-particle interactions on MSC growth in bioreactors and quality attributes

Contents

4.1 Introduction

The following chapter contains a description of the experimental approach and results to evaluate the impact of particle-particle interactions on MSC growth in bioreactors. It is a project of publication.

4.1.1 Chapter Overview

In order to obtain sufficient cells during routine expansion of mesenchymal stem cells (MSCs) in a highly regulated clinical context, the use of scalable and automatable equipments such as stirred tank reactors (STR) (*ie.* bioreactors) can lead to robust manufacturing processes. The aim of this chapter is to present the expansion of MSCs in different operating conditions. Specifically, this work focuses on the impact of particle-particle collisions on MSC growth kinetics, metabolism and quality attributes. Building upon the published results detailed in Chapter 2 in Erlenmeyer flasks (EF) and spinner flasks (SF), the approach proposed is partially similar. A graphical abstract of the important results of the previous chapters which are pre-requisites for the following work, and the methodology which was applied in this chapter is presented in Figure 4.1.

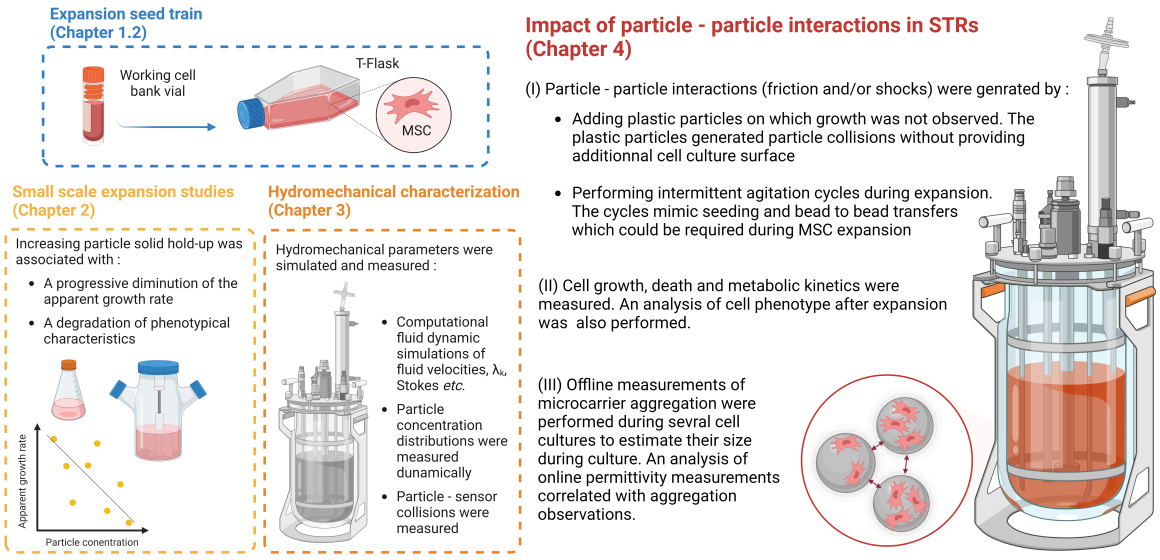

Figure 4.1: Graphical abstract of Chapter 4.

MSCs were expanded on microcarriers to which particles were added in the sole purpose of generating additional particle collisions. For this, solid particles in the system were composed of a fixed solid-hold up concentration of microcarriers providing growth surface (Synthemax II microcarriers provided by Corning) and plastic particles on which cell growth was not observed (Plastic microcarriers provided by Pall, Solohill). **To begin with, in smaller scales, a progressive diminution of the apparent growth rate was observed and quantified when increasing particle solid hold-up (Chapter 2).**

It was proposed that the apparent growth rate may result in a equilibrium between growth and death kinetics which are independently affected by particle concentration. Due to the larger scale in STRs, the range of particle concentrations tested was reduced (total solid hold-ups from 2.7 to 5 $\%_{(v/v)}$ were used in STRs while 2.7 to 9 $\%_{(v/v)}$ were used in smaller scales). This allowed the testing of other operational parameters described later. The observations with plastic particles are original in the fact that, to our knowledge, no published results specifically focus on the impact of particle-particle interactions on MSCs expanded in bioreactors. Pioneering work performed by Cheery and Papoutsakis [1] indicated a reduced observed growth rate of bovine embryonic kidney cells in parallel with increasing turbulent collision severity (TCS). This index was proposed as a way to estimate collision severity based on microcarrier concentration and compiled the existing data from other experimental results published at that time. More recently, the bead-to-bead transfer of large scale (50 to 200 L bioreactors) was validated for HEK293T and Vero cells using WAVE25 (which was found to be an efficient seed train bioreactor but not suitable for expansion due to notable aggregation observed), and single use XDR-50 and XDR-200 bioreactors (which were found to be suitable for expansion) [2]. To our knowledge, no specific robust demonstration of microcarrier optimal concentration has been demonstrated but rather typically consists in proof of concepts defined by knowledge accumulated by individual laboratories specific to their domain of expertise. This is illustrated in a review of bio processes typically used for MSC expansion [3], in the recent review of lessons learned during bioreactor process development applied to MSC cultures [4], as well as the literature review presented in Chapter 1.3.

Cell cultures were also performed with intermittent agitation cycles to define the impact that performing these cycles multiple times during cell culture could have on MSC growth and death kinetics. For this, agitation cycles were performed over 10 times during cultures specifically to detect if repeated sedimentation and suspension phases could impact MSCs. As it has been concluded in Chapter 3, microcarrier concentration at the bottom of the STR can reach concentrations up to 10 times the average microcarrier concentration during suspension phases, thus generating significant collisional and frictional forces. These phases are currently inevitable to allow cells to initially attach to the microcarriers. A classical seeding strategy consists in either adding cells directly thawed from the cell bank vial or after using trypsin to detach cells primarily expanded on T-flasks. The cells in suspension must then adhere on the microcarriers and biological adherence may take up to 120 minutes (detailed in Chapter 1.3 and reviewed in [5]). Similar agitation cycles are typically used during medium exchanges or for bead-to-bead transfers when fresh microcarriers are added during expansion. The time for cells to efficiently migrate from colonized carriers onto fresh carriers should be expected to take similar amounts of time. In addition, a phe-

notypical analysis of the cells produced was performed by flow cytometry in order to understand if the repeated intermittent agitation cycles could have an impact on MSCs produced under these conditions.

Lastly, a notable advantage of using bioreactors is the fact that the equipments can be monitored online through various probe technologies (including online measurement of pH, temperature, dissolved oxygen) and processes can be adapted to the reading of these probes. For example, pH, temperature and dissolved oxygen is routinely monitored and regulated. In parallel, online monitoring of kinetic parameters are typically put in place including growth (for which online viable cell density can be measured using various existing technologies) and metabolism (for which online glucose and lactate sensor technologies are currently being developed and tested at large scale). **In the case of this study, a novel approach to use online permittivity measurements to not only measure viable cell density but also in view of possibly evaluating elements of aggregation will be presented**. Measuring and controlling aggregation was a technical issue both in small and large scale cell cultures on microcarriers. Large aggregates of over 50 microcarriers have been described in many of the studies reviewed in [4]. Accordingly, having online measures which could detect aggregation phenomena would be extremely precious in tackling the aggregation bottleneck.

4.1.2 Bioreactor experimental setup

The Tryton bioreactor provided by Pierre Guerin equipped with a downwards pumping HTPG impeller was used for the cell cultures performed in this chapter. The description of the plunging elements and inlets used during these cultures as well as the tank and agitator dimensions can be found in Figure 4.2. To begin with, the elements presented in green concern the online probes used for online process monitoring of pH, dissolved oxygen and permittivity respectively labelled P, O and D. The pH in the tank was controlled with a setpoint of 7.4 by either injecting CO_2 for acidification (via the CO_2 / N_2 inlet presented in blue) or by adding NaOH (via the NaOH inlet presented in gray). In addition, oxygen levels were maintained at a fixed setpoint of 20 % (for which the level of 100 % was calibrated at the beginning of each culture as the level of dissolved oxygen in the medium after equilibration in air at 37 °C). This level was maintained by either gas striping of oxygen by adding N_2 (via the CO_2 / N_2 inlet presented in blue), or by adding oxygen (via the O_2 inlet presented in blue). Temperature was also regulated at 37 °C via an exterior water jacket coupled with a heating module. Lastly, two sampling ports were used during culture (respectively S0 and S1 ports presented in gray). These ports were used either for daily sampling or medium exchanges.

A characterization of notable hydro-mechanical elements including average liquid velocity, the Kolmogorov microscale of turbulence λ_k and particle expected trajecto-

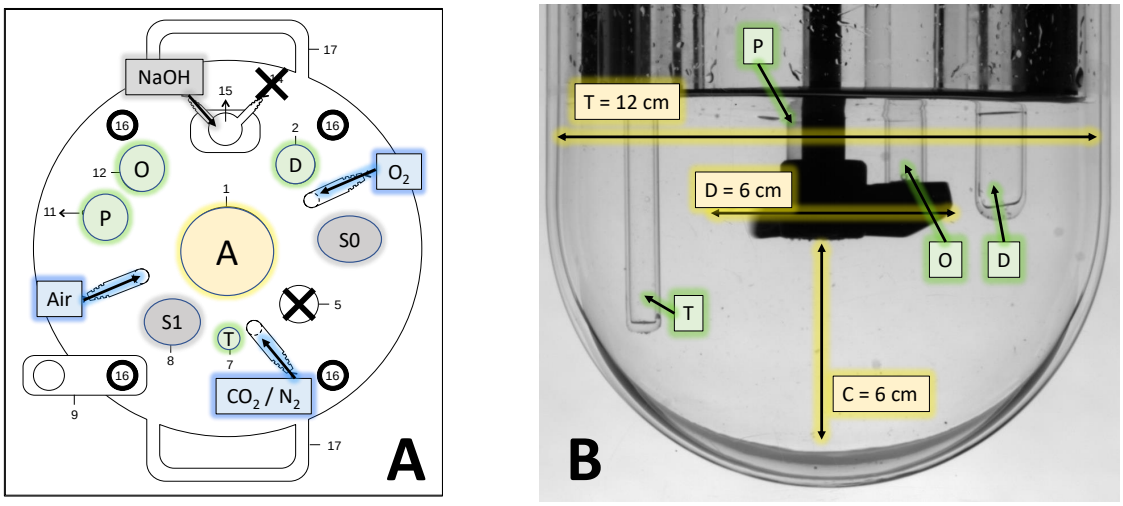

Figure 4.2: Description of the Pierre Guerin bioreactor setup. (A) Experimental setup for MSC expansion on MCs in a volume of 0.7 L. A - (yellow element) Agitator, P - O - D (green elements, plunging) pH, Dissolved Oxygen and Dielectric probes respectively, S0 - S1 - NaOH (grey elements, not plunging) sampling port, plunging cane and sodium hydroxide addition ports respectively, Air - O_2 - CO_2/N_2 (blue elements, not plunging) gas inlets. (B) Photography of the plunging elements present in the experimental setup (green probes) and elements of geometry (yellow). The photography was taken during experiments performed above measuring light attenuation for which geometry was identical to the tank geometry used for cell cultures.

ries relative to fluid movements (estimated by the Stokes number St) was detailed in Chapter 3. Readers would be advised to refer to this chapter which thoroughly details spatial heterogeneities of these key characteristics in this geometrical setup at N_{js} and which are expected to have impacts of MSC growth.

4.1.3 Material and methods for MSC expansion in STRs

Seeding strategy in STRs

All experiments in bioreactors were performed with the same cell bank of hWJ-MSCs for which the vial concentration was of 5 million viable cells per mL (during the preparation of the bank). The bank was created with cells cryopreserved at passage 1. This strategy was chosen in order to limit, as much as possible, the possible impact that donor-to-donor variability may have and essentially to increase comparability between results.

Each cell vial was thawed and cells were seeded in 175 cm^2 flasks at a concentration of 3000 cells per cm^2 for 5 days. Cells were detached using Tryp-LE and directly seeded on the microcarriers (Synthemax II Dissolvable microcarriers, 7290 Corning) in the bioreactor in half of the final working bioreactor volume (350 mL) of cell culture medium (α-MEM supplemented with 1 $\%_{(v/v)}$ antibiotic anti-mycotic solution, 3 g L^{-1} of glucose and 4 mM glutamine). Cells seeded in the bioreactors were therefore at passage 2. The cell culture media was identical to the one used for the small scale

studies in Erlenmeyer and spinner flasks with the exception of the glucose concentration in the media. Preliminary experiments (detailed in Chapter 4.5) indicated that MSC growth was enhanced by adding 3 g L^{-1} of glucose to the basal medium (ensuring a final glucose concentration of 4 g L^{-1}). As a result, glucose supplementation was performed for all bioreactor cultures. Seeding was performed in cell culture medium for which no LPH was added since in half of the final working volume (350 mL) since this was found to increase the attachment yield of MSCs on Synthemax-II microcarriers in Erlenmeyer and spinner flask cultures. During the initial seeding phase, agitation cycles were set as defined in smaller scale cultures : for the first 2 hours of attachment, agitation was set to $N_{js} = 70$ rpm for 5 minutes every 25 minutes, for the next 2 hours, agitation was set to $N_{js} = 70$ rpm for 5 minutes every 55 minutes. In Erlenmeyer and spinner flasks, the agitation rates at N_{js} were however calculated to account for the scale and geometry of these setups. As a result, the initial hydro-mechanical stresses during inoculation steps are not fully comparable. After the first 4 hours of attachment, the final volume of culture was completed to 700 mL with a medium containing 10 $\%_{(v/v)}$ of human platelet lysate (HPL) to ensure cell culture after attachment was performed at LPH concentrations of 5 $\%_{(v/v)}$.

Cell growth and death kinetics

After the initial seeding phase, bi-daily samples were taken during cell culture. For this, three independent samples of 1 mL were aseptically withdrawn and the microcarriers were left to sediment and washed twice with 1 mL of dPBS. After washing, microcarriers were left to sediment and the supernatant was replaced by 1 mL of a dissolution solution. This solution was composed of a Tryp-LE solution (Fisher, ref. 10718463) to which pectinase (Sigma, ref. 2611) and EDTA (homemade) were added per supplier recommendations. Microcarriers were gently agitated for 5 minutes at 37 °C and filtered through a cell strainer with a 70 µm mesh (Fisher, ref. 22-363-548). Live X and dead X_d cells were counted automatically (Vi-Cell XR, Beckman Coulter). The total amount of attached cells $X_{att.}$ was therefore defined as the sum of live and dead cells counted after microcarrier dissolution (Equation 4.1). In addition live cell kinetics were modelled according to Equation 4.2 to determine the apparent growth rate μ_{app} according to the modelled initial viable cell concentration X_0 during the growth phase. Specific growth rates $\mu(t)$ were calculated at each time step and modelled according to a spline polynomial fit of experimental data and Equation 4.3.

$$X_{att.} = X + X_d \tag{4.1}$$

$$X = X_0 \cdot e^{\mu_{app} t} \tag{4.2}$$

$$\mu_{app} = \frac{1}{X}\frac{dX}{dt} \tag{4.3}$$

In parallel, concentrations of lactate dehydrogenase (LDH) in the culture supernatant were quantified with an offline analyzer (Thermo fisher scientific, Gallery multi-parametric analyser). The measurement of dead cell concentration X_d was performed with this LDH quantification after calibration of LDH (described in Chapter 2.1.3). The conversion factor of 1 IU LDH to 2.1 $\times$ 10^6 lysed cells was applied. The kinetic decay constant k_d was obtained from the dead cell measurements according to Equation 4.4.

$$\frac{dX_d}{dt} = k_d X \tag{4.4}$$

Online permittivity measurement to monitor MSC growth

Dielectric spectroscopy is a technique often used in bioreactor-based expansion processes to monitor viable cell density (VCD) online during cell expansion. Briefly, cellular electrical properties are measured in an alternating electric field between two electrodes over a range of frequencies. Under this alternating electrical field, live cells act as capacitors and their membranes are polarized and depolarized accordingly (ε_{dielec}). Dead cells do not impact the measure since their membranes cannot be polarized. The change in electric-current voltage in the presence of the alternating electrical field (permittivity) is measured and can be correlated with VCD. In following cell cultures in bioreactors, the Incyte dielectric probe (Visifern, Hamilton) was used to follow VCD during expansion. This technique has successfully been validated for monitoring MSC live cell concentration during their growth on Corning Synthemax II-coated dissolvable microcarriers [6].

Cell metabolism kinetics

A metabolic analysis of glucose, lactate, glutamine and ammonium in cell culture supernatants was performed during the cell cultures with an offline analyzer (Thermo fisher scientific, Gallery multi-parametric analyser). A description of the methods for quantification can be found in more detail in 2.1.3. The cell culture medium was changed when the concentration of glucose in the supernatant was found to be below 1 g L^{-1}, if lactate concentrations were found to be above 1 g L^{-1} or every 3-4 days. During medium exchanges, agitation in the bioreactor was stopped and microcarriers were left to sediment. 350 mL of the supernatant was withdrawn and replaced with 350 mL of fresh medium with a LPH concentration of 5 $\%_{(v/v)}$.

A spline fitting of the daily supernatant metabolic concentrations and growth samples was performed via Matlab. These models of metabolic and growth were then used to define specific metabolic consumption and production rates throughout the cell culture. To begin with, average glucose consumption yields $Y_{Gluc/X}$ and lactate production yields $Y_{Lac/X}$ per cell were calculated according to Equations 4.5 and 4.6 over the entire growth phase, in a holistic approach. For this the difference between initial i and final f concentrations of the respective metabolic products were used to estimate consumption or production. In order to account for medium changes which either add glucose or strip lactate, for each medium exchange, the respective metabolic concentrations were measured before and after this step. The sum of added glucose or stripped lactate during these steps were calculated in a factor Δ over the growth phase duration. The production or consumption yields were calculates specifically based on MSC growth. Accordingly, the viable cell concentrations at the beginning of cell culture X_i and at the end of the measured growth phase X_f were used. Equations 4.5 and 4.6 were also used to calculate the consumption and production yields concerning glutamine $Y_{Glut/X}$ and ammonium $Y_{NH3/X}$ by respectively replacing glucose concentrations by glutamine concentrations and lactate concentrations by NH_3 concentrations.

$$Y_{Gluc/X} = \frac{Gluc_i - Gluc_f + \Delta Gluc}{X_f - X_0} \tag{4.5}$$

$$Y_{Lac/X} = \frac{Lac_f - Lac_i + \Delta Lac}{X_f - X_0} \tag{4.6}$$

More precisely, the specific production and consumption rates were calculated throughout the cell culture by using spline models of growth and metabolic products in the supernatant. Accordingly, the specific glucose consumption rate q_{Gluc} and lactate production rate q_{Lac} were calculated via Equations 4.7 and 4.8. These equations were also used to calculate the evolution of consumption r_{Gluc} and production r_{Lac} rates in the entire tank volume. Whereas values of q estimate the specific consumption and production per cell per unit of time for the cell culture (and therefore indicates an average cell metabolism in the tank), values of r have a "process oriented" approach since are not specific to the amount of cells in the STR. They should rather be used for process design rather than to evaluate cell metabolism. The same approaches were also used concerning glutamine consumption rates and NH_3 by using the respective concentrations of these metabolites in the respective models.

$$\frac{dGluc}{dt} = -q_{Gluc}X = r_{Gluc} \tag{4.7}$$

$$\frac{dLac}{dt} = q_{Lac}X = r_{Lac} \tag{4.8}$$

Lastly, the transformation yield of glucose to lactate during the exponential phase was calculated according to Equation 4.9. This yield is usually used as an indicator of either a preferential glycolytic metabolism or oxydative phosphorylation.

$$Y_{Lac/Gluc} = \frac{q_{Lac/X}}{q_{Gluc/X}} \tag{4.9}$$

MSC phenotyping

MSCs expanded on microcarriers were harvested after a defined cell culture duration for each condition. Control conditions and intermittent agitation cultures were performed in triplicates. Accordingly, the first two reactors were stopped after observing a stationary phase and the beginning of a death phase. The duration of the growth phase for both conditions was defined via these two cultures. For the third culture, cells were harvested at the end of the defined growth phase for phenotyping. Accordingly, cells are expected to be in similar growth phases during harvesting.

Harvesting was performed by sedimenting cells gown on microcarriers in the STR. The cell culture supernatant was removed from the STR and microcarriers were washed twice with pre-heated dPBS. Subsequently, the cells attached on the carriers were again left to sediment and the supernatant discarded and replaced by a microcarrier dissolution solution per supplier recommendations. Agitation was set to N_{js} for 15 minutes at 37 °C and the STR volume was harvested. At this stage, microcarriers were dissolved and cells were in suspension. The cell solution was filtered via cell strainers (70 µm mesh) and trypsin was inactivated by adding cell culture medium. Viable cell density of the solution was determined. The cell solution was then centrifuged for 5 minutes at 800 rpm. Cells were then re-suspended in a volume of cryprotective solution (90 $\%_{(v/v)}$ fetal bovine serum, 10 $\%_{(v/v)}$ DMSO) calculated to achieve concentrations of 5 million cells per mL. These cells were then frozen for cryopreservation.

These cells were then thawed and cultured for 3 days before phenotyping. Plastic adhesion was verified at this stage. For cytometry, approximately 1×10^5 cells were re-suspended in 100 µL phosphate buffer saline (PBS) supplemented with bovine serum albumin (BSA) and incubated with specific antibodies for 1 hour at room temperature. After incubation, MSCs were washed with PBS, centrifuged at 300 g for 5 minutes and re-suspended in 250 µL of 1% paraformaldehyde (PFA) until analysis by FACS flow cytometry (Beckman Coulter, Gallios) according to methods and specific antibodies previously described [6]. A summary of the antibodies used and a brief introduction on their target can be found in Table 4.1.

Table 4.1: Specific antibodies used for cytometric analysis of MSCs and description of the Cluster Differentiation (CD) targets.

Antibody	Description	Supplier	Clone
CD-106-PE	Vascular cell adhesion molecule-1 (VCAM-1), mediates adhesion and signal transduction [7]	BD Pharmingen, 555647	51-10C9
HLADR-FITC	MHC class II cell surface receptor	Beckman coulter, IM0463U	B8.12.2
CD34-PE	Cell surface glycoprotein and cell adhesion factor, regulates cell proliferation and differentiation [8]	BD Pharmingen, 555822	581
CD45-FITC	Transmembrane protein tyrosine phosphatase, regulates lymphocyte maturation stages, marker of hematopoietic lineages [9]	DAKO, F0861	T29/33
CD44-FITC	Homing cell adhesion molecule (HCAM), cell adhesion, migration, homing, proliferation and apoptosis of stem cells [10]	Beckman Coulter, IM1219U	J.173
CD73-PE	Ecto-5-nucleotidase enzyme asoociated with cell proliferation	BD Pharmingen, 550257	AD2
CD90-FITC	Thy-1 cell surface glycoprotein, role in cell-cell and cell-matrix interactions and cell motility [11]	Beckman Coulter, IM1839U	2G5 F15-426165
CD166-PE	ALCAM adhesion protein, role in tight cell-to-cell interaction and regulation of stem cell differentiation [12]	Beckman Coulter, A22361	3A6

4.2 Impact of particle-particle stresses on growth, metabolism and phenotype

4.2.1 Introduction

The preliminary work lead to the identification of the working glucose concentration in the cell culture medium for the rest of the study. In the operating conditions presented beforehand, particle-particle stresses were generated during MSC expansion on microcarriers in bioreactors. Two modes of mechanical stresses were evaluated.

1) **Increased microcarrier collision frequency and frictional forces during sedimentation and suspension phases**. The impact of microcarrier sedimentation and suspension phases was evaluated. These phases occurred up to 10 times in each culture and mimic the potentially numerous medium exchange and bead-to-bead transfer phases that could occur during a cell culture (for which sedimentation of the carriers is, to date, the easiest and most described strategy). These cultures aimed at defining if the results obtained in Chapter 3 (notably the significant variation in particle concentrations during sedimentation and suspension phases) could have an impact on MSC growth and metabolism.

2) **Microcarrier - particle collisional forces generated by adding plastic particles on which cell growth was not observed**. These particles added particle collisional forces without providing any cell growth surface. The methodology applied was identical to that used in smaller scale studies in Erlenmeyer and spinner flasks

(Synthemax II microcarriers provided by Corning were used for cell expansion to which a range of plastic particle concentrations were added). In bioreactor cultures, the solid hold-up of the Synthemax II microcarriers was kept identical at 2.7 $\%_{v/v}$ and cell seeding concentration was maintained at 7500 cells cm^{-2}. The aim here was to compare the results obtained at small and larger scales to extrapolate, or not, the small scale findings.

4.2.2 Impact of agitation cycles on MSC growth, metabolism and phenotype

Impact of agitation cycles on growth and death kinetics

A set of triplicate experiments were performed for which either the agitation rate was set to $N_{js} = 80$ rpm after an initial seeding phase of 4 hours (considered as the control condition), or for which agitation cycles were performed every 4 hours (considered as the intermittent agitation condition). During agitation cycles, the system was agitated at N_{js} for 5 minutes every 25 minutes for 2 hours followed by 5 minutes of agitation at N_{js} ever 55 minutes for 2 hours. Agitation was set to N_{js} in between these cycles. In both conditions, seeding was performed with an intermittent agitation cycle of 4 hours. A schematic representation of the agitation cycles applied can be found in Figure 4.3.

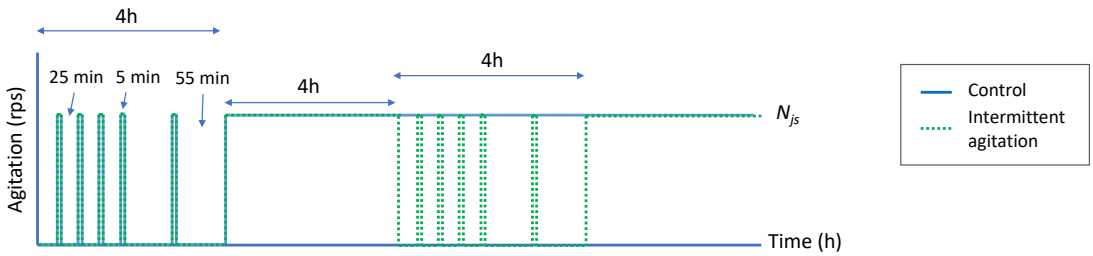

Figure 4.3: Schematic representation of agitation strategies for cell culture. A control condition consisted in performing inoculation with intermittent agitation and then maintaining agitation at N_{js} (blue). Intermittent agitation cultures were performed by alternating intermittent agitation cycles for 4 hours and maintaining agitation at N_{js} for 4 hours (green).

Daily quantification of MSC live and dead cell populations was performed. As shown in Figure 4.4 (left) which presents the evolution of X during expansion, MSC growth seems to be inhibited when cells are subject to intermittent agitation cycles throughout culture. Results represent the compiled data from 3 cell cultures in each condition. The mean calculated apparent growth rate μ_{app} (calculated by modelling the live cell concentration with an exponential model during the defined growth phase) was found to be of 0.026 h^{-1} or 0.62 day $^{-1}$ in the control condition (green), whereas it was found to be of 0.012 h^{-1} or 0.29 day $^{-1}$ in cultures subjected to agitation cycles (red). Both growth rates were calculated after compiling the results obtained in 3 cell cultures for each condition. In addition, the maximum number of live cells obtained with or

without intermittent agitation were found to be significantly different at the end of the growth phase. In the control conditions, the maximum amount of cells were observed after approximately 150 hours of culture, when the STR contained approximately 200 million cells. This is expected to correspond with the level of confluence that could routinely be obtained in STRs [6]. Conversely, when cells were subject to intermittent agitation cycles, the maximum level of cells was not only reached after a longer period of time (approximately 200 hours of cell culture), but less viable cells were also obtained (less than 100 million cells).

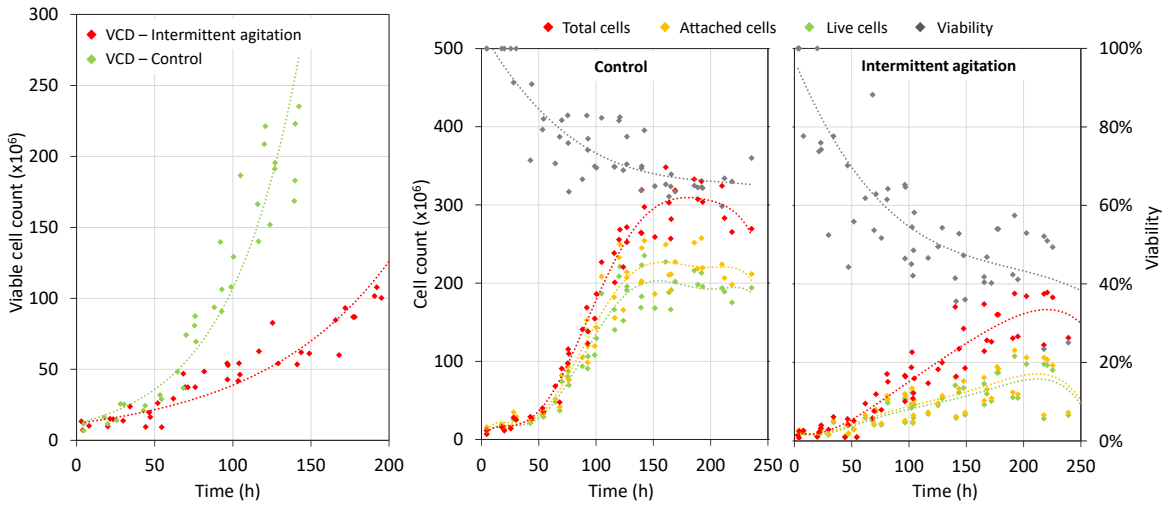

Figure 4.4: Impact of agitation cycles on MSC growth and death kinetics. Left : viable cell density measured offline and exponential fit. Middle and right : bi-daily quantification of live cells attached on microcarriers (green), total live and dead cells attached on microcarriers (orange) and total cells in the STR including lysed cells quantified by LDH measurement (red). Overall viability (live cells according to total cells) are presented in gray. Polynomial trends were plotted for comparison between conditions.

Live and dead cell populations were then quantified and are presented in the right part of Figure 4.4. Live (green), total attached (yellow) and total cells (red) are represented as well as the total viability (gray). The decreased amount of live cells at the end of cell culture observed in the previous paragraph was accompanied with increasing levels of lysed cells in the cell culture medium. Accordingly, the overall viability was found to be significantly decreased progressively during expansion. Whereas in the control conditions, the global viability decreased during the exponential growth phase until approximately 65 %, in the case of agitation cycles, the global viability continued to decrease pass this plateau and levels of viability in the bioreactor when the cell culture reached it's maximum state were close to 50 %. The viability of attached cells was however observed to be similar in both conditions (approximately 90 % of attached cells were viable in both conditions throughout culture as presented in Figure 4.5). This indicates that the decreased viability observed with intermittent agitation cycles is explained by mechanisms of cell lysis. The increased levels of cell lysis should also lead to significant intra-cellular compounds being released into the culture medium

which could potentially initiate a deleterious cascade of events further increasing MSC death.

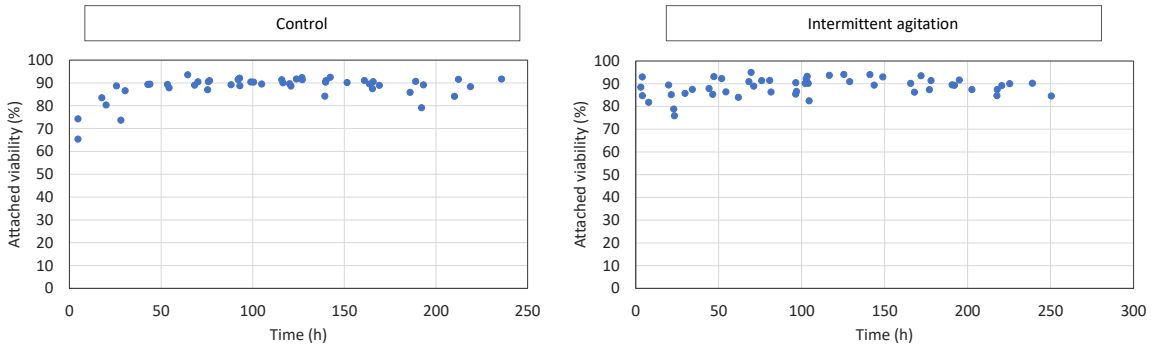

Figure 4.5: MSC attached viability in control cultures (left) and cultures with repeated intermittent agitation (right). The viability of attached cells were measured after microcarrier dissolution by automatic live and dead cell counting (Vi-cell XR, Beckman Coulter).

Specific growth and death rates were derived from the growth X and death X_d data obtained during culture and presented in Figure 4.6. In both conditions, high specific growth rates were observed at initial time points caused by the few data points at the beginning of the cell culture and the difficulty to correctly model the specific growth rates at these time points. The initial growth rates in the first 10 hours should be ignored as are not considered as having biological relevance. While a maximum growth rate μ_{max} of 0.034 h^{-1} was observed in the control condition after 56 hours of culture, this value was of 0.021 h^{-1} in intermittent agitation cultures (observed after approximately 50 hours of culture). In both conditions, cell growth rates then gradually decreased after this maximum value indicating the start of a stable linear growth phase followed by the gradual stop of cell growth and an entry in a stationary phase when this observed growth rate reached 0.

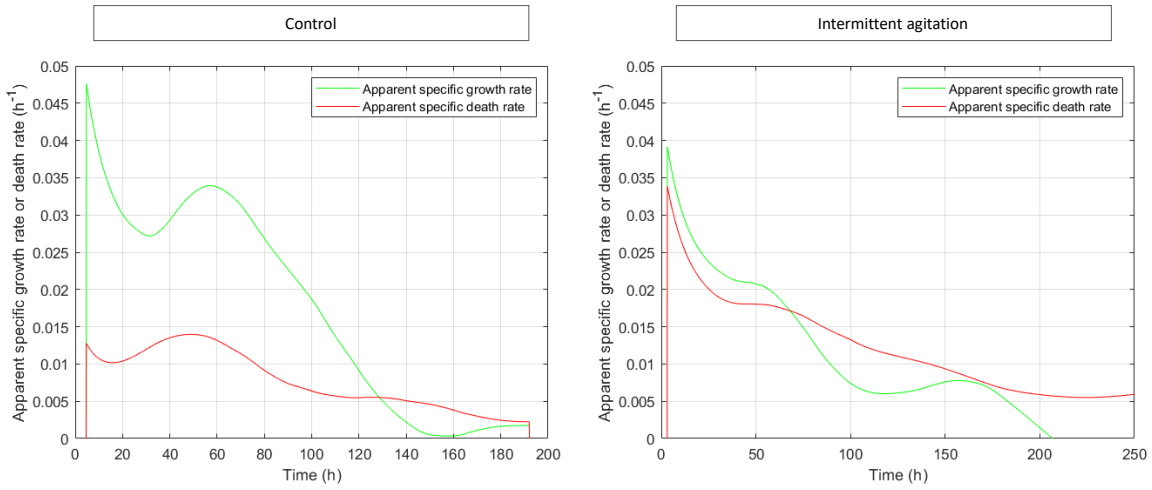

Figure 4.6: Impact of agitation cycles on MSC growth and death specific kinetic rates obtained in the control conditions (left) and with intermittent agitation cultures (right).

In addition, the measured specific death rates were also found to have similar profiles (red curves presented in Figure 4.6) but values of k_d were found to be significantly higher in cultures performed with intermittent agitation. With intermittent agitation, k_d values were of the same order of magnitude as growth rates. Maximum k_d values in the control conditions were of 0.014 h^{-1} whereas they were of 0.018 h^{-1} in intermittent agitation cultures (around the plateau observed after 55 hours of cell culture). These kinetic profiles indicate a significant impact of intermittent agitation on both growth and death kinetics.

A summary of the key kinetic growth and death constants presented above can be found in Table 4.2. This overview indicates that particular caution should be kept in mind when developing MSC processes in bioreactors. **Repeated intermittent agitation cycles during MSC expansion were associated with a decreased apparent viable growth rate μ_{app}, a decreased maximum growth rate μ_{max}, a decreased level of confluence on microcarriers after expansion, and an increase of cell decay measured with k_d. Cell death was primarily found to be associated with cell lysis and a detachment of dead cells from the carriers**.

Table 4.2: Characteristic constants of MSC experiments in STRs during the exponential growth phase with or without intermittent agitation cycles during expansion.

	Growth phase duration (h)	Exp. phase (h)	X_f (live cells)	μ_{app} (h^{-1})	μ_{max} (h^{-1})	$k_{d,max}$ (h^{-1})
Control	161 h	57 h	227 million	0.0260	0.034	0.014
Intermittent agitation	220 h	50 h	96 million	0.0120	0.021	0.018

Impact of agitation cycles on the online measurement of MSC growth

Online monitoring of the dielectric signal was compared with offline viable cell counting in conditions with or without intermittent agitation. To begin with, a very close agreement was observed for the three control cell cultures during the exponential growth phase as presented in Figure 4.7, left. These results validate the fact that online measurement of MSC growth on microcarriers is efficient as has been previously reported during MSC expansion in bioreactors [6]. However, during these cell cultures, certain aggregation phenomena were observed and is a possible cause of the unexpected variations in dielectric signal observed for example in Control condition 3. For this condition, a manual dissociation of large aggregates was performed manually by mild pipetting after 52 hours of cell culture, 70 hours of cell culture and 80 hours of cell culture. After this, a signal in agreement with offline measures was again observed.

These cell cultures brought to light the fact that although MSCs were successfully

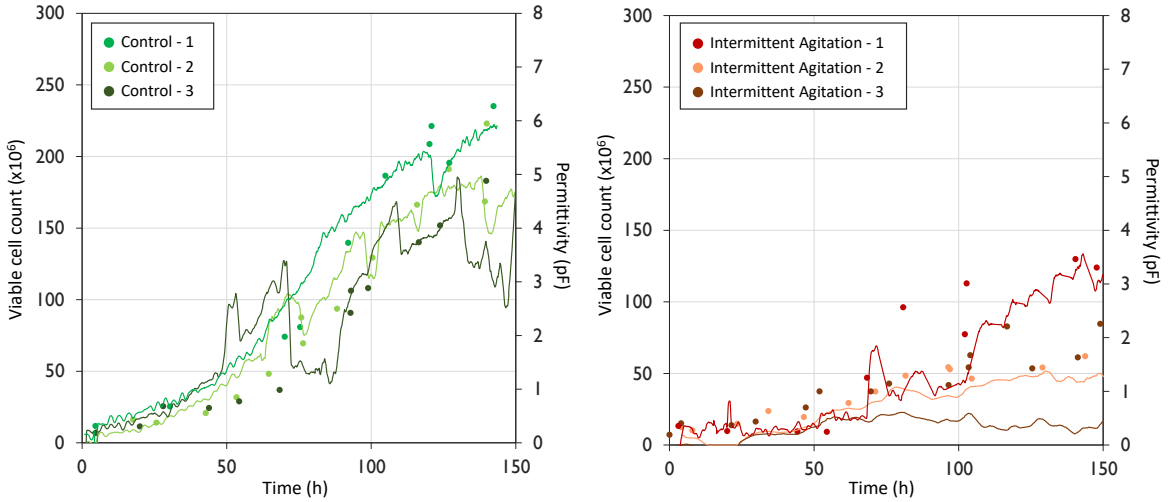

Figure 4.7: Impact of agitation cycles on MSC growth measured online and offline. Viable cell density measured offline in triplicate analysis (data points) and online dielectric signal measured (lines) in the control conditions (left) and with with agitation cycles (right).

expanded on Sythemax II microcarriers in this experimental setup, certain technical bottlenecks (including the management of aggregation) remain to be tackled. In parallel, online measurement of viable cell density was also obtained in experiments performed with intermittent agitation cycles. Again, the global trends obtained with the probe followed the offline measures. However, a greater heterogeneity and variation was observed between offline and online measures (particularly for intermittent agitation culture 3). In these conditions, aggregation is favoured by the intermittent agitation cycles since cell bridging is made possible during sedimented phases which took place every 4 hours. The online measure of viable cell density was more difficult in cultures during which large cell-microcarrier aggregates were observed. The challenges of microcarrier aggregation have been described in most published articles which focused on similar cell culture methods [6, 13]. A specific focus on this topic will be presented later in Chapter 4.3.

Impact of agitation cycles on cell metabolism

The analysis of metabolic components in the cell culture medium were used to determine if any significant metabolic changes occurred during expansion. As presented in Figure 4.8, left, all three control conditions had similar metabolic profiles since the accumulated glucose consumption and lactate production curves (in grams) almost coincide. The lactate to glucose conversion rate was constant all over the culture with an average conversion yield $Y_{Lac/Gluc}$ of 1.3. Accordingly, anaerobic metabolism was demonstrated in the control conditions during the first 200 hours of cell culture. On the other hand, in the case of intermittent agitation cultures, results are not as clear. To begin with, levels of glucose consumption and lactate production were lower than control conditions and a drift between glucose consumption and lactate production was observed

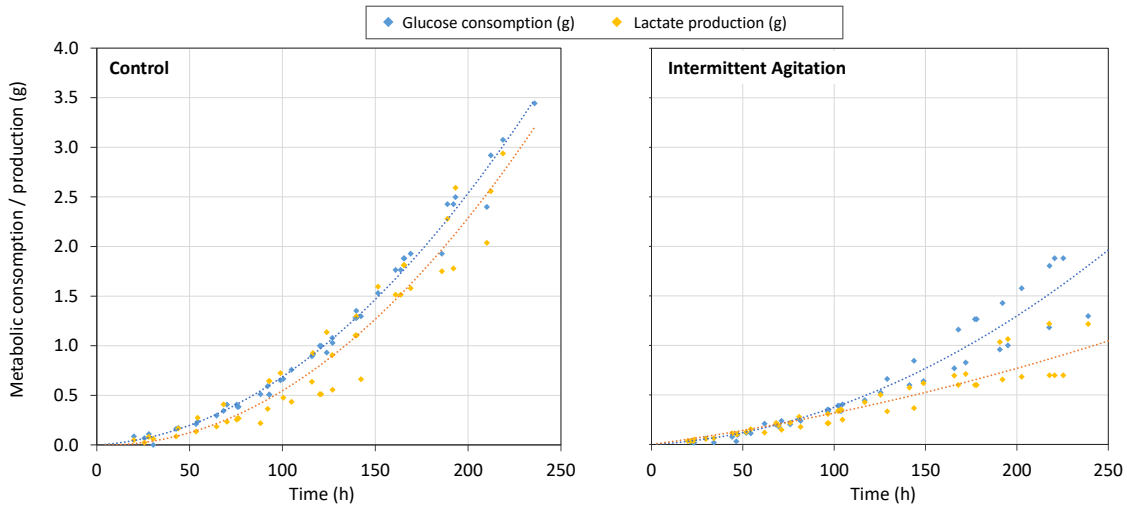

Figure 4.8: Impact of agitation cycles on MSC glucose metabolism. Accumulated glucose consumption and lactate production (total grams calculated in the bioreactor volume) during the cell culture. Left (without agitation cycles) and right (with agitation cycles). Polynomial trends were plotted for comparison between conditions.

after approximately 125 hours indicating a possible drift in metabolism. In addition, a higher discrepancy was observed between the different cell cultures. This could be caused by the difficulty of controlling phenomena such as aggregation which was increased by intermittent agitation. The average conversion yield $Y_{Lac/Gluc}$ was of 0.9 in intermittent agitation conditions indicating a possible slight change in metabolism compared to the control condition. Metabolic consumption and production yields per cell during the growth phase are summarized in Table 4.3.

Table 4.3: Metabolic yields over the growth phase in MSC experiments in STRs with or without intermittent agitation.

	$Y_{Gluc/X}$ ng/cell	$Y_{Lac/X}$ ng/cell	$Y_{Lac/Gluc}$ g/g	$Y_{Glut/X}$ nmol/cell	$Y_{NH_3/X}$ nmol/cell	Max(NH_3) mM
Control	5.6	7.2	1.3	1.3	9.1	1.8
Intermittent agitation	8.5	7.3	0.9	3.9	27.4	2.3

In order to compare metabolic kinetic profiles in both conditions, the specific glucose and glutamine consumption rates $q_{Gluc/X}$ and $q_{Glut/X}$ (expressed in mmol cell^{-1}) were calculated throughout the culture, as well as the specific lactate production rates $q_{Lac/X}$. Results are presented in Figure 4.9. Higher metabolic glucose consumption rates were observed in the control conditions compared to intermittent agitation cultures. Maximum glucose consumption rates were observed at approximately 25 hours and reached values of 4 10^{-4} g h^{-1} per million cells whereas specific consumption rates in intermittent agitation had levels close to 2.5 10^{-4} g h^{-1} per million cells at similar time points. This represents a decreased specific glucose consumption rate per cell of 37 %. Glucose consumption rates coincided well with the observed specific growth rates presented in Figure 4.6, as would be expected. Lactate specific production rates and

glutamine specific production rates had similar trends in both tested conditions and no significant variation in maximum consumption rates were observed in these trends.

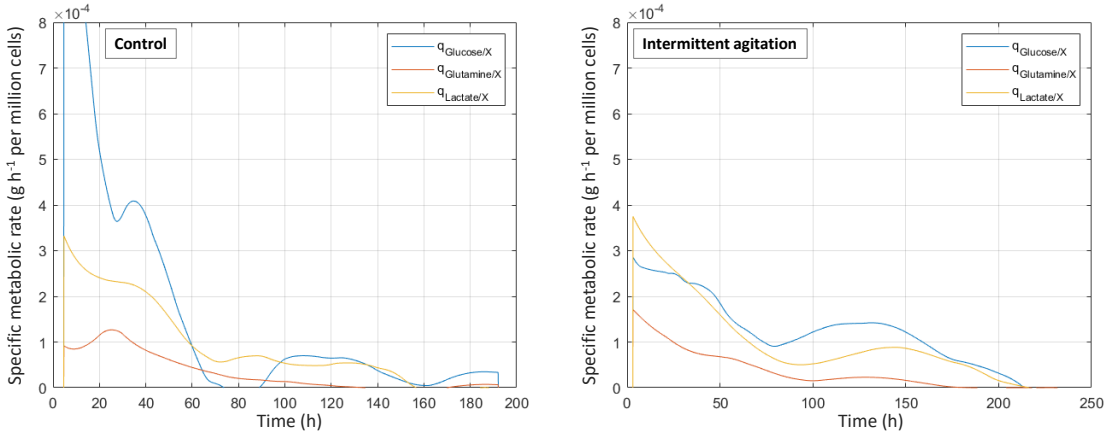

Figure 4.9: Impact of agitation cycles on MSC specific consumption and production rates in the control condition (left) and with intermittent agitation cycles (right).

Lastly, the impact of agitation cycles on glutamine consumption of MSCs was evaluated and presented in Figure 4.10. Results indicate that, in the control conditions, glutamine is progressively consumed during the cell culture and ammonium is progressively secreted in the cell culture medium. This is validated by similar specific glutamine production rates presented in orange in Figure 4.9. Discrepancies between NH_3 measures were observed for cultures performed with intermittent agitation. These variations are expected to be caused by the sensibility of measuring NH_3 concentrations with the equipment used in this study (the calibration of NH_3 was the most sensitive and indicated the highest errors during calibration, data not shown). In addition, similar discrepancies were also observed previously for glucose and lactate trends in intermittent agitation cultures. This could be caused by the difficulty of controlling phenomena such as aggregation which was increased by intermittent agitation. Holistically, maximum NH_3 values were used to compare both agitation conditions. While NH_3 concentrations never exceeded 1.8 mM in the control condition, a maximum NH_3 concentration of 2.3 mM was observed with intermittent agitation. As previously described, concentrations of NH_3 above 2.4 mM have been found to inhibit MSC growth [14]. While values were far from this threshold in the control conditions, this was not found to be the case for cultures with intermittent agitation.

Impact of agitation cycles on MSC phenotype

Cells expanded in bioreactors were separated from microcarriers by microcarrier dissolution according to the supplier recommendations. For the control and intermittent agitation conditions, two cell cultures were performed until the observed stationary and death phase in order to define the optimal time for harvesting. Accordingly, for both conditions, cell phenotyping was performed at the end of the observed growth phase

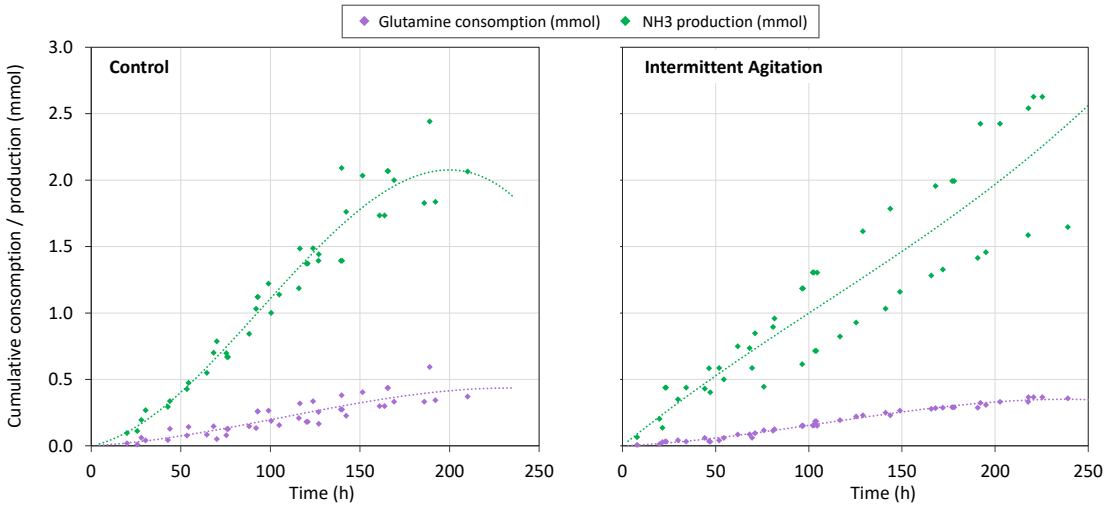

Figure 4.10: Impact of agitation cycles on MSC glutamine metabolism. Accumulated glutamine consumption and ammonium production (total milli-moles calculated in the bioreactor volume) during the cell culture. Left (without agitation cycles) and right (with agitation cycles). Polynomial trends were plotted for comparison.

after 160 and 220 hours respectively in control and intermittent agitation conditions. The level of surface marker expression was compared to the expression levels in the working cell bank (WCB) used for expansion. The WCB cells were not expanded on microcarriers. Cell phenotyping are presented in Figure 4.11 comparing the levels of surface marker expression between the WCB, cells expanded on microcarriers in the control condition and cells expanded on microcarriers with intermittent agitation cycles. Plastic adhesion was verified during these experiments. It can be noted that the cells from the three tested conditions remained plastic adherent but a difficulty in expanding the cells produced with intermittent agitation cycles was significant (cells grew less fast in T-Flasks and had more difficulty adhering on the flasks).

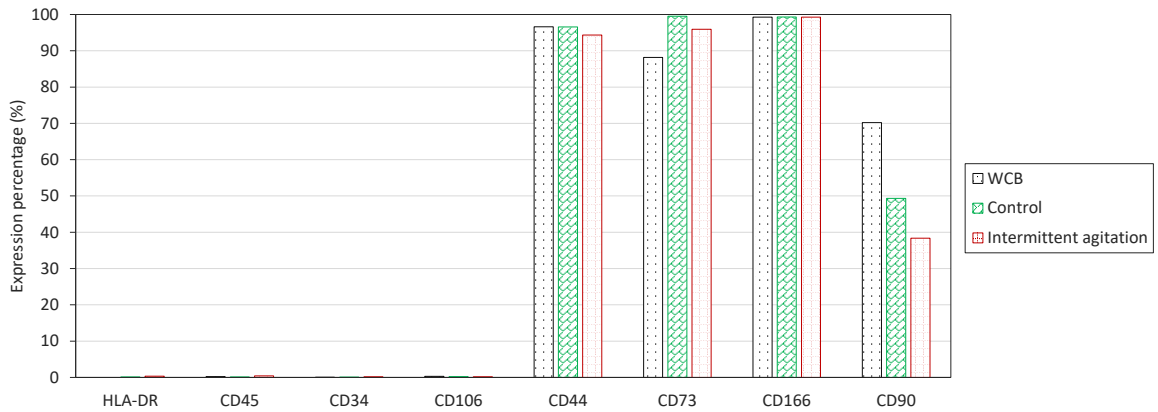

Figure 4.11: Percentage of cells expressing surface markers in the working cell bank (WCB *ie.* cells not expanded on microcarriers), in the control condition (Control) and after a culture preformed with repeated intermittent agitation cycles (Intermittent agitation). Levels of expression were obtained by FACS flow cytometry (Beckman Coulter, Gallios).

An under expression of the CD90 marker was observed in all three conditions including cells which had not been expanded on microcarriers. The results should be confirmed by repetitions since the levels of expression in the WCB are considered as abnormal when compared to results obtained at small scale. If the trend is confirmed, this could indicate a significant degradation of MSCs which should express levels of CD90 of over 95 % per the ISCT [15]. In addition, a slight over expression of the CD73 marker was observed for cells expanded on microcarriers in the control and intermittent agitation conditions compared to cells which had not been expanded on microcarriers (WCB). This marker is typically associated with cell proliferation and correlates well with the high growth rates observed during these cultures (particularly in the control condition). Overall, cells meet the surface receptor requirements suggested by the ISCT after expansion on microcarriers [15] and no significant impact of surface marker expression was noted when cells were grown with intermittent agitation cycles.

4.2.3 Impact of adding plastic particles on MSC growth, metabolism and phenotype

Impact of adding plastic particles on MSC growth and death kinetics

A set of experiments were performed to determine the effect of adding particles, on which cell growth was not possible, during MSC expansion on microcarriers in bioreactors. The aim of this study was to complete, and transpose at a larger scale, the results obtained in spinner and Erlenmeyer flasks presented in Chapter 2. Previously, MSC growth on microcarriers was found to be greatly influenced by particle concentration even when little impact was observed on the apparent growth rate at small scale [16]. In bioreactors, three cell cultures were performed with Synthemax II microcarrier concentrations of 2.73 $\%_{v/v}$ (identical to microcarrier concentrations in spinner flasks). These were considered as the control condition. In two other cultures, either 0.57 or 2.37 $\%_{v/v}$ of plastic particles (on which MSC growth was not observed) were added after MSC adhesion. The 0.57 $\%_{v/v}$ plastic particle concentration was chosen since, for Synthemax II microcarriers, adding these amounts of particles was found to have a beneficial impact on growth [16]. This condition (n = 1) was used to determine if adding small amounts of plastic particles may promote cell growth in STRs. The 2.37 $\%_{v/v}$ plastic particle concentration was chosen to have approximately twice the volume of microcarriers in the system in comparison with the control condition. This condition (n = 1) generated high levels of interactions caused by the added particles. Accordingly, the impact of adding low and high particle concentrations during culture were evaluated compared to a control condition (n = 3).

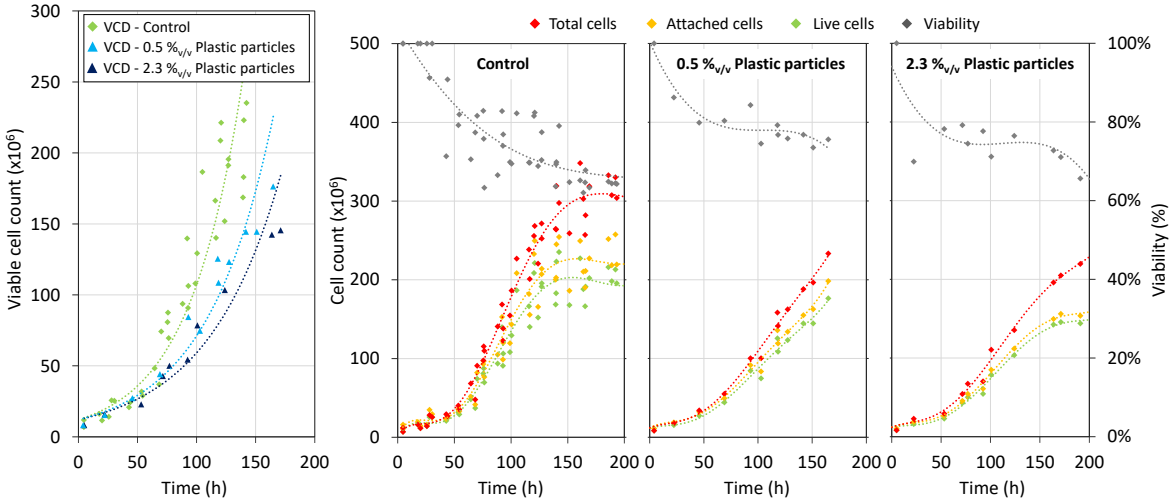

Figure 4.12: Impact of adding plastic particles on MSC growth and death kinetics. Left, viable cell density measured offline and corresponding fitted experimental models (dotted lines). The three figures on the right present bi-daily quantification of live cells attached on microcarriers (green), total live and dead cells attached on microcarriers (orange) and total cells in the STR including lysed cells quantified by LDH measurement (red) for varying levels of added plastic particles. Overall viability (live cells according to total cells) are presented in gray. Polynomial fitted trends are presented in dotted lines for visualization. n = 3 for the control and n = 1 for plastic particle conditions tested.

Daily cell counting was performed to determine the impact of adding these particles on growth and death kinetics of MSCs in these conditions. To begin with, the apparent growth rate μ_{app} was calculated by fitting an exponential model to the data obtained while growth was observed. A progressive diminution of μ_{app} was observed when adding plastic particles during MSC cultures as presented in Figure 4.12, left. The measured growth rates in the control condition were found to be of 0.026 h^{-1}, 0.018 h^{-1} when 0.5 % of plastic particles were added and 0.016 h^{-1} when 2.3 % of plastic particles were added. These correspond with a reduction of 44 % and 63 % of μ_{app} with added particle concentrations of 0.5 % and 2.3 % respectively. No significant lag phase was observed when adding plastic particles.

In addition, quantification of live and dead cell populations was performed during all cultures and are presented in Figure 4.12, right. Live cells presented in green represent the amount of live cells counted after microcarrier dissolution while the attached cells presented in orange represent the total amount of attached cells (live and dead) measured after microcarrier dissolution. Lastly, the total cells represented in red correspond with the sum of live cells counted attached on microcarriers and an estimation of dead cells by LDH quantification. The same scale is presented on the left for all counts. The total viability (represented in gray) shows the ratio between live cells counted and the the total cells. Polynomial relations were fit to each cell population in these figures for a comparison of trends.

To begin with, adding small quantities of plastic particles to the cell culture was found to lead to a slightly increased viability at the end of the growth phase (viability in the control condition after approximately 150 hours of cell culture was of 65 % while the viability in the condition with 0.5 $\%_{v/v}$ of added plastic particles after 150 hours was close to 80 %). It is possible that certain phenomena which are not yet well understood (including for example cell-microcarrier aggregation) are impacted by the addition of these plastic particles (detailed further in Chapter 4.3). Breaking large aggregates of cells could promote growth by limiting the formation of a necrotic center (observed for aggregates larger than 350 µm) which have been associated with limitations in the diffusion of oxygen and nutrients [17]. It should be kept in mind that slightly greater growth rates were observed in spinner flasks when adding these concentrations of plastic particles (Chapter 2). This was not found to be the case here, only an impact on the total viability was observed. No significant impact on the attached viability was observed by adding these particle concentrations (Figure 4.13, middle compared to control graph on the left).

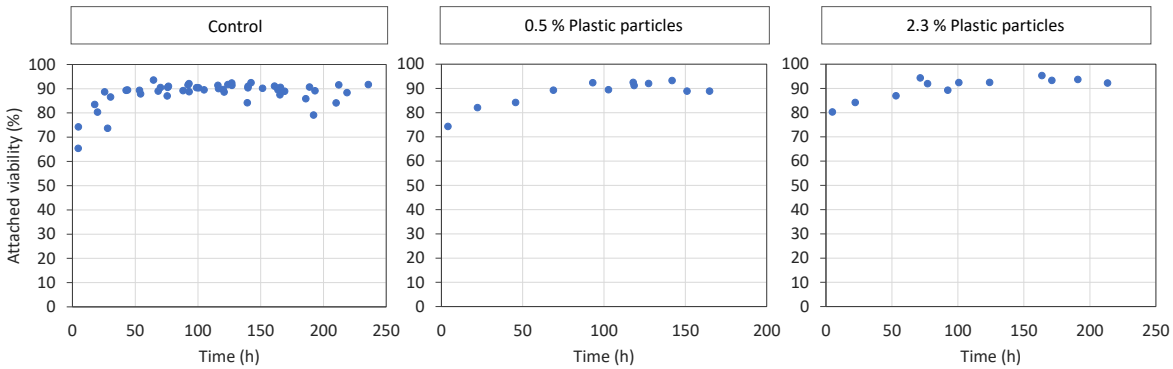

Figure 4.13: Impact of adding plastic particles on attached cell viability obtained in the control conditions (left) with the addition of 0.5 (middle) and 2.3 $\%_{v/v}$ of plastic particles (right).

Consequently, **adding small quantities of particles during MSC expansion on microcarriers could be associated with lower cell lysis levels and an overall decreased cell death**. Adding larger plastic microcarrier concentrations was found to generate similar live and dead cell evolutions compared to the control conditions (Figure 4.12, right). Maximum viable cell counts were obtained after approximately 150 hours of cell culture and a total viability of approximately 70 % was observed when adding 2.3 $\%_{v/v}$ of plastic particles. Similar levels of attached cell viability was also observed (Figure 4.13, right compared to control graph on the left). These results tend to indicate that **the apparent growth and death kinetics were found to be similar during cultures with the addition of 2.3 $\%_{v/v}$ of plastic particles compared to the control although slightly lower values of μ_{app} were observed**. Further experiments would be required to validate and explain these results in STRs as well as to define a possible optimal particle concentration which could either promote growth and/or lead to a greater viability

during culture.

Further post-treatment of the results was performed by calculating the maximum specific growth μ_{max} (green) and death rates k_d (red) as presented in Figure 4.14. As previously described, the calculated specific growth and death rates in the first hours of culture should be ignored since it is difficult to estimate these specific rates with few initial experimental data points. Results indicate that when the added particle concentration was of 0.5 $\%_{v/v}$, the growth rate reached its maximum value after approximately 60 h (which is similar to the duration in the control condition). In both conditions with added plastic particles, the maximum growth rate measured was found to be lower by approximately 40 % compared to the control. μ_{max} values of 0.022 and 0.025 h^{-1} were observed respectively for added particle concentrations of 0.5 and 2.3 $\%_{v/v}$. In addition, the kinetic death rates k_d were measured and are presented in red. In conditions with added plastic particles, the values of k_d were found to be slightly lower than the control condition with measured maximum values of 0.006 and 0.008 h^{-1} respectively with added plastic particle concentrations of 0.5 and 2.3 $\%_{v/v}$. The smaller k_d value when 0.5 $\%_{v/v}$ of plastic particles were added seems to corroborate the observed trends in the previous figures.

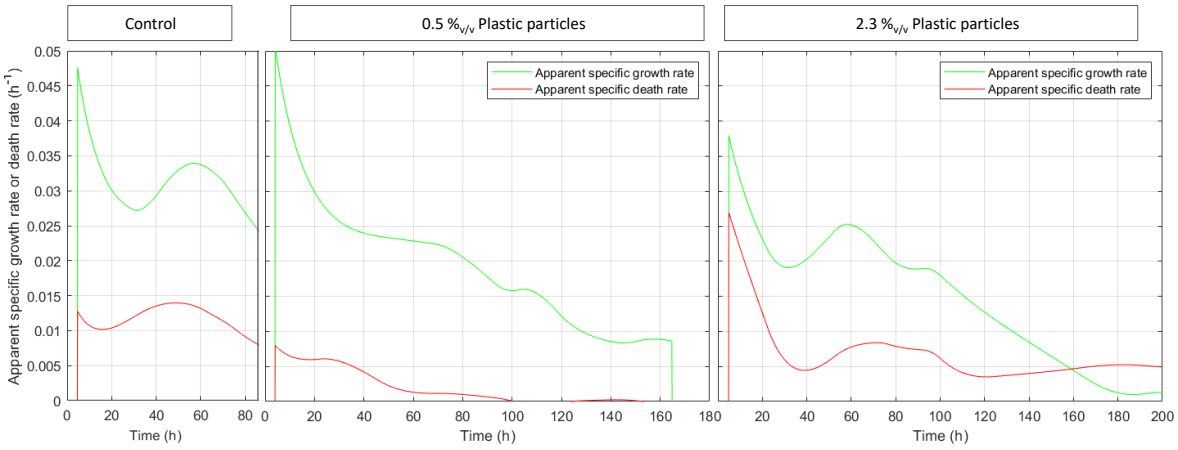

Figure 4.14: Impact of adding plastic particles on MSC growth and death specific kinetic rates obtained in the control conditions (left) with the addition of 0.5 (middle) and 2.3 $\%_{v/v}$ of plastic particles (right).

A summary of the key growth and death characteristics observed in these experiments can be found in Table 4.4. It should be kept in mind, however, that control cultures were performed in triplicate analysis while cultures with added plastic particles were performed only once. Considering the experimental variability, the trends observed above should be validated by repeating these experiments and, if possible, by using additional particle concentrations to specifically compare large scale impacts on growth and death kinetics with the observed impacts at small scale.

Table 4.4: Characteristic constants of MSC experiments in STRs during with or without added plastic particles during expansion.

	Growth phase (h)	Exp. phase (h)	X_f (live cells)	μ_{app} (h^{-1})	μ_{max} (h^{-1})	$k_{d,max}$ (h^{-1})
Control	161 h	57 h	227 million	0.026	0.034	0.014
0.5 $\%_{v/v}$ Plastic particles	165 h	58 h	176 million	0.017	0.022	0.006
2.3 $\%_{v/v}$ Plastic particles	191 h	60 h	144 million	0.016	0.025	0.008

Impact of adding plastic particles on the online measurement of MSC growth

MSC cell growth was measured online through the evolution of dielectric signals for which trends can be found in Figure 4.15. The online measures show little impact of adding small quantities (0.5 $\%_{v/v}$) of plastic particles during MSC cell cultures since dielectric values were found to be similar to the control conditions. However, when larger quantities of plastic particles were added (2.3 $\%_{v/v}$), cell growth measured online was found to be slower and achieve a lower plateau, corroborating offline measures. These results validate the use of permittivity measures to efficiently measure viable cell growth online and the fact that these measures are not impacted by additional particles. This should be kept in mind during bead-to-bead transfer processes for which fresh microcarriers, like adding plastic particles are added. A complementary discussion will be presented in Chapter 4.3.

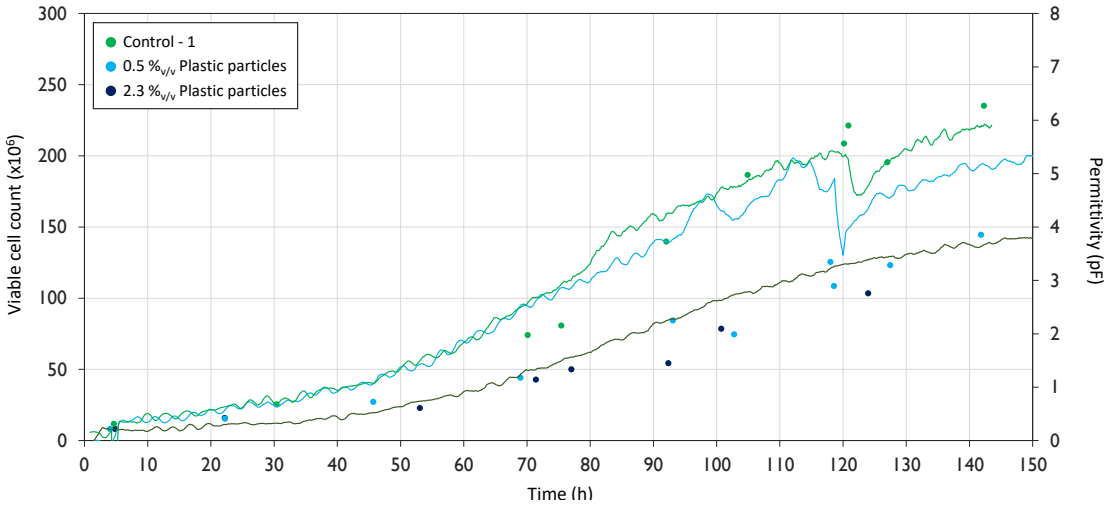

Figure 4.15: Impact of adding plastic particles on the quality of permittivity measurements. Individual points correspond to offline measures and lines correspond to online permittivity measures.

Impact of adding plastic particles on cell metabolism

Cell metabolism was evaluated by daily analysis of the cell culture supernatant. To begin with, it can be noted that the glucose consumption trends are similar between the control condition and the condition with small quantities of plastic particles (0.5 $\%_{v/v}$) as can be seen in Figure 4.16. In both conditions presented on the left side of this figure and in the middle, approximately 1.5 g of glucose was consumed in the bioreactor volume after approximately 150 hours. Since cell growth was found to be slightly slower when 0.5 $\%_{v/v}$ of plastic particles were added compared to the control, the average glucose consumption per cell $Y_{Gluc/X}$ is greater in this condition compared to the control presented in Table 4.5. Accordingly, $Y_{Gluc/X}$ was measured as 9.6 ng cell^{-1} when 0.5 $\%_{v/v}$ of plastic particles were added compared to 5.6 ng cell^{-1} in the control. In addition, cumulative lactate production trends presented in this figure indicate a lower lactate production when 0.5 $\%_{v/v}$ of plastic particles were added compared to the control. The average specific lactate production yield during the growth phase $Y_{Lac/X}$, presented in Table 4.5, was measured as 5.0 ng cell^{-1} (compared to 7.2 ng cell^{-1} in the control). As a result, the conversion factor of lactate from glucose $Y_{Lac/Gluc}$ was found to be decreased from 1.3 to 0.5 when adding 0.5 $\%_{v/v}$ of plastic particles. This could indicate a significant shift in metabolism from an anaerobic glycolysis in the control condition to an oxidative phosphorylation metabolism when adding small quantities of plastic particles, possibly indicating that oxygen transfer was enhanced with small particle concentrations.

Secondly, adding large quantities of plastic particles (2.3 $\%_{v/v}$) was associated with both a decreased glucose consumption rate and lactate production rate as indicated in the right graph presented in Figure 4.16 compared to the control condition presented on the left. Accordingly, after 200 hours of culture, the cumulative consumption of glucose in the reactor was measured as approximately 1 g when adding 2.3 $\%_{v/v}$ of plastic particles whereas this consumption reached levels of 2.5 g in the control condition. Lactate production trends indicate similar total produced quantities of lactate (measured in total grams produced in the tank). However, since cell growth was found to be decreased when adding these concentrations of plastic particles, the specific average consumption $Y_{Gluc/X}$ and production yields $Y_{Lac/X}$ values were comparable with the control as summarized in Table 4.5. Accordingly, the conversion factor of lactate from glucose $Y_{Lac/Gluc}$ were similar and close to 1 in both the control condition and wen adding large plastic particle concentrations of 2.3 $\%_{v/v}$. A preferential glycolitic metabolism was demonstrated for both the control cell cultures and cell cultures performed with the addition of 2.3 $\%_{v/v}$ plastic particles.

For comparability of consumption kinetics between conditions, the evolution of specific consumption rates $q_{Gluc/X}$ and production rates $q_{Lac/X}$ during expansion are presented over time in Figure 4.17. The maximum value of $q_{Gluc/X}$ was similar to the

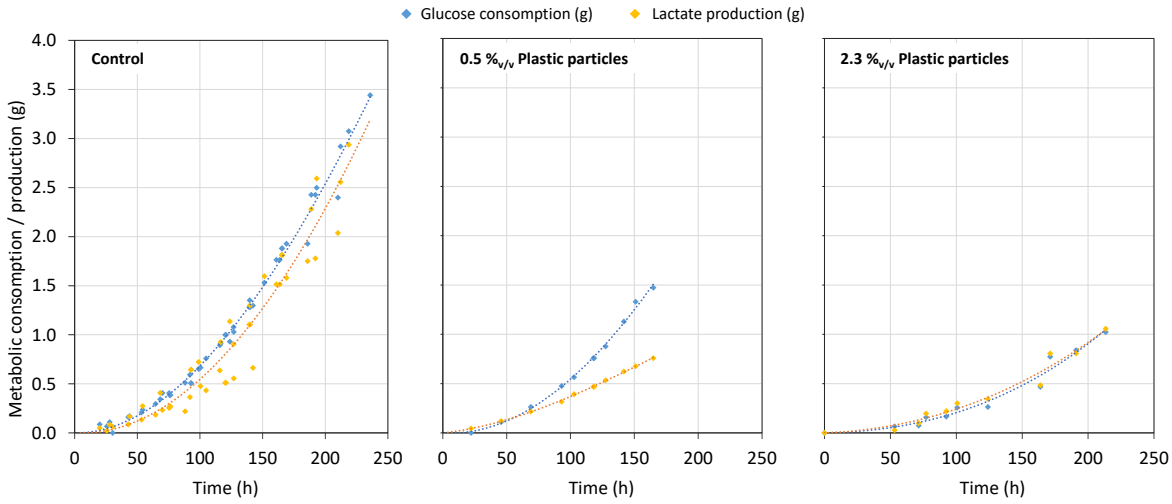

Figure 4.16: Impact of of adding plastic particles on MSC glucose metabolism. Accumulated glucose consumption and lactate production (total grams calculated in the bioreactor volume) during the cell culture in the control condition (left), and with added plastic particles (middle and right). Polynomial trends were plotted for comparison between conditions.

control but a longer duration of high glucose consumption rates was observed when 0.5 $\%_{v/v}$ particles were added. Similarly, specific consumption rates of glucose were found to be lower than in the control when 2.3 $\%_{v/v}$ plastic particles were added. While the maximum glucose consumption rate was of approximately 40 µg h^{-1} per million cells in the control, maximum $q_{Gluc/X}$ values of 20 and 10 µg h^{-1} per million cells were observed when adding 0.5 and 2.3 $\%_{v/v}$ of plastic particles respectively. Lactate production rates $q_{Lac/X}$ were found to be similar for both concentrations of plastic particles added (approximately 15 µg h^{-1} per million cells) and slightly lower than the control condition (approximately 25 µg h^{-1} per million cells).

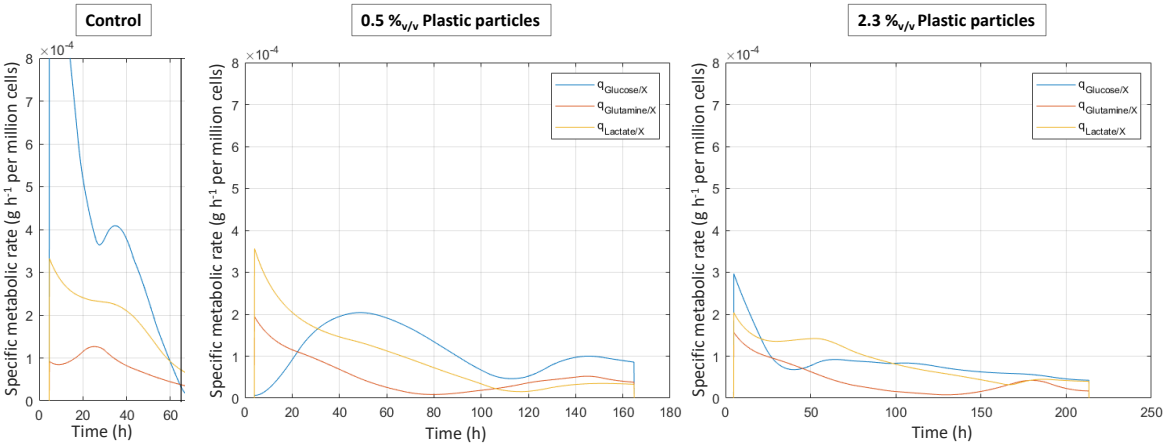

Figure 4.17: Impact of adding plastic particles on MSC specific consumption and production rates in the control condition (left), and with added plastic particles (middle and right).

Lastly, in order to further establish potential differences in metabolism, the cumulative glutamine consumption and ammonium production trends were plotted and can be found in Figure 4.18. These represent the sum of the consumed or produced metabo-

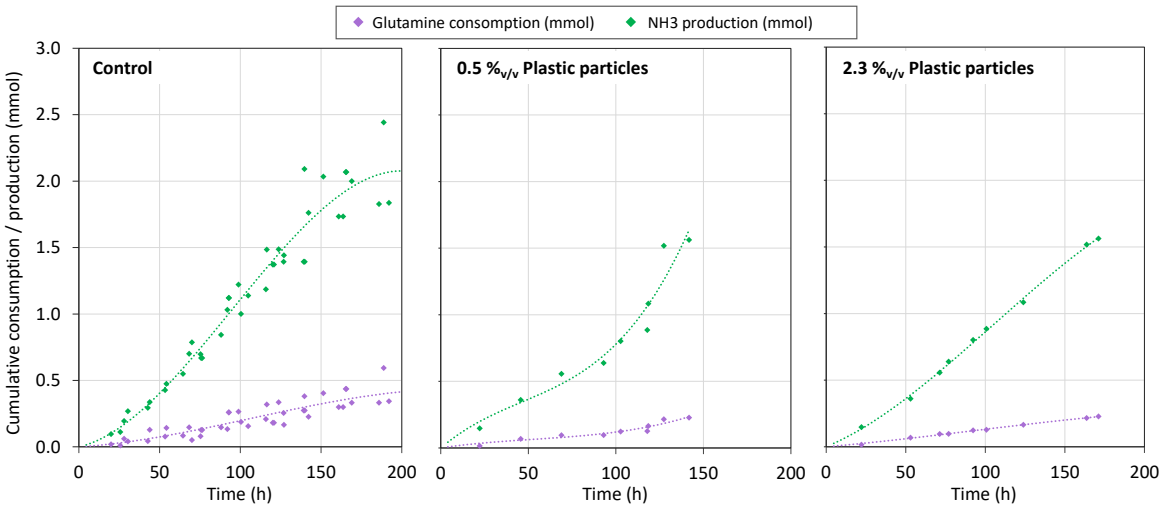

Figure 4.18: Impact of adding plastic particles on MSC glutamine metabolism. Accumulated glutamine consumption and ammonium production (total mmol calculated in the bioreactor volume) during the cell culture in the control condition (left), and with added plastic particles (middle and right). Polynomial trends were plotted for comparison between conditions.

lite in the entire bioreactor volume accumulated during culture. Results indicate in all three conditions that the glutamine consumption and ammonium production seem to have similar trends during the exponential phase. For comparability, the average glutamine consumption yield over the observed growth phase $Y_{Glut/X}$ are presented in Table 4.5. Similar values were observed in all conditions (approximately 1 - 2 nmol cell^{-1}). It can be noted that glutamine concentrations were kept above 0.2 mM during all the cultures presented here and therefore never reached inhibitory concentrations [14]. This indicates that the feeding strategy was sufficient to ensure glutamine feeding for cells and glutamine was not considered as limiting in any of the cultures. Considering the thermic degradation rate of glutamine at 37°C which was estimated as 10 % per day [18], it is difficult to measure low glutamine consumption rates (for which glutamine consumption by cells is slower than the natural degradation caused by heat). Glutamine specific consumption rates (presented in Figure 4.17) were found to have similar trends in all conditions and should primarily be measuring the constant thermal degradation of glutamine. Concerning ammonium production, the maximum values of NH_3 measured during cultures should be taken into consideration since the important parameter to consider is to define if these concentrations reach inhibitory levels of 2.5 mM [14] or not. Results indicate that this was not the case in any of the conditions tested.

Table 4.5: Metabolic yields over the growth phase in MSC experiments in STRs with or without adding plastic particles.

	$Y_{Gluc/X}$ ng/cell	$Y_{Lac/X}$ ng/cell	$Y_{Lac/Gluc}$ g/g	$Y_{Glut/X}$ nmol/cell	$Y_{NH_3/X}$ nmol/cell	Max(NH_3) mM
Control	5.6	7.2	1.3	1.3	9.1	1.8
0.5 $\%_{v/v}$ Plastic particles	9.6	5.0	0.5	2.2	14.6	2.1
2.3 $\%_{v/v}$ Plastic particles	6.1	6.3	1.0	1.5	10.5	2.1

Impact of adding plastic particles on MSC phenotype

Cells cultivated in conditions where 0.5 $\%_{v/v}$ of plastic particles were added were detached from microcarriers in order to perform a cytometric analysis of cell surface marker expression. Results compared to the control condition and the working cell bank used (cells not expanded on microcarriers) are presented in Figure 4.19. Results indicate that for cells expanded with these small concentrations of added plastic particles, no significant impact on any of the surface marker expression were observed, thus indicating that cells did not seem to have an altered phenotype after their growth on microcarriers. These results should be confirmed by a more thorough characterisation of the cells produced, including testing of the capacity of these cells to undergo differentiation when cultured in differentiation promoting conditions. Additional determination of attributes such as senescence, clonogenicity, functionality would be interesting to further expand these observations.

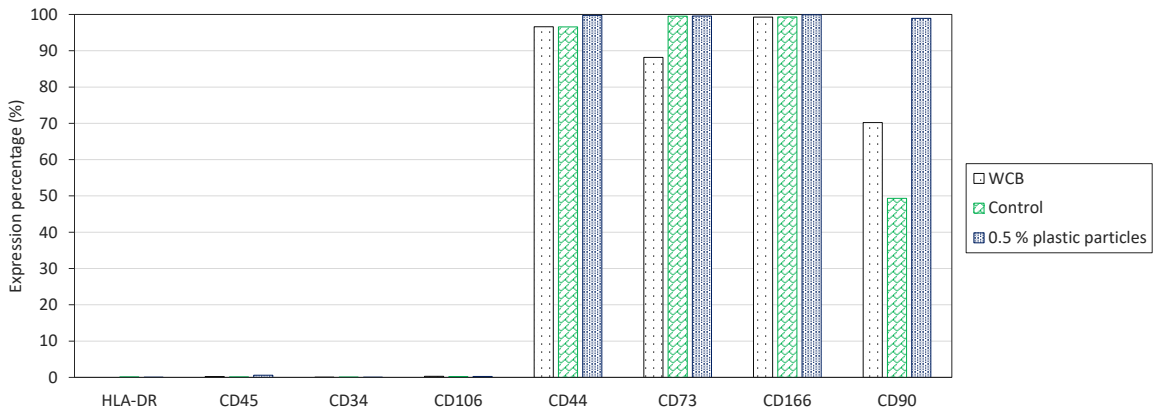

Figure 4.19: Percentage of cells expressing surface markers in the working cell bank (WCB *ie.* cells not expanded on microcarriers), in the control condition (Control) and after a culture preformed with the addition of 0.5 % of plastic particles. Levels of expression were obtained by FACS flow cytometry (Beckman Coulter, Gallios).

4.2.4 Section summary and comparison with small scale results

MSCs were expanded on microcarriers in bioreactors during which mechanical stresses were added by either performing repeated intermittent agitation cycles or by adding plastic particles during culture. Growth was significantly reduced when intermittent agitation cycles were performed. Specifically, the apparent growth rate μ_{app} was reduced by a factor of 2.2 during the duration of cell expansion. The duration of the growth phase was also found to be longer (220 hours compared to 160 hours in the control condition). In addition, growth was also found to be reduced by adding plastic particles. Specifically, the apparent growth rate μ_{app} was reduced by a factor of approximately 1.5 when plastic particles were added. The results obtained in bioreactors were compared to results obtained in spinner flasks using the same microcarrier type (Synthemax II) and the same concentration of 2.73 $\%_{v/v}$ and are presented in Figure 4.20. In small scale studies, the total microcarrier concentration was varied by adding plastic particles at different solid hold-up concentrations.

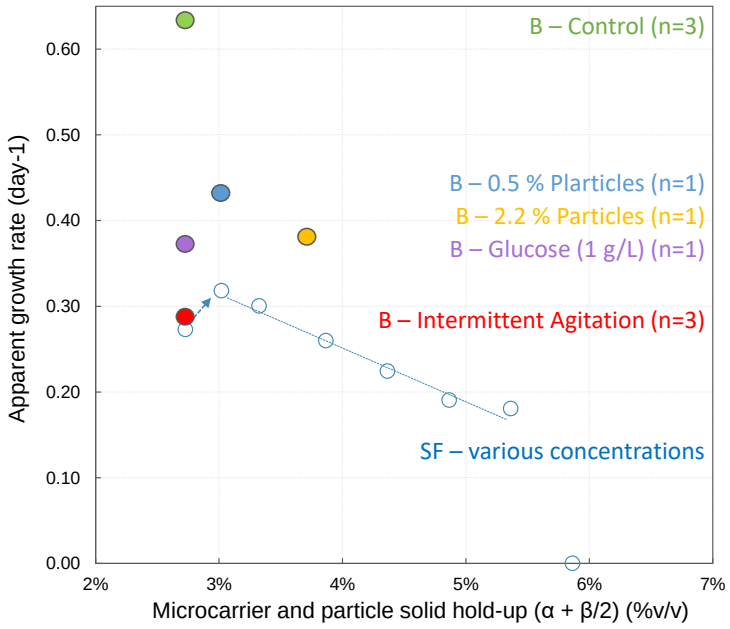

Figure 4.20: Impact of process parameters on MSC apparent growth rate in bioreactors (B) and spinner flasks (SF). Results are presented according to the Synthemax II microcarrier concentration α of 2.7 $\%_{v/v}$ and added plastic particle concentration β. Empty blue circles correspond to data obtained in spinner flasks (detailed in Chapter 2). Full circles correspond to cultures in bioreactors presented in this chapter.

To begin with, it can be observed that growth in bioreactors is significantly enhanced compared to spinner flask cultures, possibly due to the increased control (pH, pO_2, temperature *etc.*) and fine-tuning of regulation parameters in these systems. In addition, the growth rate observed in conditions which were the least favourable for growth (low glucose concentration, intermittent agitation and adding particles) were found to have growth rates similar to those obtained in the control conditions in spinner

flasks. However, the global trends observed here would require further testing to evaluate if this trend is significant and could possibly lead to a more robust understanding on how these specific parameters impact growth and death kinetic constants of MSCs grown on microcarriers in bioreactors. In addition, the impact of these parameters on certain quality attributes of the produced MSCs is currently not well understood. The phenotypical characterisation presented on the produced cells could be further validated by complimentary measures of other MSC attributes.

In addition, for all cell culture conditions (at small and large scale), aggregation phenomena were observed and difficult to measure and control. **Specifically, in cultures performed with intermittent agitation, aggregation phenomena led to large microcarrier aggregates which may also have played a role in the increased cell death observed**. Lastly, these aggregation phenomena are expected to also generate a certain level of growth heterogeneity (for example since aggregate size is a parameter which is not easily controlled and leads to heterogeneous cell oxygenation and nutrient availability) but also in the measurement of cell density (technical difficulties in measuring a representative cell culture sample and in isolating the individual viable cells from the microcarriers were found to be an additional challenge when aggregation was observed). A further analysis of aggregation phenomena will be presented in Chapter 4.3.

4.3 Measuring aggregation during MSC growth

4.3.1 Introduction

Aggregation phenomena were observed visually in the STR during the cell culture at various stages of the cell culture. For example, large homogeneous visual aggregates were observed at the end of the cell culture in certain cases for which the size was visually estimated as several millimeters. In addition, during certain cultures, larger aggregates of approximately 1 or 2 centimeters were generated overnight and observed in the morning. These technical observations were either reduced by manually increasing the agitation in the tank for several minutes to reduce the aggregate size and re-suspend the heaviest aggregates, or by manually and gently pipetting the larger aggregates to dissociate them. Accordingly, controlling and measuring the level of aggregation during MSC cultures on microcarriers may be one of the next challenges towards improving these processes. The elements present in this section aim at presenting online and offline measures during certain cell cultures for which aggregation was found to be a significant issue. Although measuring aggregation was not an initial objective of this work, it was found to be the major challenge and a possible bias which should be kept in mind.

4.3.2 Methods

Offline microscopic observation

Microscopic observations of microcarrier aggregates were performed by sampling 1 mL of the cell culture medium. Microcarriers were left to sediment for 1 minute and the cell culture supernatant was replaced with 500 µm of PBS. The aggregates were then observed with a Leica DMRB microscope at different magnification factors. White light transmission through the samples was photographed in these conditions. Between 8 and 10 pictures were taken of the sample which was entirely distributed on the microscope slide. The size of the largest visualized aggregates in the sample was measured as a qualitative estimate of aggregate size.

Online measures

Online measures of viable cell characteristics was performed via the online Visifern dielectric probe provided by Hamilton. As described in Chapter 4.2, online measurement of cell permittivity under an alternating electrical field can be correlated with viable cell density. In addition, the frequency which corresponds with the inflection point of the permittivity profile (described in Chapter 1.3 in Figure 1.19), can be used to gain additional information on cells. This frequency, called the critical frequency (F_c) typically depends on the cell membrane properties (C_M) and the conductivities of both

the cell medium (σ_M) and the cell cytoplasm (σ_C).

$$r_{aggreg.} = \frac{1}{2\pi \times F_c \times C_M \times (\frac{1}{\sigma_C} + \frac{1}{2\sigma_M})} \tag{4.10}$$

Much like cell-cell aggregation has been demonstrated by variation in the critical frequency (F_c), it should be theoretically possible to detect microcarrier-microcarrier aggregation by detecting changes in this critical frequency which supposes a direct correlation between the radius of the measured cell complex ($r_{aggreg.}$) and the critical frequency measured (Equation 4.10) [19]. However, in general, the intra-cellular conductivity (σ_C) is considered as negligible (2–4 mS cm^{-1}) in comparison to the culture medium conductivity (15–20 mS cm^{-1}) and Equation 4.10 can be reduced to Equation 4.11 [20]. We should keep in mind, however, that the dielectric responses of cells are multi-parametric and changes in cell state, such as apoptosis, have also been shown to impact the critical frequency of adherent Vero cells on Cytodex 1 microcarriers due to a cell membrane reorganization and cell fragmentation into small apoptotic bodies as well as morphological changes of the attached cells [20]. In this example, the critical frequency observed was reduced from 1400 kHz to approximately 600 kHz and was correlated with an increase in apoptotic Vero cells. However, no significant aggregation was observed in these experiments.

$$r_{aggreg.} = \frac{1}{2\pi \times F_c \times C_M} \tag{4.11}$$

Taking into account these elements, the critical frequency was measured throughout the cell cultures via the online dielectric probe. Online measures of the critical frequency were obtained every 6 minutes throughout the cell culture.

4.3.3 Results

Offline aggregation observation

To begin with, photographic observations of cell aggregates correlated with the visual observations of the STR which suggested a progressive increase of aggregate size throughout the cell culture (Figure 4.21). Accordingly, aggregation was observed after the first few hours of culture, for which in majority microcarriers were found to be isolated but occasional aggregates of two or three microcarriers were observed (as shown in the photograph taken after 20 hours of cell culture). Subsequently, the number and size of these aggregates progressively increased during the next 24 hours during which most microcarriers observed were found in aggregates of two to five microcarriers. Lastly, these aggregates were found to significantly increase in size until a maximum microcarrier size composed of over 100 microcarriers was observed as shown after 93 hours of cell culture.

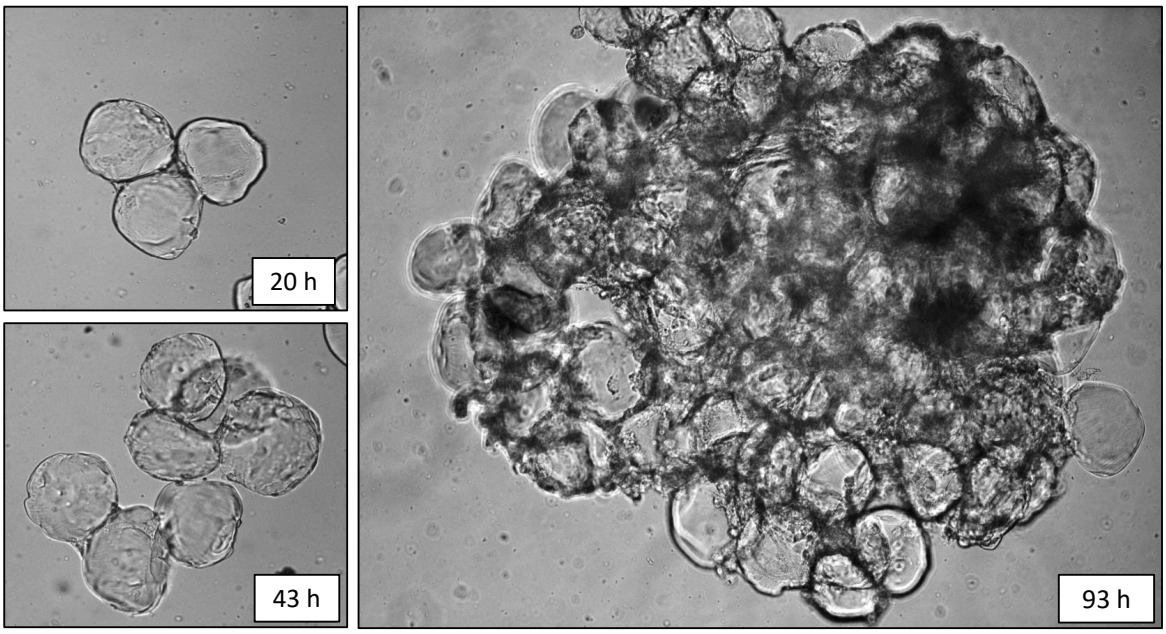

Figure 4.21: Microscopic observation of microcarrier aggregation during WJ-MSC culture on Synthemax II microcarriers in bioreactors in the control conditions.

Online measurement of critical frequency in control conditions

In parallel with the microscopic observations, the behaviour of dielectric measurements over the course of the cell culture were represented in the three control conditions. Results of the dielectric signal observed during these cell cultures can be found in Figure 4.7, left and was correlated with the offline measure of viable cell density. In parallel, the frequency with which the signal presented in Figure 4.7 was obtained, or critical frequency F_c, is presented in Figure 4.22.

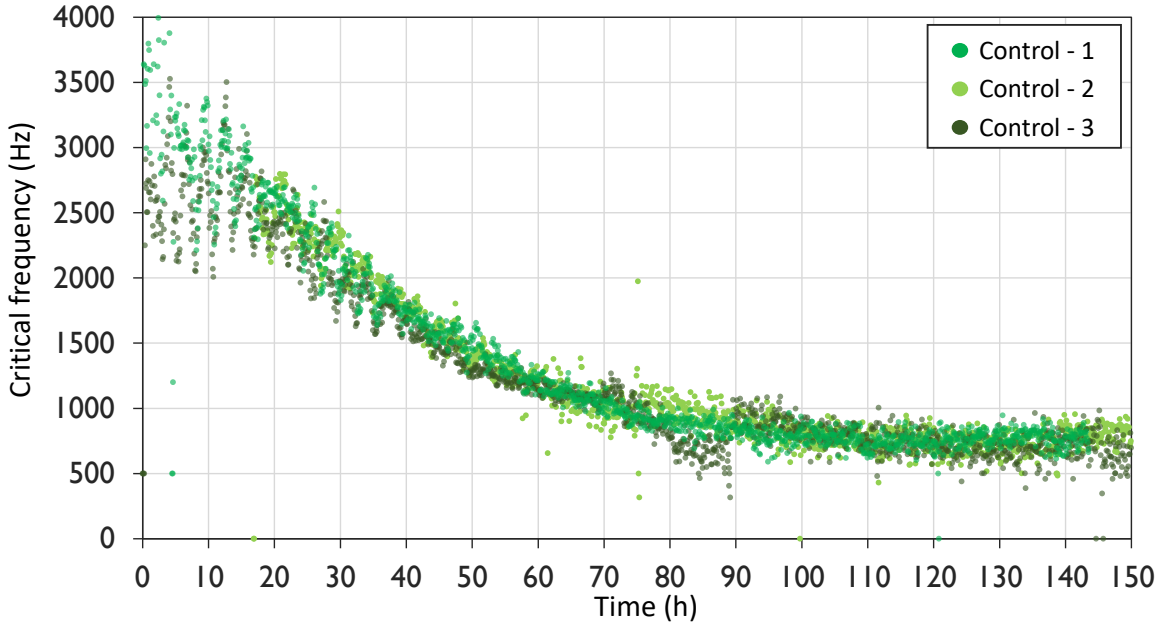

Figure 4.22: Evolution of the critical frequency during dielectric online measurements in control experiments.

To begin with, the evolution of the critical frequency in the three control conditions was found to be reproducible and, in general, follow the same trend for which a rapid decrease in critical frequency was observed during the first 80 hours of culture. During this initial phase, the critical frequency F_c was found to decrease from approximately 3000 to 1000 Hz. Subsequently, the critical frequency was found to remain stable around 750 Hz until the end of the cell culture. The decreased trend observed online regarding the dielectric critical frequency was found to globally correspond with the increased aggregate size during the first days of cell culture, and a visual observation of an aggregate size no longer increasing after approximately 90 hours. As a result, it is suggested that the online measured critical frequency could be correlated with microcarrier aggregation.

Online measurement of critical frequency in intermittent agitation conditions

Interestingly, the critical frequency profiles were also found to be similar in cell cultures performed with intermittent agitation as can be seen in Figure 4.23. For clarity, the data is only presented during the phases where the system was agitated. Inversely, when the system was in intermittent agitation phases, measuring the critical frequency in the cell culture supernatant only had no signification.

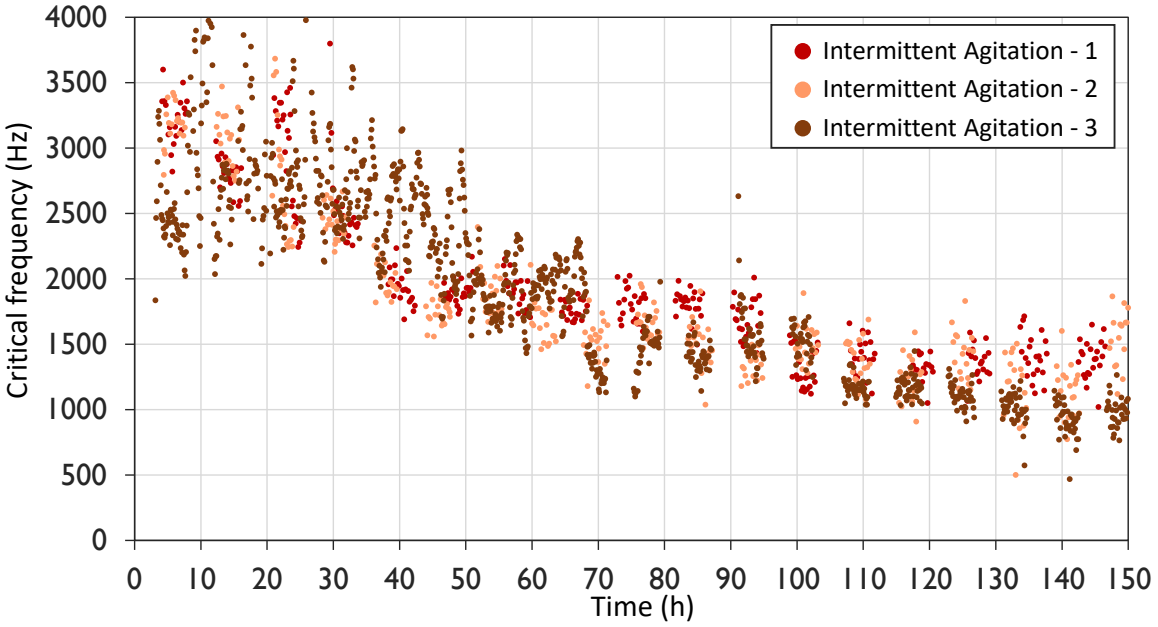

Figure 4.23: Evolution of the critical frequency C_f during dielectric online measurements in experiments with intermittent agitation. Only results obtained during suspended steps are presented.

The results presented in intermittent agitation conditions showed similar profiles to the control conditions during the first few hours of cell culture (an average Critical frequency of 3000 Hz was observed). However, the decrease in critical frequency throughout the cell culture was found to be less rapid in intermittent agitation condi-

tions. Accordingly, the critical frequency observed after approximately 90 hours was found to be around 1250 Hz (when this value was found to be around 750 Hz in the control conditions). On average, the critical frequency was found to be higher with intermittent agitation, thus indicating that it is possible that aggregate size be smaller in these conditions according to Equation 4.11, possibly due to increased mechanical constraints during the multiple re-suspension steps which could lead to aggregate dissociation. As it has been observed in Chapter 3, steps when particles change from a sedimented state to a suspended state can reach local concentrations which reach levels up to 10 times the average microcarrier concentration for up to 10 minutes. The local concentration during these steps lead to increased collisions and/or frictions between microcarriers and could break potentially forming aggregates.

Online measurement of critical frequency with added plastic carriers

Lastly, the critical frequency was also measured online during cell cultures to which plastic particles were added at various concentrations. To begin with, microscopic observations of aggregates was performed after 92 and 240 hours of cell culture when small concentrations of plastic particles were added (0.5 $\%_{v/v}$). It can be observed in these photographs that microcarrier aggregation was significantly reduced by adding the plastic particles.

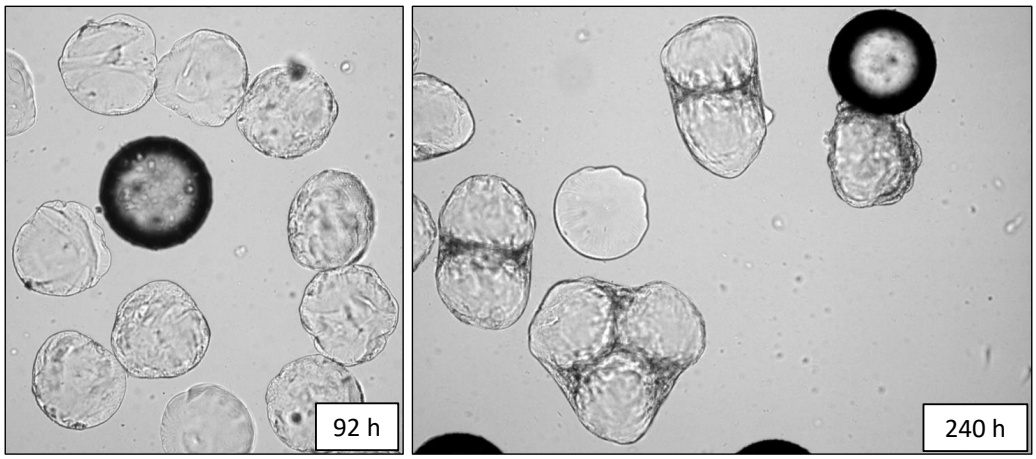

Figure 4.24: Microscopic observations during cell cultures with added plastic particles at at concentration of 0.5 $\%_{v/v}$.

Results concerning critical frequency measures during culture are presented in Figure 4.25 compared to a control cell culture without added plastic particles. As described in Chapter 4.2, adding plastic particles was expected to not affect the dielectric signal since the viable cell density measurements were not significantly affected. Accordingly, adding plastic particles was found to, during the first 80 hours of expansion, generate a lower critical frequency read. These results would tend to indicate greater aggregate sizes in these conditions, possibly due to the fact that the plastic particles could be incorporated into the microcarrier aggregates. However, this was not found to be

the case in microscopic observations as presented above. In the case of larger plastic concentrations added during culture, microscopic observations are presented in Figure 4.26. A gradual aggregation of microcarriers was observed during culture, starting at approximately 100 hours. These results qualitatively appreciate microcarrier aggregation via daily photographs.

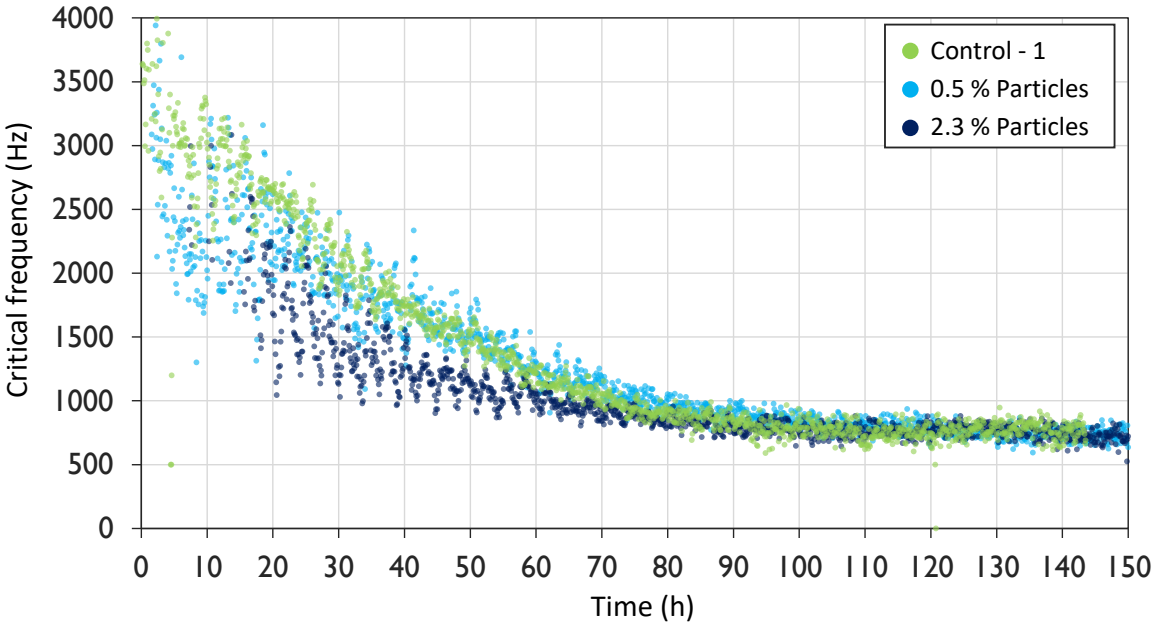

Figure 4.25: Evolution of the critical frequency during dielectric online measurements in experiments with added plastic particles.

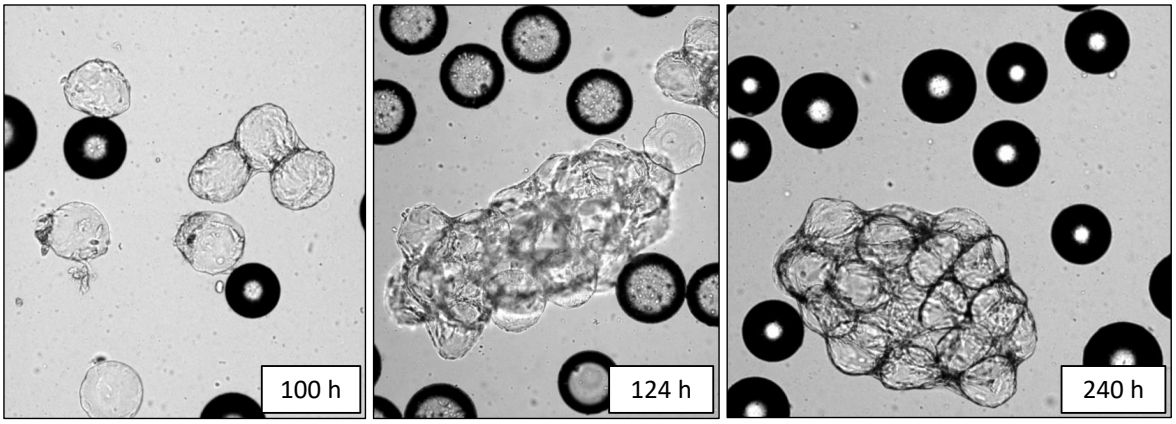

Figure 4.26: Microscopic observations during cell cultures with added plastic particles at at concentration of 2.3 $\%_{v/v}$.

4.3.4 Discussion

The aggregation phenomena have routinely been observed previously in the work of Ferrari et al. [13] and may result in mass transfer limitations and, finally, loss of stem cell properties, reduced cell growth, and even cell death. The work successfully prevented aggregation by adding fresh microcarriers during expansion sat the start of the observed aggregation (day 7). Additional work on human adipose-derived MSCs have been investigated by characterizing the mean sauter diameter of aggregates grown in spinner cultures [21]. Authors reported average aggregate sizes of 0.2 to 0.7 mm which correspond with the clumping of a large number of microcarriers (clearly indicated by the DAPI stained photographs in this work). Authors demonstrated that agitation was, as expected, an influential parameter for aggregate size and that aggregation started to become significant for most agitation conditions after day 5. These authors also reported little impact of aggregation on the expression of surface marker expression. These may correlate with the lack of modification of MSC CD expression observed although an impact on growth and death kinetics was observed in the present Chapter. In another study, the impact of aggregate size on the limitation of growth was demonstrated for aggregate sizes of 0.2 mm (the most probable cause of this would be the reduced feeding and oxygenation of cells at the center of the aggregates).

The results presented above indicate that adding plastic particles or performing intermittent agitation in microcarrier cultures affect the online measures of critical frequency. These values may be correlated with aggregation but this has not been demonstrated via offline microscopic analysis of microcarriers. However, it should be kept in mind that the offline analysis presented here are rather a qualitative visualization of aggregation. It is difficult to conclude by these offline photographs on average aggregation characteristics such as average and/or maximum aggregate size which would be required to robustly correlate, or not with online measures. Theoretically, online measures could be an efficient tool to measure aggregation but this should be further experimented.

4.4 Chapter Overview

The aim of this chapter was to evaluate the effect of repeated mechanical constraints on MSC culture on microcarriers in bioreactors. For this, mechanical constraints were provoked by two independent mechanisms.

1) **To begin with, intermittent agitation cycles were performed in cultures to detect the impact of repeated sedimentation and suspension phases on MSC growth, metabolism and phenotype.** The impact of intermittent agitation (which mimic inoculation, medium exchange or bead-to-bead steps which would be required for expansion processes) undoubtedly have an impact on MSC growth and death.

   - **Growth was reduced with intermittent agitation**. Specifically, the apparent growth rate μ_{app} was reduced by a factor of 2.2 during the duration of cell expansion. The duration of the growth phase was found to be longer (220 hours compared to 160 hours in the control condition). Whereas 227 million MSCs were observed at the end of the control condition, only 96 million cells were observed at the end of cultures with intermittent agitation cycles. In addition, the maximum cell growth observed μ_{max} was reduced by a factor of 1.6 with repeated agitation cycles. To date, few studies have looked at the impact of intermittent agitation on MSC culture. The culture of human embryonic stem cells on microcarriers for their differentiation into cardiomyocytes indicated that vigorous agitation during expansion was associated with a decreased yield reduction by a factor of 38 % [22]. Intermittent agitation strategies were however found to be beneficial for differentiation after expansion has been completed.
   - **Death was increased with intermittent agitation**. Death kinetic constant $k_{d,max}$ was measured as 0.014 h^{-1} in the control whereas it was measured as 0.018 h^{-1} with agitation cycles. Cell death was primarily found to be associated with cell lysis and a detachment of dead cells from the carriers since the attached viability was not found to vary between the tested conditions. It is unclear, however, if the increased cell lysis observed could have affected other phenotypical attributes including secretome, senescence *etc.*
   - **Online measurements of cell growth was more difficult with intermittent agitation**. Online measurement of permittivity validated the technique to monitor MSC growth in the control conditions. However, a greater difference was observed between offline and online measures in cultures with intermittent agitation, possibly due to aggregation which remains difficult to measure and control.

- **MSC metabolism was impacted by intermittent agitation**. Both maximum and average glucose specific consumption rates were found to be higher in the control conditions compared to intermittently agitated cultures, respectively maximum values of $q_{Gluc/X}$ and measured $Y_{Gluc/X}$, correlating with growth results. However, lactate production was similar in both conditions. Accordingly, the transformation yield of lactate from glucose $Y_{Lac/Gluc}$ shifted from an average value of 1.3 to 0.9 g/g between the control and intermittent agitation conditions. Both indicate a preferential glycolitic metabolism. Lastly, levels of NH_3 achieved higher concentrations with intermittent agitation (2.3 mM compared to 1.8 mM in the control). These levels are close to inhibitory concentrations for growth [14].
- **MSC phenotype may be impacted by intermittent agitation cycles**. Cells which were cultured under intermittent agitation were observed to have a slower growth in flasks after being thawed again and lower plastic adhesion levels (estimated qualitatively). The measurement of CD expression levels indicated that intermittent agitation did not significantly impact the expression of known MSC surface markers but the visual observations seem to indicate an impact on phenotype.

2) **In addition, the impact of adding plastic particles during MSC growth in STRs was estimated for low and high particle concentrations added, respectively 0.5 and 2.3 $\%_{v/v}$**. These results should be compared to the work presented in Chapter 2 at small scale. In coherence with small scale studies, the effect of adding plastic particles was found to depend on the added particle concentration.

- **Growth was reduced by adding plastic particles**. Specifically, both the apparent growth rate μ_{app} and maximum growth rates μ_{max} were reduced by a factor of approximately 1.5 when plastic particles were added. For example, μ_{max} of 0.034 h^{-1} was measured in controls compared to 0.022 and 0.025 h^{-1} with added plastic particles at concentrations of 0.5 and 2.3 $\%_{v/v}$. In addition, whereas 227 million MSCs were observed at the end of the control condition, only 176 and 144 million cells were observed at the end of cultures with added plastic particle concentrations of 0.5 and 2.3 $\%_{v/v}$ respectively. Although bead-to-bead transfer of MSCs onto fresh microcarriers was successfully demonstrated as growth promoting due to the added culture surface [6, 23, 24], the specific impact of adding particles in itself has not been, to our knowledge, investigated.
- **Death was reduced when adding small particle concentrations of 0.5 $\%_{v/v}$**. Death kinetic constant $k_{d,max}$ was measured as 0.014 h^{-1} in the control whereas it was measured as 0.006 h^{-1} when small particle concentrations

were added (not for higher particle concentrations). Cell death was primarily found to be associated with cell lysis and a detachment of dead cells from the carriers since the attached viability was not found to vary between the tested conditions. In small scale studies in spinner flasks, adding small quantities of plastic particles was associated with growth enhancement [16]. It is possible that, at large scale, adding small quantities of plastic particles may impact aggregation. By breaking the observed microcarrier aggregates, the particles may limit possible nutrient and oxygen limitations for cells at the center of large aggregates.

- **A shift in metabolism was observed when adding small particle concentrations of 0.5 $\%_{v/v}$**. The transformation yield of lactate from glucose $Y_{lac/gluc}$ shifted from an average value of 1.3 to 0.5 g/g between the control and small particle concentration conditions which may indicate a shift towards the more efficient oxydative metabolism of glucose. This shift was not observed when higher plastic particles were added of 2.3 $\%_{v/v}$. Glutamine concentrations remained above 0.2 mM in all conditions and NH_3 concentrations remained below inhibitory levels of 2.5 mM [14].
- **Online measurements of cell growth was not affected by adding plastic particles**. Online measurement of permittivity validated the technique to monitor MSC growth in control conditions and in cultures with both plastic particle concentrations. The offline and online measures correlated well for both conditions tested.

In parallel, online monitoring of cell growth was successfully validated via dielectric measures. These cell readings not only allowed the monitoring of VCD online through permittivity readings, but also may lead to measurement techniques of other parameters such as, possibly aggregation. Considering the technical difficulties associated with measuring and/or controlling aggregation in adherent cell cultures, having online measures of aggregation would be extremely valuable and could significantly impact the maximum growth and death kinetic constants as it has begin to be demonstrated in the present work. **Further analysis of these online permittivity measures would be valuable if the concept is in fact demonstrated to correlate with aggregation. However, due to the multi-parametric nature of these measures (which are also expected to be influenced by cell spreading and microcarrier confluency), a study focusing solely on the characterisation of permittivity measures would be required**. Lastly, other online measures could also be used including RAMAN spectroscopy or endoscopic measures (for which some results were presented in Chapter 3) and could also be evaluated.

In addition, it is possible that these observed variations have an impact on the cell secretome (which is the object of numerous studies) and on functionality. Elements

of accelerated cell senescence caused by these stresses may also occur during expansion and it is questionable whether cells expanded under high stress conditions still meet the criterion to characterize these cells as MSCs. For this, the characteristics suggested by the International Society for Cell and gene Therapy (ISCT) should be verified [15]. All of these elements could have significant impacts on the advancement of clinical trials. Consequently, designing processes around a defined quality target product profile QTTP should be the norm for future development according to regulatory guidelines proposed by the Food and Drug Administration (FDA), the European Medicines Agency (EMA) and also many regulatory authorities throughout the world. An example of such a methodology can be found in Chapter 1.2. The study presented below aims at participating in the scientific knowledge which could be used in this context.

Bibliography

[1] R. S. Cherry and E. T. Papoutsakis. Physical mechanisms of cell damage in microcarrier cell culture bioreactors. *Biotechnology and bioengineering*, 32(8):1001–1014, 1988.

[2] J. Yang, P. Guertin, G. Jia, Z. Lv, H. Yang, and D. Ju. Large-scale microcarrier culture of hek293t cells and vero cells in single-use bioreactors. *AMB Express*, 9(1):1–14, 2019.

[3] N. Liu, R. Zang, S.-T. Yang, and Y. Li. Stem cell engineering in bioreactors for large-scale bioprocessing. *Engineering in Life Sciences*, 14(1):4–15, 2014.

[4] P. S. Couto, M. Rotondi, A. Bersenev, C. Hewitt, A. Nienow, F. Verter, and Q. Rafiq. Expansion of human mesenchymal stem/stromal cells (hmscs) in bioreactors using microcarriers: lessons learnt and what the future holds. *Biotechnology Advances*, 45:107636, 2020.

[5] S. Derakhti, S. H. Safiabadi-Tali, G. Amoabediny, and M. Sheikhpour. Attachment and detachment strategies in microcarrier-based cell culture technology: A comprehensive review. *Materials Science and Engineering: C*, 103:109782, 2019.

[6] C. Sion, D. Ghannoum, B. Ebel, F. Gallo, N. de Isla, E. Guedon, I. Chevalot, and E. Olmos. A new perfusion mode of culture for wj-mscs expansion in a stirred and online monitored bioreactor. *Biotechnology and Bioengineering*, 118(11):4453–4464, 2021.

[7] B. Pepinsky, C. Hession, L. Chen, P. Moy, L. Burkly, A. Jakubowski, E. Chow, C. Benjamin, G. Chi-Rosso, and S. Luhowskyj. Structure/function studies on vascular cell adhesion molecule-1. *Journal of Biological Chemistry*, 267(25):17820–17826, 1992.

[8] L. E. Sidney, M. J. Branch, S. E. Dunphy, H. S. Dua, and A. Hopkinson. Concise review: Evidence for CD34 as a common marker for diverse progenitors. *Stem Cells*, 32:1380–1389, 2014.

[9] S. Shivtiel, O. Kollet, K. Lapid, A. Schajnovitz, P. Goichberg, A. Kalinkovich, E. Shezen, M. Tesio, N. Netzer, I. Petit, A. Sharir, and T. Lapidot. CD45 regulates retention, motility, and numbers of hematopoietic progenitors, and affects osteoclast remodeling of metaphyseal trabecules. *Journal of Experimental Medicine*, 205(10):2381–2395, 2008.

[10] M. Schieker, C. Pautke, K. Reitz, I. Hemraj, P. Neth, W. Mutschler, and S. Milz. The use of four-colour immunofluorescence techniques to identify mesenchymal stem cells. *Journal of Anatomy*, 204(2):133–139, 2004.

[11] T. A. Rege and J. S. Hagood. Thy-1 as a regulator of cell-cell and cell-matrix interactions in axon regeneration, apoptosis, adhesion, migration, cancer, and fibrosis. *The FASEB Journal*, 20(8):1045–1054, 2006.

[12] O. Ohneda, K. Ohneda, F. Arai, J. Lee, T. Miyamoto, Y. Fukushima, D. Dowbenko, L. A. Lasky, and T. Suda. ALCAM (CD166): its role in hematopoietic and endothelial development. *Blood*, 98(7):2134–2142, 2001.

[13] C. Ferrari, F. Balandras, E. Guedon, E. Olmos, I. Chevalot, and A. Marc. Limiting cell aggregation during mesenchymal stem cell expansion on microcarriers. *Biotechnology progress*, 28(3):780–787, 2012.

[14] D. Schop, F. W. Janssen, L. D. van Rijn, H. Fernandes, R. M. Bloem, J. D. de Bruijn, and R. van Dijkhuizen-Radersma. Growth, metabolism, and growth inhibitors of mesenchymal stem cells. *Tissue Eng*, 15:1877–1886, 2009.

[15] M. Dominici, K. Le Blanc, I. Mueller, I. Slaper-Cortenbach, F. Marini, D. Krause, R. Deans, A. Keating, D. Prockop, and E. Horwitz. Minimal criteria for defining multipotent mesenchymal stromal cells. the international society for cellular therapy position statement. *Cytotherapy*, 8:315–317, 2006.

[16] C. Maillot, N. De Isla, C. Loubiere, D. Toye, and E. Olmos. Impact of microcarrier concentration on mesenchymal stem cell growth and death: Experiments and modelling. *Biotechnology and Bioengineering*, 2022.

[17] J. M. Santos, S. P. Camões, E. Filipe, M. Cipriano, R. N. Barcia, M. Filipe, M. Teixeira, S. Simões, M. Gaspar, D. Mosqueira, et al. Three-dimensional spheroid cell culture of umbilical cord tissue-derived mesenchymal stromal cells leads to enhanced paracrine induction of wound healing. *Stem cell research & therapy*, 6(1):1–19, 2015.

[18] G. Tritsch and G. Moore. Spontaneous decomposition of glutamine in cell culture media. *Experimental cell research*, 28(2):360–364, 1962.

[19] S. Ansorge, G. Esteban, and G. Schmid. On-line monitoring of infected sf-9 insect cell cultures by scanning permittivity measurements and comparison with off-line biovolume measurements. *Cytotechnology*, 55(2):115–124, 2007.

[20] E. Petiot, A. El-Wajgali, G. Esteban, C. Gény, H. Pinton, and A. Marc. Real-time monitoring of adherent vero cell density and apoptosis in bioreactor processes. *Cytotechnology*, 64(4):429–441, 2012.

[21] V. Jossen, C. Schirmer, D. Mostafa Sindi, R. Eibl, M. Kraume, R. Pörtner, and D. Eibl. Theoretical and practical issues that are relevant when scaling up hmsc microcarrier production processes. *Stem cells international*, 2016, 2016.

[22] S. Ting, A. Chen, S. Reuveny, and S. Oh. An intermittent rocking platform for integrated expansion and differentiation of human pluripotent stem cells to cardiomyocytes in suspended microcarrier cultures. *Stem cell research*, 13(2):202–213, 2014.

[23] Y. Wang and F. Ouyang. Bead-to-bead transfer of vero cells in microcarrier culture. *Bioprocess Engineering*, 21(3):211–213, 1999.

[24] S. Frauenschuh, E. Reichmann, Y. Ibold, P. M. Goetz, M. Sittinger, and J. Ringe. A microcarrier-based cultivation

system for expansion of primary mesenchymal stem cells. *Biotechnology Progress*, 23(1):187–193, 2007.

[25] C. Sion. *Development of an optimized perfused-continuous process of culture of human umbilical cord mesenchymal stem cells (hMSC) grown on innovative adhesion supports*. PhD thesis, Université de Lorraine, 2020.

[26] A. M. A. Al-Qarakhli, N. Yusop, R. J. Waddington, and R. Moseley. Effects of high glucose conditions on the expansion and differentiation capabilities of mesenchymal stromal cells derived from rat endosteal niche. *BMC Molecular and Cell Biology*, 20(1):1–18, 2019.

[27] V. D'Esposito, M. Lecce, G. Marenzi, S. Cabaro, M. R. Ambrosio, G. Sammartino, S. Misso, T. Migliaccio, P. Liguoro, F. Oriente, et al. Platelet-rich plasma counteracts detrimental effect of high-glucose concentrations on mesenchymal stem cells from bichat fat pad. *Journal of tissue engineering and regenerative medicine*, 14(5):701–713, 2020.

[28] C. Sion, C. Loubière, M. Wlodarczyk-Biegun, N. Davoudi, C. Müller-Renno, E. Guedon, I. Chevalot, and E. Olmos. Effects of microcarriers addition and mixing on wj-msc culture in bioreactors. *Biochemical Engineering Journal*, 157:107521, 2020.

[29] C. Fehrer, R. Brunauer, G. Laschober, H. Unterluggauer, S. Reitinger, F. Kloss, C. Gülly, R. Gaßner, and G. Lepperdinger. Reduced oxygen tension attenuates differentiation capacity of human mesenchymal stem cells and prolongs their lifespan. *Aging Cell*, 6:745–757, 2007.

[30] C. Maillot, C. Sion, N. De Isla, D. Toye, and E. Olmos. Quality by design to define critical process parameters for mesenchymal stem cell expansion. *Biotechnology Advances*, 50:107765, 2021.

[31] J. Hupfeld, I. H. Gorr, C. Schwald, N. Beaucamp, K. Wiechmann, K. Kuentzer, R. Huss, B. Rieger, M. Neubauer, and H. Wegmeyer. Modulation of mesenchymal stromal cell characteristics by microcarrier culture in bioreactors. *Biotechnology and bioengineering*, 111(11):2290–2302, 2014.

4.5 Annexes and supplementary material

4.5.1 Impact of glucose concentration on MSC seeding and growth

Cell cultures in bioreactors were performed using the α-MEM medium supplemented with glutamine, an antibiotic antimycotic solution and LPH. This medium was identical to the medium used for cell cultures which were performed in spinner flasks described in Chapter 2. However, past experiments performed by Dr. Sion at the University of Lorraine identified a faster growth in bioreactors compared to spinner flasks for a same microcarrier concentration [25]. These results, as well as small scale results for which cell growth was not inhibited by adding plastic particles, indicated that feeding strategies which consisted solely on medium exchanges every 3 or 4 days were insufficient to deliver sufficient glucose for cell growth. Accordingly, glucose concentration in the cell culture media was expected to be a limiting factor for cell growth. In accordance with the work of Shop et al, human MSCs were found to have higher glucose requirements compared to other MSC cell sources (including goat MSCs) [14].

As a result, bioreactor cell cultures were performed at two glucose concentrations to define if glucose could be a limiting parameter for cell growth. To begin with, a first culture of MSCs was performed in the medium described above, identical to the medium used for small scale studies. The glucose concentration in the basal α-MEM medium was of 1 g L^{-1}. Cells were also expanded in a second operating condition to which glucose was added in the cell culture medium at a final concentration of 4 g L^{-1}. This glucose concentration was chosen in accordance with literature concerning MSC expansion on microcarriers in STRs. Inoculation and medium exchanges, performed every 3 or 4 days for feeding in both conditions, were performed with either the basal medium or the basal medium supplemented with glucose respectively.

To begin with, cultures in both conditions had similar seeding efficiencies as presented in Figure 4.27, left indicating that the added glucose did not significantly impact the seeding phase. In addition, viable cell counting indicated that cells had a greater growth rate when increasing the glucose concentration in the cell culture medium from 1 to 4 g L^{-1} as presented in this same figure. The calculated apparent growth rates μ_{app} (defined by fitting the experimental viable cell density measurements with the exponential model of Equation 4.2 during the duration where growth was observed) were of 0.016 h^{-1} and 0.026 h^{-1} respectively indicating a 30 % increased growth when glucose was supplemented in the basal medium. Both conditions indicated a maximum amount of cells on the microcarriers of approximately 225 million cells. Specifically, an average quantity of 252 million cells were estimated via sampling in conditions performed with the basal medium and the same estimation was of 227 million cells when glucose was supplemented to the basal medium. This difference was not found to be significant when considering the sampling variability illustrated by the error bars in

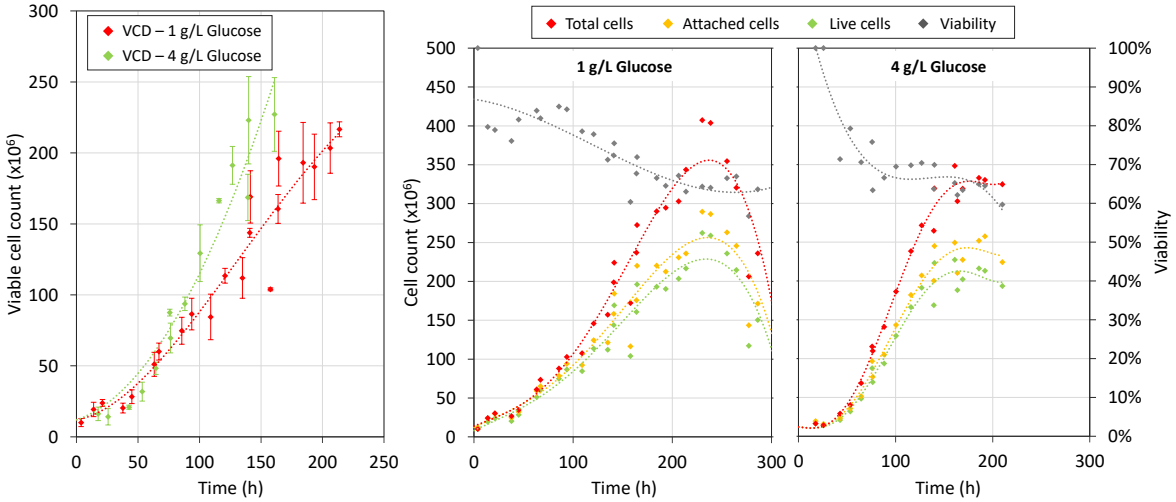

Figure 4.27: Impact of glucose concentration on MSC growth and death kinetics. Left : viable cell density measured offline in triplicate analysis. Center (without glucose addition) and right (with glucose addition) : bi-daily quantification of live cells attached on microcarriers (green), total live and dead cells attached on microcarriers (orange) and total cells in the STR including lysed cells quantified by LDH measurement (red). Overall viability (live cells according to total cells) are presented in gray. Polynomial trends were plotted for comparison between conditions.

Figure 4.27, left (representing the standard deviation between the three independent samples measured at each time point). The maximum cell concentration measured here may represent the maximum confluence cells can achieve in these conditions. However, this level of confluence was achieved after approximately 160 hours when glucose was supplemented, compared to after approximately 230 hours when glucose was not supplemented in the cell culture medium. Table 4.6 summarizes the key growth parameters observed in both conditions.

Table 4.6: Characteristic constants of MSC experiments in STRs during the growth phase with or without glucose supplementation to the basal medium

	Growth phase duration (hours)	X_f (live cells)	μ_{app} (h^{-1})
Glucose (1 g/L)	230 h	252 million	0.016
Glucose (4 g/L)	161 h	227 million	0.026

In addition, live and dead cell populations were quantified daily during both cell cultures and presented in Figure 4.27 center (no extra glucose supplementation), and right (extra glucose supplementation). For both of these graphs, the number of live (green), attached (yellow) and total (red) cells are represented with the same scale presented in million cells on the left. The attached cells represent the sum of live and dead cells counted on microcarriers after microcarrier dissolution. The total amount of cells represents the sum between the live cells measured on microcarriers and the estimated total dead cells (measured by LDH quantification). The total viability is presented in gray for which the same scale is used for both figures and presented on

the right of the figure. The number of live cells attached on microcarriers were divided by the total amount of cells measured to calculate viability. The amount of live cells which were not attached to microcarriers was considered as negligible. For each set of experimental data, polynomial relations were used to graphically represent trends.

The results tend to indicate that similar live and dead cell profiles exist in both cell cultures which were performed with the same microcarrier concentration and identical seeding conditions. In both cases, the live, attached and total cell counts are comparable at the end of the growth phase (approximately 220 hours for 1 g L^{-1} and 150 hours for 4 g L^{-1} glucose concentrations). In addition, the total viability measured gradually decreased from over 90 % to a plateau of approximately 65 % at the end of the growth phase. At this stage of the cell culture, an attached viability of 92 % was observed on the microcarriers. This viability would represent the expected viability of cells recovered from the microcarriers at the maximum harvesting time point. Live and dead cell populations at the end of the growth phase and viability were not significantly impacted by adding glucose. Similarly, the cell culture of MSCs isolated from the endosteal niche of compact rat bone also indicated a more rapid an persistent proliferation in hyperglycyamic conditions (25 mM or 4.5 g L^{-1}) compared to normoglycaemic conditions (5.5 mM or 1 g L^{-1}) [26]. Controversially, similar experiments performed with human MSCs from Bichat's buccal fat pad indicated lower cell counts after expansion in high glucose concentrations (25 mM) compared a control condition at low glucose concentration (5.5 mM) [27]. The authors however noted that using platelet rich plasma counteracted this detrimental effect. As a result, it is possible that the impact of glucose concentration on growth have multi-parametric origins for which cell source and the medium supplementation method may also need to be considered.

4.5.2 Impact of glucose concentration on MSC metabolism

In parallel, the glucose consumption and lactate production in the medium were quantified daily through offline analysis of the cell culture supernatant. For this, both the glucose and lactate concentration in the cell culture supernatant as well as the cumulative glucose consumed concentration and cumulative lactate production concentration are presented in Figure 4.28, left. Results indicate that the amount of consumed glucose corresponds with the amount of lactate produced (in grams) in both tested conditions, indicating, in general, a preferential glycolitic metabolism.

Little impact on metabolic trends were observed when increasing the glucose concentration in the basal medium. In both tested conditions, the average glucose consumption and lactate production rates (respectively $Y_{Gluc/X}$ and $Y_{Lac/X}$ were of approximately 8 ng per cell as presented in Table 4.7 during the exponential growth phases. Accordingly, in both conditions, the average transformation yield of lactate from glucose $Y_{Lac/Gluc}$ was found to be close to 1 as already noticed from the cumula-

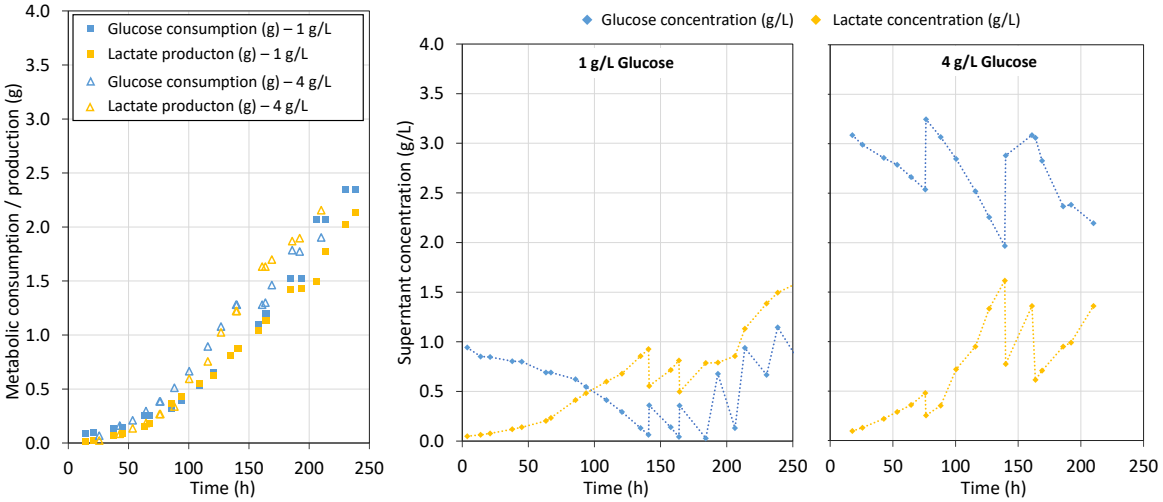

Figure 4.28: Impact of glucose concentration on MSC metabolism. Left : accumulated glucose consumption and lactate production (in grams produced or consumed in the tank) during the cell culture. Middle and right : glucose and lactate concentration in the cell culture supernatant measured offline without and with glucose supplementation respectively.

tive metabolic consumption and production trends. The data reported is coherent with similar expansion of human MSCs isolated from bone marrow which identified specific glucose consumption rates of 9.2 pmol cell^{-1} day $^{-1}$ (or 1.6 ng cell^{-1} day $^{-1}$) for a duration of approximately 10 days [14]. These authors reported $Y_{Lac/Gluc}$ values of 1.96 during expansion in normoxic conditions indicating an oxydative metabolism which is not comparable (the experiments presented in the present study were performed in hypoxic conditions). In experiments cultivating MSCs in normoxic conditions on microcarriers, authors reported $Y_{Lac/Gluc}$ values between 0.6 and 0.8 depending on the feeding strategy which are similar to the results obtained in the present work [28].

Table 4.7: Metabolic rates over the growth phase in MSC experiments in STRs with or without glucose concentration.

	$Y_{Gluc/X}$ ng/cell	$Y_{Lac/X}$ ng/cell	$Y_{Lac/Gluc}$ g/g	$Y_{Glut/X}$ nmol/cell	$Y_{NH3/X}$ nmol/cell
Glucose (1 g/L)	8.9	7.7	0.86	2.2	15.8
Glucose (4 g/L)	7.6	5.4	0.71	1.0	6.7

In addition, the supernatant concentrations of both glucose and lactate in both conditions are presented in Figure 4.28, middle (without adding glucose) and right (with the addition of glucose). It can be noted that a glucose concentration of 1 g L^{-1} in the culture medium is insufficient to allow a adequate regulation of glucose concentration during the whole culture as indicated by the repetitive drop of glucose concentration to 0 g L^{-1} after approximately 140 h (even considering daily medium exchanges). The control of glucose concentration was found to be much more adequate for cultures performed with a glucose concentration of 4 g L^{-1} in the cell culture media. In these conditions, the supernatant no longer reached critical concentrations below

0.2 g L^{-1} [14]. It can be noted that in both tested conditions, the supernatant lactate concentration reached a maximum of approximately 1 g L^{-1}. Inhibition of growth was identified for human bone marrow MSCs at concentrations of 35 mM or 0.3 g L^{-1} in normoxic conditions. The lactate concentrations in these experiments were found to be above this threshold but considering the significant growth observed, the inhibition by lactate is expected to be negligible. It is possible that the inhibition of growth by lactate be enhanced in normoxic conditions as it has been suggested that cells may have a higher susceptibility to cell death at elevated oxygen concentrations [29]. It is also possible that cell metabolic sensibility to parameters such as oxygen and lactate concentration depend on the origin of the cells which are being expanded and that this sensibility be difficult to predict without performing large scale expansion of these cells (the complexity and multi-parametric aspect of MSC cell culture should be kept in mind as reviewed in [30]).

Metabolism was also evaluated by quantifying glutamine and ammonium in the cell culture medium in order to ensure that glutamine concentration was not a limiting factor, and that ammonium concentrations did not reach inhibitory concentrations [14]. Results presented in Figure 4.29 indicate that, during the exponential growth phase, both the ammonium production and glutamine consumption followed similar trends (differences were found negligible). These observations were confirmed by calculating the average glutamine consumption $Y_{Glut/X}$ and ammonium production $Y_{NH_3/X}$ rates which were of approximately 15.8 and 6.7 nmol $cell^{-1}$ respectively (presented in Table 4.7). It can be noted that the feeding strategy in both experiments regulated glutamine concentration between 0.25 mM and 0.5 mM and therefore that glutamine was not a limiting factor. In addition, the produced ammonium was found to have similar profiles with or without glucose supplementation in the cell culture medium although higher NH_3 concentrations were obtained without the addition of glucose. Specifically, NH_3 concentrations were maintained around approximately 2 mM when using the basal cell culture medium and around 1 mM when this medium was supplemented with glucose. It should be noted that inhibitory levels of ammonia have been reported for bone marrow MSCs grown in medium containing over 2.4 mM of NH_3 [14]. Although the reasons for the decreased NH_3 concentrations are not fully understood, the reduction of the NH_3 concentration range during culture is an added benefit to conducing MSC expansion with higher glucose concentrations.

Lastly, the metabolic consumption rates of glucose, glutamine and production rates of lactate NH_3 were plotted for the culture condition which was most favorable for growth (*ie.* basal medium supplemented with glucose at a final concentration of 4 g L^{-1}). Results can be found in Figure 4.30. The values of r can be used as a tool during process development to estimate the expected metabolic consumption or production over time and specifically depending on growth phases. Globally, glucose consumption and lactate production rates were found to be highest at the beginning of the station-

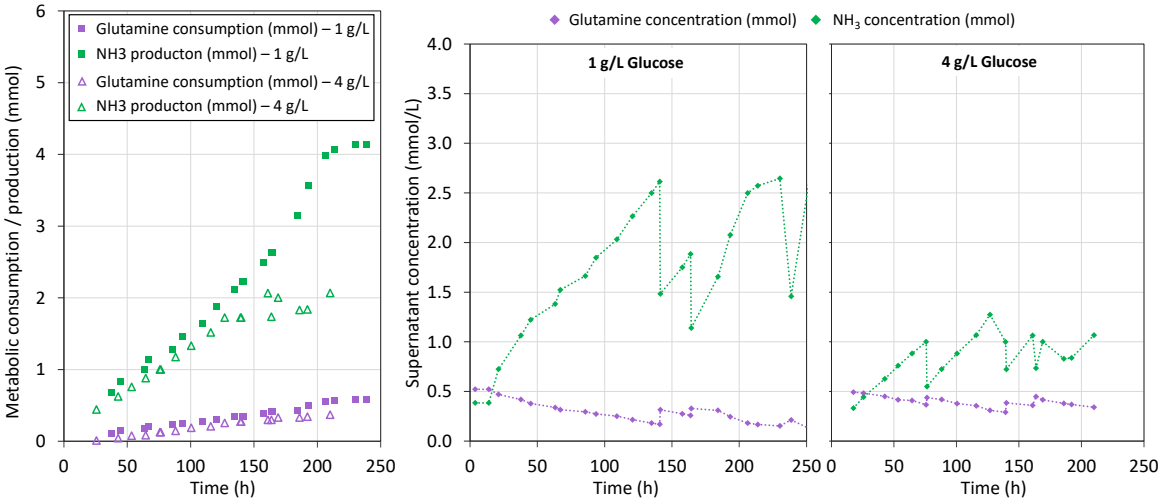

Figure 4.29: Impact of glucose concentration on MSC glutamine metabolism. Left : accumulated glutamine consumption and ammonium production (in milli-moles produced or consumed in the tank) during culture. Middle and right : glutamine and ammonium concentration in the supernatant measured offline without and with glucose supplementation respectively.

ary phase (approximately 120 hours after inoculation). This was associated with a decreased consumption of glutamine and production of NH_3. The results presented in Figure 4.30 will be considered as a control for future experiments.

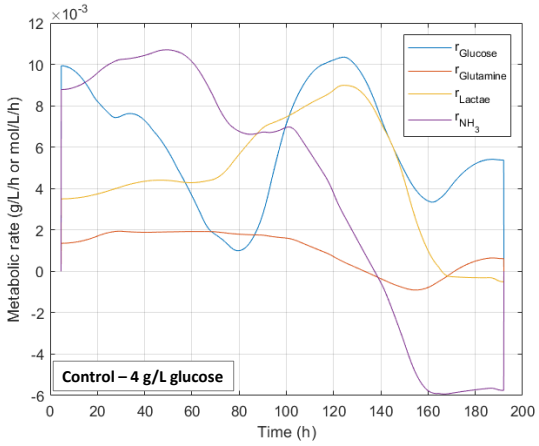

Figure 4.30: Typical consumption and production rates observed in bioreactor cultures fed with medium supplemented with glucose at a final concentration of 4 g L^{-1}.

4.5.3 Discussion

Considering the results presented above, the addition of glucose in the cell culture medium was found to not significantly impact either cell metabolism or cell death. **The addition of glucose to the minimal α-MEM medium was found to be beneficial for MSC cell culture in bioreactors since (1) the apparent viable growth rate was found to be approximately 30 % higher, (2) glucose concentration could be maintained above a critical concentration of 0.2 g $\mathbf{L}^{-1}$ during the entire growth phase and (3) $\mathbf{NH_3}$ supernatant concentration were significantly reduced. These observations were paralleled with the fact that the lactate concentrations were not significantly higher (which could inhibit growth) and glutamine was never found to be completely consumed indicating it was not a limiting factor for growth. As a result, the following cell cultures were performed with a glucose supplementation to the basal cell culture medium to achieve a final concentration of 4 g $\mathbf{L}^{-1}$.**

It can be noted that the feeding strategy presented throughout this chapter consisted in medium exchanges performed every 3 - 4 days by replacing half of the working volume of cell culture supernatant by fresh medium containing glucose (and nutrients required for cell growth). Although the semi-continuous feeding strategy successfully supported MSC expansion (at both glucose concentrations), it could be possible to also reduce metabolic concentration variations during expansion by putting in place a continuous perfused process [6], or a continuous feeding strategy based solely on feeding glucose via the introduction of small volumes of a highly concentrated glucose solution [31]. These feeding strategies could further enhance MSC expansion in bioreactors.

Lastly, it can be noted that the impact of glucose concentration on MSC quality was not demonstrated in this work. It is possible that certain MSC attributed be modified via the increased glucose concentration. For example telomere lengths were found to vary at different rates throughout rat MSC culture expansion at different glucose concentrations [26]. Specifically, hyperglycaemia (25 mM) reduced telomere lengths compared to cultures performed at lower glucose concentrations (4.5 mM). However, phenotyping of the produced cells indicated similar expression of MSC surface markers including CD73, CD90 and CD105 while maintaining negligible levels of CD34 and CD45. Osteogenic differentiation (and adipogenic to a lesser extent) was also generally inhibited by hyperglycaemia. Phenotyping of the cells produced at high glucose concentration will be presented in subsequent chapters and indicated no significant degradation of MSC surface markers tested. This should be confirmed by differentiation testing and also possibly testing of MSC senescence markers to detect if the added glucose in hypoxic conditions in bioreactors could lead to a prematurely senescent phenotype.

Conclusion & perspectives

Concluding remarks

The present work aimed at providing experimental and theoretical approaches towards the quantification of microcarrier-microcarrier collisions in bioreactors and to determine the impact that these collisions could have on MSCs grown on microcarriers.

- For this, MSC cultures were preformed at small (Erlenmeyer and spinner flasks) and large scale (Tryton 0.7 L bioreactor) to which different particle concentrations were added in the sole purpose of generating collisions with microcarriers (these particles did not provide any additional cell culture surface for growth). **Comparing results obtained at both scales indicated that microcarrier-microcarrier collisions had significant impacts on MSC growth and death kinetics which are, for now, still not extremely well described**. At small scale, two microcarriers were tested (Cytodex 1 and Synthemax II) at various concentrations and with microcarrier and plastic particles from 4 to 9 $\%_{v/v}$ in Erlenmeyer and from 2 to 7 $\%_{v/v}$ in spinner flasks. At larger scales, the concentrations were reduced and only one microcarrier type was tested (Synthemax II).

- In addition, the impact of microcarrier sedimentation and suspension phases on MSC expansion in bioreactors was determined. For this, cultures in 0.7 L during which intermittent agitation cycles were performed were compared to cultures for which agitation was kept at N_{js}. **Cultures with intermittent agitation were found to have reduced growth and increased death kinetics. Characterizing the particle concentration distribution during suspension phases via light attenuation measures identified that, for low particle concentrations, it may not be advised to suspend at N_{js} due to an increased local particle concentration which could damage cells**. It is expected that the overly concentrated phases determined via these measures may lead to increased particle frictions and collisions which could explain, in part, the cell damage observed.

- Lastly, **experimental techniques that could be used to detect and characterize microcarrier-microcarrier collisions were evaluated**. Few experimental techniques, to this day, allow the direct measurement of small particles such as mi-

crocarriers in STRs and even less focus on particle collision detection. In this work, endoscopic microscopy and acoustic measures were tested in hope to detect individual particle-particle collisions. The endoscopic technology tested was found to not have sufficient resolution to detect collisions and was not used further. High frequency acoustic acoustic measures, on the other hand, were found to have a temporal resolution which could be used to detect particle-sensor collisions when the size of particles was increased. Unfortunately, the detection of individual microcarrier-sensor collisions was not successfully validated. However, individual particle collision detection was used with larger tracer particles in a STR equipped with impellers of different geometries and size and at different agitation rates to detect how these parameters could affect the number and intensity of collisions detected. Accordingly, **a method is proposed to detect, analyse, and model particle-sensor collisions which could be transposed to the detection of microcarriers if individual microcarrier-sensor collisions were to be be validated**.

Perspectives

Although MSC cultures on microcarrier were performed with a rather large range of process parameters in this work (varying scale, microcarrier type, concentration, agitation *etc.*), the results at large scale remained limited. In order to further transpose, or not, the observed results from small scale to larger scales, it would be important to not only repeat the experiments but also complete them with other operating conditions. Additional characterisation of the cellular mechanisms behind the observed kinetic profiles would be valuable including morphological, metabolic or genetic functional alterations. It is possible that the repeated collisional forces, which ultimately depend on particle speed and concentration, may affect other aspects of MSCs not measured in this study as it has been shown that repeated intermittent agitation may affect MSC phenotype [1, 2].

In addition it would be advised to further describe microcarrier concentration distributions throughout the cell culture process for typical microcarrier concentrations and agitation rates which would be applied during MSC expansion. For this, the attenuation measures described could be completed with studies specifically designed for lower microcarrier concentrations. This would typically require the development and calibration of low concentration measurements which would need to need smaller experimental errors at these concentrations. The dynamics of particle suspension but also particle sedimentation could also be investigated [3]. This type of approach could allow a science-based justification of certain process parameters such as agitation and particle concentration for larger scale manufacturing of MSCs.

Lastly, direct measures of microcarrier-microcarrier frictions and collisions should

be developed. These could include extrapolation of local concentration measures and velocity [4] but also local direct measurements of collisions and could be based on indicators such as turbulent collision severity [5]. For this, microscopic endoscopic techniques could be further tested as it has been determined that these online measures can efficiently detect microcarriers in suspension but for which acquisition frequency is currently not sufficient to detect particles colliding withing the fluid flow. Acoustic techniques could be further developed to detect these small particles by either increasing sensibility (for example by changing the piezoelectric technology used, or also possibly by using a frequency analysis after Fourier transformation of the acoustic measures). Both these approaches (individual collision detection and holistic collision detection by frequency analysis) could be complementary to further describe the physical impacts that cells grown on microcarriers may be subjected to.

Overall this work is fully coherent with the general context of ATMP manufacturing, for which current challenges in the way the cell products are and will be produced remain significant bottlenecks. As detailed in this study, certain critical parameters are, to date, still not fully understood. Since measuring cell confluency on the carriers is still quite complex, a separate study focused on this topic may be required. Using online measures such as permittivity profiles or endoscopic microscopy could be useful to define a science-based agitation strategy and ensure the cell-loaded carriers remain in suspension. In addition, aggregation phenomena were observed in this study both at small and large scale and in literature [6, 7]. This is expected to be an issue since may provoke oxygen and nutrient limitations for cells at the center of these large aggregates, sampling difficulty, errors in online measures, and also a degradation of cell quality and growth kinetics. It would be advised to continue the work on aggregation dynamics in order to robustly characterize the size distribution over time of these aggregates depending on controllable process parameters. It is possible that controlling aggregation by process development could lead to a substantial increase in process robustness and possibly increased productivity and product quality.

The approaches detailed in this work typically focused on a holistic approach to process design. No specific applications were envisioned. However, the product of MSC cultures have been shown to be extremely diverse. To begin with, MSCs can be used as cell factories for the production of extracellular vesicles. In this mindset, it would be important to keep in mind that MSC secretome should depend on the level of stress that cells undergo during culture and that the process-based approach detailed here (which primarily focuses on growth, death and metabolic kinetics) may not fully describe all potential impacts. A dynamic analysis of the evolution of the cell secretome throughout MSC cultures (by analysing the content of EVs) would not only be of use for therapeutics where the EVs themselves are the product, but could also be important indicators of cell stress and/or metabolic shifts which could take place during culture. In addition, cell therapy products may require the production of MSCs

for their subsequent differentiation for certain therapeutic applications. For this, cell susceptibility to stress may typically depend on the source of cells used which in turn should individually target individual applications. In addition, increasing mechanical stresses during culture could also be beneficial, for example in differentiation processes which could be performed in bioreactors.

Lastly, it is important to keep in mind that the work presented here is an approach which could aid the development of future ATMP large scale processes in bioreactors. These processes, which for now are not robust and need development, have an immense room for innovation. In this general context, it would be advised to take a step back and routinely think about the context in which the pharmaceutical industry is developing. In a context where global access to healthcare is a major issue worldwide and the source of immense inequalities, it would be interesting to think about the coherency and ethics behind developing personalized medicines which may even further the gap between more economically developed and less economically developed countries. As developers of high-cost therapeutics, it is of our responsibility to value the technological advances which allow us to develop ATMPs, but also the think about ways in which process development could also play a role in limiting inequalities of access to healthcare. In addition, following the repeated alerts by the Intergovernmental Panel on Climate Change (IPCC) on the urgency to tackle climate change, the question of not only the economic cost of developing these advanced therapeutics, but also their ecologic cost should be central. It would be advised to be actors of innovation within the highly pollutant health sector and request that ecological problematics be as central as safety and efficacy problematics. In the health sector, it should be kept in mind that climate change has already harmed human physical and mental health and that this trend is expected to continue. It is crucial that the development of innovative pharmaceutical products not be at the expense of others. For this, we are all actors.

Be the change you want to see in the world - M. Gandhi

Bibliography

[1] D. A. Lee, M. M. Knight, J. J. Campbell, and D. L. Bader. Stem cell mechanobiology. *Journal of Cellular Biochemistry*, 112(1):1–9, 2011.

[2] V. Frank, S. Kaufmann, R. Wright, P. Horn, H. Y. Yoshikawa, P. Wuchter, J. Madsen, A. L. Lewis, S. P. Armes, A. D. Ho, et al. Frequent mechanical stress suppresses proliferation of mesenchymal stem cells from human bone marrow without loss of multipotency. *Scientific reports*, 6(1):1–12, 2016.

[3] A. Tamburini, A. Cipollina, G. Micale, A. Brucato, and M. Ciofalo. Cfd simulations of dense solid–liquid suspensions in baffled stirred tanks: Prediction of suspension curves. *Chemical Engineering Journal*, 178:324–341, 2011.

[4] M. V. Sardeshpande, V. Juvekar, and V. V. Ranade. Solid suspension in stirred tanks: Uvp measurements and cfd simulations. *The Canadian Journal of Chemical Engineering*, 89(5):1112–1121, 2011.

[5] R. Cherry and E. Papoutsakis. Growth and death rates of bovine embryonic kidney cells in turbulent microcarrier bioreactors. *Bioprocess Engineering*, 4(2):81–89, 1989.

[6] Y. Yuan, M. S. Kallos, C. Hunter, and A. Sen. Improved expansion of human bone marrow-derived mesenchymal stem cells in microcarrier-based suspension culture. *Journal of tissue engineering and regenerative medicine*, 8(3):210–225, 2014.

[7] C. Ferrari, F. Balandras, E. Guedon, E. Olmos, I. Chevalot, and A. Marc. Limiting cell aggregation during mesenchymal stem cell expansion on microcarriers. *Biotechnology progress*, 28(3):780–787, 2012.

Chapter 5

Résumé du travail de thèse

5.1 Introduction

Les thérapies cellulaires et tissulaires sont des thérapies innovantes à base de cellules du patient (on parle alors de thérapies autologues) ou de cellules d'un donneur compatible (on parle alors de thérapies allogéniques). Contrairement aux médicaments chimiques ou à base des protéines souvent recombinantes (anticorps monoclonaux par exemple), le fait d'utiliser des cellules en tant que produit permet d'envisager de nouvelles cibles thérapeutiques qui peuvent être difficiles d'accès, et aussi d'augmeter la spécificité en engageant une transition vers des médecines ciblées et personnalisées. Cependant, le caractère vivant des thérapies (pour lesquelles les cellules en elles-même constituent la thérapie) amène aussi une technicité en terme de production. En effet, les procéssus de production de ces nouvelles médecines doivent garantir une qualité des produits cellulaires dont les attributs et moyens de vérification d'activité sont souvent peu définis et/ou complexes. C'est d'autant plus une problématique que la qualité des matières premières peut être variable d'un doneur à un autre, particulièrement dans le cas de thérapies autologues pour lesquelles les patients ont bien souvent un système immunitaire et une qualité de don affecté par leur maladie.

Le contexte actuel des biotechnologies et de la santé est en plein essor suite aux nombreux travaux de recherche et développment, à la progression des études cliniques et à l'autorisation de mise sur le marché (AMM) des premierères thérapies cellulaires. La croissance du marché des biothérapies (actuellement d'environ 200 milliards d'euros) est estimé à 8 - 9 % d'ici 2025. Pour celà, la France a annoncé en 2022 d'investir 800 millions d'euros afin de se positionner en tant que leader des biothérapies et dans la bioproduction de thérapies innovantes en réponse à cet augmentation prévisionnel de marché. Elle vise aussi à renforcer son indépendence des biothérapies étrangères (actuellement 95 % des biothérapies sont importées). En France, et globalement dans le monde, les moyens de produire des thérapies à base de cellules vivantes, adhérentes ou non, sont au coeur des problématiques d'intérêt. Ainsi, le développement de procédés rentables et facilement mis à l'échelle devient nécéssaire pour rendre les nouvelles médecines accessible au plus grand nombre.

Dans ce contexte, la culture de cellules adhérentes, dont les cellules souches mésenchymateuses, peut se faire en bioréacteurs, équipements bien connus des industries pharmaceutiques pour lesquels les procédés de nettoyage, de validation, de contrôle *etc.* sont déjà validés. Afin de favoriser la culture des cellules souches, une culture en aggrégats, en capsules, ou sur des surfaces de culture souvent sphériques appelés microporteurs peuvent être mis en place. Cependant, à nôtre connaissance, aucun essai clinique actuellemnt en cours n'utilise des moyens d'expansion des cellules souches via l'apport de surfaces de culture sous forme de microporteurs. Cette observation est probablement causée par le fait que les essais cliniques actuellement en cours concernent principalement des lots de petites tailles pour lesquels la mise en échelle n'est pas

actuellement une problématique. Cependant, au vu de la progression des essais cliniques ces denières années et des nombreuses AMM accordées par les autorités de santé, les moyens de production des thérapies cellulaires et tissulaires vont devenir une problématique centrale. Ainsi l'étude détaillé dans le présent document tente d'apporter des éléments caractérisant l'impact de paramètres de culture (specifiquement les collisions entre microporteurs) sur la production de CSM dans une optique de production de nouvelles thérapies.

Une présentation de la structure de la thèse est résumée dans la Figure 5.1. Le contexte général, qui fait l'objet du chapitre de l'état de l'art résume les publications connues à ce jour concernant la culture de CSM à visée thérapeutique ainsi que des moyens théoriques et expérimentaux pour estimer les collisions entre microporteurs dans une cuve agitée. Sur cette base, le chapitre 2 présente des études à petite échelle (en flasques Erlenmeyer et spinner) qui ont été effectuées en changeant la concentration en microporteurs. L'impact sur des paramètres cinétiques (taux de croissance, de mort *etc.*) a été évalué. En parallèle, des études ont été réalisées à plus grande échelle dans un bioréacteur avec un volume de travail de 700 mL. D'une part, des expériences d'atténuation de la lumière ont été effectuées dans le labratoire Produit Environnement et Process de l'Université de Liège afin de déterminer l'évolution de concentrations locales en microporteurs au cours de procédés de remise en suspension. Ces expériences ont été complétées par des mesures acoustiques effectuées au Laboratoire des Réactions et de Génie des Procédés de l'Université de Lorraine à Nancy dans l'optique de proposer une méthode expérimentale pour mesurer des colissions que pourraient avoir des microporteurs en contact avec des éléments plongeants du bioréacteur. Ces deux aspects proposent des approches complémentaires pour estimer la fréquence et l'intensité de collisions dans des cultures de CSM sur microporteurs et sont présentées dans le Chapitre 3. Enfin, pour terminer, des cultures de CSM sur microporteurs en biorécateurs ont été effectuées et font l'objet du Chapitre 4. Ces cultures ont été réalisées en utilisant des paramètres opératoires similaires aux études à petite échelle. Les cultures ont été réalisées en présence de deux sources de stress physique : d'une part la mise en place d'agitation intermittente lors de la culture lors desquelles les microporteurs ont été sédimenté et remis en suspension plusieurs fois ; et d'une autre part, via l'ajout de particules plastiques qui avaient pour but de générer des collisions additionnelles sans pour autant ajouter de surface de culture.

Context

Mesenchymal Stem Cells isolated from the Wharton's Jelly of human umbilical cords (hWJ-MSC's) can be expanded in scalable bioreactors using microcarriers (MC).

Current bottlenecks - Impact of MC solid hold-up on MSC growth

Little information on :
1. How microcarrier solid hold-up impacts MSC growth & quality attributes
2. How microcarrier type & size impacts MSC attachment, growth and detachment
3. What physical attributes could be used to define cell death and degradation due to microcarrier collisions

Current bottlenecks - Physical characterization of particles

Little caracterization of :
1. Spatial particle distribution at N_{js} & heterogeneity
2. Particle-particle collision estimations (frequency & intensity)
3. Evolution of local particle solid hold-up during sedimentation - suspension phases

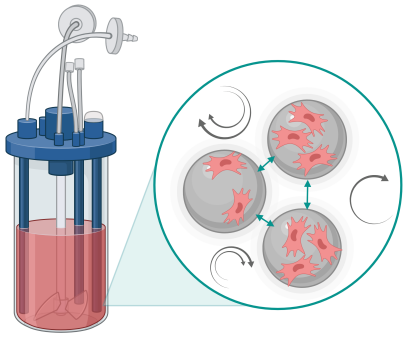

Increasing MC solid hold-up

⊕ Increases the available cell culture surface ⊕

⊖ Provokes additional hydromechanical stresses (friction or MC collisions) which have a possible impact on productivity ⊖

Chapter 2 : Impact of MC solid hold-up on MSC growth and quality attributes

Using different culture systems (Spinner Flasks, Erlenmeyer Flasks) and different microcarriers (Synthemax II & Cytodex-1) at various volume fractions (2.7 - 9 % (v/v)) with or without the additon of particles

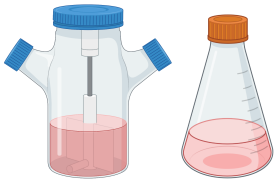

Determination of growth rate, death rate, defined quality attributes

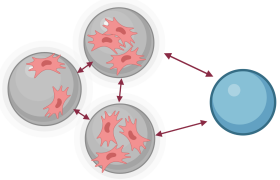

Modelling, prediction and characterization of the impact of particle-particle interactions

Chapter 3 : Particle measurements in STRs

Characterization of particle - sensor collisions based on acoustic measurements

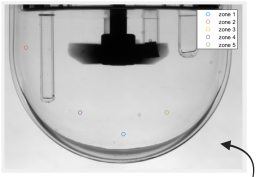

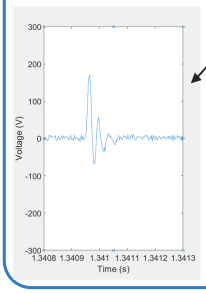

Light attenuation to characterize the solid spatial distribution for various agitation rates and in transient phases (re-suspension)

Chapter 4 : Impact of agitation in automated bioreactors

Cultivating WJ-MSCs at various microcarrier concentrations and using various agitation strategies in order to determine the impact of agitation, sedimentation - resuspension phases and particle solid hold-up on cell growth in controlled and scalable bioreactors

Figure 5.1: Représentation graphique de la structure de la thèse.

5.2 Etat de l'art

Depuis la découverte des cellules souches mésenchymateuses (CSM) et de leurs propriétés de cellules précurseurs mais aussi de leur capacité à orchestrer des réponses via un sécrétome complexe, les applications therapeutiques fleurissent. En effet, en 2011, 123 études cliniques utilisant des cellules souches mésenchymateuses étaient répértoriées par les autorités de santé américaine (archivées par la US National Library of Medicine) [1] alors que ce chiffre s'élevait à 374 études en 2015 [2] et à 803 études cliniques en 2020. Il est cependant intéressant de remarquer que la répartition des études par phase (représentant l'avancement des essais cliniques et démontrant la sureté et l'éfficacité thérapeutique des produits) n'a pas spécialement évolué depuis 2011. L'équipe de Trounson propose dans leurs études que des freins techniques sur la production robuste des cellules pourraient être à l'origine de certains échecs d'essais cliniques. Ainsi, la qualité des produits sont actuellement potentiellement difficilement maitrisables et les auteurs encouragent la recherche et développemnt sur les procédés d'expansion dans ce contexte hautement réglementé.

Pour celà, différentes sources CSM peuvent être envisagées. Typiquement, les sources les plus utilisées concernent la moelle osseuse (qui a historiquement été utilisé dans le plus d'études et d'essais cliniques), le tissu adipeux (qui permet l'isolation des MSC de jusqu'à 500 fois grande que dans les échantillons de moelle osseuse), et du cordon oblilical (qui a l'avantage principal de permettre une isolation des CSM via une méthode non invasive et pour laquelle la source est typiquement jetée). Ces sources présentent chacune des avantages et inconvénients spécifiques au tissu d'origine et à l'indication thérapeutique visée. En particulier, le sécrétome des cellules devrait dépendre, en partie, de la source des cellules car les mécanismes d'actions des cellules sont intimement liées à leur emplacement dans le corps et donc à leur fonction localement. Afin de comprendre, de manière détaillée, les liens possibles entre paramètres de production et cellules produites, un article de revue intitulé **Quality by design to define critical process parameters for mesenchymal stem cell expansion** a été publié en 2021 dans la revue *Biotechnology Advances* [3]. Pour ce faire, une approche basée sur les recommendations des autorités de santé (principalement les 21-CFR proposés par la food and drug administration américaine, FDA) a compilé les données d'une centaine de publications qui ont évalué l'impact d'un ou plusieurs paramètres de culture en plaques de culture (tissue flask) sur un ou plusieurs attributs qualité. Cette étude à clairement mis en avant l'hétérogénité de procédés de culture dans le monde de la recherche. De plus, il semblerait que l'expertise des différents laboratoires se centre principalement sur des niches de paramètres opératoires plus ou moins étendues, compte tenu du grand nombre de paramètres à optimmiser. Les 14 grandes familles de paramètres opératoires définies dans cette étude montrent aussi la compléxité de la culture de CSM qui est effectué dans un environnement très variable pour lesquels

l'interdépendence des paramètres opératoires est certain.

Dans un environnement plus complexe mais plus facilement controlable, les bioréacteurs, cette interdépendence des paramètres opératoires est aussi anticipée. Ainsi, il est probable que l'impact de certain paramètres démontrés dans une condition opératoire ne le soit pas dans un autre contexte (par exemple en changeant la source des cellules étudiées). De ce fait, le contôle en ligne de paramètres de croissance, de métabolisme *etc.* permettrait de détecter d'éventuelles dérives au cours de la culture qui pourraient être causées par des variations de qualité de cellule initiale, de choix de milieu de culture *etc.* Une revue des techniques de culture des CSM en biorécateurs à été effectuée et montre, comme les études à petite échelle en plaques, que les étudues publiées par des équipes de recherche témoignent généralement d'une expértise spécifique sur un ensemble de paramètres opératoires et avec un équipement donné. Par exemple, certaines equipes se sont spécialisées sur la culture de CSM dans des systèmes de roues verticales (virtical wheel) [4], alors que d'autres, comme le LRGP, se sont spécialisés principalement sur des techniques de culture en bioréacteurs [5]. En ce qui concerne la culture de CSM sur micoroporteurs en biorécateurs, l'absence d'études robustes qualifiant et quantifiant l'impact de collisions entre microporteurs nous a semblé être un point particulièrement critique.

En effet, certaines études démontrent que l'augmentation de la concentration en microporteurs est associée (après un certain seuil) à une baisse du taux de croissance apparent de fibroblasts [6]. Ces études, précurseures mais détaillées, n'ont pas été répétées pour d'autres types cellulaires dont les CSM. Alors qu'une baisse du taux de colonisation de CSM pour de fortes concentrations en microporteurs a été notée lors de cultures en spinners [7], la quantité d'études à ce sujet restent extrêmement limitéesbien qu'un fort impact soit anticipé. En parallèle, les méthodes de quantification des collisions entre particules de petites tailles et de faible densité, tels les micropr-teurs, restent actuellement limitées et peu appliquées pour ce type de procédés de cultures dont les volumes et équipements ont une certaine spécificité. Ainsi, l'approche multi-disciplinaire visant à regrouper (1) des méthodes expérimentales pour estimer des collisons dans un bioréacteur utilisé pour les cultures de CSM et (2) des mesures biologiques obtenues lors de cultures de CSM réalisées à différentes échelles en variant la quantité de collisions que subissent les cellules cultivées lors de leur expansion semble être un sujet d'étude pertinent.

5.3 Impact de la concentration en microporteurs sur la croissance de CSM à petite échelle

Le Chapitre 2 avait pour objectif de présenter l'impact de la concentration en microporteurs sur les cinétiques de croissance des CSM sur microporteurs. Pour celà,

une approche similaire à celle proposée par Croughan et al. [6] a été mis en place. L'approche ainsi que les résultats obtenus à petite échelle (en flasquer Erlenmeyer et spinner) ont fait l'objet d'un article intitulé **Impact of microcarrier concentration on mesenchymal stem cell growth and death : experiments and modelling** publié en 2022 dans la revue *Biotechnology Bioengineering* [8]. Les principaux résultats démontrés concernent la corrélation entre la concentration en particules plastiques rajoutées lors des cultures (qui simulaient des collisions particules - microporteurs sans pour autant rajouter de surface colonisable par les cellules) et une baisse du taux de croissance apparent à la fois pour les cultures en Erlenmeyer et en spinner, et pour deux types de microporteurs testés (Cytodex 1 et Synthemax II). Les résultats sont présentés en Figure 5.2. Plus précisément, cette baisse de taux de croissance n'était pas observée uniquement en variant la concentration en microporteurs totales dans les cultures à petites échelles. Ces résultats indiquent, que l'effet du changement de concentration en microporteurs lors de cultures de CSM fait surement l'objet de deux phénomènes antagonistes :

- L'ajout de microporteurs rajoute des surfaces colonisables lors de la culture de CSM et donc la concentration cellulaire volumique. Comme les CSM produisent des facteurs de croissance il est possible que l'augmentation de cette concentration cellulaire soit associé à un effet bénéfique sur la croissance.

- L'ajout de microporteurs rajoute des phénomènes physiques entre porteurs (frictions, collisions *etc.*). Ces phénomènes sont associés à une augmentation de la constante de mort et provoquent une lyse prématurée des cellules.

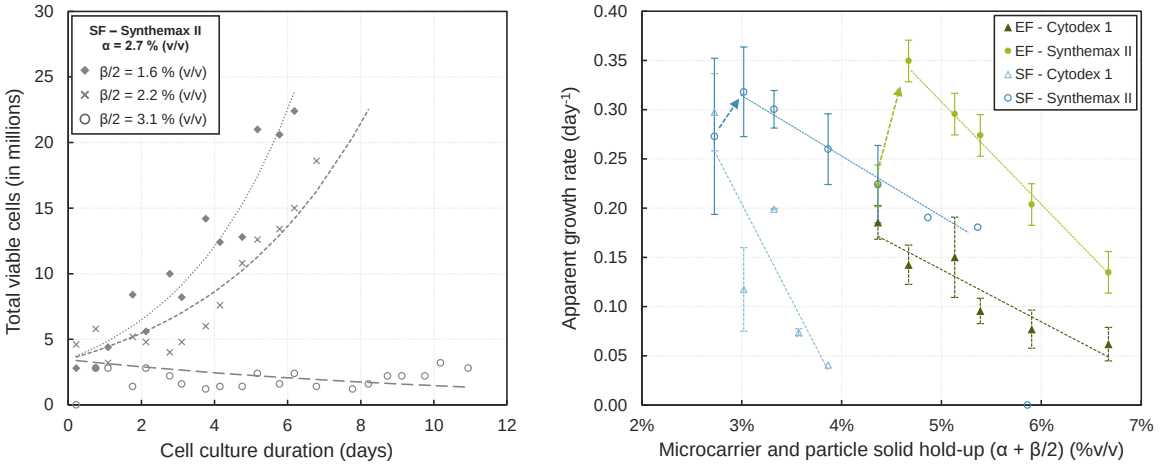

Figure 5.2: Impact de l'ajout de particules plastiques sur le taux de croissance apparent des MSC. Gauche : comptage des cellules viables à différentes concentrations de particules plastiques ajoutées et modèles exponentiels correspondents permettant l'estimation du taux de croissance apparent. Droite : taux de croissance apparent mesuré pour des expériences en flasques Erlenmeyer (EF) et spinner (SF) pour des microporteurs Synthemax II et Cytodex 1.

De plus, une modélisation de la baisse de taux de croissance apparent en fonction de paramètres physiques tels que le ratio entre la distance moyenne entre particules h et la valeur moyenne de l'échelle de Kolmogorov λ_k a été proposé afin de modéliser, au mieux, les résultats expérimentaux obtenus à la fois en flasques Erlenmeyer et spinner et en tenant compte des résultats obtenus sur les microporteurs Cytodex 1 et Synthemax II.

5.4 Caractérisation de collisions entre microporteurs via des techniques d'atténuation de la lumière et l'analyse de signaux acoustiques

Ce chapitre avait pour objectif de mettre au point des méthodes expérimentales et des traitements automatiques de ces données afin de proposer une démarche pour estimer le nombre et l'intensité de collisions entre mcroporteurs dans un bioréacteur en fonction del'agitation, de la géométrie de l'équipement mais aussi de la concentration en porteurs.

Pour commencer, une analyse approfondie des écoulements a été effectuée par simulation de la dynamique des fluides. Cette analyse a été réalisée par la docteure Loubière à l'Université de Lorraine en se basant sur les précédents travaux publiés [9]. Ces résultats prélimiaires ont permi d'avoir une notion assez précise de la répartition spatiale de grandeurs physiques telles que l'échelle de Kolmogorov, le nombre de Stokes, le nombre de Reynolds *etc.*

Ensuite, des mesures d'atténuation de la lumière ont été réalisées à l'Université de Liège se basant sur la mise au point expérimentale réalisée par la docteure Delafosse [10]. L'analyse de vidéos dans ce montage expérimental ont permis d'appécier les phénomènes de remise en suspension de microporteurs Cytodex 1 à deux vitesses d'agitation comme l'est visible sur la Figure 5.3.

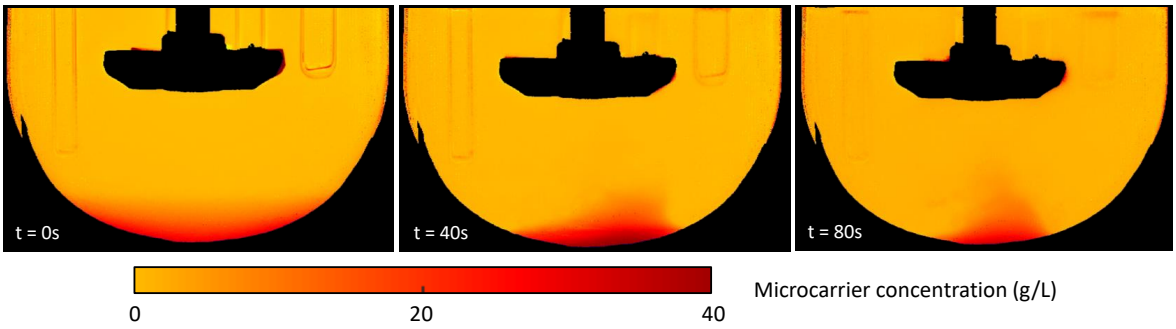

Figure 5.3: Distribution des concentrations en microporteurs lors de la remise en suspension à 70 rpm. Les images correspondendent aux concentrations recalculées après 0, 40 et 80 secondes d'agitation.

Une proposition d'analyse d'image en définissant des grandeurs tels que des facteurs

de sur-concentration ou des temps de mélange ont été proposés dans le Chapitre 3.2. Ces approches quantitiatives permettent de comparer des procédés de remise en suspension entre eux. Les enjeux sont particuliers concernant la remise en suspension de microporteurs principalement à cause de leur petite taille et de leur densité proche de celle de l'eau ce qui rend les modèles typiquement utilisés pour caractériser la suspension difficilement applicables. De plus, ces approches sont intéressantes concernant les procédés de culture à base de cellules humaines car, encore au jourd'hui, peu d'études publiées caractérisent la suspension des microporteurs alors qu'ils sont probablement voués à être de plus en plus utilisés pour l'expansion de cellules adhérentes en réacteurs.

En parallèle, des mesures acoustiques ont été décrites dans le but de montrer une preuve de concept concernant la possibilité de détecter des collisions individelles entre des particules et un capteur placé dans le bioréacteur. Pour ce faire, des particules avec la même densité que les microporteurs mais environ 8 fois plus grosses ont été utilisées. les collisions individuelles ont été détéctées, caractérisées et modélisées en tenant compte d'agitateurs de différentes géométries et tailles. La modélisation finale est présentée en Figure 5.4 et montre une bonne corrélation entre les collisions détectées et le modèle (basée sur une mesure coréllée au nombre de Reynolds). La même approche a été réalisée en utilisant un modèle adimentionnel se basant sur la puissance et indique les mêmes résultats. Une approche similaire a démontré la possibilité de modéliser les intensités moyennes mesurées de la même manière. Ces résultats n'ont pas pour vocation d'être pris en tant que tel mais surtout de démontrer une démarche et une preuve de concept sur l'utilisation de capteurs acoustiques en bioprocédés. Il serrait intéressant de compléter ces résultats avec des résultats dont les paramètres opératoires ont été modifiés par exemple en modifiant la viscosité du fluide, l'emplacement du capteur, la taille de la cuve et surtout, en développant la technique pour détecter les collisions individuelles de plus petites particules comme les microporteurs.

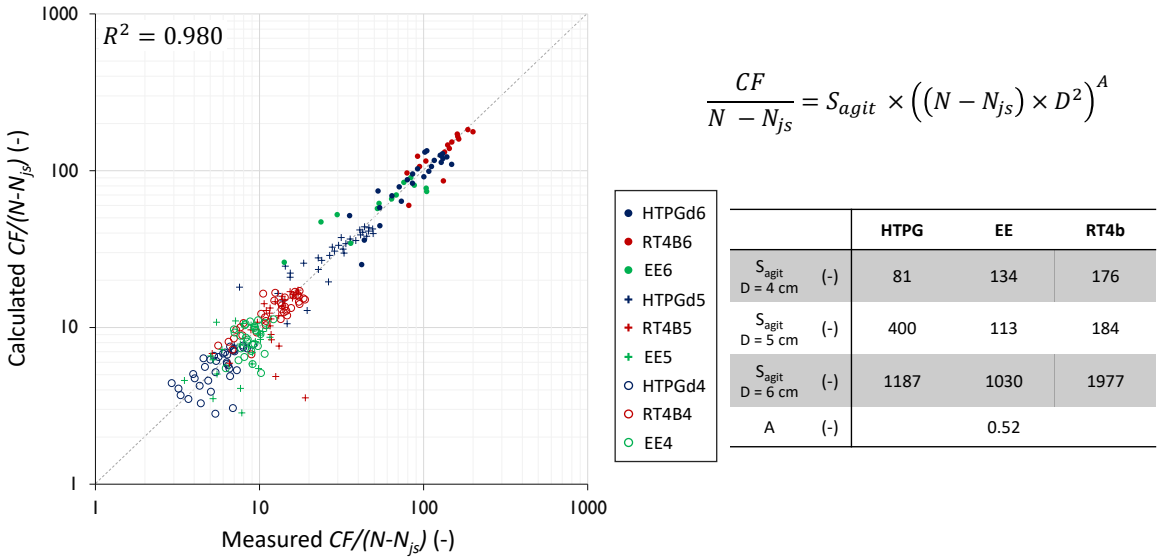

$$\frac{CF}{N - N_{js}} = S_{agit} \times \left((N - N_{js}) \times D^2\right)^A$$

		HTPG	EE	RT4b
S_{agit} D = 4 cm	(-)	81	134	176
S_{agit} D = 5 cm	(-)	400	113	184
S_{agit} D = 6 cm	(-)	1187	1030	1977
A	(-)		0.52	

Figure 5.4: Comparaison entre la fréquence de collisions estimée via le modèle et les mesures expérimentales.

5.5 Impact des intéractions entre particules lors de la culture de CSM en bioréacteurs

Des cultures de CSM ont été mis en place en bioréacteurs en prolongement de travaux précédents ayant démontré l'expansion possible de cellules issus de cordons ombilicaux sur des microporteurs Synthemax II fournis par Corning [5]. Comme démontré prédécement, les cellules ont pu être cultivées dans ces conditions. De plus, l'impact des intéractions entre particules a été évalué pas deux méthodes. Premièrement, l'impact de cycles d'agitation intérmittente a été déterminé. Ces cycles ont été définis afin de mimer d'éventuelles phases de *bead-to-bead* permettant la migration de CSM vers de nouveaux microporteurs ajoutés au cours de la culture, ou d'éventuels changements de mileux qui requierent la sédimentation et la mise en suspension des microporteurs. Comme défini dans le Chapitre 3.2, les phases de remise en suspension génèrent des concentrations locales en particules très concentrées qui peuvent avoir des impacts actuellement peu connus sur la croissance. Dans le cadre de ce Chapitre, ces phases de remise en suspension ont provoqué une baisse du taux de croissance apparent ainsi qu'une augmentation de la constante de mort comme indiqué en Figure5.5.

De plus, des cultures ont été effectuées avec l'ajout de particules plastiques à des concentrations de 0.5 et 2.3 $\%_{v/v}$. Ces cultures avaient pour but d'être comparé aux résultats similaires obtenus à petite échelle en flasques Erlenmeyer et spinner présentées dans le Chapitre 2. Dans les deux cas, une baisse du taux de croissance apparent a été observé avec l'ajout de ces particules, comme celà avait été observé à petite échelle. De plus, une baisse de la constante de mort a été remarqué avec l'avout de la plus faible concentration en particules plastiques. Cette baisse de la mort peut être causée par des phénomènes d'aggrégation qui peuvent être réduits par l'ajout de faibles concentrations

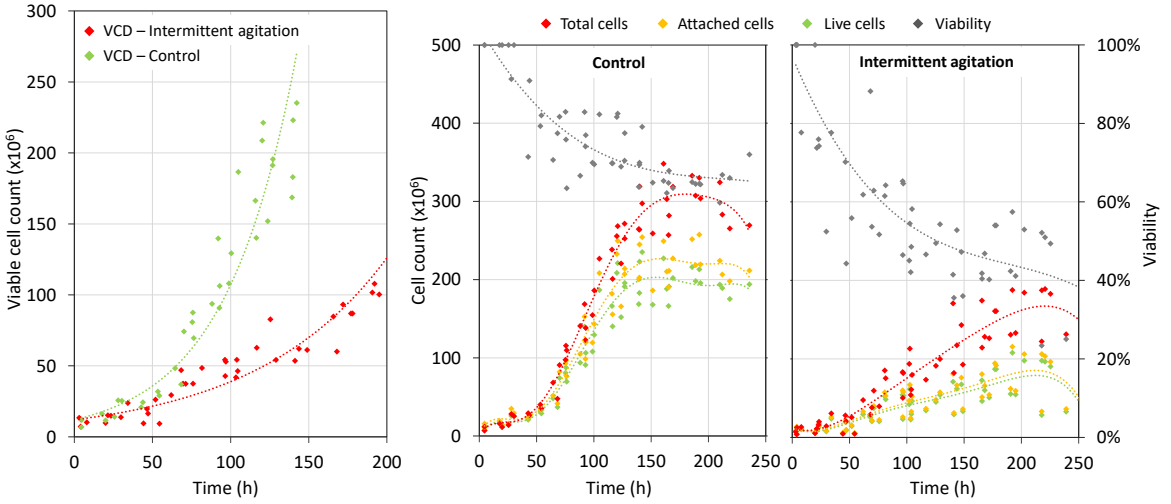

Figure 5.5: Impact de cycles d'agitation intermittente sur les cinétiques de croissance et de mort. Les mesures hors ligne de densité cellulaire viable sont représentés à gauche et les mesures de cellules vivantes (vert), cellules totales attachées (orange) et cellules totales (rouge) sont représentées sur les graphiques du mulieu et à droite

de particules. Ces résultats sont présentés en Figure 5.6.

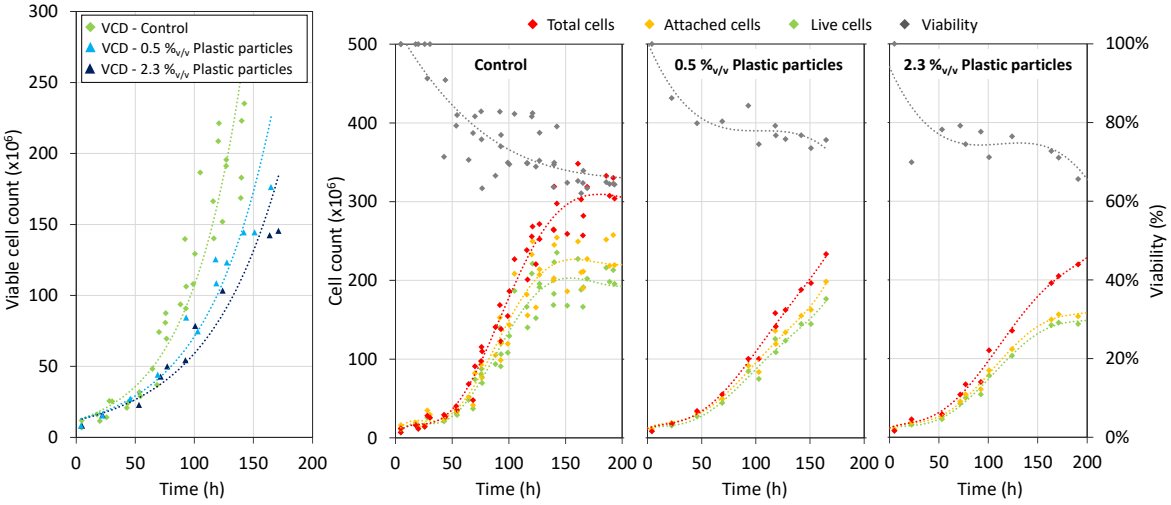

Figure 5.6: Impact de l'ajout de particules plastiques sur les cinétiques de croissance et de mort. Les mesures hors ligne de densité cellulaire viable sont représentés à gauche et les mesures de cellules vivantes (vert), cellules totales attachées (orange) et cellules totales (rouge) sont représentées sur les graphiques du mulieu et à droite

5.6 Conclusion et perspéctives

Les différentes études présentées ont eu pour but d'évaluer, de quantifier et de caractériser l'impact des collisions entre microporteurs sur la culture de cellules souches mésenchymateuses. Pour celà, des cultures de cellules à petite et à grande échelle ont montré l'impact certain de collisions sur les cinétiques de croissance et de mort des CSM qui peuvent être mis en relation avec des estimations de ces collisions proposées via

la mise en place de techniques optiques et acoustiques dans des bioréacteurs de même géométrie. L'ensemble de ces travaux présente une approche précisement détaillé en ce sens.

Cependant, de nombreuses études complémentaires serraient utiles afin de compléter les résultats présentés et apporter un lien entre les différentes études. Premièrement, les cultures cellulaires réalisées ont toutes été effectuées à partir de cellules isolées de cordons ombilicaux. Il est difficile d'estimer à ce stade comment les impacts observés pourraient être extrapolés à d'autres types cellulaires qui pourraient avoir une sensibilité ou une résistence différente face aux contraintes hydro-mécaniques. De plus, il est connu que les collisions seules ne sont pas résponsable de toutes les cinétiques de croissance et de mort observés. Notemment, il est difficile d'estimer la part de l'impact des containtes hydrodynamiques sur les phénomènes observés. Par exemple, l'ajout de particules qui, certes, génèrent des forces de collisions supplémentaires, peuvent avoir des effets sur la phase liquide non évalué à ce stade (par exemple en affectant la viscosité locale qui pourrait aussi entrainer une modification de l'échelle de Kolmogorov locale. En effet, le ratio entre la taille des microporteurs et l'échelle de kolmogorov est souvent utilisée afin d'estimer les valeurs de mort qui pourraient être causées par la turbulence locale. Ainsi, il serrait intéressant d'intégrer des données locales sur les échelles de kolmogorov, les concentrations mesurées, et les estimations de collisions.

De plus, certaines méthodes décrites doivent être considérées à ce jour d'avantage comme une preuve de concept (notemment concernant les mesures acoustiques) qui ne sont pas forcément extrapolable à de plus petites particules. Un modèle global devrait être développé, prenant en compte (1) l'estimation des forces collisionnelles entre une particule sur laquelle les cellules se miltiplient et des éléments fixes du bioréacteur comme d'éventuelles sondes, (2) des estimations de collisions particules - particules et (3) l'impact d'éventiuelles forces frictionnelles qui pourraient être générées par la surconcentration locale en porteurs (qui n'a fait l'objet d'aucune étude ici). Dans un contexte d'autant plus régulé que les thérapies obtiennent des autorisations de mise sur le marché, des approches visant à garder la qualité du produit au centre du développement des procédés vont être nécéssaires. Ces études ont tenté de mesurer l'impact d'un paramètre de culture parmi tous les autres qui interviennent lors d'une culture de cellule sur microporteurs. Des études plus poussés montrant les mécanismes mis en jeu lorsqu'une cellule est soumis à des forces de collision serraient extrèmement intéressantes. De plus, ce type d'études pourraient expliquer, de manière métabolisque, quels mécanismes de dégradation des cellules pourraient expliquer les résultats présentés.

Enfin, les phénomènes d'aggrégation ont fait l'objet d'études préliminaires et parallèles lors des cultures en bioracteurs car ces phénomènes ont été les causes des principaux problèmes techniques dans les études de croissance. Certaines pistes de réflexion ont été abordées, via des mesures en ligne ou hors ligne qui restent relativement sommaires à ce stade. Le fait de comprendre comment maitriser les phénomènes

d'aggrégations pourraient lever un des principaux vérrou actuel technique et permettrait ainsi de réduire l'inhomoénéité dans les bioréacteurs et de limiter l'inhibition de la croissance (et aussi possiblement une dégradation des cellules en parallèle) causée par des difficultés d'apport en nutriments essentiels et d'oxygène au coeur de ces aggrégats.

En ouverture, il serrait inétressant de garder en tête le contexte actuel dans lequel l'industrie pharmaceutique se développe. Malgré les mises en gardes répétés du Groupe International d'Experts sur le Climat (GIEC) sur l'impact certain des activités humaines sur la biodiversité, le changement climatique, mais aussi les problématiques de santé globales, force est de constater que peu de mesures concrètes sont mises en place dans les grandes industries dont fait partie l'industrie pharmaceutique. D'après le sixième rapport du GIEC, les impacts dur réchauffement climatique sur la santé mondiale est significative (avec un degré de confiance *très élevé*). Ainsi, le réchauffement climatique provoquera l'agrandissement de la zone d'impact de certaines maladies, un impact sur la disponibilité et la distribution des ressources en nourriture et en eau qui pourraient être d'autant plus contaminés suite au réchauffement, l'impact de blessures graves causées par des catastrophes naturelles tels les feux de forêt *etc.* Il est primordial de prendre en compte l'impact du développement de nouveaux procédés pharmaceutiques sur les problématiques de santé mondiales dans une approche d'ensemble. En tant que chercheurs, ingénieurs, gestionnaires de projets, enseignants, scientifiques, il est de notre devoir de mesurer l'impact du développement de nos futures innovations.

Bibliography

[1] A. Trounson, R. G. Thakar, G. Lomax, and D. Gibbons. Clinical trials for stem cell therapies. *BMC Medicine*, 9:52, 2011.

[2] A. Trounson and C. McDonald. Stem cell therapies in clinical trials: progress and challenges. *Cell Stem Cell*, 17:11–22, 2015.

[3] C. Maillot, C. Sion, N. De Isla, D. Toye, and E. Olmos. Quality by design to define critical process parameters for mesenchymal stem cell expansion. *Biotechnology Advances*, 50:107765, 2021.

[4] D. de Sousa Pinto, C. Bandeiras, M. de Almeida Fuzeta, C. A. Rodrigues, S. Jung, Y. Hashimura, R.-J. Tseng, W. Milligan, B. Lee, F. C. Ferreira, et al. Scalable manufacturing of human mesenchymal stromal cells in the vertical-wheel bioreactor system: an experimental and economic approach. *Biotechnology journal*, 14(8):1800716, 2019.

[5] C. Sion, D. Ghannoum, B. Ebel, F. Gallo, N. de Isla, E. Guedon, I. Chevalot, and E. Olmos. A new perfusion mode of culture for wj-mscs expansion in a stirred and online monitored bioreactor. *Biotechnology and Bioengineering*, 118(11):4453–4464, 2021.

[6] M. S. Croughan, J.-F. P. Hamel, and D. I. Wang. Effects of microcarrier concentration in animal cell culture. *Biotechnology and bioengineering*, 32(8):975–982, 1988.

[7] A. K.-L. Chen, Y. K. Chew, H. Y. Tan, S. Reuveny, and S. K. W. Oh. Increasing efficiency of human mesenchymal stromal cell culture by optimization of microcarrier concentration and design of medium feed. *Cytotherapy*, 17(2):163–173, 2015.

[8] C. Maillot, N. De Isla, C. Loubiere, D. Toye, and E. Olmos. Impact of microcarrier concentration on mesenchymal stem cell growth and death: Experiments and modelling. *Biotechnology and Bioengineering*, 2022.

[9] C. Loubière, A. Delafosse, E. Guedon, I. Chevalot, D. Toye, and E. Olmos. Dimensional analysis and cfd simulations of microcarrier 'just-suspended'state in mesenchymal stromal cells bioreactors. *Chemical Engineering Science*, 203:464–474, 2019.

[10] A. Delafosse, C. Loubière, S. Calvo, D. Toye, and E. Olmos. Solid-liquid suspension of microcarriers in stirred tank bioreactor – experimental and numerical analysis. *Chemical Engineering Science*, 180:52–63, 2018.

Communications

Publications

Impact of microcarrier concentration on mesenchymal stem cell growth and death : experiments and modelling - *Biotechnology Bioengineering*, 2022 - C. Maillot, N. De Isla, C. Loubiere, D. Toye, E. Olmos

Quality by design to define critical process parameters for Mesenchymal Stem Cell Expansion - *Biotechnology Advances*, 2021 - C. Maillot, C. Sion, N. De Isla, D. Toye, E. Olmos

Oral Communications

Using acoustic sensors to monitor microcarrier interactions during adherent cell culture processes in bioreactors - *13th European Congress of Chemical Engineering and 6th European Congress of Applied Biotechnology*, September 20-23 2021 Virtual

Impact of microcarrier concentration on mesenchymal stem cell expansion during their culture in bioreactors - *13th European Congress of Chemical Engineering and 6th European Congress of Applied Biotechnology*, September 20-23 2021 Virtual

Poster Communications

Effects of microcarrier concentration on mesenchymal stem cell culture - *27th ESACT Meeting - European Society for Animal Cell Technology* - June 26-29 2022 Lisbon

Impact of microcarrier concentration on mesenchymal stem cell expansion during their culture in bioreactors - *ISCT New Orleans Virtual Meeting - International Society for Cell and Gene Therapy*, May 26-28 2021 Virtual